THIN FILM PALLADIUM – YTTRIUM MEMBRANES FOR HYDROGEN SEPARATION

by

SEAN FLETCHER

A thesis submitted to

The University of Birmingham

for the degree of

DOCTOR OF PHILOSOPHY

School of Metallurgy and Materials

College of Engineering and Physical Sciences

The University of Birmingham

November 2009

Synopsis

The permeability of hydrogen in thin film Pd-Y composite membranes has been investigated for the first time. Thin (5 μm) Pd-Y films were deposited onto macroporous 316L stainless steel substrates by magnetron sputtering. Prior to deposition, a novel laser melting technique was employed in an attempt to reduce the surface roughness and pore size, thus facilitating the deposition of defect-free films. The active hydrogen transport mechanisms of each layer have been determined, and the observed hydrogen permeability was analysed using a series resistance type model.

Despite the laser melting process, the composite membranes exhibited a certain level of pinholes within the Pd-Y films. The two composite membranes investigated in detail demonstrated H_2 / N_2 selectivity ratios of 5.86 and 5.40.

When corrected for pinholes, the composite membranes exhibited non-diffusion limited permeation. The exponential pressure dependence for permeation, *n*, of the composite membranes was calculated as 0.70 and 0.74. This is in contrast to the values of 0.52 and 0.54, calculated for bulk, self-supporting Pd-Y membranes with corresponding compositions. In addition, the permeability of the composite membranes at 400°C was just 4.1 and 3.2 % of the self-supporting membranes. Such permeability behaviour is in good agreement to that typically reported for Pd, Pd-Ag and Pd-Cu composite membranes.

Application of a series resistance type model revealed that the porous substrate contributes significantly to the observed permeation. At 450°C, the substrates accounted for 40.2 % and 34.6 % of the total resistance of the composite membranes.

When corrected for substrate resistance, the composite membranes, and therefore the Pd-Y thin films, exhibited diffusion-limited permeation. The calculated pressure exponents *n* of 0.53 and 0.58 are in good agreement with those calculated for the self-supporting membranes. Despite correcting for substrate resistance, the permeability of the Pd-Y thin films were only 6.3 % and 4.7 % of that in the self-supporting membranes. It is proposed that, in addition to offering permeation resistance, the porous substrate reduces the active membrane area. The average surface porosity of the substrates was found to be 9.8 % and 5.2 %.

When the appropriate corrections were made for the reduced active area and the substrate resistance, the permeability of the Pd-Y thin films at 400°C were 65.5 % and 90.5 % of the self-supporting membranes. This observation is in good agreement with reported data for free-standing thin film Pd, Pd-Ag and Pd-Cu membranes.

It was concluded that the permeability deviations observed for the composite membranes, were due to the presence of the porous substrate. Thus, in order to achieve the hydrogen flux potentially offered by Pd-Y thin films, further refinements to the structure of the substrate are required.

Acknowledgments

Firstly, I express my sincere thanks to Dr. John Speight and Dr. David Book for their help and advice during the supervision of this project.

I am grateful for the expertise and assistance offered by the external collaborators involved in this work, Dr. Joanne Hampshire, Dr. Ann-Marie Carey and Prof. Lin Li.

Thanks are extended to my friends and colleagues in the Hydrogen Materials Group, both past and present, for their useful discussions, contributions and friendship over the last 4 years.

Finally, a special thank you to Sara. Without your love and support this would not have been possible.

Table of Contents

Chapter 1 – Introduction 1

Section 1 – Introduction 1

Chapter 2 – Literature Review 5

Section 2 – Hydrogen Separation 5

2.1 – Introduction 5
2.2 – Pressure Swing Adsorption 5
2.3 – Cryogenic Distillation 6
2.4 – Hydrogen Selective Membranes 7
2.4.1 – Porous Separation Membranes 7
2.4.2 – Dense Separation Membranes 9

Section 3 – Palladium-based Dense Metal Membranes 12

3.1 – Introduction 12
3.2 – Palladium and Palladium Alloys 13
3.3 – Absorption of Hydrogen in Palladium and Palladium-Yttrium 19
3.4 – Diffusion of Hydrogen in Palladium and Palladium-Yttrium 29
3.5 – Hydrogen Permeation in Palladium and Palladium-Yttrium Membranes 41
3.6 – Current Limitations of Palladium-based Membranes 48

Section 4 – Thin Film Palladium and Palladium-alloy Membranes 51

4.1 – Introduction 51
4.2 – Palladium and Palladium-alloy Thin Film 52
4.2.1 – Membrane Deposition 53
4.2.2 – Membrane Integrity and Defects 60
4.3 – Porous Substrates 62
4.4 – Thin Film / PSS Interface Layer 67
4.5 – Current Limitations of Pd / PSS Composite Membranes 71

Section 5 – Hydrogen Permeation in Pd / PSS Composite Membranes 82

5.1 – Introduction 82
5.2 – Palladium-based Thin Film 84
5.3 – Porous Substrate 86
5.4 – Thin Film / Substrate Interface Layer 91
5.5 – Hydrogen Permeation through Multilayered Composite Membranes 93

Section 6 – Palladium Yttrium / PSS Composite Membranes 97

Section 7 – Project Aims 99

Chapter 3 – Experimental Techniques 100

Section 8 – Experimental Techniques 100

8.1 – Introduction 100
8.2 – Material and Sample Preparation 100
8.2.1 – Rolled Foils / Bulk Alloys 100
8.2.2 – Thin Film Alloys 102
8.2.3 – Porous Substrates 104
8.2.4 – Substrate Surface Modification 104
8.2.5 – Composite Pd-Y / PSS Membrane Production 107
8.3 – Material Characterisation and Analysis 110
8.3.1 – Membrane Composition and Structure 110
8.3.1.1 – Scanning Electron Microscopy 110
8.3.1.2 – X-Ray Diffraction 110
8.3.2 – Membrane Surface Metrology 111
8.3.2.1 – Confocal Laser Microscopy 111
8.3.3 – Membrane Alloy Hydrogen Solubility 112
8.3.3.1 – Gravimetric Analysis 112
8.3.4 – Membrane Permeability Assessment 114
8.3.4.1 – Membrane Testing Facility 114

Chapter 4 – Results and Discussion 122

Section 9 – Dense Pd-Y Membrane 122

9.1. – Rolled Foils 123
9.1.1 – Alloy Assessment and Composition 123
9.1.2 – Hydrogen Permeability 129
9.2. – Thin Films 149
9.2.1 – Alloy Assessment and Composition 149
9.2.2 – Film Adhesion, Integrity and Thickness 153
9.2.3 – Projected Hydrogen Flux 156

Section 10 – Porous Substrate 157

10.1 – Introduction 157
10.2 – Structure and Topography 157
10.2.1 – As-Received PSS 157
10.2.2 – Stainless Steel Coated PSS 159
10.2.3 – Laser Melted PSS 160
10.3 – Gas Permeability 168
10.3.1 – As-Received PSS 169
10.3.1.1– The Effect of Temperature 173
10.3.2 – Laser Melted PSS 178
10.3.2.1 – The Effect of Temperature 182
10.3.2.2 – The Effect of Gas Species 185

Section 11 – Composite Pd-Y / PSS membrane 188

11.1 – Introduction 188
11.2 – Composite Membrane Structure 189
11.3 – Composite Membrane Permeability 195
11.3.1 – Molecular Transport 195
11.3.2 – Measured Hydrogen Flux 199
11.3.3 – Composite Membrane Permeability - General Permeability Equation 202
11.3.4 – Composite Membrane Permeability - Series Resistance Model 211

Section 12 – General Discussion 235

Chapter 5 - Conclusions 240

Section 13 – General Conclusions 240

Section 14 – Further Work 245

Appendix I **247**

Method for Determining Membrane Geometry **247**

Appendix II **249**

Calculating the Composite Membrane Interface Pressure **249**

Reference List **251**

Chapter 1 – Introduction

Section 1 – Introduction

Hydrogen is an extremely useful chemical with many industrial applications including: hydro-desulphurisation and hydro-cracking within the petrochemical industry [1], as a reducing agent for metals in Fischer-Tropsch reactions [2]; ammonia production for fertilisers [3]; and as a carrier gas for the doping of silicon wafers in the semi-conductor industry [4]. Current global concerns regarding energy security and in particular climate change, are likely to significantly increase the demand for hydrogen as an energy carrier. When combined with oxygen in a Proton Exchange Membrane (PEM) fuel cell, electricity is produced with only pure water as a by-product. The potential market for such a clean and sustainable fuel is widespread with PEM fuel cells particularly suited to the transport sector. However, PEM fuel cells are susceptible to contamination by even trace levels of impurity gases such as CO, CO_2 and the sulphur species H_2S and SO_2 [5]. Therefore, the hydrogen feed gas needs to be 'ultra-pure', typically 99.99999 % volume. The supply of such high purity hydrogen is undoubtedly one of the key factors in the growth of the PEM fuel cell market and the development of the hydrogen economy in general.

Although hydrogen is amongst one of the most abundant elements on earth, molecular hydrogen is only present at trace quantities. Molecular hydrogen can be produced via electrolysis of water or by high temperature processing of various hydrocarbons. By 2006, the annual production of hydrogen exceeded 37 billion kilograms [2], the vast majority of which was produced via stream reformation of methane (SMR) [6]. This process involves a two stage

reaction, carried out above 800°C, and yields 4 mol hydrogen and 1 mol carbon dioxide for every mole of methane consumed [7]. The first stage involves reacting methane with steam to produce hydrogen and carbon monoxide,

$$CH_4 + H_2O \leftrightarrow CO + 3H_2 \qquad \textit{Eqn 1.1}$$

The unwanted carbon monoxide by-product is then mixed with steam in the water-gas shift reaction to produce additional hydrogen and carbon dioxide,

$$CO + H_2O \leftrightarrow CO_2 + H_2 \qquad \textit{Eqn 1.2}$$

The whole SMR process can then be summarised by,

$$CH_4 + 2H_2O \leftrightarrow CO_2 + 4H_2 \qquad \textit{Eqn 1.3}$$

Typically, the product gas stream is comprised of 74 % H_2, 18 % CO_2, 7 % CH_4 and 1 % CO [7]. Given that most applications require at least 99.99 % H_2 purity, with some (including PEM fuel cells) requiring up to 99.99999 %, hydrogen separation is clearly an essential process, often accounting for up to 50 % of the total production cost [2].

Dense metal membranes offer a convenient separation method as both stand alone devices, or in combination with the SMR process as a membrane reactor. Commercial membrane systems

are based on the Pd-Ag alloy system and are manufactured as either self-supporting rolled foils or drawn tubes, with a typical thickness of ~ 50 µm. However, the hydrogen flux through such membranes is around an order of magnitude below that specified by the US Department of Energy (DoE) performance targets [8]. Thin film (< 5 µm) membranes have the potential to meet the targets whilst also reducing the amount of costly Pd required. However, such thin membranes no longer have the tensile strength to resist the thermal and mechanical stresses experienced during operation and therefore require mechanical support. A wide variety of porous materials have been considered including alumina [9], silicon [10], stainless steel [11], nickel [12] and glass [13]. Porous stainless steel substrates appear to offer the best combination of strength and ruggedness, whilst also being easily sealable / weldable and possessing similar thermal expansion properties to Pd, ensuring good adhesion between the two layers [14]. However, depositing a defect-free < 5 µm thick Pd or Pd alloy film onto such a substrate is non-trivial, with considerable effort needed to reduce the surface porosity of the support to guarantee a defect-free membrane. At the temperatures required for adequate hydrogen flux (~ 400°C) intermetallic diffusion between the membrane and substrate can considerably reduce the hydrogen permeability, often requiring the use of an intermediate diffusion barrier.

Palladium-Yttrium has previously been proposed as a superior membrane material [15]. Pd-Y alloys demonstrate greater hydrogen permeability than Pd-Ag and possess significantly higher tensile strengths. However, Pd-Y alloys experience considerable strain hardening on deformation which leads to manufacturing difficulties. The strain hardening experienced by Pd-Y is likely to be the predominant reason these alloys have not been adopted commercially as rolled foils / drawn tube membranes.

A thin film Pd-Y membrane produced using a suitable deposition technique would eliminate such manufacturing issues and has the potential to meet the current US DoE performance

targets [8] at lower temperatures than either thin film Pd or Pd-Ag membranes, due to the enhanced hydrogen permeability. A reduction in operating temperature of between 50 to 100°C would considerably reduce membrane-support intermetallic diffusion, thus increasing the operating lifespan of the membrane. In addition, the superior hydrogen permeability of Pd-Y compared to Pd-Ag would allow an equivalent hydrogen flux at greater membrane thicknesses, thus potentially reducing the defect level of the membrane.

The primary objective of this work has been to investigate the performance of a novel, thin film Pd-Y / PSS composite membrane. In particular, the hydrogen transport mechanism across each layer of the composite membrane will be studied. The permeation data will be compared to the numerous studies on thin film Pd, Pd-Ag and Pd-Cu composite membranes reported in the literature. The hydrogen permeability of thin film Pd-Y will be compared to that in bulk alloys and any potential performance advantage of Pd-Y / PSS composite membranes will be quantified.

Chapter 2 – Literature Review

Section 2 – Hydrogen Separation

2.1 – Introduction

There are several hydrogen separation technologies currently available, predominantly, zeolite based impurity adsorption, cryogenic distillation and hydrogen selective membranes. The chosen separation technology will depend on many factors including the required hydrogen purity, impurity species, process cost and production / operation scale.

2.2 – Pressure Swing Adsorption

The pressure swing adsorption (PSA) process is based upon the ability of certain materials to readily adsorb impurity molecules at high partial pressures and to then subsequently desorb the impurities at low partial pressures.

The contaminated feed gas flows through an appropriate high surface area adsorbent, typically a zeolite, at relatively high partial pressures (1500 – 2000 kPa). The impurity gases adsorb to the adsorbent surface and ‘pure’ hydrogen permeates through. When the adsorbent has reached saturation, the impurity partial pressure is lowered by ‘swinging’ the system pressure from the feed gas pressure to the pure hydrogen permeate pressure. A low pressure, high purity hydrogen purge gas is then applied and the adsorbed impurities desorb and are

removed. Although the process operates on a cyclic basis, continuous hydrogen flow can be achieved by using multiple staggered adsorbers.

The main benefits of the PSA process are the ability to provide hydrogen over a wide range of purities, to produce relatively high purity hydrogen if required (99.99 %) and durability – the adsorbents will remain fully functional for the life of the equipment [16]. However, due to the nature of the process, PSA is only effective over a limited pressure range. The high purity hydrogen is delivered at < 200 kPa, necessitating costly additional post-process compression. The main limitation of the PSA process is however, the scale of operation and necessary infrastructure. PSA operates at high and medium volume levels but is impractical to scale down for use in either small scale or portable applications.

2.3 – Cryogenic Distillation

Cryogenic distillation is a low temperature separation process which uses the difference in boiling points of the feed components. Since only helium has a lower boiling point (-268.9ºC) than hydrogen (-252.9ºC), all impurities liquefy allowing the removal of pure hydrogen. In practise however, the achieved hydrogen purity is limited to ~ 99 % volume [17]. Although the process is extremely energy intensive the separated hydrogen can then be stored as a liquid relatively easily [18]. Similar to the PSA process, cryogenic separation is performed on large scales and is unsuitable for small scale and portable applications.

2.4 – Hydrogen Selective Membranes

The principle behind membrane separation is relatively simple; a concentration gradient, in this case a hydrogen partial pressure gradient, is applied across a properly sealed semi-permeable barrier. Hydrogen will then selectively 'permeate' across the membrane whilst the impurity species are rejected. The performance of a separation membrane can be assessed broadly in terms of flux, the rate of gas flow through the membrane, and selectivity, the ratio of hydrogen to any impurity species after separation. Depending on the selective barrier used, separation membranes have the unique potential of infinite selectivity. Membranes can operate over a wide range of temperatures and pressures and have an advantage of being entirely scalable, being equally effective at industrial production scale as in small-scale portable applications.

There are two main classes of separation membrane; porous and dense. Porous membranes are usually micro-porous ceramic, achieving separation by selective gas-phase diffusion, whilst dense membranes can be either polymeric or metallic and are selective by solution diffusion.

2.4.1 – Porous Separation Membranes

Porous membranes can be made from any material with finely controlled pore sizes. Porous structures suitable for hydrogen separation include zeolites [19], Vycor glass [20], sintered metals such as nickel [21] and various ceramics including alumina and zirconia [22]. Separation is based on a competitive process in which individual molecules move by free molecule, or Knudsen, diffusion along the connected porous network. Knudsen diffusion occurs when

collisions between gas molecules and flow boundaries are more frequent than inter-molecular collisions. In the case of separation membranes, Knudsen diffusion occurs when the mean free path of the gas molecules is greater than the average pore diameter *i.e.* the number of molecule to pore wall collisions is dominant. The mean free path of hydrogen under ambient conditions is 110.6 nm [23]. Knudsen diffusion of a single gas along a cylindrical pore is directly proportional to the pore radius and inversely proportional to both the membrane thickness and the square root of the molecular mass [24]. As a result, porous separation membranes are much more effective at separating hydrogen from heavy gas species such as CO_2 or H_2S compared to the lighter molecules CH_4 or H_2O. A full treatment of Knudsen diffusion can be found in Section 5.3.

The nature of a porous membrane means 100 % selectivity can never be achieved, whilst high selectivity values are only possible at the expense of low gas flux and vice versa. Multilayered asymmetric membranes offer the best combination of flux and selectivity (Figure 2.1).

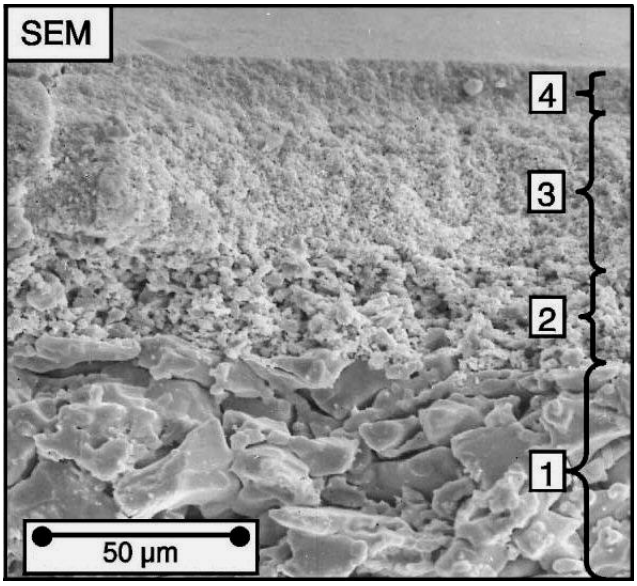

Figure 2.1 – A multilayered α-alumina asymmetric porous separation membrane. Taken from Hollein [25]

Most multilayered structures are comprised of at least 3 distinct layers, each with different pore sizes. The International Union of Pure and Applied Chemistry (IUPAC) define the following pore size classifications using pore diameter (d_p) [26];

- Microporous : $d_p < 2$ nm
- Mesoporous : d_p 2 – 50 nm
- Macroporous : $d_p > 50$ nm

A thin (< 1 µm) microporous separation layer is supported by a relatively thick (> 1 mm) macroporous substrate, with at least one intermediate mesoporous layer. The initial thin microporous layer is solely responsible for separation and should be as thin as possible to maximise the Knudsen diffusion through the pores. The subsequent layers provide mechanical strength and have larger pore sizes to minimise resistance to gas flow.

Porous membranes can be produced with a wide variety of structures depending on the impurity feed gas and purity requirements of an application. They can operate over a wide range of temperatures and pressures and are resistant to poisoning / contamination. However, hydrogen purity is limited to 99.9 % and such high purities are only achieved at the expense of very low hydrogen flux [22]. Multilayered membranes are also highly susceptible to defects within the microporous separation layer, which can considerably reduce the selectivity of the membrane [22].

2.4.2 – Dense Separation Membranes

Dense membranes can be either polymeric or metallic. Polymeric membranes are typically based on polyamide-imide block co-polymers [2] and, although they offer low cost benefits,

selectivity values are poor, especially in the presence of CO_2, H_2O and H_2S [16]. In addition, polymeric membranes can only operate over a limited temperature range making them unsuitable for many hydrogen separation applications.

Dense metallic membranes, however, offer the unique possibility of infinite selectivity. In practise, this is usually limited to 10's of parts per billion (ppb) purity due to tiny amounts of carbon and other impurities which may diffuse through the metal lattice and along grain boundaries [27]. Metallic membranes are easily formable and sealable, offer reasonable gas flux and can operate over a wide temperature range. Maximum flux varies with alloy composition and structure, but generally falls within the temperature range 400 – 600°C, coinciding with the SMR product gas stream temperature. This raises the possibility of combining the two steps of hydrogen production and separation within a single unit; a so-called membrane reactor [28].

Currently, both membrane reactors and commercially available stand-alone purifiers are based on the Pd-Ag alloy system, typically $Pd_{76}Ag_{24}$ atomic percent (all compositions within this work are at.%, unless otherwise noted). They are designed as either a series, or stack, of rolled planar foils or as long drawn tubular systems. Both configurations typically have a membrane thickness of 50 – 100 μm depending on the intended operating conditions. Tubular systems are designed to work 'outside in' (Figure 2.2) and are self-supporting, although a stainless steel coil is sometimes used within the tube to provide additional strength [29].

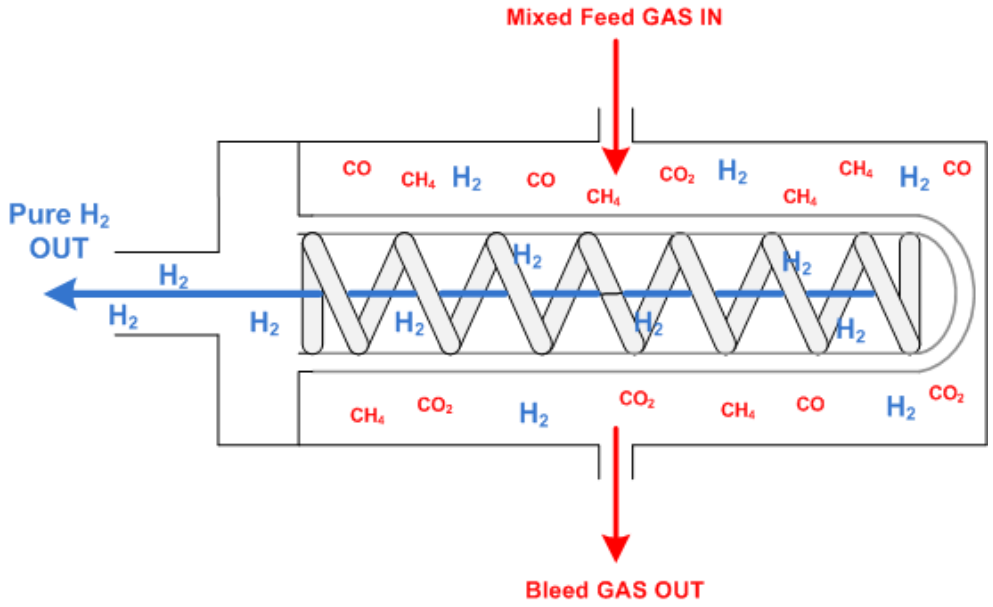

Figure 2.2 – Schematic representation of the 'outside-in' configuration used in commercial Pd-Ag hydrogen purification membranes. In practise a series, or bank, of tubes will be used to maximise the surface area.

Dense metal membrane technology has remained relatively unchanged since the 1960's, primarily due to the low demand for 'ultra-high' purity hydrogen. However, the demand for such high purity hydrogen is expected to increase significantly as the hydrogen economy establishes itself. There is considerable scope for the development of dense metal membranes with current international research focused on reducing membrane thickness, improving permeability and increasing resistance to certain contaminants (poisoning). The supply of cheap, high purity hydrogen will almost certainly be a key factor in the development of the hydrogen economy.

Section 3 – Palladium-based Dense Metal Membranes

3.1 – Introduction

Hydrogen dissolves in a wide range of metals and alloys to form either interstitial solid solutions or metal hydrides. Some systems require extreme temperatures and / or pressures to absorb hydrogen whilst others readily form very stable hydrides. Some suffer hydrogen embrittlement whilst certain intermetallic compounds are capable of absorbing such large quantities of hydrogen that the hydrogen density is greater than that in liquid form [30]. Hydrogen is capable of rapid diffusion through certain elements, particularly refractory metals with the Body Centred Cubic (BCC) crystal structure such as vanadium and niobium, however these metals possess very inactive surfaces for the dissociation of molecular hydrogen and thus have slow surface absorption and desorption rates [31].

The palladium-hydrogen system is unique in that palladium has a very high affinity for dissociating molecular hydrogen into its atomic state thus enabling fast absorption / desorption, is capable of absorbing large volumes of hydrogen whilst still retaining its physical properties / structural integrity and possesses particularly high hydrogen diffusion rates.

The notion of palladium as a hydrogen selective membrane is almost 150 years old. In 1866, Thomas Graham discovered that palladium was capable of absorbing more than 600 times its own volume of hydrogen, and of practical importance, if coal gas were substituted for hydrogen, only the hydrogen would permeate through the palladium [32].

Palladium membranes were largely restricted to obtaining high purity hydrogen at a laboratory scale until the 1950's when demand arose for the development of hydrogen isotope

separation in the nuclear fission industry. However, the most widespread use of palladium membranes has since become the production of ultra-pure hydrogen for the semi-conductor industry [33].

3.2 – Palladium and Palladium Alloys

Palladium is a Group 10 transition metal with a Face Centred Cubic (FCC) crystal lattice. It has both the lowest density (12.023 $g.cm^{-3}$) and melting point (1555°C) of the Platinum Group Metals (PGMs) and possesses remarkable catalytic properties typical of the PGMs. Currently the major industrial application of palladium is as the active constituent in automotive catalytic converters.

In the free atomic state Pd has an outer electron configuration of $[Kr]4d^{10}5s^{0}$ with some overlapping energy levels between the 4d and 5s bands, characteristic of transition metals. Accordingly, transition metals have an affinity for donor electrons from other atoms. Upon filling, the low energy 5s bands are energetically favourable and fill preferentially over the higher energy 4d bands. It is these electronic properties of palladium which determine its unique chemical and metallurgical interactions with the other elements.

The FCC crystal lattice has a co-ordination number of 12 and, based on a solid sphere model, a packing factor of 0.74. Thus, 74 % of the available space is occupied by host atoms. The remaining 26 % can be divided into two types of interstitial site; octahedral and tetrahedral. There are two tetrahedral and one octahedral interstitial sites per host atom within the FCC lattice (Figure 3.1). An interstitial solid solution alloy can be formed when solute atoms are capable of fitting into these interstitial sites. The size of the available interstitial sites is

restricted and consequently only small non-metallic atoms such as hydrogen, boron and carbon can be accommodated. The site preference of an interstitial solute atom is determined by a combination of the potential energy due to position, the kinetic energy based on its vibration and the elastic strain energy of the lattice due to expansion. Assuming the lattice is free from defects (voids etc) and local solvent-solute interactions dominate over solute-solute interactions, both the kinetic and elastic strain energies vary little with site, whilst the potential energy is considerably different in the octahedral and tetrahedral positions. Although both positions represent minima of potential energy, the octahedral sites are much deeper in a FCC lattice due to the greater distance between nearest neighbour solvent atoms. As a result, octahedral occupation is favoured in a FCC lattice. It is generally accepted that when hydrogen forms an interstitial solid solution alloy with palladium, the monatomic hydrogen is located at the octahedral interstices [34].

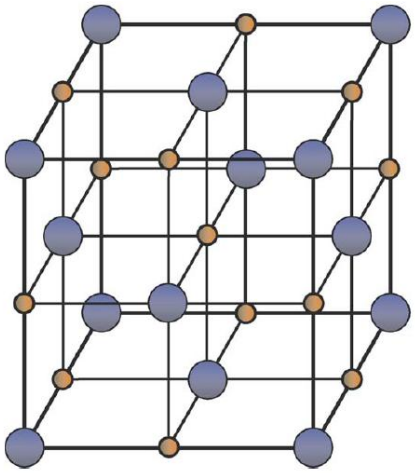

Figure 3.1 – Octahedral interstitial sites in a FCC crystal lattice. Taken from Jewell [34]

The palladium-hydrogen system exhibits two immiscible FCC phases designated α (interstitial solid solution) and β (palladium hydride). At room temperature, the α phase exists over a range of compositions up to an α_{max} at an approximate H / Pd value of ~ 0.02. Above

this composition (α_{max}) both phases co-exist up to the β_{min} composition of ~ 0.6 (Figure 3.4). Although both phases have an FCC structure there is a considerable difference in lattice parameter. Pure palladium has a lattice parameter of 3.89 Å whilst the α_{max} and β_{min} parameters are 3.895 Å and 4.025 Å respectively [35]. Thus, the transition between purely α to β corresponds to a volume increase of 10 %, which results in high internal stresses, deformation and ultimately, failure of a membrane. Cycling through this phase transition has also been shown to produce very large dislocation densities [35]. The co-existence of the two immiscible phases is known as the miscibility gap. Both phases exist in the Pd-H system up to a critical temperature of 293°C, above which only the α solid solution phase exists, therefore eliminating the miscibility gap [34].

Although the typical operating temperature of a palladium membrane would be > 293°C, it is unrealistic to try and ensure the temperature never drops below this. Any pure palladium membrane must therefore be produced with the necessary inert gas purge / vacuum equipment, adding considerable cost to the membrane unit.

Alloying palladium can eliminate many of the crystallographic problems experienced by pure palladium membranes. Numerous elements including Ag, Au, Cu, Y and Pt can be added to palladium to form substitutional solid solutions. In these alloys the critical temperature (T_c) for the $\alpha \rightarrow \beta$ phase transition is reduced, thereby suppressing the miscibility gap to below room temperature. Additionally, several Pd alloy systems demonstrate superior hydrogen permeability and often possess substantially greater tensile strengths and other mechanical properties when compared to pure palladium.

The Pd-Ag alloy system is the most widely studied and exhibits a wide range of mutual solid solubility. The α / β miscibility gap is closed at room temperature when the concentration of

Ag reaches ~ 24 at%. Pd-Ag_{24} absorbs hydrogen more quickly and is approximately twice as permeable as pure palladium [36, 37]. Indeed, this is the alloy composition currently used in commercial purifiers. However, although considerably better than pure palladium, Pd-Ag still has relatively low strength, expands significantly on hydrogen absorption (Pd → α), and can experience grain coarsening during extended periods at high temperatures [27]. For these reasons commercial purifiers have limited life cycles.

The Pd-Cu system demonstrates a maximum hydrogen permeability at ~ Pd-$Cu_{40wt\%}$. Reported values vary between unity and a 50 % increase when compared to pure palladium [38]. Although Pd-Cu is less permeable to hydrogen than Pd-Ag_{24} it offers superior mechanical properties, increased cyclability and greater resistance to poisoning by gaseous impurities such as H_2S [39, 40]. However, long term stability may be an issue with Pd-Cu membranes due to an unstable FCC / BCC mixed phase occurring in the Pd-Cu system around the high permeability Pd-$Cu_{40wt.\%}$ composition [38]. Interstitial hydrogen has also been shown to extend the composition range at which the mixed FCC / BCC phase occurs [41].

The highest reported hydrogen permeability of any binary palladium alloy system is that of Pd-Y [15]. The solid solubility of yttrium and other rare earth metals in palladium was first investigated by Harris & Norman [42]. They found that yttrium is soluble up to 12 at.% (Figure 3.2), despite the fact that the nominal size factor of yttrium atoms with respect to palladium is approximately 29 % larger; considerably in excess of the 15 % size limit suggested by Hume-Rothery [43]. This atomic size mismatch is the predominant factor in the significant solid solution strengthening of Pd-Y, providing superior tensile strength when compared to both Pd-Ag and Pd-Cu membranes.

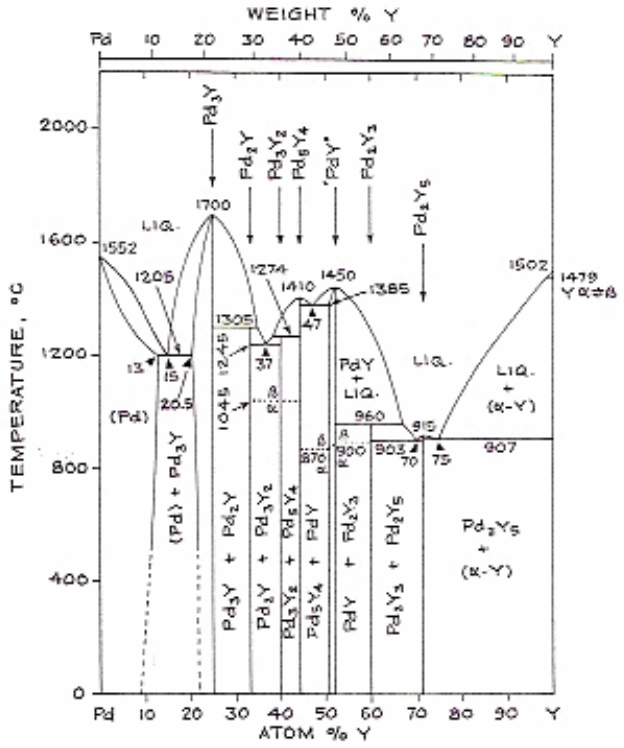

Figure 3.2 – The Palladium – Yttrium phase diagram. Taken from Loebich [44]

X-ray diffraction studies of the Pd-Y miscibility gap reveal that the critical temperature (T_c) for β-hydride phase formation decreases with increasing yttrium concentration, until at a composition of Pd-$Y_{7.8}$ the β phase does not form at room temperature, *i.e.* the miscibility gap is closed [35]. Interestingly, there appears to be a correlation between solute valency and concentration in determining miscibility gap closure. When the α_{max} and β_{min} lattice parameters are plotted against C_sV_s (solute concentration x solute valency) for a range of binary Pd alloy systems, the traces converge at the same point (Figure 3.3). This C_sV_s value corresponds to an e / a value of approximately 0.24, coinciding with the suggested electron concentration that can be accommodated in s-p bands below the 4d level in Pd β phase [45]. This would imply a dominant electronic effect in determining the extent of the miscibility gap [46].

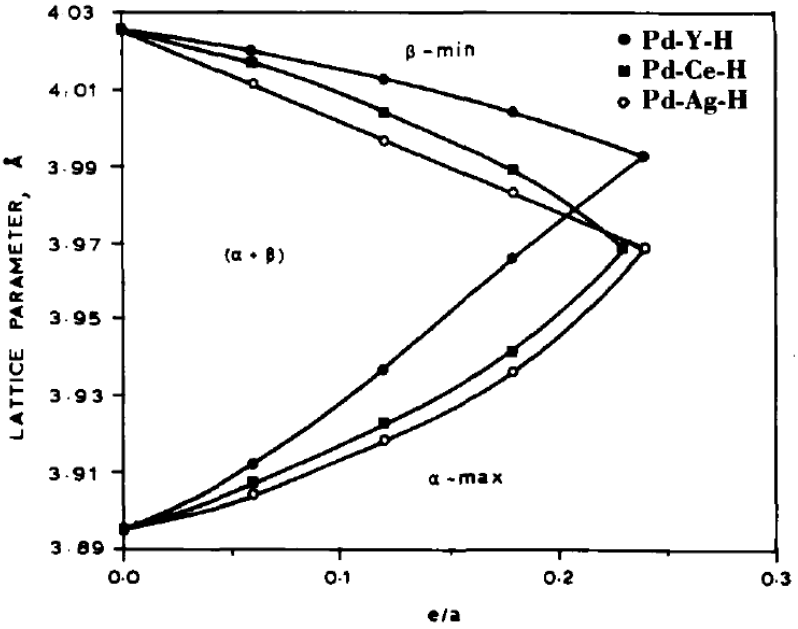

Figure 3.3 – Room temperature lattice spacings against e / a for Pd-Y, Pd-Ag and Pd-Ce. Taken from Doyle [47].

Although the hydrogen permeability of Pd-Y_8 at 400°C is almost 2.5 times greater than Pd-Ag_{24} and offers superior mechanical properties, it has not been adopted commercially. A likely reason for this is the considerable strain hardening Pd-Y undergoes during cold work. Manufacturing a Pd-Y membrane would therefore require several intermediate anneals, whereas Pd-Ag can be drawn / rolled to a final thickness of 50 – 100 µm in a single process.

3.3 – Absorption of Hydrogen in Palladium and Palladium-Yttrium

In order for molecular hydrogen to enter a metal lattice it must first dissociate into atoms,

$$H_2 \rightarrow 2H \qquad \textit{Eqn 3.1}$$

The dissociation reaction takes place on the metal surface with the resultant hydrogen atoms bonded, or chemisorbed, to the surface. There is an activation energy associated with this reaction and in some metal hydride systems, the overall reaction kinetics of hydride formation are limited by slow dissociation. The hydrogen atoms can then diffuse from the surface into the bulk metal to form either an interstitial solid solution or a metal hydride.

As previously mentioned, palladium is a transition metal with some overlapping outer energy levels between the 4d and 5s bands, typical of the transition metals. Accordingly, palladium has an affinity for donor electrons from other atoms. When a hydrogen atom enters the palladium lattice it occupies an octahedral interstitial site which will affect the host lattice in several ways. Firstly, its presence will distort the palladium lattice due to the elastic strain energy. Interestingly, the relative distortion appears to be independent of the host material. The addition of a single hydrogen atom has been calculated to expand a FCC lattice by ΔV=2.9 $Å^3$ [48]. Secondly, the interstitial hydrogen will also change the local electron density as its electron is taken into the 'electron cloud' of the host, effectively screening the charge of the proton (H^+). Hydrogen in solution is often referred to as a 'screened proton'. The effects of hydrogen absorption on the host lattice are signified by an energy change known as the partial enthalpy change (ΔH_H), encapsulating all the associated physical processes,

$$\Delta H_H = {}^1/_2\, H_D + H_I - \Phi + E_S + E_{Pr} + E_{rep} \qquad Eqn\ 3.2$$

Where,

H_D is the dissociation energy of a hydrogen molecule

H_I is the ionisation energy of a hydrogen atom

Φ is the work function of the metal

E_S is the elastic strain energy due to the dissolved hydrogen atom

E_{Pr} is the energy of electron movement around the hydrogen nucleus

E_{rep} is the interaction energy of the hydrogen nucleus with the ion cores of the host lattice

H_D and H_I are independent of the host metal and the work function varies little between metals. E_{rep} is dependent on the charge on the ion core of the host metal, whilst both E_{Pr} and E_S are dependent on the density of states in the host lattice as this in turn affects the screening of the proton. The overall effect is that ΔH_H is usually very small and, depending on the host metal, either positive or negative. A negative value signifies the liberation of heat during hydrogen absorption by an exothermic hydrogen absorber. Such systems readily absorb hydrogen under moderate conditions and will form stable hydrides. A positive value represents the absorption of heat by an endothermic hydrogen absorber, these systems require extreme temperatures and / or pressures to absorb hydrogen. Therefore, endothermic absorbers demonstrate increasing hydrogen solubility with temperature. Palladium absorbs hydrogen exothermically and thus exhibits decreasing hydrogen solubility with increasing temperature [34].

The thermodynamic properties of a metal hydrogen system can be assessed using a series of pressure-composition-temperature (PCT) isotherms which relate hydrogen concentration at a given temperature to the pressure. The PCT diagram is especially useful for identifying the presence and extent of the miscibility gap (Figure 3.4). The minimum temperature at which

the miscibility gap is closed can also be determined; a critical parameter for any palladium alloy membrane in order to avoid β hydride formation and its associated stresses.

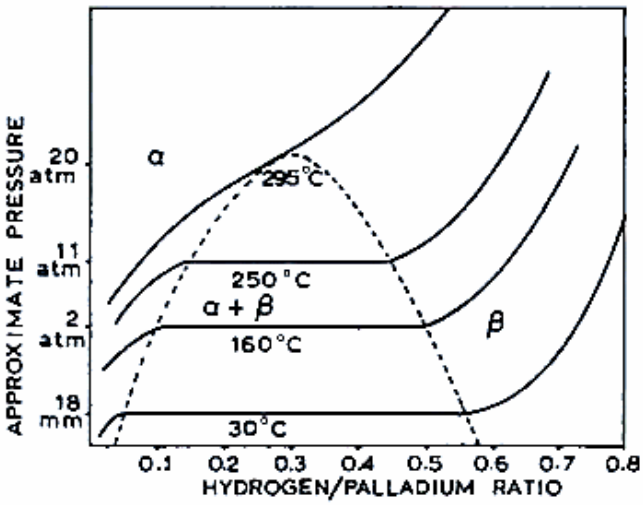

Figure 3.4 – PCT diagram of the palladium – hydrogen system. Taken from Knapton [49]

From the PCT diagram three distinct regions can be distinguished, the α solid solution, α + β solvus region and the β hydride region. The length of the plateau between the α and β phases corresponds to the miscibility gap. As the temperature increases the extent of the miscibility gap decreases until a certain critical temperature (T_c), above which, the β hydride phase does not form. The majority of the alloys investigated in this study (Pd-$Y_{8\text{-}10}$ and Pd-Ag_{24}) were chosen because their miscibility gaps are closed above room temperature, whilst the remainder (Pd and Pd-$Y_{2\text{-}6}$) were appropriately heated to above the critical temperature prior to hydrogen exposure. Therefore, particular emphasis is placed on the solid solution α phase. Throughout this work the term 'solubility' refers to the α phase solubility unless otherwise stated.

The absorption of a single hydrogen atom into a metal lattice to form a solid solution can be expressed by the reaction,

$$^1/_2\, H_{2\,(gas)} \rightarrow H_{(metal)} \qquad \textit{Eqn 3.3}$$

Hydrogen atoms are uniformly distributed throughout the metal lattice. The concentration of hydrogen, or solubility, is directly proportional to the square root of the external hydrogen pressure. This relationship is known as Sievert's law of ideal dilute solubility,

$$\sqrt{P_{H_2}} = K_s X \qquad \textit{Eqn 3.4}$$

where P_{H_2} is the hydrogen gas pressure, X is the hydrogen concentration and K_S is Sievert's constant. K_S is traditionally defined as an equilibrium constant for the reaction in Eqn. 3.4 under conditions where the hydrogen concentration, X, is <<1. Under such conditions an expression for K_S can be defined,

$$K_S = exp\left(\frac{\Delta H_H^0}{RT} - \frac{\Delta S_H^0}{R}\right) \qquad \textit{Eqn 3.5}$$

Where ΔH_H^0 and ΔS_H^0 are the partial molar enthalpy and entropy of dissolution respectively, R is the gas constant and T is the temperature. At low hydrogen concentrations (X) Sievert's law

is valid for many experimentally observed systems. However, as *X* increases, deviations from the ideal occur due to the changing nature of the metal-hydrogen system. As *X* increases [46],

- The host lattice expands, due the elastic strain energy of the interstitial hydrogen, until it becomes a significant factor in determining further hydrogen solubility.
- The number of free electrons to free metal atoms ratio increases, thus altering the electronic properties of the system.
- Local hydrogen-hydrogen interactions become significant. These can be either attractive or repulsive.
- The entropy no longer corresponds to a random distribution of dissolved hydrogen atoms among the available interstices.

However, assuming a low hydrogen concentration ($X = <<1$) has been shown to be a reasonable approximation for most Pd membrane operating conditions [50]. Therefore, Sievert's law is assumed to be valid and forms the basis of several hydrogen permeation models. Deviations from Sievert's law are experienced by Pd and Pd-Y membranes under certain operating conditions, however, these are attributed to factors other than high hydrogen concentration and will be discussed further in Section 4.5.

Yoshihara [51] investigated the effect of temperature and solute concentration on the hydrogen solubility of the Pd-Y system (Figure 3.5). The solubility was shown to increase with yttrium concentration across the whole Pd-Y solid solution range. The exothermic nature of hydrogen absorption by Pd-Y is clearly shown as the maximum solubility decreases with increasing temperature (Figure 3.5).

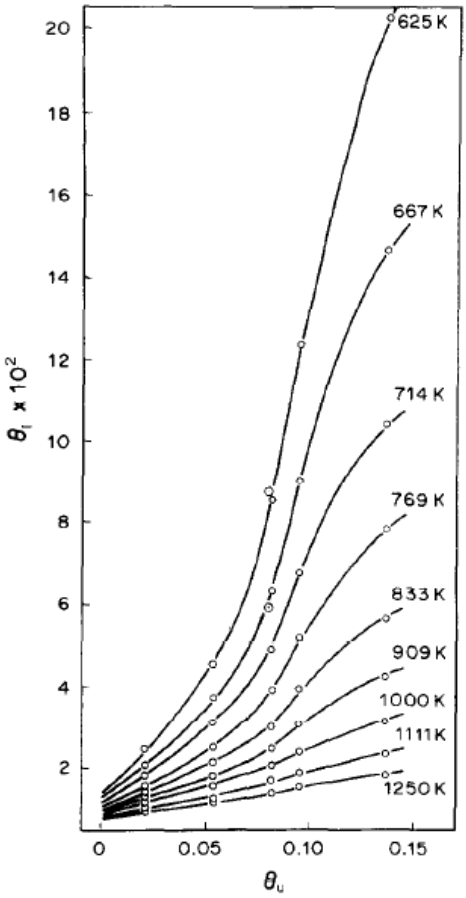

Figure 3.5 – The effect of Y concentration on the hydrogen solubility of Pd-Y alloys. Taken from Yoshihara [51]

The solubility enhancing effect of increasing yttrium concentration has also been demonstrated by Yoshinari [52] who measured the room temperature solubility of Pd, Pd-Y_2 and Pd-Y_5 using an electrolytic technique. The solubilities were shown to increase by a factor of 1.7 and 2.3 respectively when compared to pure Pd.

A precise explanation for the increased solubility remains unclear. Yoshihara [51] also demonstrated that both the partial molar enthalpy (ΔH_H^0) and partial molar entropy (ΔS_H^0) of dissolution decreased with increasing yttrium concentration and proposed that these effects, along with the increased solubility, were due to the significant lattice expansion that coincides with yttrium concentration. However, cerium expands the lattice to a greater extent than yttrium [42], yet Pd-Ce alloys demonstrate much lower solubility than Pd-Y [53]. Some authors

suggest a hydrogen trapping effect of yttrium atoms in Pd-Y [51], whereas Yoshinari [52] ruled out any trapping effect above 150 K. The solubility has also been shown to be sensitive to the thermal history of the sample, especially at high yttrium concentrations [54]. Several investigators including Wileman [55, 56], Hughes [57], Doyle [46, 47] and Poyser [58] have all reported evidence of ordering in bulk Pd-Y alloys with high Y contents. When cooled under vacuum from above a certain critical temperature, estimated as 495°C in Pd-Y_{12} and 455°C in Pd-Y_{10} by Doyle [46], the alloy forms the ordered cubic Pd_7Y-type structure. However, when cooled in a hydrogen atmosphere, the alloy remains disordered. Doyle [54] reported that the ordered structure has a higher hydrogen solubility than the disordered structure (Figure 3.6).

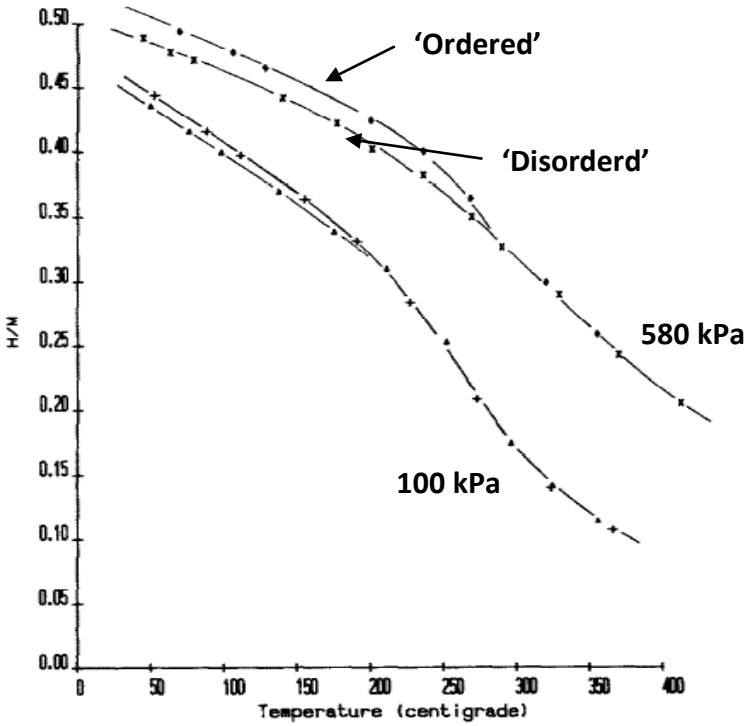

Figure 3.6 – Effect of order / disorder on the hydrogen solubility of Pd-Y_8. Taken from Doyle [54]

The solubility data of both Yoshihara [51] and Yoshinari [52] are from samples measured under equilibrium conditions, *i.e.* the whole sample was subject to the same hydrogen concentration. However, a Pd-Y membrane operates under non-equilibrium conditions. The driving force for

permeation is a hydrogen partial pressure across the membrane. From Sievert's law the concentration of hydrogen within the membrane is proportional to the square root of the external partial pressure, it follows therefore, that the hydrogen concentration is different at either side of the membrane; a concentration gradient exists across the membrane. Assuming that the near-surface hydrogen concentration at either side of the membrane is in equilibrium with the external gas-phase pressure, the concentration (solubility) gradient may be deduced from the equilibrium solubility data. Hughes [53] successfully used this technique to compare the solubility gradient in Pd-Y_8 to Pd-Ag_{25}, a composition used in commercial membrane purifiers and which has been shown to possess greater solubility than pure palladium. At both the high (Figure 3.7) and low (Figure 3.8) pressure conditions, Pd-Y_8 possesses greater solubility across the entire temperature range studied (RT – 450°C).

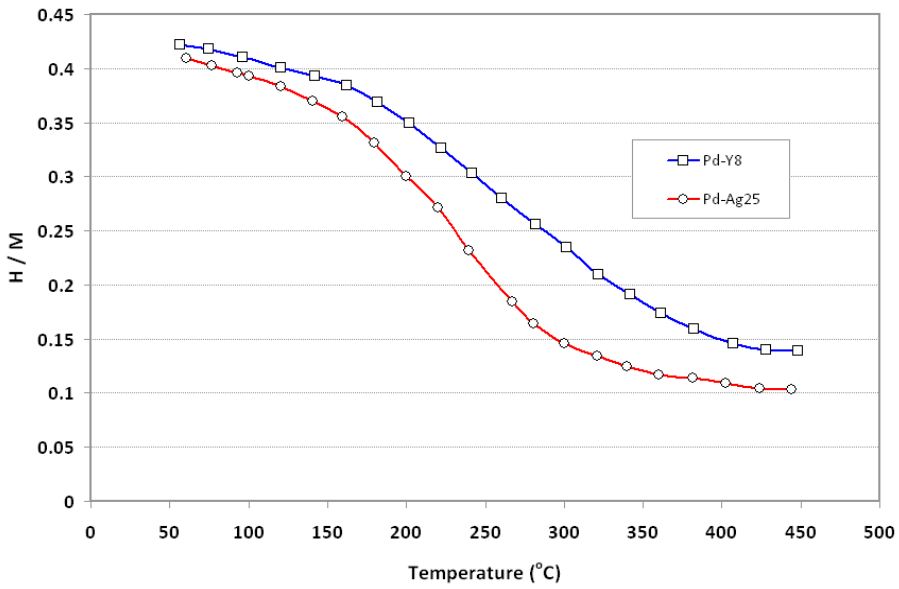

Figure 3.7 – Equilibrium hydrogen solubility in Pd-Y_8 and Pd-Ag_{25} at 445 kPa. Reproduced from Hughes [53]

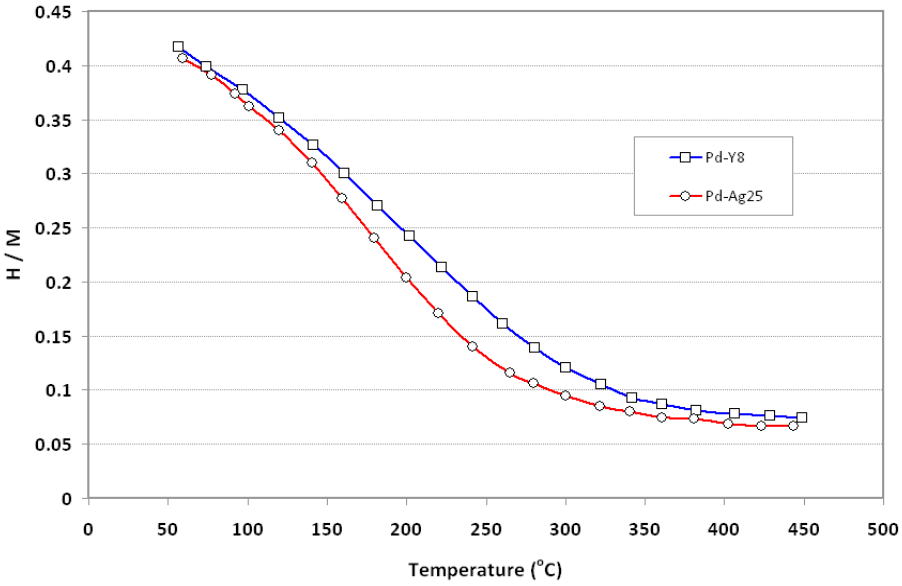

Figure 3.8 – Equilibrium hydrogen solubility in Pd-Y_8 and Pd-Ag_{25} at 100 kPa. Reproduced from Hughes [53]

Subtracting the low pressure data from the high pressure gives the effective solubility gradient for each alloy (Figure 3.9). Both alloys demonstrate similar shaped curves and, although the maximum solubility has been shown to progressively decrease with increasing temperature, distinct maxima occur at ~ 250°C for Pd-Ag_{25} and ~ 280°C for Pd-Y_8.

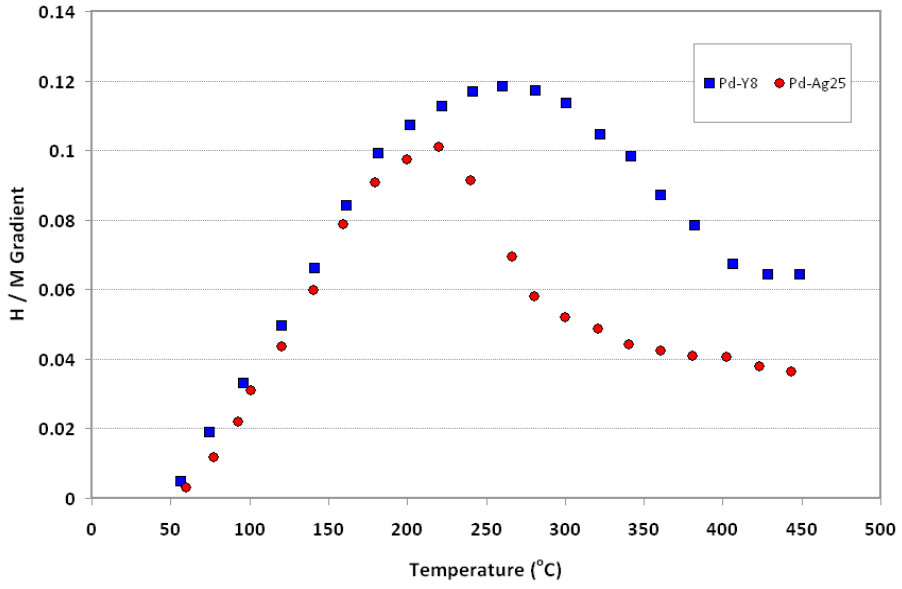

Figure 3.9 – Solubility gradient in Pd-Y_8 and Pd-Ag_{25} (Δ 345 kPa). Reproduced from Hughes [53]

The initial increase in solubility gradient with temperature can be explained by the low temperature solubility approaching saturation regardless of pressure, indeed at room temperature the solubility was shown to be effectively independent of pressure [53].

Measurements of the effective solubility gradient and hydrogen permeability can be used to calculate the diffusion coefficient. Hughes [53] found no significant difference in the diffusion coefficient between the alloys and therefore attributed the enhanced hydrogen permeability of Pd-Y_8 compared to Pd-Ag_{25} to the greater solubility gradient. This will be discussed further in later sections.

3.4 – Diffusion of Hydrogen in Palladium and Palladium-Yttrium

Hydrogen has been shown to occupy the interstitial sites in metal lattices and demonstrates extremely high diffusion rates, close to those for atomic diffusion in liquids [59]. Such high diffusivity far exceeds other interstitial species such as carbon by 15-20 orders of magnitude, particularly at low temperatures (Figure 3.10). Hence, the diffusion of hydrogen in metals has been the subject of both theoretical and experimental research for more than 50 years.

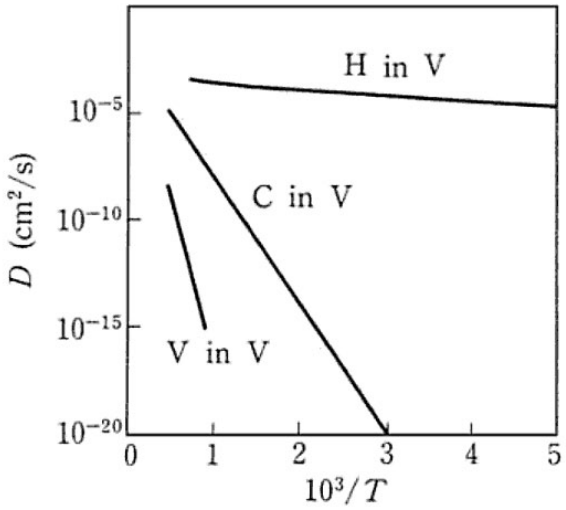

Figure 3.10 – Diffusion of interstitial hydrogen, carbon and self-diffusion of vanadium. Taken from Fukai [59]

Diffusion takes place because of an activity gradient or difference in chemical potential. In the case of membranes, this is caused by a hydrogen partial pressure gradient across the membrane. The precise mechanism by which hydrogen interstitially diffuses through a metal lattice is subject to a great deal of speculation, and a variety of models, both classical [60] and quantum [61], have been proposed. It is generally expected that the diffusion of a hydrogen atom proceeds via several different mechanisms, with any predominate mechanism largely dependent on temperature. Kehr [62] proposed four different diffusion mechanisms with no distinct boundaries except at either extreme temperatures (Figure 3.11).

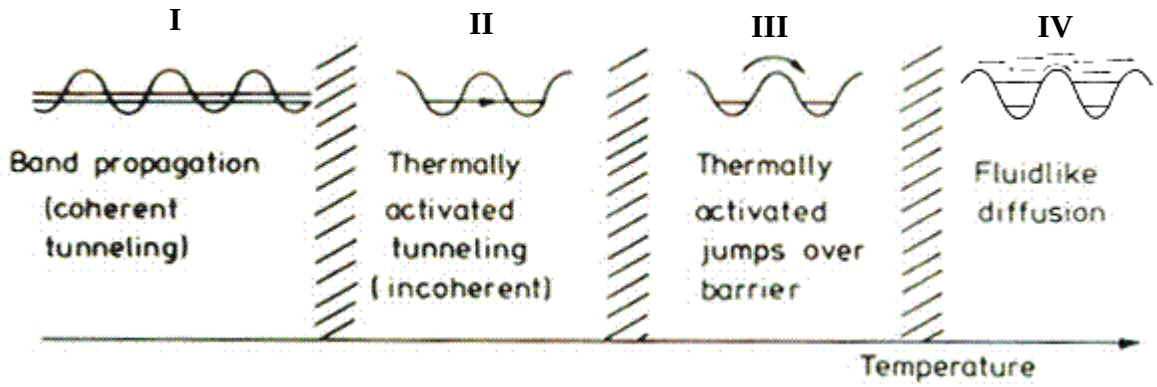

Figure 3.11– Proposed diffusion mechanisms of hydrogen in metals. Adapted from Kehr [62]

At very low temperatures (region I) there are virtually no thermal vibrations, or, phonons. Hydrogen atoms, which have become 'self trapped' due to the relaxation of the surrounding lattice, are thought to progress to the next interstitial site via a quantum mechanical tunnelling process termed 'band propagation'. As temperature is raised transport mechanisms involving phonons may take place and hydrogen atoms move via thermally activated tunnelling (region II). A phonon brings the occupied low energy site and the neighbouring high energy site into coincidence, allowing the transition of the hydrogen atom between the sites. The lattice then relaxes about the atoms new position. At higher temperatures (region III), the hydrogen atoms can be regarded as classical particles which execute over-barrier jumps between neighbouring sites via thermal excitation. At much higher temperatures (region IV) the hydrogen atoms no longer remain within potential wells of interstitial sites. In this region diffusion occurs via free motion, similar to that in gases and liquids. As noted by Kehr [62], these proposed mechanisms are only broad qualitative ideas with the probability that at a given temperature, diffusion occurs by a combination of these mechanisms. Furthermore, it is not expected that all four mechanisms will be observed in every metal-hydrogen system [59].

The predominant diffusion mechanism expected at typical membrane operating temperatures (200 – 600°C) is via thermally activated over-barrier jumps (region III). Therefore, hydrogen diffusion in palladium and palladium-yttrium membranes can be analysed using the over-barrier mechanism, which is adequately described using classical rate theory [60]. The jump rate of an interstitial hydrogen atom (Γ) can be written as,

$$\Gamma = nv\ exp\left(\frac{-E_A}{k_B T}\right) \qquad Eqn\ 3.6$$

Where n is the number of nearest neighbour interstitial sites, v is the vibrational frequency of the hydrogen atom, E_A is the thermal activation energy and k_B is Boltzmann's constant. The theoretical diffusion coefficient (D) for interstitials in a cubic lattice can then be calculated as,

$$D = a^2\ \alpha\ \Gamma \qquad Eqn\ 3.7$$

Where a is the lattice parameter and α is a coefficient determined by the geometric relationship between interstitial sites (1/12th for octahedral site in an FCC lattice). Equations 3.6 and 3.7 can be combined to give,

$$D = a^2\ \alpha\ nv\ exp\left(\frac{-E_A}{k_B T}\right) \qquad Eqn\ 3.8$$

The activation energy (E_A) can be split into its components, the change in molar enthalpy due to the lattice distortion as the hydrogen atom jumps between interstitial sites (ΔH), and the change in molar entropy due to the change in vibrational frequency (ΔS).

$$E_A = \Delta H - T\Delta S \qquad \textit{Eqn 3.9}$$

Combining Equations 3.8 and 3.9 gives,

$$D = a^2\ \alpha\ nv\ exp\left(\frac{-\Delta H}{RT}\right) exp\left(\frac{\Delta S}{R}\right) \qquad \textit{Eqn 3.10}$$

Several terms can be combined into a pre-exponential constant (D_0) to give the diffusion equation,

$$D = D_0\ exp\left(\frac{-E_A}{RT}\right) \qquad \textit{Eqn 3.11}$$

From Eqn 3.11 it is clear that the diffusion coefficient (D) has an Arrhenius-type relationship with temperature. The diffusion characteristics of a metal-hydrogen system are usually expressed in terms of the two constants E_A and D_o.

The diffusion equation (Eqn 3.11) is, however, only experimentally valid under certain conditions. Significant deviations occur at low temperatures (< 100 K), at high hydrogen

concentrations and between hydrogen isotopes, thus highlighting that the elementary process of diffusion in metals is non-classical. Under these conditions a quantum theory of diffusion is therefore needed [59]. However, no model has yet been proposed which accurately determines diffusion in all regimes. For membrane applications, typical operating temperatures are between 200 – 600°C, hydrogen concentrations are relatively low and the classical diffusion model (Eqn 3.11) adequately describes the observed hydrogen diffusion and forms the basis of most hydrogen flux based analyses, which are reviewed in Section 3.5.

Hydrogen diffusion in palladium has been widely studied using several techniques including permeation, electrochemical, mechanical relaxation and x-ray methods. Most diffusion data is gathered using non-equilibrium methods such as the Gorsky effect or permeation measurements. The Gorsky effect uses the lattice relaxation effect of hydrogen as it diffuses from the compression side of a deformed specimen to the tension side [59]. The time taken for this elastic relaxation is used to determine the chemical diffusion coefficient. Diffusion data gathered using this method are very reliable as any possible surface effects are eliminated. Diffusion data can be collected using equilibrium measurements such as nuclear magnetic resonance (NMR) and quasi-elastic neutron scattering (QNS) where the jump frequency of hydrogen atoms can be determined. Careful consideration is therefore required when comparing diffusion data from different sources.

Volkl and Alefeld [63] collected Pd-H diffusion data from 25 authors and calculated the best fit values of D_o = 2.90 x10^{-3} cm^2s^{-1} and E_A = 0.23 eV (22.2 $kJ.mol^{-1}$). Both these values are approximately an order of magnitude larger than for the other transition metals niobium and vanadium, which have the BCC structure.

Palladium Alloys

The addition of substitutional alloying elements to palladium almost always decreases hydrogen diffusivity, regardless of whether the solute atom expands (Ag and Au) or contracts (Cu and Fe) the lattice. One notable exception is Pd-$Cu_{40\text{-}50wt.\%}$, which forms the ordered BCC β-CuPd phase. This ordered phase has been shown to have the highest room temperature diffusivity of any metal-hydrogen system, with $D = 2.0 \times 10^{-5}$ cm^2s^{-1} compared to the value in pure Pd of 2.0×10^{-7} cm^2s^{-1} [41]. However, such a large increase in diffusivity does not correspond to an equivalent increase in permeability because, unlike Y and Ag, Cu additions to Pd reduce the hydrogen solubility.

Barlag et al [64] investigated the room temperature hydrogen diffusivity in a range of FCC Pd alloys formed by elements with both a low hydrogen solubility when compared to Pd (Ag, Cu and Ni) and a high solubility (Nb and V). Small additions of Ag (≤ 20 at.%) were shown to have little effect on the diffusivity, which is in good agreement with diffusion data reported by Holleck [65] who found little change in the activation energy from Pd to Pd-Ag_{20} followed by a progressive increase with additional silver content. Barlag et al [64] found that above 20 at.% the diffusivity dropped sharply to a minimum value at approximately Pd-Ag_{60} (see Figure 3.12). The diffusivity progressively increased with further Ag additions until the value for pure Ag was reached.

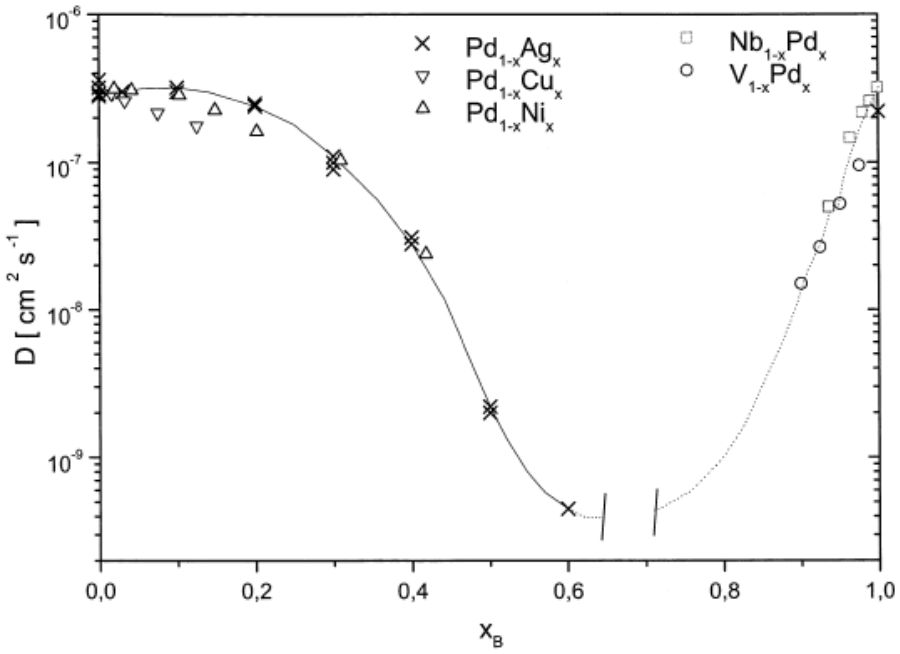

Figure 3.12 – Diffusion of hydrogen in a range of FCC palladium alloys. Taken from Barlag [64]

Barlag et al [64] proposed a simple two site model to explain the shape of the curve. In this model two different octahedral sites (Pd and Ag) are assumed to exist, both possessing a different hydrogen occupation probability, or solubility. Small silver additions to palladium partly block the energetically favoured diffusion paths in the palladium matrix leading to a round-about way diffusion [64]. At high silver concentrations, palladium atoms act as traps for hydrogen in a silver matrix. If Ag is substituted by Ni or Cu a similar trend is observed, although small additions reduce the diffusivity to a greater extent. This was attributed to the lattice contraction experienced by Pd-Cu and Pd-Ni as opposed to the lattice expansion of Pd-Ag. Silver, nickel and copper are similar in that they have lower hydrogen solubilties than Pd. If alloyed with small amounts of V or Nb, which have higher solubilities, the diffusion behaviour is analogous to Pd in a Ag matrix. Barlag et al [64] proposed that small additions of a high solubility species in a lower solubility host act as hydrogen traps, thus greatly reducing the diffusivity. Therefore, alloying Pd with yttrium would be expected to greatly reduce the

diffusivity, however, Pd-Y alloys have been shown to possess higher diffusivities than pure palladium [52, 66].

Palladium - Yttrium

Yoshinari et al [52] measured the room temperature diffusion coefficient in a range of solid solution Pd-Y alloys using an electrolytic technique and compared the data with previous, conflicting, diffusion data reported by Sakamoto [66] and Ishikawa [67] (Figure 3.13). Although the data reported by Sakamoto [66] and Ishikawa [67] were obtained at the same temperature using similar electrolytic techniques there is clear disagreement, with Sakamoto [66] reporting an increase and Ishikawa [67] reporting a decrease in diffusivity when compared to pure Pd (Figure 3.13). Both the activation energy (E_A) and the pre-exponential factor (D_o) determined by Ishikawa are considerably greater than those found by Sakamoto, across the whole range of yttrium concentrations investigated. Yoshinari's [52] data is qualitatively consistent with Sakamoto [66], in that small yttrium additions to palladium increase the diffusivity, although there is approximately a 30 % difference between the two sets of data.

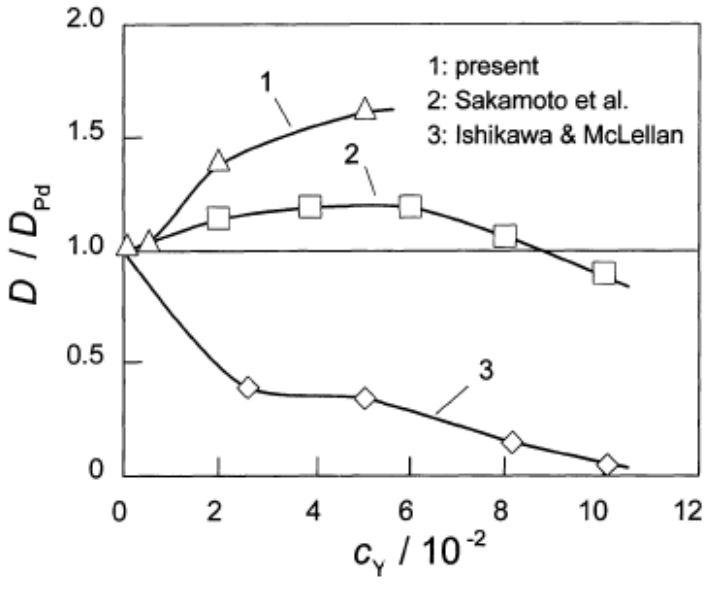

Figure 3.13 – The effect of Y concentration on the hydrogen diffusivity in Pd-Y alloys. Taken from Yoshinari [52]

A possible explanation for the differences in diffusion data becomes apparent on comparison of the Pd-Y thermal history. Prior to any diffusion measurements, all authors prepared their samples by annealing above 600°C before cooling to room temperature. However, both Sakamoto [66] and Yoshinari [52] performed this under a vacuum, whereas Ishikawa [67] used a hydrogen atmosphere. Yoshinari [52] proposed the differences were due to the large number of dislocations introduced to the Pd-Y lattice on formation of the β-hydride phase as the samples are cooled in hydrogen. Although any absorbed hydrogen was allowed to desorb before the diffusion measurements, thus removing the β hydride phase, Yoshinari [52] suggested that the residual dislocations would act as hydrogen traps, accounting for the reduced diffusivity compared to the vacuum annealed samples. It is important to note that despite the low temperatures employed during the diffusion measurements, β-hydride phase formation was avoided due to the low hydrogen concentrations (c = < 0.01).

However, as discussed in Section 3.2 the miscibility gap is closed at room temperature in Pd-Y alloys with a yttrium concentration greater than 7.8% [35], thus eliminating any possible β-hydride phase formation and associated dislocations, on cooling in hydrogen. If Yoshinari's [52] proposal is correct, the diffusion coefficients should progressively converge with increasing yttrium content (as the proportion of β-hydride phase formed decreases) until, at compositions of Pd-$Y_{7.8}$ and above, the reported diffusion coefficients should be identical. However, a similar difference between authors is still evident, with Sakamoto [66] reporting ~ 10 % increase compared to pure Pd and Ishikawa [67] ~ 80 % decrease in Pd-Y_8.

An alternative, and perhaps more likely, explanation for the discrepancies in diffusion data is offered by Doyle et al [46, 47] based on their own measurements of the Pd-Y system, and those of Hughes [57] and Wileman [55, 56]. As previously noted, several investigators have reported evidence of ordering in bulk Pd-Y alloys with high Y contents. When cooled under vacuum

from above a certain critical temperature (as performed by Sakamoto [66]) the alloy forms the ordered cubic Pd_7Y-type structure. If however, as in the experiments performed by Ishikawa [67], the alloy is cooled in a hydrogen atmosphere it does not order and will remain in the disordered condition. Once cooled, the alloy can be repeatedly cycled in hydrogen, below the critical temperature, and remain in either the ordered or disordered state. A disordered sample will only re-order when cooled from above the critical temperature after being thoroughly degassed of hydrogen. Hydrogen diffusion through the ordered alloy has been shown to be considerably higher than through the disordered alloy (Figure 3.14) [47, 57].

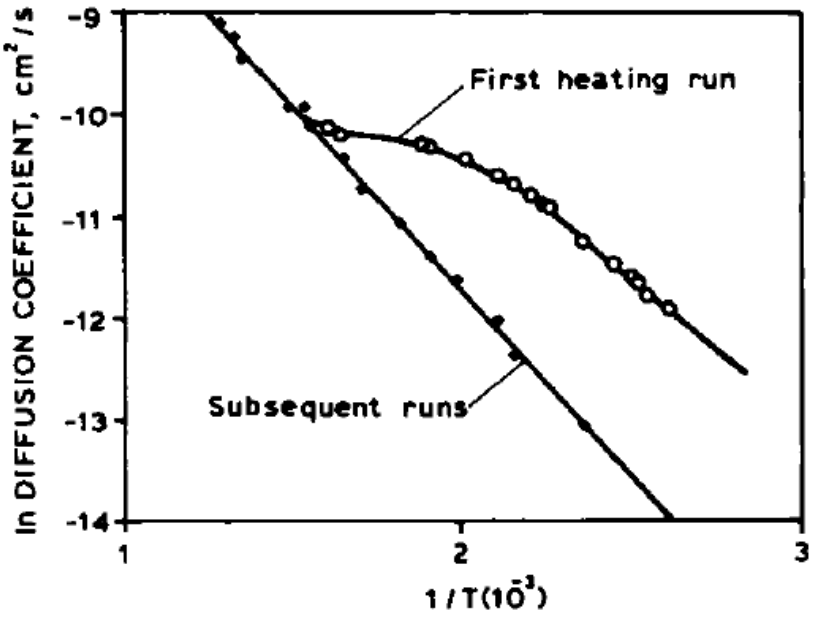

Figure 3.14 – Hydrogen diffusion through Pd-Y_8 in the ordered (first heating run) and disordered condition (subsequent runs). Taken from Doyle [47]

Both the diffusion parameters E_A and D_o of the disordered alloy are greater than those found for the ordered alloy, with the net result of a lower diffusivity at a given temperature [55]. The diffusion data presented by Sakamoto [66] was obtained for samples prepared by cooling from 850°C under a vacuum and would therefore be expected to be in the ordered state. The

activation energy (E_A) reported by Sakamoto [66] of 19.2 ± 1.0 kJ.mol^{-1} for Pd-Y_8 is similar to the 'ordered' value obtained by Wileman of 22.5 ± 0.5 kJ.mol^{-1} [55]. Accordingly, the samples prepared by Ishikawa [67] are expected to be in the disordered state after being cooled from 627°C in hydrogen. Although the activation energy reported for Pd-$Y_{8.1}$ of 42 kJ.mol^{-1} by Ishikawa [67] is considerably higher than Wileman's disordered value of 30.5 kJ.mol^{-1} [55], they are both well in excess of the ordered values.

Electronic considerations have also been shown to be a major factor in determining the diffusion activation energy of Pd alloys compared to pure Pd [68]. The changes in activation energy have been shown to be proportional to the valence electron concentration (C_sV_s) of the alloy. Buchold [68] suggested that an observed increase in activation energy with solute concentration was due to the breakdown of effective electronic screening as the Pd d-band is filled. The increase in activation energy can therefore be correlated with the electron concentration (C_sV_s).

Buchold's proposal was corroborated experimentally by Hughes [53], who investigated the diffusivity of hydrogen in the approximately isoelectronic alloys Pd-Y_8, Pd-Ag_{25} and Pd-$Ce_{5.75}$ using a permeation method. These alloys all have an approximate C_sV_s value of 0.24. The calculated diffusion coefficient of each alloy demonstrates Arrhenius-type behaviour with temperature and, within the experimental error, fall on the same slope (Figure 3.15). This indicates that the diffusion constants E_A and D_o are approximately equal for the three alloys. The calculated values are shown, together with a range of literature values on Pd, Pd-Ag and Pd-Y, in Table 3.1. The similarity in hydrogen diffusivity between Pd-Y_8 and Pd-Ag_{25} reported by Hughes [53] highlights the importance of the solubility gradient (as discussed in Section 3.3) on the hydrogen permeability, which is discussed further in next section.

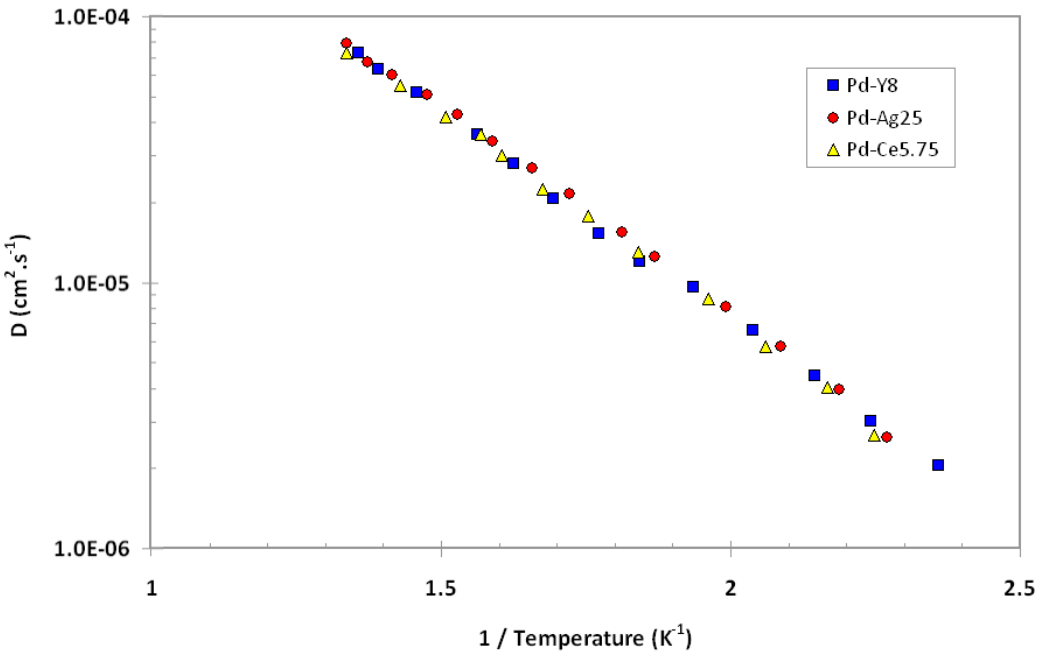

Figure 3.15 – Diffusion coefficient of hydrogen in the isoelectronic alloys Pd-Y_8, Pd-Ag_{25} and Pd-$Ce_{5.75}$ calculated from solubility and permeability data. Reproduced from Hughes et al [53]

Table 3.1 – Hydrogen diffusion data for a variety of Pd-alloys

Alloy	E_A ($kJ.mol^{-1}$)	D_o ($cm^2.s^{-1}$)	Reference
Pd	22.2	2.90×10^{-3}	Volkl & Alefeld [63]
Pd	22.0	2.94×10^{-3}	Holleck [65]
$Pd\text{-}Ag_{10}$	22.2	2.69×10^{-3}	Holleck [65]
$Pd\text{-}Ag_{20}$	22.3	2.33×10^{-3}	Holleck [65]
$Pd\text{-}Ag_{25}$	25.9	3.07×10^{-3}	Serra [37]
$Pd\text{-}Ag_{25}$	29.6	1.04×10^{-3}	Wileman [55]
$Pd\text{-}Cu_{47.5}$	2.4	3.0×10^{-3}	Piper [41]
$Pd\text{-}Ce_{5.75\ Ordered}$	21.7	–	Hughes [53]
$Pd\text{-}Ce_{5.75\ Disordered}$	30.9	–	Hughes [53]
$Pd\text{-}Y_{8\ Ordered}$	22.5	0.78×10^{-3}	Wileman [55]
$Pd\text{-}Y_{8\ Disordered}$	30.9	1.23×10^{-3}	Wileman [55]

3.5 – Hydrogen Permeation in Palladium and Palladium-Yttrium Membranes

The permeation rate, or flux, of hydrogen through a metal membrane can be quantified in terms of the hydrogen permeability (Φ). The permeability of a metal is a function of the hydrogen solubility and the hydrogen diffusivity, described in the two preceding sections. Alloying additions to Pd will modify either the hydrogen solubility or diffusivity, or both, to have a combined effect on the permeability. For example, although the ordered BCC β-CuPd phase, with a composition of Pd-$Cu_{40\text{-}50wt.\%}$, has a diffusivity 2 orders of magnitude higher than pure Pd, this alloy demonstrates a lower hydrogen permeability, and therefore flux, due to a much lower solubility.

However, the overall flux of hydrogen is not entirely dependent on the permeability alone. The permeation of hydrogen across a metal membrane takes place via a solution-diffusion mechanism which may be considered as several stages in series [50].

i. Molecular transport from the bulk gas to the gas layer adjacent to the surface
ii. Dissociative adsorption of molecular hydrogen onto the high pressure surface where atomic H is held at active surface sites
iii. Transition of atomic H from the surface into the bulk metal
iv. Atomic (screened proton) diffusion of H through the metal lattice to a point just inside the low pressure surface
v. Transition from the bulk metal to active surface sites on the low pressure surface
vi. Recombinative desorption on the surface
vii. Gas transport away from the surface into the bulk gas

Each step is characterised by an intrinsic forward and reverse rate, with the overall observed permeation rate governed by the relative contributions of each step under the given operating conditions. The permeation may be limited by just one step if it much slower than the others. In the case of the BCC transition metals V and Nb, which tend to form thick stable surface oxides, the permeation rate is controlled by the surface dissociation reaction. Therefore, although both V and Nb possess a higher theoretical permeability than Pd, these metals achieve lower fluxes due to the lack of available surface sites for adsorption and dissociation [31]. Palladium however, has a remarkable affinity for hydrogen dissociation and, under most operating conditions, bulk diffusion is the limiting step for Pd and Pd-Y membranes.

The diffusion flux, or permeance J_H (mol.m^{-2}.s^{-1}), of hydrogen through a Pd-Y membrane can then be described in terms of the diffusion coefficient (D) and the concentration gradient ($\Delta c_H / x$) by Fick's 1st law,

$$J_H = -D \frac{\Delta c_H}{x} \qquad \textit{Eqn 3.12}$$

Where J_H is the hydrogen flux, or flow rate per unit area (mol.m^{-2}.s^{-1}), D is the diffusion coefficient as described in Eqn 3.11 (m^2.s^{-1}), c_H is the atomic concentration of hydrogen (mol.m^{-3}) and x is the membrane thickness (m).

Assuming that the near-surface hydrogen concentration at either side of the membrane corresponds to the equilibrium hydrogen solubility for the particular conditions of

temperature and pressure, then application of Sievert's law gives the atomic concentration of hydrogen (c_H) in terms of the partial pressure.

$$c_H = K_S \, P_{H_2}^{0.5} \qquad \textit{Eqn 3.13}$$

where, K_S denotes Sievert's constant and P_{H_2} is the gas-phase pressure of molecular hydrogen. Combining Equations 3.12 and 3.13 and integrating through the membrane thickness (l), gives the hydrogen permeation (J) in terms of the partial pressure of hydrogen at both the high and low pressure sides of the membrane, the so-called Richardson equation [31].

$$J_{H_2} = -\frac{DK_S}{2}\frac{\left(Pi_{H_2}^{0.5} - Pii_{H_2}^{0.5}\right)}{l(x)} \qquad \textit{Eqn 3.14}$$

where *Pi* and *Pii* denote the external gas-phase hydrogen pressure at the high pressure and low pressure sides respectively and *l(x)* is the membrane thickness. The first term in Eqn 3.14 can be combined to give the hydrogen permeability Φ (mol.m^{-1}.s^{-1}.Pa$^{-0.5}$) of the membrane.

$$J_{H_2} = \Phi \frac{\left(Pi_{H_2}^{0.5} - Pii_{H_2}^{0.5}\right)}{l(x)} \qquad \textit{Eqn 3.15}$$

In the majority of cases, Eqn 3.15 accurately describes diffusion-limited hydrogen flux through dense metal membranes. In certain situations however, bulk diffusion does not

exclusively determine the permeation and the rate of molecular dissociation / recombination at the membrane surfaces can contribute to the overall rate (Steps *ii* and *vi* as identified by Ward & Dao [50]). In such circumstances, the near surface hydrogen concentration is not in equilibrium with the external gas-phase pressure, thus Sievert's law is no longer valid and the overall driving force for diffusion is reduced (Figure 3.16).

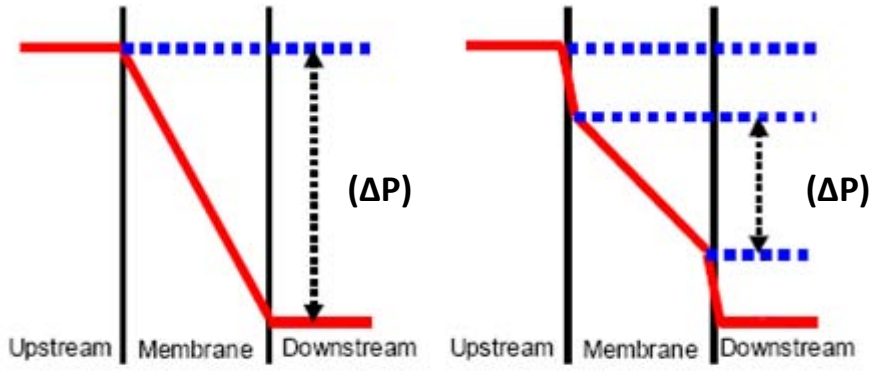

Large driving force (ΔP) Small driving force (ΔP)

Figure 3.16 – Effect of surface activity on the driving force across a membrane. Taken from Unemoto [69]

If hydrogen dissociation at the membrane surface is the sole rate-limiting step, the partial pressure exponent increases from 0.5 to 1. When surface effects and bulk diffusion have a combined contribution to the overall permeation, the pressure exponent will range between 0.5 and 1, with the exact value determined by the relative contribution of each step. A more general form of the membrane permeation equation (Eqn 3.15), which compensates for the various rate determining steps can therefore be given as,

$$J_{H_2} = \Phi \frac{\left(Pi_{H_2}^{n} - Pii_{H_2}^{n}\right)}{l(x)} \qquad Eqn\ 3.16$$

Where the value of n is calculated via least-squares regression of experimental data and varies between $n = 0.5$ and $n = 1$ for bulk diffusion limited and surface limited permeation respectively. In addition to surface activity, other factors including Knudsen diffusion of molecular hydrogen along defects and grain boundaries, surface contamination, changes in structure and internal stresses have been shown to increase the value of n [27, 70, 71]. Palladium and palladium alloys possess extremely active surfaces for hydrogen dissociation, thus, the predominant reason for values of n greater than 0.5 are due to surface poisoning by contaminants such as CO [70, 72] and H_2S [39, 73].

From Eqn 3.16 is clear that the hydrogen flux through a membrane is inversely proportional to the membrane thickness (l) and directly proportional to both the permeability (Φ) and the partial pressure gradient across the membrane. Given that the operating pressure conditions will be determined by the particular application and are effectively 'external' to the membrane, the maximum potential flux can be increased by reducing the thickness and / or increasing the permeability. The membrane thickness is generally determined by a combination of the production technique (rolling, drawing etc) and the minimum required to provide the necessary mechanical strength during operation. It follows, therefore, that efforts to increase the attainable flux have traditionally been focused on improving the membrane permeability. A considerable volume of work has been performed since the 1960's on various systems including numerous binary [49] and ternary alloys [74] of Pd, Pd coated refractory metals V and Nb [31], and complex alloys of V-Ti-Ni [75], Ni-Ti-Nb [76] and Nb-Ti-Co [77] in an attempt to improve the permeability relative to Pd. A selection of these are listed in Table 3.2. However, relatively few systems offer an enhanced permeability and only a minority of those retain structural integrity upon repeated exposure to hydrogen and thermal cycling. One such system is Pd-Y, with Pd-$Y_{7.5}$ [56], Pd-Y_8 [53, 78] and Pd-Y_{10} [15] all demonstrating significantly

greater permeability than Pd-Ag_{24}. The superior permeability of Pd-Y alloys has been attributed to a significantly enhanced solubility gradient, and thus concentration gradient, when compared to Pd-Ag_{24} [53].

As noted in the previous sections, the solubility and diffusivity of hydrogen in Pd-Y alloys is dependent on the degree of order, with both parameters significantly greater in the ordered condition. Given that the permeability of an alloy is the product of the solubility and the diffusivity, it follows therefore, that the permeability of Pd-Y is considerably greater in the ordered condition than the disordered condition (Figure 3.17).

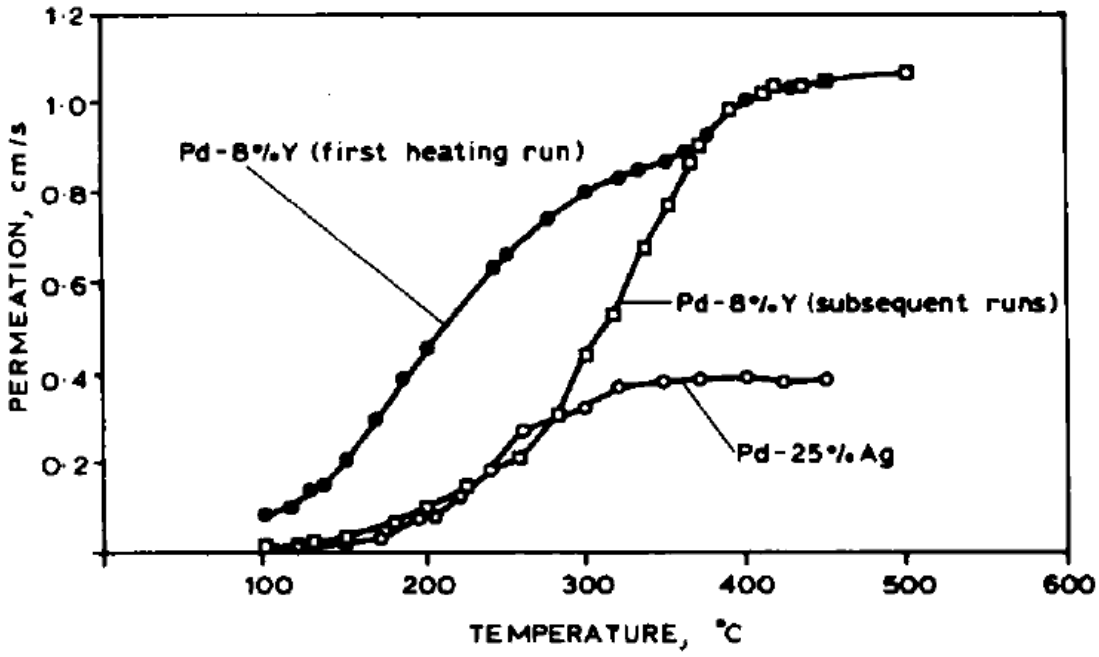

Figure 3.17 – Effect of order / disorder on the permeability of Pd-Y_8 compared to Pd-Ag_{25}. The alloy is ordered in the first heating run and disordered in the subsequent runs. Taken from Doyle [47]

Comparison of the permeability in the disordered Pd-Y_8 alloy and Pd-Ag_{25} to the solubility data reported by Hughes [53] (see Section 3.3) clearly demonstrates the enhanced permeability of Pd-Y alloys compared to Pd-Ag is due to a greater solubility gradient, and thus a greater concentration gradient.

Table 3.2 – Hydrogen permeability of various alloys

Alloy / Composition	Temperature	Permeability ($mol.m^{-1}.s^{-1}.Pa^{-0.5}$) (x 10^{-8})	Reference
Pd	350ºC	1.34	Morreale [79]
Pd	350ºC	1.20	Holleck [65]
Pd-Ag_{25}	350ºC	1.65	Serra [37]
Pd-Ag_{25}	350ºC	2.00	Holleck [65]
Pd-$Au_{5wt\%}$	350ºC	1.47	McKinley [80]
Pd-$Au_{20wt\%}$	350ºC	0.58	McKinley [80]
Pd-$Cu_{20wt\%}$	350ºC	0.267	Morreale [39]
Pd-$Cu_{40wt\%}$	350ºC	0.646	Morreale [39]
Pd-$Cu_{53wt\%}$	350ºC	0.107	Morreale [39]
Pd-$Cu_{40wt\%}$	350ºC	1.48	McKinley [80]
Pd-$Ce_{5.75}$	350ºC	2.44	Hughes [53]
Pd-$Ru_{5wt\%}$	350ºC	0.454	McKinley [80]
Pd-$Ni_{10wt\%}$	350ºC	0.261	McKinley [80]
Pd-Fe_{7}	200ºC	0.047	Bryden [81]
Pd-Gd_{8}	350ºC	5.31	Sakamoto [78]
Pd-$Gd_{6.3}$-Ag_{5}	350ºC	5.33	Sakamoto [78]
Pd-$Y_{4.7}$-Ag_{10}	350ºC	3.71	Sakamoto [78]
Nb_{30}-Ti_{35}-Co_{35}	350ºC	1.8	Hashi [77]
Ta_{53}-Ti_{28}-Ni_{19}	350ºC	1.2	Hashi [75]
V_{41}–Ti_{30}–Ni_{29}	350ºC	1.0	Hashi [75]
Pd-$Y_{7.5}$	350ºC	5.60	Wileman [56]
Pd-Y_{8}	350ºC	3.92	Sakamoto [78]
Pd-Y_{8}	350ºC	5.52	Hughes [53]
Pd-Y_{10}	350ºC	4.26	Fort [15]

3.6 – Current Limitations of Palladium-based Membranes

The United States Department of Energy (DoE) has established a series of performance targets for all 'hydrogen economy' related technologies [8]. Those for dense metal membrane systems are classified in terms of hydrogen production using a membrane reactor (Table 3.3).

Table 3.3 – Current US DoE performance targets for dense metallic membranes [8].

Performance Criteria	Units	2010 Target	2015 Target
H_2 Flux @ 400°C	$Scfh.ft^{-2}$ ($mol.m^{-2}.s^{-1}$)	250 (0.945)	300 (1.134)
Cost	$\$US.ft^{-2}$	1000	<500
Durability	hr	26,280	43,800
Operating Pressure	Psi (kPa)	400 (2670)	400-600 (2670-4000)

Commercial Pd-Ag membrane systems typically have a thickness of 50 µm and operate at around 400°C. At this temperature the hydrogen permeability of $Pd\text{-}Ag_{24}$ is approximately 3.0×10^{-8} $mol.m^{-1}.s^{-1}.Pa^{-0.5}$. Under the pressure conditions specified by the DoE, a commercial membrane system would achieve a hydrogen flux of around 0.1 $mol.m^{-2}.s^{-1}$, approximately an order of magnitude below that required for the 2015 targets. From the general permeability equation (Eqn 3.16) it is clear that, at any given operating pressure conditions, the hydrogen flux is increased by either increasing the membrane permeability or by reducing the thickness. Considering the highest reported permeability of any Pd alloy system is that of Pd-Y, which possesses values between 2 - 3 times that of Pd-Ag, this is still far from the 2015 target values. It is apparent therefore, that in order to meet or exceed the DoE flux targets, the membrane thickness must be reduced.

From the general permeability equation (Eqn 3.16) it is clear that hydrogen flux has a hyperbolic relationship with membrane thickness. Halving the thickness will double the flux and for relatively thick membranes (> 12 μm), this relationship is experimentally valid [82, 83]. There is some debate as to the extent of the validity of this relationship however, primarily because it is assumed that Sievert's law is valid and thus, the flux through the membrane is diffusion controlled. However as thickness is reduced there will come a critical value, below which, diffusion through the membrane is so fast that surface reactions are expected to limit the flux. Under these conditions, further reducing the thickness would be expected to have little, if any, effect on the flux. There is wide disagreement as to the value of thickness below which permeation is surface controlled and therefore independent of thickness. Ward [50] concluded that at suitably high temperatures (> 300°C) and in the absence of external mass transfer resistance, diffusion-limited permeation is expected for clean Pd at thicknesses down to 1 μm. This has recently been corroborated experimentally by Mejdell et al [84] and Gade et al [85] for free-standing Pd, Pd-Ag and Pd-Cu thin films down to just 1.3 μm in thickness. It is reasonable to assume similar behaviour for Pd-Y alloys considering the similarity in hydrogen diffusivity compared to Pd-Ag [53]. Based on the validity of the general permeability equation (Eqn 3.16), the minimum thickness required to meet the DoE 2015 flux targets for a Pd-Ag_{24} membrane is 4.5 μm.

Reducing the membrane thickness not only increases the flux, but has the additional advantage of dramatically reducing the amount of expensive palladium required to produce a given flow rate. Assuming a commercial, drawn tube membrane with a thickness (t) of 50 μm produces a hydrogen flow, F, over an area, A, and has a volume V, a 5 μm membrane with the same area has a flow rate equal to F / 0.1, or 10F. Therefore to maintain F, an area of just 0.1 A is required. The total volume of Pd-Ag required is then 0.1 A multiplied by 0.1 t: a 100

fold reduction in volume. The material cost of the membrane system is reduced by two orders of magnitude and can then be considered insignificant to the overall cost of producing the membrane.

Section 4 – Thin Film Palladium and Palladium-alloy Membranes

4.1 – Introduction

The minimum thickness of a membrane fabricated using traditional methods such as rolling or drawing is ~ 20 μm. Below this thickness, pinholes and other defects are often present which reduce the potential gas selectivity of the membrane. Thin film deposition techniques are therefore required to produce membranes with the necessary thicknesses of < 5 μm required to meet the 2015 DoE flux targets [8]. Such thin membranes do not have the mechanical strength to resist the stresses associated with typical operational regimes, and require a relatively thick underlying porous support to fully withstand the thermal expansion, lattice expansion, and pressure gradient across the membrane during use. The nature of any thin film deposition technique requires the use of a substrate onto which the film is deposited. In the case of thin film membranes it is convenient to deposit the membrane directly onto the porous support. The resulting multilayered structure is often referred to as a composite membrane (Figure 4.1).

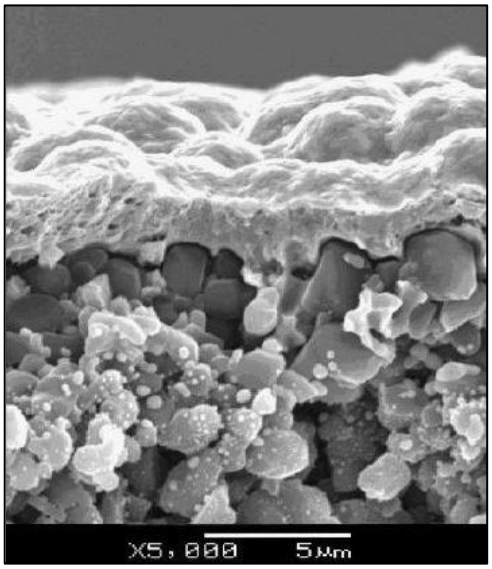

Figure 4.1 – A Pd-Ag_5 / α-alumina thin film composite membrane. Taken from Zeng et al [86].

A variety of Pd and Pd alloy thin film membranes have been deposited onto a diverse range of underlying porous supports. By far the most common composite membrane structure is pure palladium deposited onto either porous stainless steel or a porous ceramic such as alumina. The open nature of a macroporous surface often requires the use of intermediate layers with a finer pore size, in order to produce a defect-free thin film [87]. Composite membranes often have extremely complicated structures and, in order to accurately quantify the performance and to enable comparisons between membranes to be made, each component of the composite membrane must be analysed individually. This approach has been employed throughout the present work.

4.2 – Palladium and Palladium-alloy Thin Film

The dense thin film acts as the selective barrier for hydrogen separation, exactly the same as with traditional self-supporting membranes. Therefore, in order to separate ultra high purity hydrogen, the film must be completely continuous with no defects. Physical defects within a thin film membrane are broadly referred to as pinholes and can include both macroscopic and microscopic defects, such as open pores or voids within the crystal structure. Even a low pinhole density will greatly reduce the potential selectivity of the membrane [88]. Palladium and palladium alloy thin films have been deposited using a wide variety of techniques including electroless plating, chemical vapour deposition, electrodeposition and physical vapour deposition such as magnetron sputtering. Most published information regarding composite membranes is based on the use of electroless plated pure palladium as the selective thin film, presumably for ease of manufacture. However, some thin film Pd alloys have been studied including Pd-Ag [89], Pd-Cu [90], Pd-Ni [91] and Pd-Ru [92].

4.2.1 – Membrane Deposition

Electroless Plating

Electroless plating is a prevalent form of palladium membrane production, primarily because of its simplicity but also because of the potential to deposit a wide range of thicknesses onto most substrates even with complex geometries. Numerous authors have reported successful deposition of defect-free palladium films varying between 1 μm [93] and 33 μm [82]. Electroless plating is an autocatalytic reaction, which typically involves three stages; surface cleaning, surface activation, and film deposition. Surface cleaning is an essential step prior to any deposition technique and typically involves washing in dilute acid, alcohol or acetone and rinsing with de-ionised water. After cleaning, the substrate surface is then activated prior to plating, commonly using tin chloride sensitising and palladium activation baths to deposit small Pd clusters on the surface, although a significant amount of Sn can also be deposited [94, 95]. The substrate is then said to be 'seeded' with the Pd clusters acting as catalysts for the plating reaction. Electroless plating baths usually consist of a palladium-amine complex stabilised by a sequestering agent such as Na_2EDTA. Controlled deposition of palladium is achieved via chemical reduction of Pd ions using a suitable reducing agent [94, 96, 97],

$$2Pd(NH_3)_4^{2+} + N_2H_4 + 4OH^- \rightarrow 2Pd + N_2 + 8NH_3 + 4H_2O \qquad Eqn\ 4.1$$

To facilitate uniform deposition the plating solution is usually mechanically agitated which also prevents gas bubbles from adhering to the surface forming defects within the film. Once the Pd solution has been fully consumed, the substrate is removed and the plating bath

replenished. These steps are repeated until the desired palladium thickness is achieved. Finally, the deposited film is vacuum annealed to ensure homogeneity.

Although electroless deposition of palladium is a relatively established technique for the production of composite Pd membranes, there are several limitations. Electroless plated films often possess significantly lower densities than the equivalent bulk material due to voids and impurities such as carbon or tin. Indeed, carbon contents of up 6.5 wt.% have been reported within electrolessly deposited Pd membranes [98]. The actual deposition rate, and both the film structure and morphology depend strongly on many variables. High plating temperatures typically produce small closely packed palladium crystallites due to a higher deposition rate than at low temperatures. This results in a more dense structure with a smaller grain size, which typically contains fewer defects and therefore offers greater selectivity. However, if the deposition rate is too high, voids may be formed within the film thus introducing defects and potentially reducing the selectivity [99]. The observed deposition rate however, is not only dependent on temperature. The plating bath concentration, substrate surface topography, substrate composition and activation conditions will all affect the observed deposition rate.

When depositing onto a porous substrate, non-uniform film thicknesses are commonly observed, even with the use of an agitator. Relatively thick ‘peaks’ are formed above the dense outer surfaces of the substrate whilst much thinner sections form over the pore walls. The non-uniform thickness combined with the uncertainty over deposition rate make manufacturing composite palladium membranes with reproducible thicknesses extremely difficult. Average film thickness estimates are predominantly made using mass gain techniques, which are often unreliable. Without a known thickness, hydrogen flux through composite membranes is often presented as a permeance, or flux per unit pressure

($mol.m^{-2}.s^{-1}.Pa^{-0.5}$) rather than as a thickness independent permeability ($mol.m^{-1}.s^{-1}.Pa^{-0.5}$) [82, 89, 93, 100], giving an extremely large degree of uncertainty between published data.

Perhaps the major limitation of the electroless plating technique however, is its unsuitability for depositing Pd alloys. Thin film Pd membranes are subject to the same limitations as traditional self-supporting Pd membranes, namely β-hydride phase formation below 300°C, low tensile strength and low hydrogen permeability when compared to Pd alloys. Numerous attempts have been made to co-deposit solid solution Pd-Ag alloys via electroless plating with only limited success [97, 101, 102]. Electroless co-deposition of Pd-Ag is a catalytic process with individual deposition rates of Pd and Ag dependent on the catalytic activity of the active seeds or substrate. Shu et al [101] investigated the effect of Pd / Ag ratio of the plating bath on the deposited film composition. Silver was found to deposit preferentially and actually inhibit palladium deposition, unless the plating bath was highly Pd rich (> 80% Pd). A plating bath ratio of Pd 83% / Ag 17% was found to deposit distinct Pd and Ag phases with a dominant silver phase. A small amount of solid solution Pd-Ag was detected, although this was Pd-rich. The deposited films were subsequently annealed under hydrogen to produce a single homogenous alloy, with a composition of $Pd\text{-}Ag_{56}$.

Another option is the sequential deposition of distinct layers followed by an appropriate heat treatment to produce a homogenous alloy film. This technique has been performed on a variety of substrates to form both Pd-Ag [89, 103-108] and Pd-Cu [90, 108-110] composite membranes. Although the composition control appears greater than that achieved via co-deposition, significant discrepancies still exist. Keuler [89] produced a number of sequentially deposited Pd-Ag membranes which, despite identical production conditions, varied in thickness by up to 57 % and ranged in composition between $Pd\text{-}Ag_{20\text{-}25wt\%}$. Given that at a composition of $Pd\text{-}Ag_{20wt\%}$, β-hydride formation would still be expected above room

temperature [102], greater compositional control is required. In addition, very high temperatures are required to produce fully homogenous films. Ma [108] concluded that annealing at 600°C was insufficient to produce a homogenous Pd-Ag film due to the non-uniform deposition of Ag, although homogenous Pd-Cu films were successfully produced. However, Hou [104, 105] successfully homogenised 5 µm thick Pd-Ag membranes after annealing under a hydrogen atmosphere at 600°C for 50 hrs. Hydrogen may act as a catalyst for homogenisation by facilitating atomic diffusion [111]. Temperatures as high as 800°C have been required for effective homogenisation [107]. Such high temperature annealing is unsuitable for films supported on metallic substrates due to the possible intermetallic diffusion between the alloy film and the substrate. Iron diffusion into Pd is a particular problem for films supported on porous stainless steel substrates [112]. Although non-metallic substrates are not susceptible to interdiffusion, they possess significantly different coefficients of thermal expansion to Pd alloy films. Therefore, the associated thermal mismatch during high temperature annealing can introduce defects within the Pd film.

Annealing sequentially deposited layers to form a homogenous Pd-Ag alloy has been attempted using various other deposition techniques including both electro-deposition [100, 113] and chemical vapour deposition [114] with similar difficulties in composition and thickness control, as those noted above for electroless plating.

Magnetron Sputtering

Single-phase solid solution Pd-Ag and Pd-Cu alloys have been deposited without the need for subsequent thermal homogenisation using magnetron sputtering [115, 116]. During the sputtering process a thin film is deposited when a gas plasma, usually argon, bombards the metal target

dislodging metal atoms from the surface which subsequently condense on the substrate surface. The deposited film thickness is directly proportional to sputtering time, thus allowing accurate control over membrane thickness. Prior to membrane deposition, the gas plasma can be directly applied to the substrates in order to remove any contaminants leaving a clean surface for deposition. The required membrane material can then be deposited to any thickness, without breaking the vacuum, in a single process. In order to enhance the uniformity of the deposited film, substrates are usually rotated during deposition. Membranes can be sputtered on to external surfaces of both conducting and non-conducting substrates with excellent thickness uniformity.

Xomeritakis & Lin [117] deposited thin (100 – 500 nm) Pd-Ag membranes using a single Pd-Ag_{25} target. They found the silver concentration of the membranes (Pd-Ag_{15}) to be significantly lower than the target and attributed this to the dissimilar sputter rates of Pd and Ag, due to differences in atomic mass and binding energy. A subsequent study by McCool [115] attempted to address this issue by performing a pre-sputter routine to clean the target surface and achieve a degree of surface equilibration, which they define as when both species are ejected at the same ratio as the target composition. During pre-sputtering the substrates are shielded to prevent any unwanted deposition. The pre-sputter equilibration time was varied between 1 – 15 mins with a greater composition match after longer pre-sputtering times. McCool [115] estimated that approximately 100 nm of target should be removed in order to reach equilibration. Successful target pre-sputtering techniques have also been reported by Jayaraman [88] and Mejdell [84] to sputter 100 nm – 5 µm Pd-Ag_{23} membranes from a single target with an identical composition.

More recently a range of Pd-Ag [118-120] and Pd-Cu [116, 121] membranes have been co-sputtered using separate, pure metal, targets. The experimental conditions are similar for all studies with

the substrate positioned centrally between the Pd target and either the Ag or Cu target. During deposition the voltage to the Pd target is kept constant whilst the voltage to the alloying target is varied in order to control the composition. Zhang [118] deposited 100 nm Pd-Ag membranes with compositions ranging between 0 - 45 at.% Ag. X-ray diffraction (XRD) and energy dispersive spectroscopy (EDS) techniques were used to determine the composition and to confirm the membranes were homogenous single phase. Above a certain voltage, dependent on the Pd target voltage, the composition of the membrane was found to be directly proportional to the voltage on the Ag target (Figure 4.2).

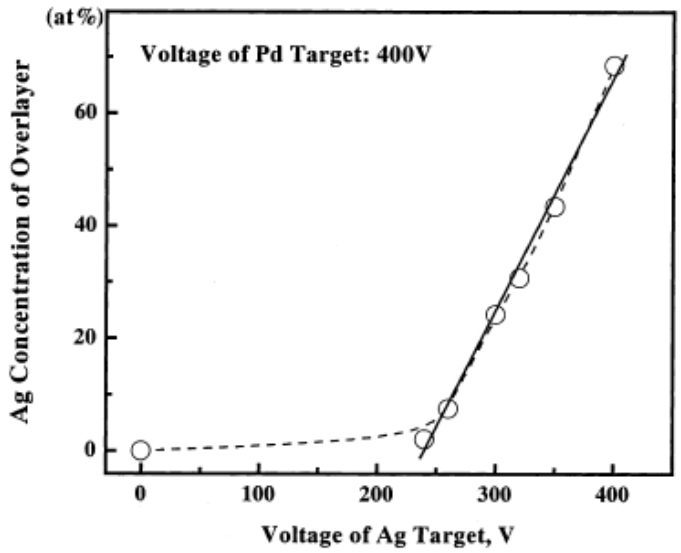

Figure 4.2 – Effect of Ag target voltage on co-sputtered Pd-Ag membrane composition. Taken from Zhang [118]

The linear relationship between target voltage and alloy composition has also been demonstrated for Pd-Cu membranes by Yang et al [116], who deposited fully homogenous single phase Pd-Cu membranes with Cu concentrations from 0 to 60 wt.% (Figure 4.3). Interestingly, all compositions were found to have the FCC crystal structure. However, from the binary Pd-Cu phase diagram, at Cu concentrations above approximately 30 wt.%Cu, Pd-Cu films would be expected to have a mixed BCC / FCC structure, whilst at compositions

between 40 and 55 wt.%Cu, it should be purely BCC. Yang [116] suggested that the formation of, what is likely to be, the metastable super-saturated solid solution was due to an increase in the Gibbs free energy when compared to bulk alloys, brought about by the nano-crystalline microstructure.

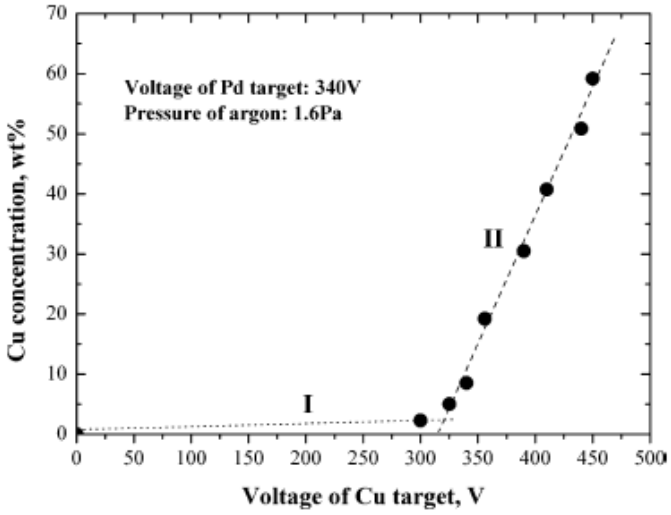

Figure 4.3 – Effect of Cu target voltage on co-sputtered Pd-Cu membrane composition. Taken from Yang [116]

Yang [116] also demonstrated the membrane thickness increased linearly with deposition time. The target voltages required to produce a Pd-$Cu_{40wt.\%}$ membrane gave a sputter rate of 3.5 $nm.s^{-1}$, which permitted excellent thickness and composition reproducibility.

In summary, magnetron sputtering appears to be a deposition technique ideally suited to the production of Pd alloy composite membranes. In addition to the excellent compositional control, membranes deposited by magnetron sputtering do not require a post-deposition thermal treatment in order to achieve a homogenous solid solution film. The substrate surface can be cleaned and the membrane deposited in a single process, without breaking the vacuum, and both conducting and non-conducting substrates can be coated.

Currently, there is no published information regarding thin film Pd-Y membranes. However, the use of magnetron sputtering to deposit fully homogenous, single phase Pd-Ag and Pd-Cu membranes suggests that solid solution Pd-Y membranes could also be produced using this technique.

4.2.2 – Membrane Integrity and Defects

The quality of the deposited Pd alloy film is usually assessed in terms of selectivity or separation factor, which is defined as the H_2 / N_2 flux ratio across the membrane. A defect-free membrane would demonstrate infinite selectivity, as only hydrogen would permeate the continuous layer. Reported selectivity values vary considerably, but currently rarely exceed 5000. Some authors have reported infinite selectivity values for as-deposited membranes which subsequently decrease on heating or hydrogen absorption as pinholes develop [14].

The term ‘pinhole’ is broadly used to describe a variety of defects, both microscopic and macroscopic. Microscopic defects include breaks in the film along grain boundaries or due to voids within the crystal structure and typically affect electroless plated membranes to a greater extent than sputtered membranes due to the film growth mechanism. Macroscopic defects can include open pores due simply to poor coverage, and splits / cracks due to localised areas of delamination during thermal cycling or to the lattice expansion experienced during hydrogen absorption (Figure 4.4). Macroscopic defects have the greatest effect on selectivity and a large volume of work has been published on membrane fabrication methods to eliminate such pinholes, many of which are discussed further in Section 4.4.

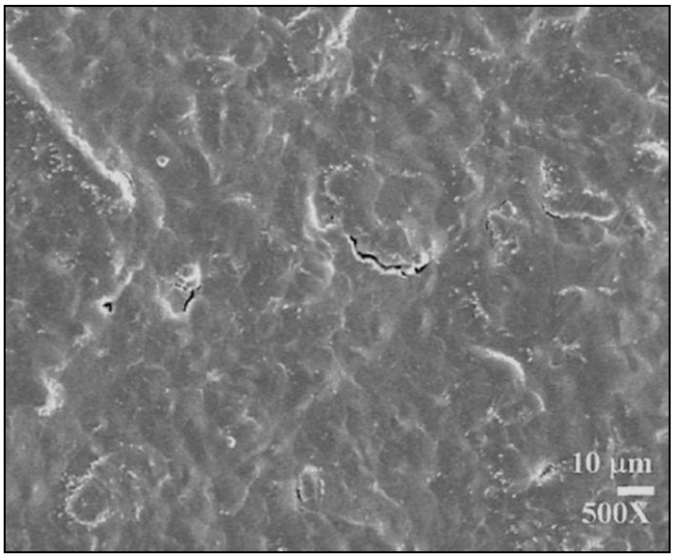

Figure 4.4 – An example of macroscopic defects in a sputtered 5µm Pd membrane. Taken from Checcetto [122]

Given a clean, debris-free surface, the minimum film thickness required to guarantee a continuous membrane is predominantly determined by both the surface pore size and surface roughness of the substrate [115, 117, 123, 124]. The minimum thickness of the membrane required for complete coverage generally decreases with surface pore size, although several authors have reported there may be a limit, beneath which the surface may be too smooth [109, 125]. The membranes may then delaminate due to a lack of mechanical interlocking, reducing the membrane adhesion. Ye et al [125] suggested a pore size lower limit of 20 nm, which is in good agreement with the findings of Roa et al [109], who were unable to deposit defect-free membranes on γ-alumina substrates with surface pore sizes of 5 nm, yet highly selective membranes were deposited onto substrates with 50 nm and 200 nm surface pore sizes.

Ma et al [126] suggested that in order to deposit a defect-free membrane, the minimum film thickness required is approximately 3 times the maximum surface pore size. Subsequent studies on both porous nickel [12] and porous stainless steel [82] substrates support this general rule.

Undoubtedly, the quality of a thin film membrane is predominantly determined by the underlying substrate surface onto which it is deposited. Pinhole formation during both film deposition and membrane operation are directly related to the substrate surface in terms of pore size, roughness, cleanliness, adhesion, thermal compatibility and stability under hydrogen atmospheres.

4.3 – Porous Substrates

A wide variety of porous materials have been used to support thin film membranes. Typically the Pd / Pd alloy film is deposited on or within the surface pores of the support by one of the deposition techniques outlined in preceding section.

The predominant requirement of a porous substrate is simply to provide enough mechanical strength to resist the stresses experienced by the composite membrane during operation. However, in order to do this effectively, in terms of both cost and performance, there are several other requirements a potential substrate must meet;

- The substrate must be completely compatible, both chemically and physically, with the Pd / Pd alloy film,
- Must provide sufficient adhesion between the Pd / Pd alloy film and the substrate surface to resist the stresses experienced during operation due to both thermal expansion and hydrogen induced lattice expansion,
- The substrate should be stable at high temperatures and under a hydrogen atmosphere,
- Be resistant to possible contaminants within the feed gas stream and,

- In terms of economical requirements, the substrate should have a low production cost and be easily formable / sealable into a suitable membrane module.

Above all however, if thin film composite membranes are to fulfil the potential performance advantage over traditional self-supporting rolled / drawn Pd-Ag membranes, the substrate must offer minimal resistance to hydrogen transport. If a substrate offers considerable resistance to hydrogen flow the potential flux of the thin film membrane will not be realised.

Many composite Pd-based membranes have been produced using commercially available porous ceramics such as alumina [94, 109, 123, 127], titania [128, 129] and zirconia [110], porous glass [13, 130] and porous metals including stainless steel [14, 82, 87, 100, 126] and Inconel [131]. Whilst others have attempted to manufacture novel substrates specifically designed to support a thin film Pd-based membrane including porous nickel [12, 21, 121], porous silicon [10], mixed ceramics [92] and lithographically deposited dense nickel strips [132, 133].

Currently, no single substrate material meets all the ideal requirements, each having economic and performance trade-offs. Ceramic substrates, particularly alumina, are widely used due to the fine pore size with a narrow size distribution and chemical stability at high temperature. Alumina substrates are commonly used for electrolessly deposited Pd alloy films to enable the high temperature homogenisation required to produce a single phase alloy membrane [104, 105, 107]. Hou [105] electrolessly deposited sequential layers of Pd and Ag on α-alumina with a surface pore size of 180 nm, followed by homogenisation under hydrogen for 50 hrs above 600°C. The high temperatures required for successful homogenisation, some in excess of 800°C [107], are unsuited to a metallic substrate due to the intermetallic diffusion between substrate and the membrane. Iron diffusion into the Pd alloy membrane is a particular problem encountered when using porous stainless steel substrates [112].

Ceramic substrates can possess very fine pore sizes, and hence allow a reduction of the minimum film thickness required to form a defect-free membrane. However, hydrogen flux through the substrate decreases with pore size, thus negating the performance advantage of the reduced membrane thickness. Hydrogen flux through ceramic substrates can be increased using a multilayered, asymmetric, structure. Asymmetric substrates usually comprise at least 3 distinct layers, each with a different pore size and are similar in nature to porous separation membranes. The International Union of Pure and Applied Chemistry (IUPAC) define the following pore size classifications using pore diameter (d_p) [26];

- Microporous : $d_p < 2$ nm
- Mesoporous : d_p 2 – 50 nm
- Macroporous : $d_p > 50$ nm

Typically, a relatively thin (~ 1 μm) micro- or mesoporous layer is supported by a thick (~ 1 mm) macroporous layer, usually with at least one intermediate mesoporous layer. Titania, zirconia and γ-alumina are commonly used as the top layer [22]. Although asymmetric ceramic substrates offer the combination of small surface pores and low mass transfer resistance, the top layer is much more susceptible to defects than uniform symmetric substrates [134] and the multi-stage manufacturing process makes them more costly than other types of porous media [27]. The major disadvantage of ceramic substrates however, is the relatively weak adhesion with the metallic film. There is a significant thermal expansion mismatch between the Pd alloy and the ceramic substrate which results in high stresses during thermal cycling. When combined with the lattice expansion due to hydrogen absorption, the stresses within the film overcome the adhesive force, thus resulting in delamination and ultimately membrane failure [9].

Keuler [89] used electroless plating to sequentially deposit Pd-Ag on to asymmetric alumina substrates. The Pd-Ag films had an approximate thickness of 2 μm, ten times the surface pore size and more than 3 times the minimum thickness recommended by Ma et al in order to achieve a defect-free continuous film [126]. As expected, the membranes initially demonstrated relatively high selectivity, thus indicating a low pinhole density. However, both the hydrogen and argon flux rapidly increased at temperatures around 550°C as a result of defect formation and film delamination.

In addition to the relatively poor adhesion and thermal expansion mismatch, ceramic substrates are rather brittle and can be difficult to join / seal into a membrane module [27]. Typically, porous metallic substrates do not experience such problems and would seem inherently more suited for use in composite membranes.

Porous metals are fabricated by sintering either milled or atomised metal powders, with various grades of stainless steel, Inconel, aluminium and titanium all available commercially [135]. Porous stainless steel (PSS) substrates are widely used for composite membranes as they are relatively cheap, easily weldable / sealable, offer low mass transfer resistance, posses similar thermal expansion properties to palladium and, with careful surface preparation, provide excellent adhesion to the Pd alloy film when compared to non-metallic substrates.

However, there are two distinct disadvantages when using PSS substrates. Even the best commercially available PSS has a much larger pore size with a wider pore size distribution when compared to ceramic substrates. Mardilovich et al [82] used mercury intrusion to determine the pore size distribution of PSS with varying porosity. The finest pore size available, designated 0.1 μm media grade by the manufacturer [135], was found to have an

average pore size of ~ 5 µm with much larger surface pores, indeed other authors typically report surface pore sizes of between 10 and 20 µm [136]. Based on the minimum film thickness rule proposed by Ma [126], a membrane of ~ 30 to 60 µm would be required to ensure the absence of pinholes when using such a substrate. After depositing several thicknesses, Li et al [137] concluded a film of at least 35 µm was required to produce a defect free membrane on PSS. Ryi et al developed a porous nickel substrate with a much finer average surface pore size of ~ 30 nm [12, 21, 121]. However, due to the uniform symmetric structure, hydrogen flux through the substrate was poor.

Another issue with PSS substrates is that of intermetallic diffusion between the substrate and the Pd based thin film. A mixed Pd / Fe alloy interface layer with much lower hydrogen permeability can be formed, thus deteriorating the membrane performance. Even relatively small amounts of Fe in Pd have a large effect on hydrogen permeability. Bryden & Ying [81] found the hydrogen permeability of Pd-$Fe_{2.5at.\%}$ is over 50 % lower than pure Pd and decreases with increasing Fe content until, at a concentration of Pd-$Fe_{20at\%}$, the permeability was so low that no flux could be detected.

Many authors have attempted to resolve these issues by modifying the substrate surface. Numerous oxides / ceramics [110, 138] have been deposited on or within the surface pores to act as diffusion barriers, whilst efforts to reduce the surface pore size range from simple mechanical abrasion [14] to filling the surface pores with fine nickel powder [11, 139]. A limited number of studies have attempted to combine both surface modification steps. Any surface modification of the substrate will effectively create an additional interface layer within the composite membrane. The distinct interface layer will behave differently during thermal cycling, affect membrane adhesion and, if the surface pore size is reduced, will contribute to the overall mass transfer resistance of the membrane. Hence, the interface layer will largely

determine the success of the thin film composite membrane. Considerable care is therefore required when selecting an appropriate surface treatment.

4.4 – Thin Film / PSS Interface Layer

In order to meet the DoE 2015 performance targets [8], the membrane thickness must not exceed either 4.5 µm or 8 µm for Pd-Ag_{24} and Pd-Y_8 respectively; although lower thicknesses are preferred due to the considerable flux gains. Using a target Pd-Y_8 membrane thickness of 5 µm and assuming the minimum thickness rule proposed by Ma [126], the maximum surface pore size of a PSS substrate would need to be reduced by an order of magnitude from 10 - 20 µm to ~ 1.5 µm. Additionally, the modified surface pores should have a narrow size distribution to further facilitate the formation of a defect-free membrane [140].

A number of authors have successfully reduced the porosity of the surface through simple mechanical abrasion [14, 141]. Plastic deformation of the SS particles reduces the surface roughness and closes the surface pores. However, the resultant surface is virtually fully dense and almost impermeable to hydrogen. Using this technique, Mardilovich et al [14] observed a nitrogen flux of < 0.1 % the original, pre-treated value. The presence of such a dense layer would undoubtedly become the predominant resistance to hydrogen flux, thus negating the thin film membrane. Ideally, in order to minimise the flux resistance of the substrate, the modified substrate surface should possess a large number of small (1.5 µm diameter) uniform pores.

The underlying pores of a mechanically deformed surface can be re-opened with an appropriate acid treatment [136, 141]. Whilst this is successful in retaining the reduced surface

roughness, the etchant appears to preferentially open the larger, deeper pores, presumably because the deformed dense layer has a reduced thickness over such large pores.

Checcetto et al [122] devised a novel technique whereby a semi-porous polymeric film was used to both reduce surface roughness and pore size. A polycarbonate solution was spin-deposited onto the PSS surface. Once the solvent had evaporated, the resultant film successfully filled the surface pores and had numerous sub-micron pinholes. After coating with 5 μm Pd the membrane possessed high selectivity values, however, only low temperature flux data was reported, presumably due to the temperature limitations of the polycarbonate film.

Another approach is to fill the large surface pores of the PSS using a fine (< 1 μm) powder. Tong et al [100] successfully deposited a defect-free Pd-Ag membrane with a thickness of 3 μm on to PSS after surface modification with aluminium hydroxide gel. Although a 3 μm Pd-Ag film has the potential to meet and exceed the DoE flux target [8], the aluminium hydroxide reduced under hydrogen at around 500°C, thus increasing the likelihood of pinhole formation during operation. Other groups have attempted to fill surface pores with sub-micron atomised nickel powder [11, 139]. Using this technique, Nam et al [139] deposited a defect-free Pd-Ni membrane with a thickness of ~ 10 μm. However, due to the direct contact of the Pd-Ni film with the PSS / Ni substrate, the membrane is likely to suffer from intermetallic diffusion, reducing the hydrogen permeability and possibly leading to pinhole formation.

Li et al [136, 137] combined the successful surface roughness reduction observed by the abrasion-acid technique with the pore filling approach used by Lee [11] and Nam [139]. In an attempt to combine pore size reduction with the introduction of an intermetallic diffusion barrier; α-alumina powder deposited via a sol-gel technique was used to fill the surface pores.

An initial layer with a 2.5 µm particle size was deposited within the pores, followed by a layer with a 0.3 µm particle size to further smooth the surface (Figure 4.5). The resultant surface pore size was reduced to ~ 1 µm, which allowed the deposition of a defect-free Pd membrane with a thickness of 5 µm.

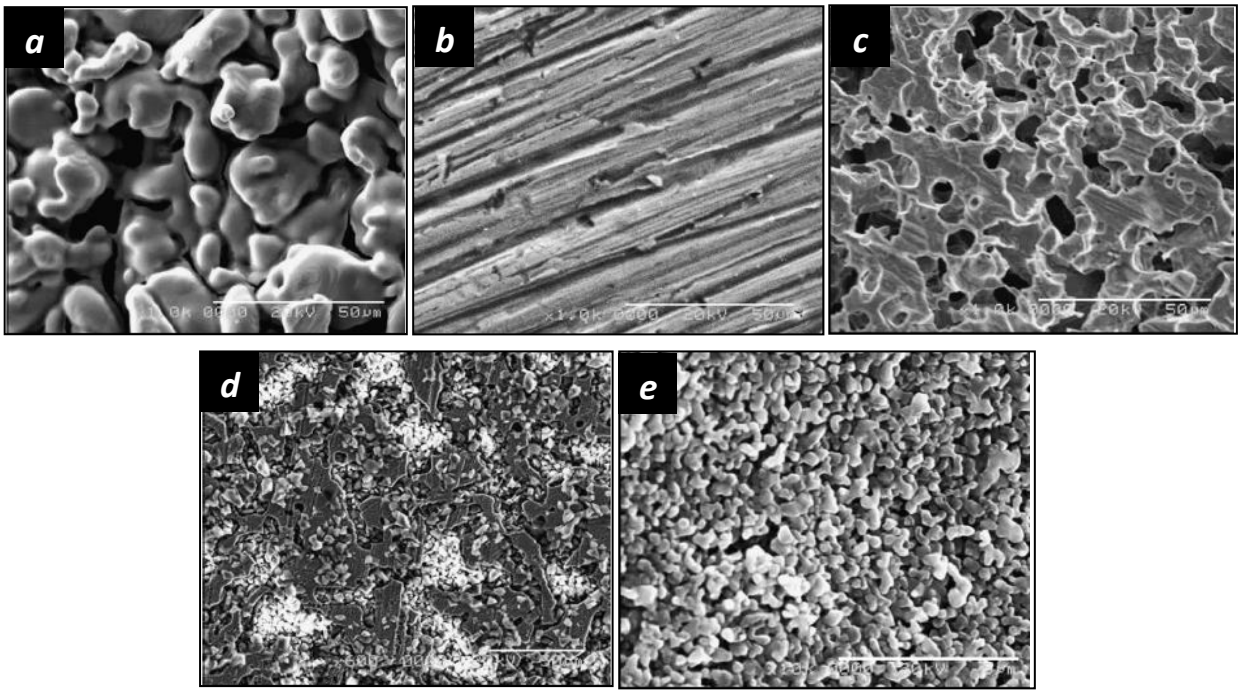

Figure 4.5 – Multistage PSS substrate surface preparation sequence as used by Li [136]. a) As-received PSS, b) Surface abrasion, c) Acid etch to re-open pores, d) Pore filling with 2.5 µm α-alumina powder, e) Final pore filling with 0.3 µm α-alumina powder.

When compared to an unmodified Pd / PSS membrane, the α-alumina layer effectively reduced intermetallic diffusion of both Fe and Pd at temperatures up to 650°C, thus preventing the resultant deterioration of hydrogen permeability. Similar results have been observed using a variety of diffusion barriers including sputter deposited titanium nitride [142, 143] and sol-gel deposited ceramics such as silica [113], zirconia [110, 144], yttria stabilised

zirconia [145], titania [138] and γ-alumina [106]. Despite the success of these layers at preventing intermetallic diffusion, to some extent they are susceptible to the same limitations as porous ceramic substrates, namely, delamination and membrane failure during thermal cycling due to the thermal expansion mismatch and poor adhesion between the metal-ceramic layers [9]. In addition, the use of a ceramic interdiffusion barrier creates two metal-ceramic interfaces, possibly augmenting the adhesion and thermal expansion issues.

In an attempt to eliminate the thermal expansion mismatch between the individual layers, Gryaznov et al [92] replaced the ceramic intermetallic diffusion barrier with thin layers of high melting point metals, such as tungsten, niobium and tantalum. Tungsten has a melting point of 3410°C and significant atomic diffusion would not be expected below ~1500°C, the so called Tamman temperature [92]. After 1000 hrs operation at 800°C, the tungsten intermediate layer (0.8 μm thickness) was found to prevent intermetallic diffusion between the Pd-Ru membrane and PSS substrate more effectively than an equivalent alumina layer. Although successful, the interdiffusion barriers were not combined with any reduction in surface pore size, thus requiring relatively thick (> 10 μm) Pd-Ru membranes. Increasing the thickness of the tungsten layer would reduce the effective surface pore size, enabling the use of thinner Pd membranes. However, some small pores would become fully covered and the intended diffusion barrier may act as a hydrogen flux barrier.

Ayturk et al [146] electrolessly deposited a thick, porous, Pd-Ag layer on to PSS substrates prior to depositing a dense Pd-Ag membrane layer. Although the porous Pd-Ag layer acted as a diffusion buffer, very high thicknesses were required to sufficiently reduce the pore size to enable the deposition of a dense Pd-Ag layer. The combined Pd-Ag thickness ranged between 70 and 85 μm.

Ma et al [108, 147] have reported good adhesion of both Pd-Ag and Pd-Cu membranes deposited on oxidised porous stainless steel. Prior to membrane deposition, the substrates were heated in air to temperatures of up to 800°C. The resultant surface was shown to be a mixed layer of Fe_2O_3 and Cr_2O_3 ranging from 1 to 6 µm in thickness. Of all the oxides formed by the constituent elements of stainless steel, Cr_2O_3 is the most desirable as an intermetallic diffusion barrier due to its low Gibbs free energy and high stability under a hydrogen atmosphere [108]. Indeed, the use of reducible oxides as interdiffusion barriers between palladium and porous stainless steel has been shown to contribute to defects and membrane failure under hydrogen at high temperatures [11]. Ma et al [108, 147] sequentially deposited 15 µm thick Pd-Cu membranes on to PSS oxidised at 800°C, which were subsequently homogenised at 600°C. The resultant single phase Pd-Cu membrane contained no traces of Fe, Cr or Ni, thus indicating the success of the mixed Fe_2O_3 and Cr_2O_3 interdiffusion layer. Although Fe_2O_3 is reducible at high temperatures under hydrogen, the Pd-Cu membranes were found to be stable for over 6000 hours in the temperature range of between 350 and 450°C. Additionally, Ma et al [108, 147] suggested that the non-uniform topography of the oxidised PSS surface actually increased the membrane adhesion by acting as anchor sites for the Pd-Cu film. However, similar to the successful interdiffusion barriers produced by Gryaznov [92], the oxidation process used by Ma et al [108, 147] does not significantly reduce the surface pore size, necessitating the use of relatively thick (15 µm) membrane layers.

4.5 – Current Limitations of Pd / PSS Composite Membranes

Whilst the use of an intermediate layer to both reduce surface pore size and prevent intermetallic diffusion is undoubtedly necessary for a successful Pd / PSS composite membrane, significant additional problems regarding both production and operation are

introduced by the intermediate layer. In general, the predominant problem reported during operation regards defect formation during hydrogen absorption and temperature cycling. Materials most effective at preventing intermetallic diffusion, such as ceramics, adhere poorly to both the metallic substrate and membrane which leads to defect formation and ultimately, membrane failure. However, some efforts have been made to overcome this structurally [108, 147]. Similarly, the major production issue is ensuring deposition of a defect-free membrane. In order to meet the DoE flux targets [8] the maximum membrane thickness for Pd-Ag is ~ 5 μm which, based on the work by Ma et al [82, 126], requires the maximum surface pore size of the substrate to be ~ 1.5 μm in order to guarantee complete coverage. Whilst it is relatively easy to deposit thick layers of mesoporous alumina or zirconia on to the PSS surface, thus sufficiently reducing the pore size, the hydrogen flux through this layer is proportional to the pore size. Particularly fine pore sizes can offer significant mass transfer resistance, thus eliminating the flux potential of the thin film membrane [148]. In addition, whilst mesoporous alumina or zirconia are effective at preventing intermetallic diffusion the membrane adhesion limitations remain.

In addition to the various production issues regarding Pd / PSS composite membranes noted above, there are also significant problems in quantifying membrane performance. For self-supporting membranes, the general permeability equation (Eqn 4.2) has been shown to accurately describe hydrogen flux (J_{H_2}),

$$J_{H_2} = \Phi \frac{\left(Pi_{H_2}^{n} - Pii_{H_2}^{n}\right)}{l(x)} \qquad \textit{Eqn 4.2}$$

where *Pi* and *Pii* denote the external hydrogen pressure at the high pressure and low pressure sides respectively and *l(x)* is the membrane thickness. The pressure exponent *n* varies between $n = 0.5$ and $n = 1$ for bulk-diffusion limited and surface-dissociation limited flux respectively. The hydrogen flux is quantified in terms of the temperature dependent permeability, Φ ($mol.m^{-1}.s^{-1}.Pa^{-0.5}$), of the membrane. The permeability is independent of both membrane geometry and applied pressure, thus permitting direct comparison between membranes to be made. There is broad agreement between most authors, across a wide range of temperatures, on measured permeability values for Pd, Pd-Ag, Pd-Cu and Pd-Y self-supporting membranes.

Analysing the hydrogen flux performance of a composite membrane however, is somewhat more complicated. Flux values between membranes with nominally identical composition and thickness vary considerably, and there is often little correlation between authors or alloy systems.

The wide divergence in hydrogen flux data may be, in part, due to the uncertainty over exact membrane thickness. The average membrane thickness, particularly of electrolessly deposited membranes, is usually estimated using mass gain techniques and must therefore be viewed with some caution. Deposited membranes often possess extremely non-uniform thickness due to the topography of the porous substrate surface (Figure 4.6). Rothenburger et al [149] deposited defect-free Pd membranes on to oxidised porous stainless steel. The oxidation process does not sufficiently reduce the surface pore size, necessitating a relatively thick membrane to ensure complete coverage. The resultant Pd membrane had an average thickness of approximately 20 – 25 µm but had extremes of 10 – 50 µm, due to the topography of the substrate (Figure 4.6).

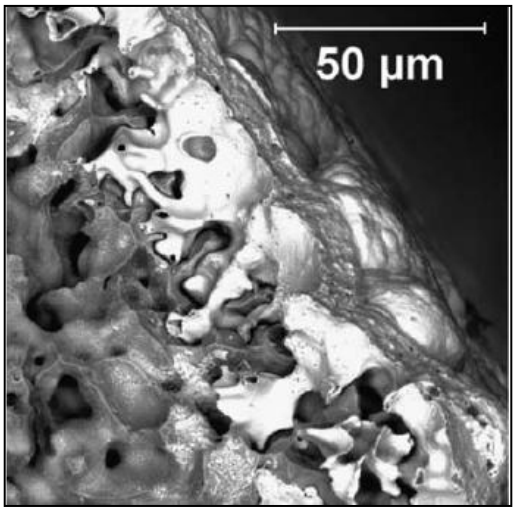

Figure 4.6 – Non-uniform thickness of a 25 µm Pd / PSS composite membrane with an oxide interface layer. Taken from Rothenburger et al [149]

The average thickness of a sputtered membrane may be estimated with a higher degree of certainty, due to the uniform deposition rate observed during sputtering, although the exact thickness at any given point will depend on the surface topography. Similarly, the thickness of membranes deposited onto substrates with a particularly fine pore size, such as γ-alumina, may be estimated with greater accuracy due to the smoother surface and increase in film thickness / pore size ratio (Figure 4.7).

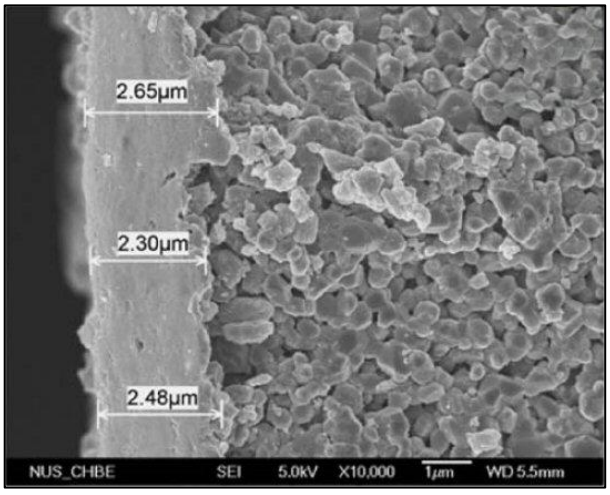

Figure 4.7 – Uniform thickness of a 2.5µm Pd membrane deposited on an alumina substrate. Taken from Sun [94]

Due to the uncertainty over membrane thickness, many authors report the hydrogen flux simply as a permeance, Φ/l (mol.m^{-2}.s^{-1}.Pa$^{-0.5}$), rather than permeability. Direct comparisons between composite membranes are therefore difficult, and any assessment of the effect of membrane thickness on hydrogen flux has a wide degree of uncertainty.

When the average membrane thickness is used to calculate the hydrogen permeability, the reported values, almost without exception, are significantly lower than the established values for self-supporting bulk membranes (Figure 4.8). There is a wide degree of scatter between permeability values for membranes with similar thicknesses tested under identical conditions. The permeability data for several Pd composite membranes with various thicknesses are listed in Table 4.1.

Compared to bulk Pd, permeability values of composite membranes commonly vary by up to 3 or 4 orders of magnitude, particularly for film thicknesses < 5 µm. The majority of Pd composite membranes demonstrate a hydrogen permeability ~ 1 to 2 orders of magnitude lower than that found in bulk Pd (Figure 4.8).

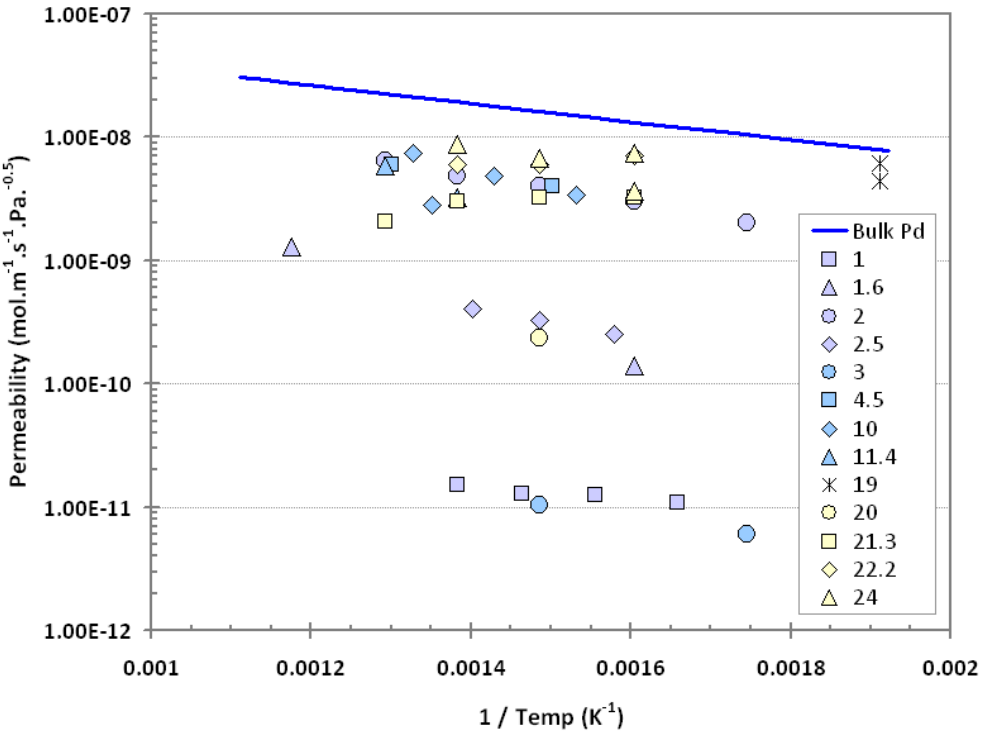

Figure 4.8 – Hydrogen permeability of various Pd composite membranes with a range of Pd film thickness compared to bulk Pd. References for each are given in Table 4.1. (Legend = Pd thickness in µm).

Similar wide variations in permeability values are observed for both Pd-Ag and Pd-Cu composite membranes. However, the uncertainty over membrane thickness alone is insufficient to explain the wide discrepancies between permeability values. Although the composite membranes produced by Rothenberger et al [149] had a wide thickness distribution of ~ 25 ± 20 µm (Figure 4.6), the hydrogen permeability at 400°C was ~ 3.50 x10^{-9} mol.m^{-1}.s^{-1}.$Pa^{-0.5}$ compared to 1.60 x10^{-8} mol.m^{-1}.s^{-1}.$Pa^{-0.5}$ for bulk palladium [79].

Table 4.1 – Examples of published permeability values and n-values for Pd composite membranes

Reference	Pd thickness (μm)	Temperature (°C)	*n* value	Permeability ($mol.m^{-1}.s^{-1}.Pa^{-0.5}$)
Keuler et al [93]	1	330	1	1.1×10^{-11}
	1	370	1	1.25×10^{-11}
	1	410	1	1.3×10^{-11}
	1	450	1	1.5×10^{-11}
Yeung et al [150]	1.6	350	0.5	1.4×10^{-10}
	1.6	577	0.5	1.28×10^{-9}
Shu et al [151]	2	300	0.5	2.0×10^{-9}
	2	350	0.5	3.0×10^{-9}
	2	400	0.5	4.0×10^{-9}
	2	450	0.5	4.8×10^{-9}
	2	500	0.5	6.4×10^{-9}
Zhang et al [152]	2.5	360	1	2.53×10^{-10}
	2.5	400	1	3.27×10^{-10}
	2.5	440	1	4.03×10^{-10}
Kusakabe [153]	3	300	1	6.0×10^{-12}
	3	400	1	1.05×10^{-11}
Kikuchi [154]	4.5	393	0.5	4.02×10^{-9}
	4.5	496	0.5	6.03×10^{-9}
Li et al [155]	10	380	0.5	3.43×10^{-9}
	10	427	0.5	4.9×10^{-9}
	10	480	0.5	7.35×10^{-9}
Li et al [156]	10	467	0.65	2.8×10^{-9}
Collins [157]	11.4	450	0.6	3.23×10^{-9}
	11.4	500	0.57	5.84×10^{-9}
Guazzone [158]	19	250	0.58	6.18×10^{-9}
	19	250	0.64	4.45×10^{-9}
Uemiya et al [159]	20	400	0.76	2.33×10^{-10}
Rothenburger [149]	21.3	350	0.62	3.25×10^{-9}
	21.3	400	0.61	3.22×10^{-9}
	21.3	450	0.62	3.04×10^{-9}
	21.3	500	0.72	2.09×10^{-9}
	22.2	350	0.53	7.15×10^{-9}
	22.2	400	0.53	5.97×10^{-9}
	22.2	450	0.58	5.95×10^{-9}
Mardilovich [14]	24	350	0.5	7.41×10^{-9}
	24	350	0.5	3.67×10^{-9}
	24	400	0.5	6.7×10^{-9}
	24	450	0.5	8.69×10^{-9}

Interestingly, in addition to low permeability values, the pressure exponent *n* of composite membranes is frequently reported to deviate significantly from 0.5; Sievert's law of ideal solubility. Values of *n* as high as 1 have been reported for composite Pd membranes with thicknesses < 3 µm [88, 93, 153], whilst most values range between 0.6 and 0.75 [121, 156-159].

An *n* value greater than 0.5 indicates that the hydrogen flux through a composite membrane is not solely limited by atomic diffusion through the Pd lattice. For thick walled self-supporting membranes, any value of *n* greater than 0.5 is usually interpreted as a sign of surface contamination or poisoning, where the number of active sites for dissociation is reduced sufficiently to limit the rate of absorption. However, the hydrogen permeability of most Pd and Pd alloy composite membranes is generally determined using pure hydrogen, thus surface poisoning can largely be discounted.

For all Pd based membranes there must theoretically come a certain critical thickness, below which, atomic diffusion is so rapid that surface dissociation and absorption rates limit hydrogen flux. Such surface effects have an increasing influence on permeance until the hydrogen flux becomes almost independent of thickness, hence a reduction in apparent permeability and deviation of the pressure exponent *n* from 0.5. Many authors attribute the permeability discrepancies and *n*-value deviations observed for thin film composite membranes to such surface effects. However, low permeabilities and *n*-values above 0.7 have been reported for composite membranes with relatively thick (> 20 µm) palladium layers [14, 149]. Self-supporting membranes of equivalent thickness do not show such deviations [85]. Indeed, based on Ward & Dao's [50] model for hydrogen permeation through self-supporting membranes, diffusion limited flux, and therefore Sievert's type behaviour, would be expected down to thicknesses of 1 µm.

Several other mechanisms have been proposed as possible causes including, mass transport resistance of the substrate, membrane-substrate interface effects, hydrogen flow across grain boundaries, lattice defects which act as hydrogen traps, and hydrogen bypass through membrane defects [149].

Whilst it may seem intuitive that pinholes and other membrane defects would significantly contribute to the overall hydrogen flux, thus increasing the apparent permeability and *n*-value, Guazzone et al [158] determined that the effect of pinholes on *n*-value was negligible if the H_2 / N_2 selectivity is above 400. Yet, even though the relatively thick membranes (22 µm) prepared by Rothenberger et al [149] exhibited infinite selectivity, an *n*-value of 0.58 was reported.

Additionally, Jayaraman and Lin [88] determined the hydrogen flux due to pinholes in a 500 nm Pd-Ag / γ-alumina composite membrane with a H_2 / N_2 selectivity of just 5.69. The pinhole flux was isolated using a subtraction model, yet the corrected hydrogen flux through the dense Pd-Ag membrane correlated to an *n*-value of ~ 1. It would appear therefore, that although defects within the Pd layer reduce the selectivity of the membrane, they are not the major source of either the permeability or *n*-value deviations reported by most authors.

Both the permeability and *n*-value are calculated using the general permeability equation (Eqn. 4.2). In these calculations, the substrate is assumed to have infinite permeance, *i.e.* negligible resistance to hydrogen flux when compared to the dense palladium layer. However, Liang & Hughes [160], Goto et al [161] and Ryi et al [162] have all reported that the apparent permeability of a composite membrane is dependent on permeation direction. All authors observed a greater hydrogen flux in the substrate → film direction. If the substrate offered negligible flux resistance the permeation behaviour for both directions should be identical.

Ryi et al [162] proposed that under identical external pressure conditions, the mass transfer resistance *i.e.* the pressure drop across each layer, would be identical in both directions (Figure 4.9).

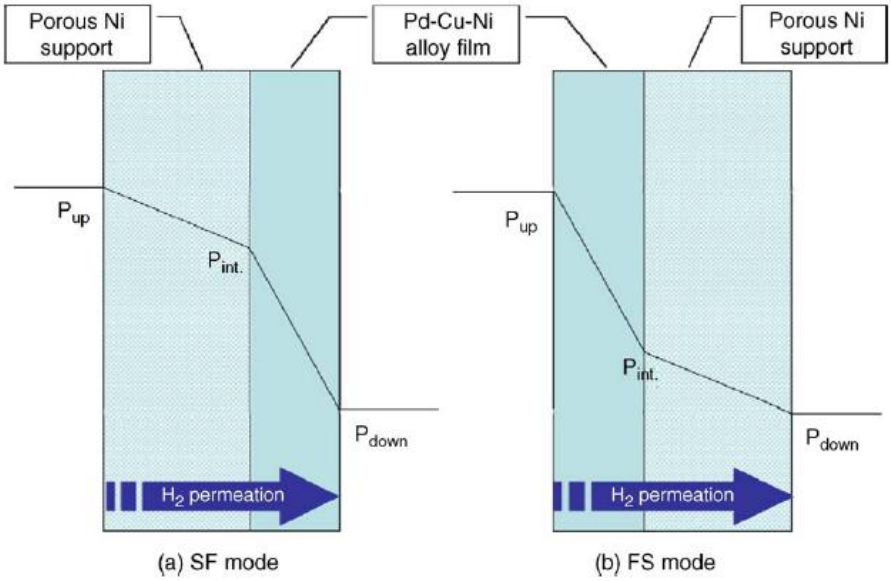

Figure 4.9 – Effect of permeation direction on the driving force / pressure drop across a composite membrane. Taken from Ryi et al [162].

Although the total pressure drop (ΔP) across the dense palladium layer is identical for both directions, the hydrogen flux through the Pd layer is proportional to $\left(Pi_{H_2}^{0.5} - Pii_{H_2}^{0.5}\right)$, hence the direction with the lowest downstream pressure, *Pii*, will demonstrate higher flux and therefore greater apparent permeability.

Interestingly, both Liang & Hughes [160] and Ryi et al [162] observed that the permeation direction not only influences the permeability but also significantly effects the *n*-value of the composite membrane. Liang & Hughes [160] deposited a Pd membrane with a thickness of 20 μm onto porous stainless steel and, when measured in the traditional film → substrate (FS) direction, observed an *n* value of 0.66 which is in excellent agreement with literature values for similar membrane configurations [149]. When measured in the substrate → film (SF)

direction the observed *n*-value was 0.5. A similar trend was observed by Ryi et al [162] for 4 µm thick Pd-Cu-Ni membranes deposited on to mesoporous nickel substrates. An *n*-value of 0.75 was measured in the FS direction whilst in the SF direction the value dropped to 0.6.

From these results it is clear that the porous substrate can offer considerable resistance to hydrogen flux, thus reducing the effective permeability of the composite membrane and also significantly shifting the pressure dependency of permeation. Although experimentally valid for self-supporting membranes, the general permeability equation (Eqn 4.2), which assumes infinite substrate permeability, may not sufficiently describe the hydrogen flux mechanism through a composite membrane. To both fully understand the hydrogen flux mechanism and determine the potential performance of a composite membrane, it is necessary to characterise the transport of hydrogen through each individual component of the composite membrane.

Section 5 – Hydrogen Permeation in Pd / PSS Composite Membranes

5.1 – Introduction

Hydrogen permeation through bulk, self-supporting, membranes is adequately described using the general permeability equation (Eqn 5.1). There is broad agreement between most authors regarding permeability values for Pd, Pd-Ag, Pd-Cu and Pd-Y membrane systems,

$$J_{H_2} = \Phi \frac{\left(Pi_{H_2}^n - Pii_{H_2}^n\right)}{l(x)} \qquad Eqn\ 5.1$$

where *Pi* and *Pii* denote the external hydrogen pressure at the high pressure and low pressure sides respectively, Φ is the permeability, *l(x)* is the membrane thickness and, in the absence of surface poisoning / contamination, *n* has a value of 0.5. When the general permeability equation is applied to composite membranes however, there is a distinct lack of correlation between apparently identical structures and compositions. As described in Section 4.5, even the permeability of pure Pd composite membranes has been found to vary by up to 4 orders of magnitude. Such a divergence in permeability data suggests that the hydrogen transport mechanism through a composite membrane is more complex than in self-supporting membranes.

A major shortcoming of the general permeability equation, when applied to composite membranes, is that infinite permeance through the substrate is assumed *i.e.* the substrate offers zero resistance to flow. However, the work of Liang [160] , Goto [161] and Ryi [162] has shown that hydrogen permeation through a composite membrane is strongly dependent on the

direction of permeation. In each case the permeability was significantly greater in the substrate → film direction. In addition, the *n*-value was also found to vary with permeation direction.

It would therefore seem apparent, that either the substrate or the film / substrate interface contribute significantly to the overall hydrogen transport mechanism. However, despite these observations many authors persist in analysing hydrogen flux using the general permeability equation, simply attributing the discrepancies to increased surface effects due to the thickness of the film.

A notable exception to this is the work reported by Huang et al [163]. In an attempt to quantify the contribution of the substrate to the overall permeation, Huang et al [163] proposed a mass transfer resistance model, similar to that of Henis & Tripodi [164] regarding polymer membranes, whereby the permeation of hydrogen through the Pd / alumina composite membrane is analogous to the flow of electricity through resistors in series (Figure 5.1).

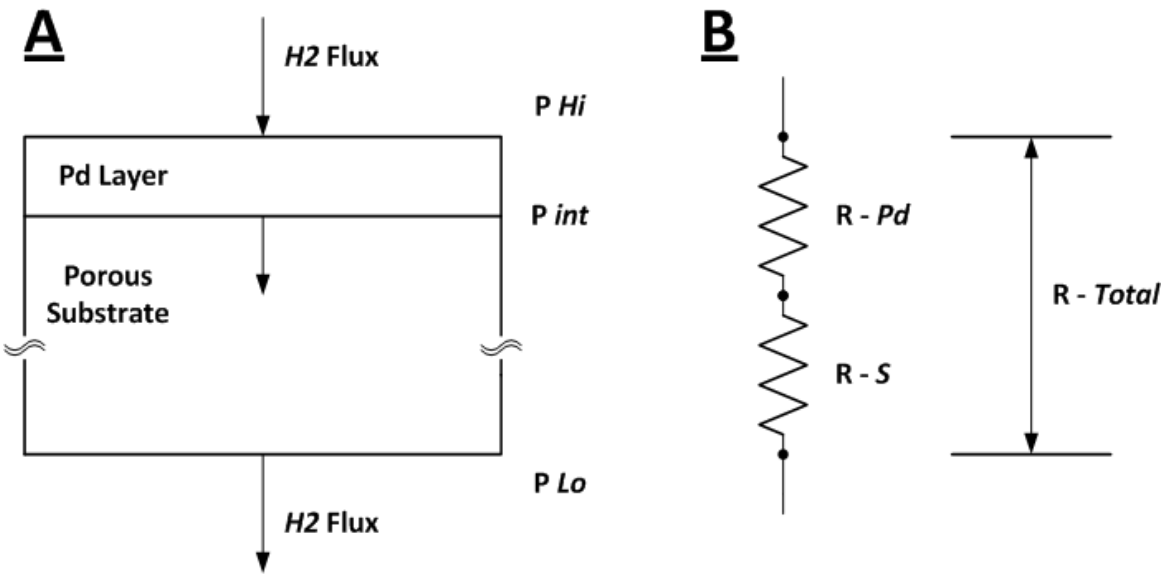

Figure 5.1 – Mass transport resistance model of a composite membrane. Reproduced from Huang et al [163].

Under steady state conditions, the overall transport resistance (R-*Total*) is equal to the sum of the film resistance (R-*Pd*) and the substrate resistance (R-*S*). Thus, in order to quantify the hydrogen flux through the Pd film, the hydrogen flux through the substrate must first be subtracted from the overall measured flux.

Determining the resistance of each layer allows the hydrogen flux though the composite membrane to be characterised in terms of three pressures; the external high and low pressures (P*i* and P*ii*) and the internal interface pressure (P*int*). In order to determine the effective resistance of each layer, the relevant hydrogen transport mechanism must be fully understood.

5.2 – Palladium-based Thin Film

In a similar manner to bulk self-supporting membranes, hydrogen permeation through a thin film membrane takes place via a solution-diffusion process which can be considered as several stages in series [50],

i. Molecular transport from the bulk gas to the gas layer adjacent to the surface
ii. Dissociative adsorption of molecular hydrogen onto the high pressure surface
iii. Transition of atomic H from the surface into the bulk metal
iv. Atomic (screened proton) diffusion of H through the metal lattice to a point just inside the low pressure surface
v. Transition from the bulk metal to active surface sites on the low pressure surface
vi. Recombinative desorption on the surface
vii. Gas transport away from the surface

For bulk self-supporting membranes the rate of permeation is largely governed by atomic diffusion through the lattice (Stage iv). Undoubtedly, there will come a certain critical thickness, beneath which, atomic diffusion through the film is so rapid that it no longer limits the rate of permeation. In such circumstances, the rate of surface dissociation / recombination or gas transport away from the surface are likely to limit the rate of permeation. However, although the critical thickness remains unknown, based on the model developed by Ward & Dao [50], atomic diffusion limited flux can be expected for Pd films with clean surfaces down to thicknesses of 1 µm. Indeed, this prediction has recently been corroborated experimentally using free-standing thin film membranes [84, 85, 165]. Mejdell et al [84] deposited Pd-Ag films of various thickness onto Si wafers using magnetron sputtering. The films were removed mechanically, and the hydrogen permeability determined using low feed gas pressures. Bulk diffusion limited permeation was found for all membranes, the thinnest of which were just 1.3 µm. Additionally, the permeability values were in excellent agreement with those reported for bulk self-supporting membranes. Similar results have been reported for both pure Pd and Pd-Cu free-standing thin films by Gade et al [85]. At 400°C the permeability of 7.2 µm thick Pd films was found to be ~1.3 x10^{-8} mol.m^{-1}.s^{-1}.$Pa^{-0.5}$ which is in excellent agreement with the bulk data [79].

The permeation of hydrogen through the dense thin film section can therefore be represented by a modified version of the general permeability equation,

$$J_{H_2} = \Phi \frac{\left(Pi_{H_2}^{n} - Pint_{H_2}^{n}\right)}{l(x)} \qquad \textit{Eqn 5.2}$$

where *Pi* represents the external high pressure and *Pint* the internal film-substrate interface pressure as identified in Figure 5.1. The modified permeability equation only accounts for the transport of hydrogen via atomic diffusion through the crystal lattice. Any molecular flow through defects or along grain boundaries must be quantified separately and can be treated as an extension of the film / substrate interface, which will be discussed later.

5.3 – Porous Substrate

Molecular gas transport through porous solids may take place via four different mechanisms; viscous, or Poiseuille flow, slip flow, Knudsen diffusion and continuum diffusion [166]. The dominant transport mechanism depends on both the pore size distribution and the conditions of temperature and pressure. In many cases, several transport mechanisms act simultaneously and addition rules must be applied. In general, it has been shown that flow and diffusion are completely independent and are therefore additive [167]. Various different approaches have been made to describe gas transport through porous solids. The most widely used are the dusty gas model [168, 169], phenomenological approaches based on Maxwell-Stefan equations [19], Darcy's law [170] and modified kinetic gas theory [171]. However, regardless of the mathematical derivation of the transport equations used, each model represents some combination of Poiseuille flow, slip flow, Knudsen diffusion and continuum diffusion. Another common feature of each approach is that at least some part of the model or equation must be determined experimentally.

For pure gases continuum diffusion can be ignored as it describes the transport of mixed gas species. Additionally, the pore size regimes of most porous substrates used in composite membranes are sufficiently small so that the Poiseuille flow is laminar. As such, the gas

velocity at the pore walls is assumed to be zero, *i.e.* no slip, thus slip flow may be largely discounted.

As flow and diffusion are independent of each other, the overall transport of hydrogen through homogenous porous media can be described as the sum of the Poiseuille flow and the Knudsen diffusion. The relative contribution of each transport mechanism is dependent on the ratio of the number of molecule-molecule collisions to that of the molecule-wall collisions. This ratio is often described using the Knudsen number, K_n,

$$K_n = \frac{\lambda}{r} \qquad \textit{Eqn 5.3}$$

where λ is the mean free path of the gas molecules and r is the mean pore radius. If the Knudsen number, K_n, is much larger than unity (>> 1) then the number of molecule to wall collisions are dominant and gas transport is by Knudsen diffusion, where the flux of hydrogen (J_K) can be described by the Knudsen equation [22],

$$J_K = -\frac{2}{3} c\, r \frac{1}{RT} \frac{\Delta P}{\Delta x} \qquad \textit{Eqn 5.4}$$

where r is the mean pore radius, R the gas constant, T the absolute temperature, P the pressure and x the distance. The mean thermal velocity of the gas molecules, c, is given by [172],

$$c = \sqrt{\left(\frac{8RT}{\pi M}\right)} \qquad \textit{Eqn 5.5}$$

where *M* is the molecular mass of the gas. In order to account for the shape of the pores and hence the diffusion path, two geometrical factors must be introduced. The porosity (ε) which is simply defined as the fraction of the media which is open space, and the tortuosity (τ) which accounts for the increase in distance compared to the total substrate thickness, due to the tortuous nature of the structure. After the introduction of the geometrical factors and integration over the substrate thickness, the flux due to Knudsen diffusion is given by,

$$J_K = \frac{2}{3}\,\frac{\varepsilon\, r}{\tau}\,\frac{1}{l}\left(\frac{8}{\pi\, R\, T\, M}\right)^{0.5}\Delta P \qquad \textit{Eqn 5.6}$$

From Eqn. 5.6, it is clear that the flux due to Knudsen diffusion is proportional to the average pore radius *r* and, importantly, the square root of the molecular mass *M*. This dependency on molecular mass forms the basis of separation in porous membranes.

When the Knudsen number K_n is much smaller that unity ($<< 1$), the number of intermolecular collision are strongly dominant and the gas flux is predominantly due to laminar Poiseuille flow. The hydrogen flux can then be described using the Hagan-Poiseuille law [22],

$$J_V = -\frac{r^2}{8\eta}\frac{P_T}{R\,T}\frac{\Delta P}{\Delta x} \qquad \textit{Eqn 5.7}$$

where η denotes the viscosity and P_T the total pressure. Similar to Knudsen diffusion, Eqn 5.7 needs to be modified to account for the geometrical factors. In addition, under steady state

conditions the flux into and out of a pore are equal, thus $P\frac{\Delta P}{\Delta x}$ is constant. After integration across the substrate thickness *l*, the flux is given by,

$$J_V = \frac{1}{8}\frac{\varepsilon}{\tau\,\eta}\frac{r^2}{R\,T\,l}\,P_{av}\,\Delta P \qquad \textit{Eqn 5.8}$$

where P_{av} is the average pressure across the substrate. From Equation 5.8 it is clear that the Poiseuille flow is proportional to both the mean pore radius squared, r^2, and the average pressure across the substrate P_{av}.

For pores with an average radius of greater than 1.5 nm there will be a combined contribution to flux [173]. Knudsen diffusion and Poiseuille flow are additive, therefore the total hydrogen flux through the porous substrate may be expressed as,

$$J_{Total} = \left[\frac{2}{3}\frac{\varepsilon\,r}{\tau}\frac{1}{l}\left(\frac{8}{\pi\,R\,T\,M}\right)^{0.5}\right] + \left[\left(\frac{1}{8}\frac{\varepsilon}{\tau\,\eta}\frac{r^2}{R\,T\,l}\right)P_{av}\right]\Delta P \qquad \textit{Eqn 5.9}$$

Equation 5.8 is usually simplified to give the linear expression,

$$J_{Total} = [\,\alpha_K + (\beta_V\,P_{av})\,]\,\Delta P \qquad \textit{Eqn 5.10}$$

where α_K and β_V denote the Knudsen and Poiseuille permeation coefficients respectively.

Assuming a linear pressure drop across the substrate, the values of α_K and β_V can be determined by plotting $J_{Total} / \Delta P$ against P_{av}, where α_K is the intercept and β_V the gradient. Using the experimentally derived values for α_K and β_V, the unknown geometrical factors in Eqn 5.9 can be calculated. However, it is difficult to isolate either the porosity or the tortuosity uniquely, as a result they are usually reported as the ratio ε/τ.

The main observations which can be drawn from Eqn 5.9 are the dependence of the flux on both average pore size and temperature. As noted in Section 4.4, there are many reports of reducing the surface pore size in order to deposit a defect-free Pd film. However, Lin & Burggraaf reported that halving the pore size of alumina decreased the effective permeability by a factor of 150 [174]. Hence, whilst enabling the deposition of thinner films, smaller pore sizes may add considerable resistance to permeation, thus negating the apparent advantage of a thinner film. The typical pore size of porous stainless steel substrates commonly reported (5 to 20 μm) [14, 82] suggests that Poiseuille flow would be the dominant mechanism. From Equation 5.9 it is clear that Poiseuille flow is approximately proportional to $T^{-3/2}$. Therefore, the resistance of the substrate would be expected to increase with increasing temperature. Indeed, this may well explain why Guazzone et al [158] reported an increase in *n*-value for a 19 μm Pd / PSS composite membrane with increasing temperature (Figure 5.2).

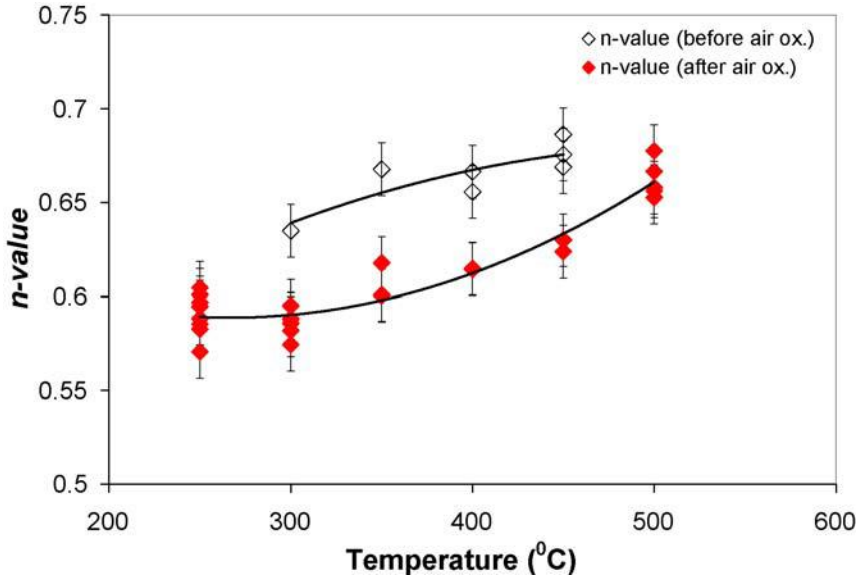

Figure 5.2 – Effect of temperature on n-value for a 19µm Pd / PSS membrane. Taken from Guazzone [158]

Assuming that the geometric factors ε, τ and r do not vary with temperature, the α_K and β_V permeation coefficients can be used to predict the hydrogen flux through the substrate under any conditions of pressure and temperature. Therefore, in order to analyse the substrate contribution to the total transport resistance of a composite membrane, it is essential that the α_K and β_V coefficients be determined prior to the deposition of the Pd film.

5.4 – Thin Film / Substrate Interface Layer

The term 'interface layer' encompasses both inner surfaces of a composite membrane and the region between the two. Most composite membranes are produced using non-homogenous substrates, *i.e.* with modified surface layers. In terms of analysing hydrogen permeation across a composite membrane, the modified surface region can be categorised as part of the interface layer.

As discussed previously in Section 4.2.2, the topography and pore size of the substrate surface largely determines the quality of the deposited film. Whilst it is desirable to reduce the surface pore size in order to facilitate the deposition of a defect-free film, hydrogen permeation across this layer follows the transport mechanism described for the underlying substrate, which is strongly dependent on pore radius.

The importance of this layer to the overall transport resistance has recently been documented by Zhang et al [152] who compared the hydrogen permeation across Pd / α-alumina composite membranes using interface layers of γ-alumina and yttria-stabilised zirconia (YSZ) with a thickness of 3 μm. Although both the Pd film and underlying α-alumina substrate were identical, the hydrogen flux through the Pd / γ-alumina / α-alumina membrane was only ~ 50 % that of the Pd / YSZ / α-alumina membrane.

A major difficulty in evaluating the interface layer however, is a lack of direct measurement techniques to determine either pore size or porosity. Subtraction methods have been used with some success for porous separation membranes, where the α_K and β_V co-efficients of the interface layer can be deduced from the values determined for the substrate before and after modification [174]. However, as we are primarily concerned with the hydrogen flux across this layer, as opposed to the separative properties, the porous interface layer can be viewed as an extension of the substrate, adequately described by a single set of α_K and β_V permeation coefficients.

As discussed in Section 5.2, any defects within the Pd layer can also be classified as part of the interface layer. Molecular flow through pinholes follows the Knudsen / Poiseuille transport mechanism of the porous substrate. Hence, pinholes and other defects within the Pd layer simply act as modified pores with their own set of geometric factors (Figure 5.3).

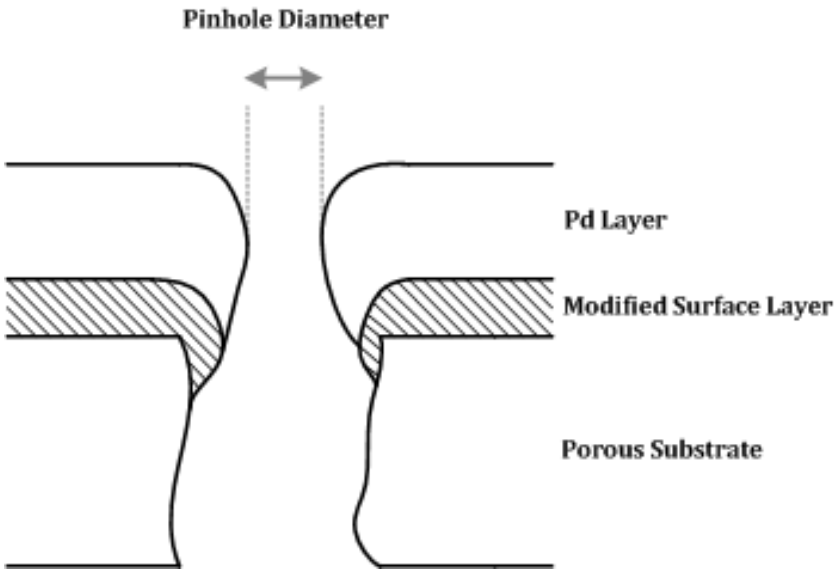

Figure 5.3 – Schematic drawing of a pinhole in the Pd layer. The pinhole acts as a modified surface pore.

Therefore, if a composite membrane contains defects, additional α_K and β_V coefficients must be determined in order to account for the additional molecular flow. From Eqn 5.9, described in Section 5.3, it is clear that Poiseuille flow through pinholes and other defects is directly proportional to the average pressure across the membrane. Hence, as the applied pressure increases the relative proportion of flux due to pinholes increases. The net effect of this would be a significant reduction in selectivity and greater deviation from diffusion limited behaviour as the applied pressure is increased.

5.5 – Hydrogen Permeation through Multilayered Composite Membranes

As evidenced by the wide range of reported permeability values, hydrogen transport across a composite membrane is a particularly complicated process which cannot be adequately described using the general permeability equation. Recently, Gabitto et al [170] and Caravella et al [175] independently proposed similar theoretical models of permeation in composite

membranes, based largely on the work of Ward & Dao [50] and Burggraaf [19, 22] as described previously in Sections 5.2 and 5.3. Both models comprise multiple stages in series, with Gabitto et al [170] proposing 8 different regions within a 3 layer composite membrane (Figure 5.4).

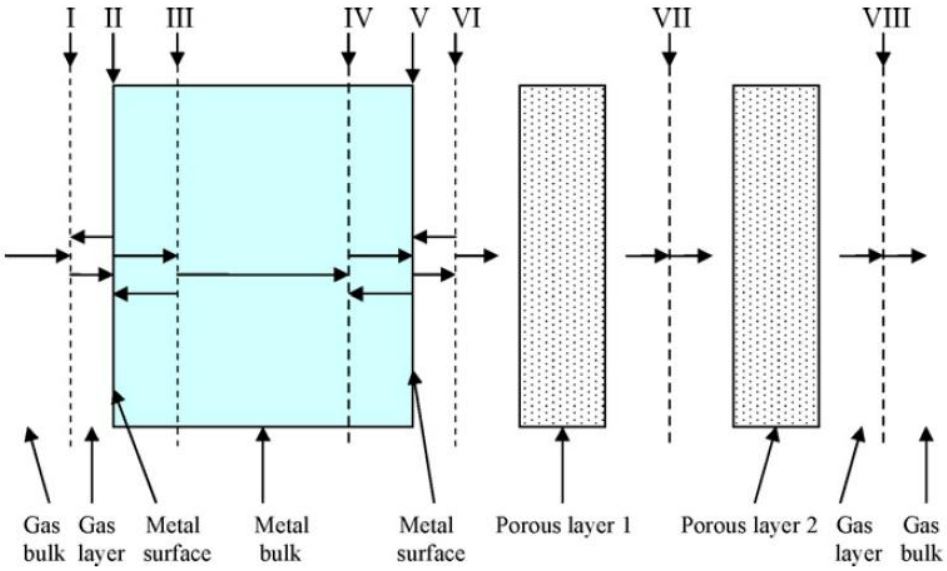

Figure 5.4 – Multi-stage transport model across a 3 layer composite membrane. Taken from Gabitto et al [170]

Stages I – VI are taken from the model for hydrogen permeation in bulk alloys developed by Ward & Dao [50]. Indeed, Ward & Dao proposed that for self-supporting Pd membranes, in the absence of surface contamination, atomic diffusion-limited flux would be observed down to thicknesses of 1 µm. This has since largely been corroborated experimentally using free-standing Pd, Pd-Ag and Pd-Cu thin films down to 1.3 µm in thickness [84, 85, 165]. Therefore, for free-standing thin films > 1 µm, regions I – VI can be described using the general permeability equation. However, in order to account for substrate resistance in supported membranes, the modified permeability equation must be used,

$$J_{H_2} = \Phi \frac{\left(Pi_{H_2}^n - Pint_{H_2}^n\right)}{l(x)} \qquad Eqn\ 5.11$$

where Φ is the permeability, l the membrane thickness, *Pi* represents the external high pressure and *Pint* the internal film-substrate interface pressure.

Although regions VI – VIII possess different structures and hydrogen transport characteristics, assuming structural stability at high temperature and hydrogen atmospheres, in terms of hydrogen permeation they can be regarded as a single entity. Hydrogen transport through this region is due to a combination of Knudsen diffusion and Poiseuille flow, which is expressed as,

$$J_{Total} = \left[\frac{2}{3}\frac{\varepsilon\, r}{\tau}\frac{1}{l}\left(\frac{8}{\pi\, R\, T\, M}\right)^{0.5}\right] + \left[\left(\frac{1}{8}\frac{\varepsilon}{\tau\,\eta}\frac{r^2}{R\, T\, l}\right) P_{av}\right] \Delta P \qquad Eqn\ 5.12$$

The terms used in Equation 5.12 have been described previously in Section 5.3. Equation 5.12 can be grouped to give the two experimentally determined values α_K and β_V with which, hydrogen transport through regions VI – VIII can be characterised.

Neither the model proposed by Gabitto et al [170] nor Caravella et al [175] accounts for molecular transport of hydrogen across defects within the Pd layer. Pinholes and other defects have been shown to have a significant effect on both effective permeability and *n*-value [158]. Therefore, any experimentally determined permeation data must be evaluated for pinhole flux.

Pinholes may be treated as an extension of the interface layer where hydrogen transport follows Eqn 5.12 and can, therefore, be characterised by a discrete set of α_K and β_V permeation coefficients.

In terms of transport resistance, a composite membrane is a dynamic system. The relative contributions of each region depend on the instantaneous conditions of temperature and pressure. Each region requires a driving force for hydrogen transport and, in order to quantify each driving force and thus quantify the observed permeation, the active transport mechanism in each region must be accounted for.

Section 6 – Palladium Yttrium / PSS Composite Membranes

The superior hydrogen permeability and tensile strength of Pd-Y alloys compared to Pd-Ag and Pd-Cu is well documented [15, 53, 56, 78, 176]. A likely reason for why Pd-Y alloys have not been adopted commercially as self-supporting rolled foils / drawn tubes, is the difficulty in manufacture arising from considerable strain hardening on deformation. However, a thin film Pd-Y membrane manufactured using a suitable deposition technique would eliminate such manufacturing issues.

Based on the properties of bulk alloys, Pd-Y appears to be particularly suited for use in composite membranes. The enhanced permeability of Pd-Y compared to Pd-Ag would allow a reduction in operating temperature without compromising hydrogen flux. A reduction in operating temperature has several advantages, the most important of which is the potential improvement in membrane durability. At operating temperatures of around 400 to 500°C intermetallic diffusion is a particular problem for Pd / PSS composite membranes. The superior permeability of Pd-Y alloys would allow a reduction of operating temperature, considerably reducing membrane-support intermetallic diffusion and thus increasing the operating lifespan of the membrane. In addition, due to the predominant transport mechanism of the substrate, the resistance to flow increases with temperature. Therefore, a reduction in operating temperature has the potential to reduce the pressure drop across the substrate, thus increasing the pressure gradient across the Pd-Y film and increasing the hydrogen flux.

Composite membranes are particularly susceptible to defect formation during operation, due mainly, to thermal expansion gradients between the Pd film and the substrate, coupled with lattice expansion associated with hydrogen absorption. The significantly greater tensile

strength of Pd-Y may contain the stresses during operation to a greater extent than Pd, Pd-Ag or Pd-Cu, thus reducing defect formation and potentially enhancing durability.

Additionally, the superior permeability of Pd-Y alloys would allow equivalent hydrogen flux to that obtained using either Pd-Ag or Pd-Cu, at greater membrane thicknesses. Depositing defect-free membranes is non-trivial; success depends on the ratio of the pore size to membrane thickness. Whilst an increase in membrane thickness of a few microns would not add appreciably to the cost of the membrane, this would facilitate the deposition of a defect-free film significantly.

Considering the well documented superior properties of Pd-Y for use as hydrogen separation membranes, it is perhaps surprising that currently there is no published information regarding the use of thin film Pd-Y in composite membranes. A possible explanation for this is the incompatibility of Y with electroless deposition, which is by far the most common membrane deposition technique. Thin film Pd-Y membranes deposited by magnetron sputtering may offer potential performance benefits compared to the widely studied Pd, Pd-Ag and Pd-Cu systems.

Section 7 – Project Aims

The primary objective of this work is to investigate the performance of a novel, thin film Pd-Y / PSS composite membrane. In particular, the hydrogen transport mechanism across each layer of the composite membrane will be determined. This will enable analysis of each component and the relative contribution to transport resistance.

The permeation data will be compared to the numerous studies on thin film Pd, Pd-Ag and Pd-Cu composite membranes reported in the literature. The hydrogen permeability of thin film Pd-Y will be compared to that in bulk alloys, and any potential performance advantage of Pd-Y / PSS composite membranes will be quantified.

The Pd-Y thin film membranes will be co-deposited onto porous stainless steel via magnetron sputtering. Prior to membrane deposition, the surface of the porous stainless steel substrates will be modified using a novel, laser melting technique. It is proposed that laser melting the surface of porous stainless steel may combine the reduction in pore size, necessary for the deposition of defect-free membranes, with the formation of a surface oxide, thus reducing possible intermetallic diffusion during operation.

Chapter 3 – Experimental Techniques

Section 8 – Experimental Techniques

8.1 – Introduction

This chapter is divided into three sections: the first presents details on sample preparation and the membrane production process; the second deals with membrane composition and materials characterisation; whilst the final section details the hydrogen permeability and membrane performance measurements.

All the analysis and sample handling carried out during the course of this work was performed using techniques and laboratory practise intended to minimise contamination of the final membrane surfaces. Samples were handled with latex gloves and stored under argon. At various stages of production both the rolled membranes and the thin film composite membranes were cleaned in an ultra-sonic bath with acetone and, where necessary, physically abraded with SiC paper. The cleaning process was repeated prior to any experimental analysis.

8.2 – Material and Sample Preparation

8.2.1 – Rolled Foils / Bulk Alloys

The range of Pd-Y and Pd-Ag bulk alloys examined within this work were prepared by melting the appropriate weights of palladium (Umicore, 99.95 % purity), yttrium (Rare Earth

Products, 99.9 % purity) and silver (Sigma-Aldrich, 99.9+ % purity) in a non-consumable electrode arc furnace under argon (100 kPa). The buttons were then homogenised at 950ºC for 160 hrs under high vacuum (10^{-5} mbar), replicating successful membrane production processes reported previously [53, 54, 56]. Small sections were then cut using a diamond wheel, mounted and polished with diamond paste down to 1 µm. The homogeneity was then assessed using a JOEL 6060 Scanning Electron Microscope equipped with INCA EDX (Section 8.3).

The Pd-Y buttons were then hydrogenated (200 kPa H_2, 2 hrs, 400ºC) in an attempt to reduce the strain hardening experienced during rolling [15, 177]. All alloys were cold rolled to a thickness of 100 ± 8 µm, using stainless steel foil to protect the sample surface from any contamination or surface texture due to the rolling process. Strain hardening was experienced for all alloys and a series of intermediate strain relief anneals (4 hrs, 650ºC, 10^{-5} mbar) were necessary in order to avoid cracking during rolling. Consistent with previous work, Pd-Y alloys undergo much more extensive strain hardening than either Pd or Pd-Ag and required more frequent annealing [15, 53, 54, 56]. Once the desired thickness of 100 µm was achieved the foils were given a final strain relief anneal. To prevent any possible contamination, all samples were wrapped in stainless steel foil prior to any heat treatment, while ensuring no area of pressure or close contact to avoid interdiffusion.

The rolled foils were cut into 21 mm diameter discs. This geometry allowed hydrogen permeability, X-ray diffraction, SEM and laser microscopy analysis to be performed on the same sample. Cut-off sections were retained and used, as necessary, for hydrogen solubility measurements and further X-ray diffraction studies.

It has been reported previously that Y_2O_3 can develop as flakes on the surface of Pd-Y alloys leaving a Pd-rich near surface layer [15]. Prior to any measurement therefore, all samples were

subject to surface abrasion with 800 grade SiC paper followed by cleaning with acetone in an ultra-sonic bath. This ensured a clean, homogenous surface free from contamination.

8.2.2 – Thin Film Alloys

The thin film samples investigated in this work were produced at Teer Coatings Ltd using the proprietary Closed Field Unbalanced Magnetron Sputter Ion Plating (CFUBMSIP) technique (Figure 8.1). This system uses an even number of opposing magnetrons, thus inducing field linking between the north and south outer poles of adjacent cathodes. A typical 4 magnetron system, as used in this work, is shown below.

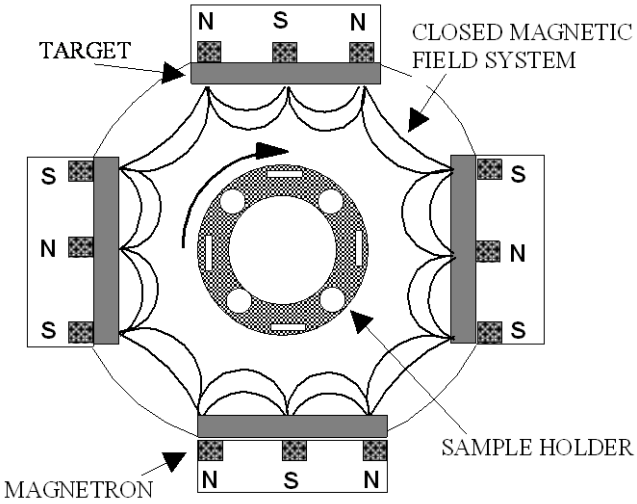

Figure 8.1 – Schematic diagram of the CFUBMSIP deposition technique. Taken from Teer Coatings [178].

The surface cleanliness of a sample prior to coating is a major factor in determining the quality of the coating, both in terms of pinhole density, compositional consistency and adhesion. For thin film membranes, a contaminated surface would undoubtedly give rise to pinholes and other defects which reduce the hydrogen selectivity of the membrane. Therefore, all the samples coated during this work were subject to a 3 stage cleaning process in order to

minimise the possibility of defects. The first stage was to wash with acetone in an ultrasonic bath, the samples were then thoroughly dried before being sprayed with an anti-static gun to remove any dust particles. Once mounted within the chamber the system was evacuated (10^{-6} mbar) and the samples were subject to a final ion clean using an argon plasma.

Two types of coating were produced during this work, a range of co-deposited Pd-Y alloys with a thickness of between 2 and 5 µm, and stainless steel coatings between 0.5 and 20 µm thick. The stainless steel coatings were produced using a single 316 stainless steel target. The co-deposited Pd-Y coatings were performed using a single Pd target (99.9 % purity) and a single Y target (99.9 % purity). The targets were mounted adjacently to allow the co-deposition of a homogenous solid solution alloy. If the targets were mounted in opposite positions, a multi-layered structure would be formed. A fast sample rotation speed of 8 rpm was chosen to further facilitate the homogeneity of the co-deposited solid solution alloys.

All coating parameters, other than the ratio of powers to the targets, were kept constant for all Pd-Y depositions regardless of the desired composition. The power to the Pd target was kept constant at 250 W, whilst the power to the Y target was varied between 40 and 100 W, thus controlling the sputter rate of Y and therefore the coating composition. In the case of a pure Pd coating, the voltage bias to the Y target was switched off and a shutter system was used to shield the Y surface from any Pd contamination. All coatings were performed in a single continuous process without breaking the vacuum in order to prevent any undue surface contamination, thus maximising the quality of the film. The film thickness was estimated during deposition using the average sputter rate of 1 $\mu m.hr^{-1}$ experienced by Pd using a power of 250 W and argon flux of 36 $cm^3.min^{-1}$. The precise film thickness was later established using an Olympus LEXT confocal laser microscope (see Section 8.3.2).

The actual sputter characteristics of both Pd and Y are sensitive to many factors including the target thickness (new targets have a higher sputter rate than worn targets), target surface condition and vacuum level. Therefore, prior to each membrane deposition, an initial test coating was deposited onto stainless steel tokens, and XRD measurements were then made to obtain the lattice spacings, from which the composition could be estimated (see Section 8.3.1.2). Minor adjustments to the power settings could then be made to obtain the desired composition.

8.2.3 – Porous Substrates

The porous substrates used in this work were sintered austenitic 316L Stainless Steel (PSS), purchased from Mott Corp, USA. The substrates were supplied in disc form (21 mm diameter, 1 mm thickness) fabricated by stamping from sheet material. Porous metal is classified in terms of media filtration grade, which is defined as the minimum size of a hard spherical particle retained by the interconnected porosity [179]. Substrates with media grade of 0.1 µm, the finest commercially available grade, were employed throughout this work. It should be noted that the media grade does not correspond to the average pore size. The typical surface pore sizes of 0.1 µm PSS ranged between 10 and 20 µm.

8.2.4 – Substrate Surface Modification

Laser melting of the 316L PSS surfaces was performed at the Laser Processing Research Centre (LPRC) at the University of Manchester. A GSI Lumonics IPEX-848 excimer laser

using Krypton Fluoride gas was used to perform a wide range of melts with varying operating parameters.

Perhaps surprisingly, to the best of our knowledge, there is no published information regarding the use of an excimer laser to melt the near surface of porous metals. Therefore, the laser operating parameters were established after a series of trial and error experiments. Once a reasonable melted surface was produced, it was decided to limit the number of variable parameters to facilitate more manageable interpretation of data. The laser parameters selected to be kept constant were those considered to have less of a significant effect on the surface finish. They were;

- Frequency – The number of beam pulses per second – 50 Hz
- Beam Dimension – The time, in seconds, per pulse – 12 ns
- Beam Overlap – The percentage overlap between adjacent tracks – 50%
- Beam Direction – Path of laser in adjacent tracks (Figure 8.2)

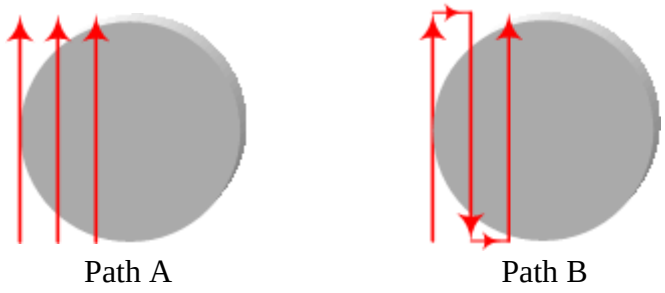

Figure 8.2 – The different laser paths across the PSS discs. Path A was selected to maximise surface uniformity

The variable parameters were: the fluence; the number of pulses which interact uniformly with the surface (burst size); and the pre-treatment surface condition. The fluence can be defined as the energy per unit area that uniformly interacts with the entire surface, and can be expressed as,

$$Fluence\ (mJ.cm^{-2}) = \frac{Laser\ Energy\ (mJ)}{Beam\ Interaction\ Area\ (cm^2)} \qquad Eqn.\ 8.1$$

As shown in Eqn. 8.1, the fluence can be controlled by adjusting either the laser energy, or the beam size / area. The beam size is controlled by the positioning of mirrors in the beam path, thereby varying the focal length. The laser energy is primarily dependent on the gas (Krypton Fluoride) pressure. When the pressure is low, high energies are not achievable and therefore high fluence values are attained by adjusting the focal length to reduce the beam size. In theory, laser energy and beam size should be totally interchangeable to give the same fluence. In practise however, there are slight discrepancies between the actual fluence at the disc surface. To minimise this effect, the beam size was kept between 1.4 and 1.5 mm and the laser energy was measured using a Gentec-e SOLO PE laser power / energy meter. If the desired energy was not achievable the gas was replenished rather than reducing the beam size.

The number of pulses which interact with each point on the surface (the burst size) is determined by the rate at which the beam rasters across the surface, this in turn is controlled by the sample speed (Eqn. 8.2).

$$Number\ of\ Pulses = \frac{Beam\ Diameter(cm) \times Frequency(s^{-1})}{Sample\ Speed(cm.s^{-1})} \qquad Eqn.\ 8.2$$

When the beam diameter and the frequency are kept constant, the number of pulses is directly proportional to the sample speed. The sample is manoeuvred using a fully automated

Aerotech ATS100 stepping table which provides accurate and consistent movement in the X, Y and Z directions.

Fluence values between 400 and 3500 $mJ.cm^{-2}$ and pulse numbers ranging from 100 to 400 were investigated for a variety of surface conditions to establish near optimum conditions for the required topographies.

8.2.5 – Composite Pd-Y / PSS Membrane Production

Thin film Pd-Y / PSS membranes were produced via a multi-stage process. Between each stage the samples were thoroughly cleaned using acetone in an ultra-sonic bath and left to dry overnight.

The initial production step was to melt the surface of both as-received and SS-coated PSS substrates (as described in Section 8.2.4). The surfaces were then examined optically using a SEM (Section 8.3.1.1) and an Olympus LEXT 3100 confocal laser microscope (see Section 8.3.2) to ensure uniformity. Using a lathe, the samples were then turned to a final diameter of 16 mm. This step was necessary to remove any edge imperfections introduced during the laser melting and also, to eliminate the inherent edge porosity of the substrate. A machined disc diameter of 16 mm was selected to ensure a tight fit when the substrates were pressed into $1^{1/3"}$ CF ultra-high vacuum (UHV) copper gaskets.

The copper gaskets were used to create a gas-tight seal across the membrane. In order to guarantee both the structural strength and gas seal between the substrate and the gasket, a Rofin 60 W laser spot welder was used to circumferentially weld the two pieces together (Figure 8.3).

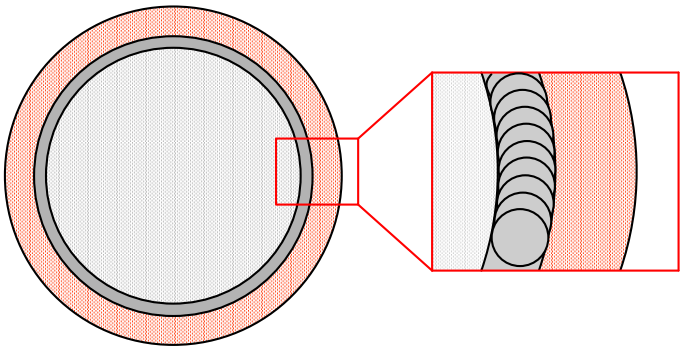

Figure 8.3 – Overview of composite membrane showing overlapping laser spot welds. Not to scale.

The laser spot welding was performed at the Jewellery Industry Innovation Centre at Birmingham City University. The welds were assessed for macroscopic uniformity by visual examination under an optical microscope, and by using a simple but effective back-lighting technique. This involved shining high intensity light on the reverse side of the sample in a photographic dark room. The weld was considered to be successful, or gas-tight, if no illuminated 'pinholes' could be detected. This criterion was tested using samples in which the porous substrate was replaced with a dense stainless steel disc and applying a helium gas pressure of 500 kPa across the weld to ensure no gas flux through the sample.

Following welding, the laser-melted substrates were then tested for hydrogen, nitrogen and argon permeance between RT and 500ºC and over a pressure range of 100 to 800 kPa, thus enabling the gas permeation characteristics of each substrate to be established. Such measurements are essential in order to develop an understanding of the hydrogen transport through a Pd-Y / PSS composite membrane.

The laser melting of the substrates was performed under ambient conditions, thus the melted surfaces were rather oxidised as evidenced by a brown discolouration. Therefore, a thin

(500 nm) layer of 316 stainless steel was sputter deposited prior to Pd-Y deposition, in an attempt to enhance the adhesion between the substrate and Pd-Y film. A 500 nm layer was found to be sufficiently thin so as to not significantly affect any surface feature. After SS deposition the coated substrates were vacuum annealed (10^{-5} mbar, 30 mins, 750°C) in order to promote some interdiffusion between the SS layer and the substrate whilst maintaining a metallic outer surface for Pd-Y deposition. The modified substrates were again assessed for gas permeance to establish the effect of the SS adhesion layer to the overall resistance to flow.

The penultimate production stage was to co-deposit the Pd-Y thin film via magnetron sputtering (as described in Section 8.2.2). Pd-Y films with thicknesses between 2 and 5 µm were deposited to enable the effect of film thickness on adhesion and defect level to be assessed. However, in order to minimise the risk of pinholes and defect formation, a target thickness of 5 µm was set for the composite membranes. After deposition the composite membranes were subject to a final low-temperature vacuum anneal (10^{-5} mbar, 6 hrs, 400°C) to promote film adhesion, but prevent excessive intermetallic diffusion. The Pd-Y film adhesion was assessed via a simple peel test using Sellotape, which was performed on parallel samples. The adhesion was assumed to be good if no delamination occurred after 3 tests.

The final production step was to check for pinholes and other defects within the Pd-Y film. A pressure gradient of nitrogen was applied across the composite membrane, a defect-free Pd-Y layer is impermeable to nitrogen and therefore, any flux through the membrane indicates a defect. If pinholes were found to be present, the membranes were imaged using a SEM to determine pinhole density and geometry.

8.3 – Material Characterisation and Analysis

8.3.1 – Membrane Composition and Structure

8.3.1.1 – Scanning Electron Microscopy

Throughout this work, at various production and experimental stages the surface topography and composition of both rolled and thin film membranes were analysed using a Joel 6060 SEM and a Joel 7000 FEG-SEM. Both microscopes are equipped with INCA EDAX software. Where necessary, cross-sectioned samples were prepared by mounting in conducting Bakelite and polished down to 1 µm using conventional metallography.

8.3.1.2 – X-Ray Diffraction

A Bruker D8-Advance diffractometer using monochromatic CuKα_1 radiation (λ = 1.54056 Å) was used to gather the diffraction data of both bulk and thin film membranes over a 2θ range of 20 – 100º.

Detailed analysis of the X-ray diffraction pattern can be used to determine alloy composition and structure, identify different phases and, particularly for thin film membranes, detect any interdiffusion or texture within the films. The diffraction patterns were analysed using Bragg's law which states,

$$\lambda = 2d_{hkl}\, sin\theta \qquad \textit{Eqn. 8.3}$$

where, λ is the wavelength of the incident radiation, θ is the angle of incidence of diffraction and d_{hkl} is the inter-planar spacing. All the alloys examined in this work have the face centred cubic (FCC) crystal structure. The Miller indices of the diffracted planes in an FCC lattice are

[111], [200], [220], [311], [222] and [400]. The inter-planar spacing associated with each plane is related to the lattice parameter by,

$$d_{hkl} = \frac{a}{\sqrt{h^2 + k^2 + l^2}} \qquad \textit{Eqn. 8.4}$$

where *a* is the lattice parameter and *h*, *k* and *l* are the Miller indices of the particular plane. Within this work, the lattice parameter, *a*, was primarily used to calculate alloy composition through comparison with established literature values. The [111], [200], [220] and [311] planes were used to calculate the lattice parameter, *a*, of the bulk alloys whilst the [111] plane was used for the thin film samples due to a high degree of texture within the sputtered Pd-Y films. Thin film diffraction patterns were gathered between membrane production stages to detect any possible intermetallic diffusion between the film and support during annealing and hydrogen flux measurements.

8.3.2 – Membrane Surface Metrology

8.3.2.1 – Confocal Laser Microscopy

Surface metrology data for porous substrates, rolled foils and composite membranes was obtained using an Olympus LEXT OLS3100 mounted on a TableStable anti-vibration table. The microscope uses a 408 nm class II ultraviolet laser source and has a plane resolution (X and Y) of 120 nm and a space pattern (Z resolution) of 10 nm. This allows accurate

measurements of roughness, pore depth, pore volume, step profiles, effective surface area and film thicknesses which conform to current ISO standards.

The surface metrology data is calculated using a series of 'stacked' confocal images along the Z axis. As the laser is reflected by the surface it passes back through the objective and converges at a second focal point, which is optically conjugate to the first. A circular pinhole positioned within this confocal plane ensures that only light from the focal plane is detected, with light reflected from others regions rejected. This information is used to generate an optical section of the sample. The sample is then moved along the Z axis in 5 – 100 nm increments and another optical section is created at a higher / lower focal plane. As the position of the Z axis progresses, a 3-D stack of images is generated. It contains the intensity levels for each individual point defined by the laser focus co-ordinates. Using this data, a single composite image is generated, from which accurate surface metrology measurements can be made, including membrane thickness and average pore diameter / depth. The composite membranes were also examined for pinholes. If present, both pinhole density and diameter were calculated which can then be used to quantify the permeation and separation characteristics of the membrane.

8.3.3 – Membrane Alloy Hydrogen Solubility

8.3.3.1 – Gravimetric Analysis

Gravimetric hydrogen solubility measurements were performed on both Pd-Y and Pd-Ag alloys using a thermogravimetric analyser produced by Hiden Isochema Ltd, called an Intelligent Gravimetric Analyser (IGA). The measured samples were 'cut-off' sections from

the rolled membranes, this ensured corresponding compositions with the membrane permeability measurements. Gravimetric solubility analysis is based on the principle that as a metal absorbs hydrogen, the sample mass increases proportionally with the quantity of hydrogen absorbed. If the sample mass, temperature and hydrogen pressure are monitored during absorption / desorption the maximum hydrogen solubility, reaction kinetics and other absorption / desorption characteristics can be determined.

Samples are held in a quartz sample holder, which is suspended from a microbalance with a maximum sensitivity of ± 0.001 milligrams. The sample holder is housed within a stainless steel reactor vessel with a maximum working pressure of 20 bar hydrogen, over a temperature range -196 to 500°C. The pressure within the reactor is controlled to within ± 1 mbar using two stepper motors, one connected to a high pressure hydrogen line and the other to a Pfeiffer turbo molecular pumping station capable of a 10^{-7} mbar vacuum.

For the present work, samples with a starting mass of about 150 milligrams were activated at room temperature in 20 bar hydrogen until saturated. The samples were then heated to 400ºC and thoroughly de-gassed under a 10^{-6} mbar vacuum prior to cooling. The ‘dry mass’ of the sample can then be determined and used as the reference starting mass. Solubility measurements were performed between 100 and 500 kPa, and 25 and 500 °C, thus corresponding to the membrane operating conditions investigated. Corrections for buoyancy were made where necessary.

8.3.4 – Membrane Permeability Assessment

8.3.4.1 – Membrane Testing Facility

A bespoke hydrogen permeation system was designed and built to assess the performance of both rolled and thin film composite membranes (Figure. 8.4). The basic principle of the system is to apply a controlled feed gas to the high-pressure side of a properly sealed membrane, and to monitor the gas which permeates through the membrane on the downstream side. All the necessary measurement devices were controlled and monitored using a PC and SpecView data logging software.

The feed gas is controlled using four Brookes 5850S Mass Flow Controllers (MFC) calibrated over a range of 6-600 $ml.min^{-1}$ with an accuracy of ± 6 $ml.min^{-1}$. This enables either pure or mixed gas feed streams to be applied to the membrane. The gases used in this work were, hydrogen (99.99995 %), argon (99.995 %), nitrogen (99.95 %) and helium (99.95 %). All gases were supplied in high-pressure cylinders by BOC.

To eliminate the problem of decreasing hydrogen partial pressure with time (as hydrogen permeates through the membrane) the feed gas was continually flowing and bled through another Brookes 5850S MFC (6-600 ± 6 $ml.min^{-1}$). This also prevented the build-up of any possible contaminants as the gas which does not permeate through the membrane is continually swept away. The bleed MFC was coupled electronically with the four inlet MFCs to accurately control and maintain the feed gas pressure between 100 and 1100 ± 0.5 kPa.

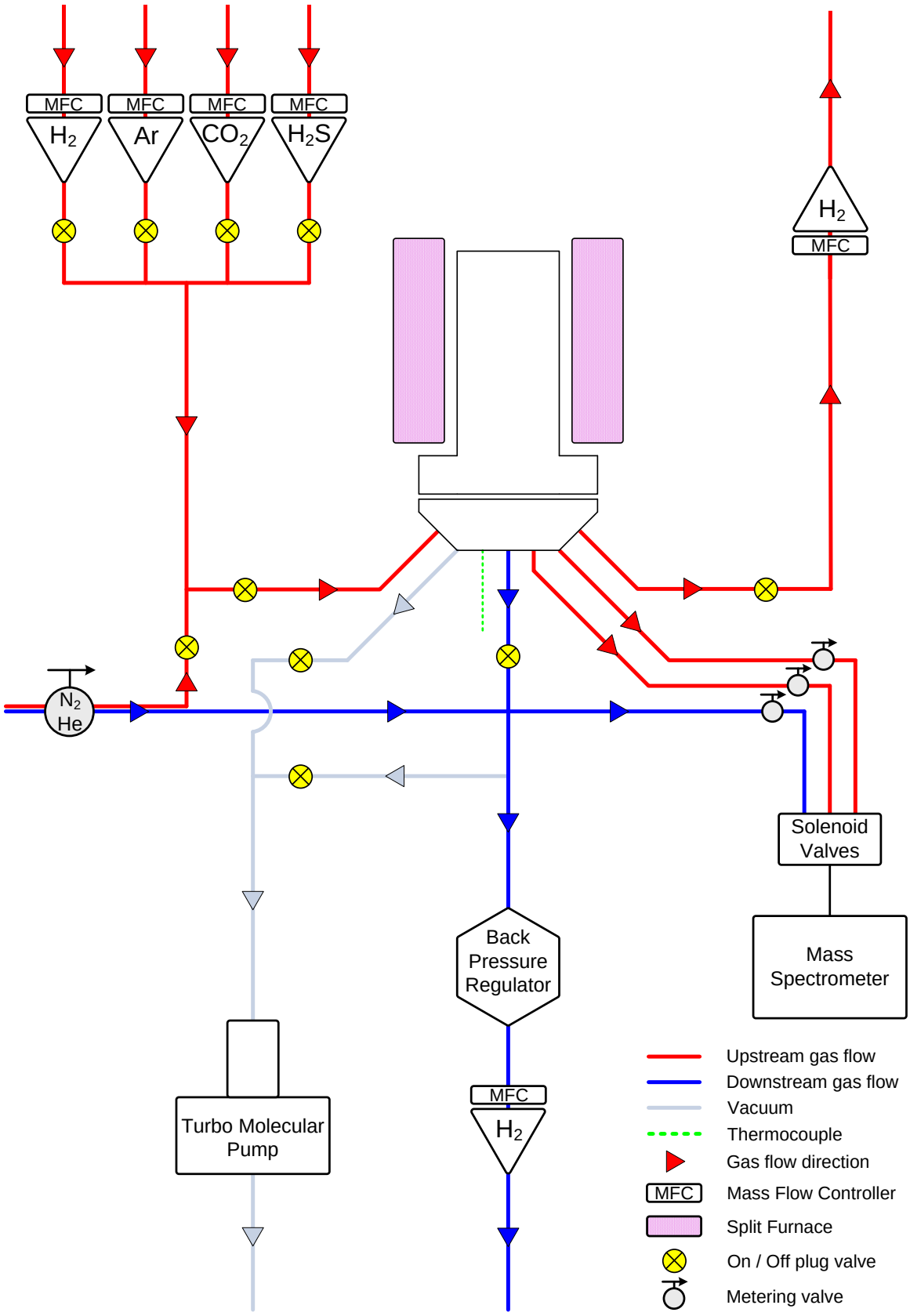

Figure 8.4 – Schematic diagram of the hydrogen permeation system

The amount of gas which permeates through the membrane was monitored using two Brookes 5850S MFC calibrated for different flow rates. For membranes through which a low flux was expected a range of 2-200 ± 2 $ml.min^{-1}$ was used, whilst a 6-600 ± 6 $ml.min^{-1}$ range was used for high flux membranes. The downstream pressure was controlled using a Swagelok KFB series back-pressure regulator with a range of 100 – 1800 ± 5 kPa. The pressure at either side of the membrane was measured using Hawco-Direct 408-857 digital pressure transducers with a range of 100 – 1700 ± 5 kPa. When required, both sides of the membrane were evacuated using a Pfeiffer TSU-071E turbo-molecular drag pumping station with a membrane backing pump capable of producing a vacuum of 10^{-7} mbar.

The temperature of both the membrane and the upstream atmosphere was controlled using an Elite Thermal Systems Ltd split furnace with a controllable ramp-rate of between 0.1 and 10°$C.min^{-1}$ and a maximum temperature of 1100ºC. The temperature was monitored using 3 Inconel K-type thermocouples, one located within the furnace heating zone measuring the furnace temperature, one measuring the upstream atmosphere temperature and the third positioned approximately 1 mm from the downstream membrane surface to measure the membrane temperature.

The reactor vessel (Figure 8.5) was machined from single rod of Inconel 625 grade II alloy, and uses a pure silver compression gasket to seal the cover with the mounted base. The reactor has a large internal diameter of 55 mm and volume of 1200 cm^3, allowing a range of potential membrane geometries to be used. The reactor vessel has a maximum operating pressure of 2100 kPa hydrogen at a temperature of 850ºC. All the gas connections use Swagelok 316L stainless steel fittings, which are bored through to allow the gas tubing to be positioned up within the reactor, and the membrane to be placed within the furnace heating zone.

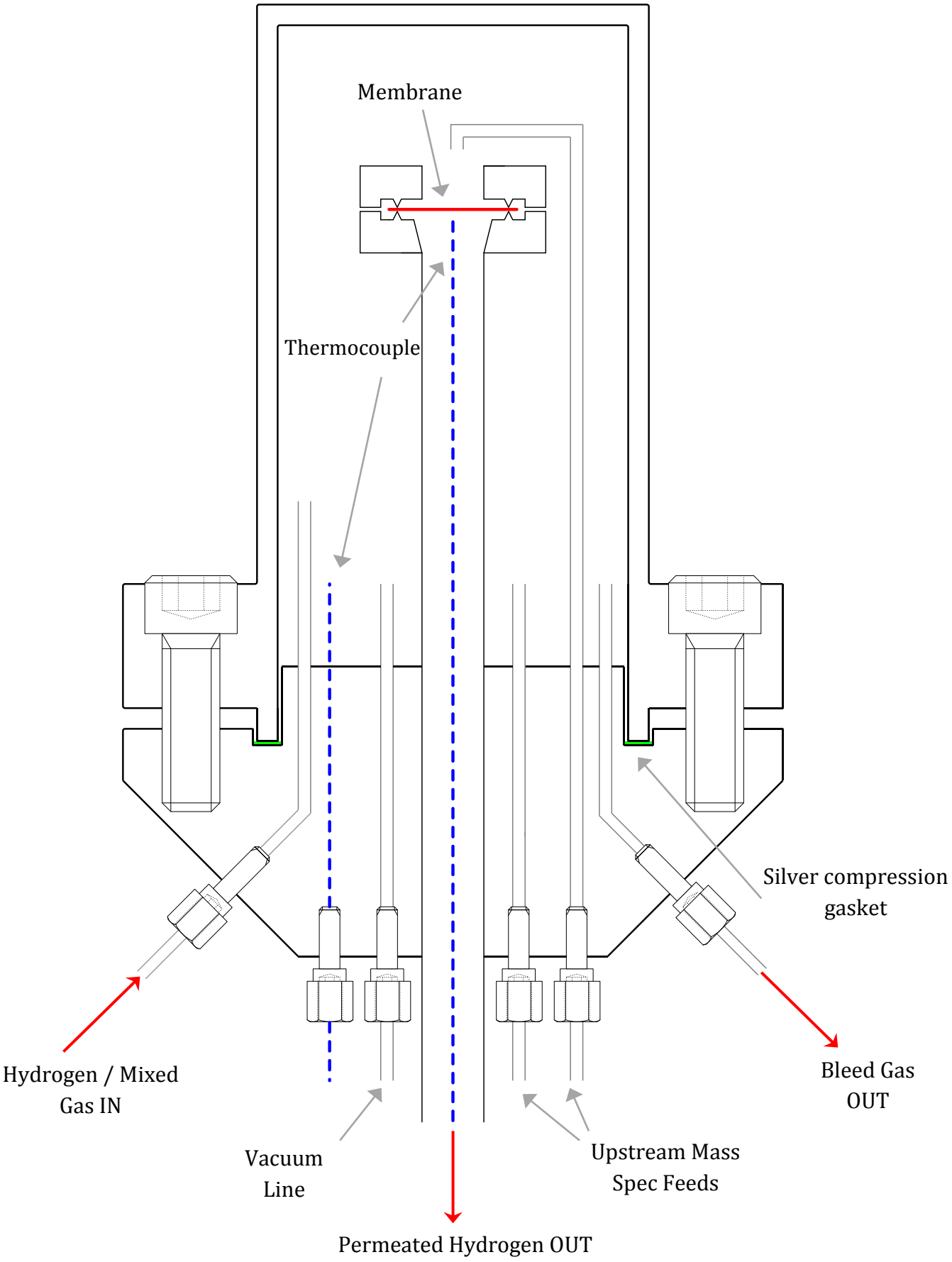

Figure 8.5 – Schematic diagram of the membrane reactor vessel. (Not to scale)

The membrane holder consisted of two hardened 316LN stainless steel CF vacuum flanges, both with a 12.7 mm (½") bore. The first was welded to ½" 316L stainless steel gas tubing and was positioned within the heating zone of the furnace. The second flange was used as a 'cap' to provide the necessary compression to produce a gas tight seal. The two were secured together using low thermal expansion hex bolts. Different configurations were used to achieve a gas tight seal for the two types of membrane, although the principle of compression with a hard knife-edge to deform a softer metal was common. The rolled self-supporting membranes were secured as shown in Figure 8.6.

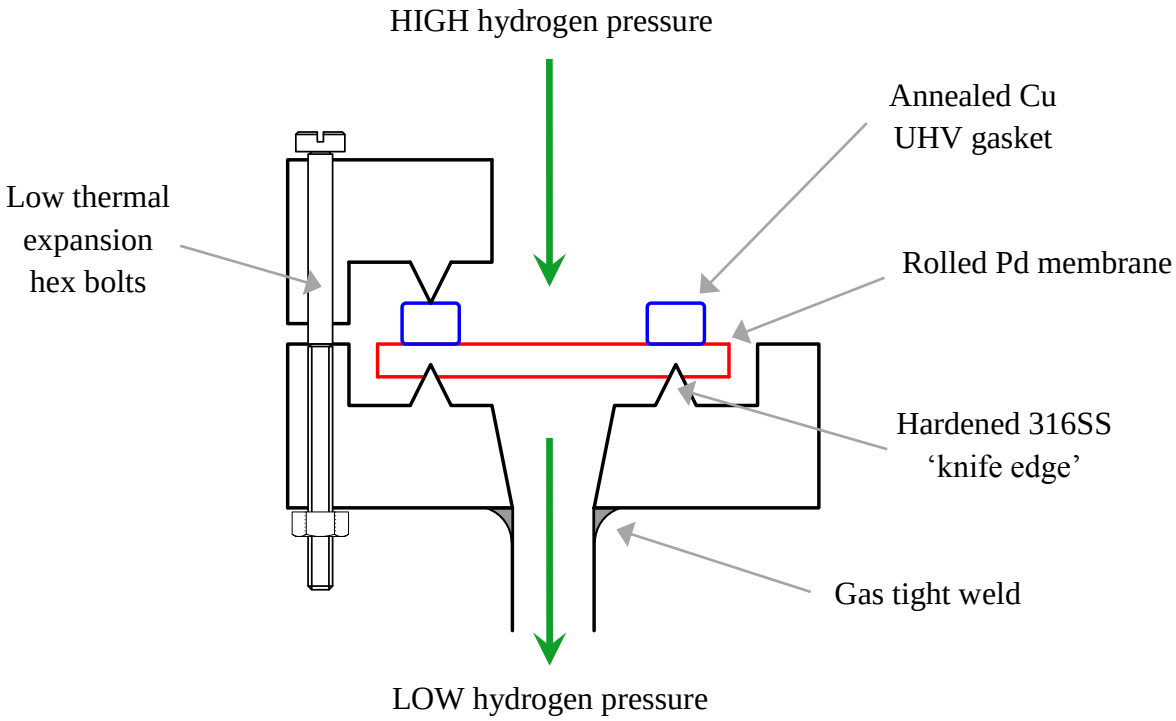

Figure 8.6 – Partial cross section of rolled membrane holder and sealing mechanism. (Not to scale)

A gas-tight seal is created by deforming the membrane around the underlying knife-edge. A copper gasket was used to uniformly distribute the compressive force directly over the knife edge as the bolts were tightened. The success of the compression seal was assessed by applying a 345 kPa helium pressure gradient across the membrane. A small gas by-pass of

< 2 ml.min^{-1} is beneath the detectable range of the downstream MFC, so the seal was considered successful if there was no increase in the downstream pressure after 30 minutes.

The thin film composite membranes were sealed using the standard ultra high vacuum (UHV) method, with a knife edge deforming both sides of an annealed copper gasket (Figure 8.7).

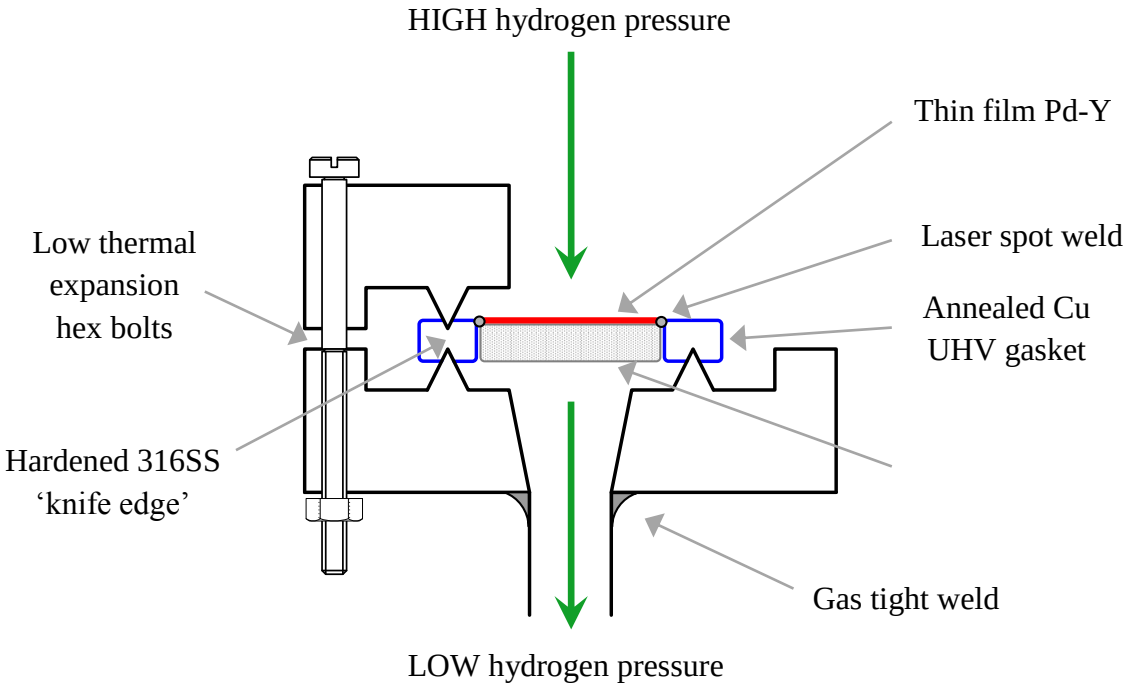

Figure 8.7 – Partial cross section of composite membrane holder and sealing mechanism. (Not to scale)

The UHV gas seal is a well-established, reliable method of achieving a gas tight seal. Therefore, any helium, nitrogen or argon flux across the sealed composite membrane was assumed to be due to pinholes within the Pd-Y layer.

During the course of this work permeability measurements were made on three sample types: rolled self-supporting membranes; porous substrates; and thin film composite membranes. A testing procedure was developed for each sample type in order to maximise consistency and aid comparison between samples. A temperature ramp rate of 2ºC.min^{-1} and a pressure ramp

rate of 250 mbar.min^{-1} were common for each procedure. The testing procedure for the self-supporting rolled membranes followed the common procedure employed by previous investigators of bulk Pd-Y membranes [53, 55, 56]. Once the membranes were cut into 21 mm diameter discs, the surfaces were lightly abraded with 1200 grit SiC paper. The membranes were then ultrasonically cleaned in acetone and secured using the 'foil type' sealing method (Figure 8.6). A leak check was then performed using a helium pressure gradient (345 kPa). If a leak was detected the membrane was removed and re-secured using a new Cu gasket. Once a successful seal was formed, both sides of the membrane were evacuated to about 10^{-5} mbar. Hydrogen was then admitted to both sides of the membrane. Regardless of whether a permeability isotherm or isobar measurement was performed the system was left to reach equilibrium prior to the initiation of the measurement. It has previously been reported that heating a Pd-Y membrane to around 400ºC followed by cooling in air prior to a permeability measurement increased the maximum permeability of the membrane [15]. However, initial comparative permeability isobars showed no significant difference between the 'as-annealed' condition and the 'air cooled' condition. All rolled membranes were therefore tested in the 'as-annealed' condition.

The thin film composite membranes were cleaned with acetone in an ultrasonic bath and left to dry overnight under an argon atmosphere. The membranes were secured using the UHV method (Figure 8.7) and then both sides of the membrane were evacuated to about 10^{-5} mbar. In order to prevent a negative pressure gradient across the membrane, potentially delaminating the Pd-Y layer, the low pressure side of the membrane was evacuated prior to the high pressure side. Nitrogen was admitted to both sides of the membrane in order to assess the pinhole density of the Pd-Y layer. The system was then evacuated, low pressure side first, prior to the admission of hydrogen.

Prior to loading, both the as-received and laser melted substrates were cleaned with acetone in an ultrasonic bath. The substrates were left to dry overnight under an argon atmosphere before being secured using the UHV method (Figure 8.7). After evacuating both sides of the substrate to about 10^{-5} mbar, the desired gas was admitted. Between each gas species the system was evacuated.

Chapter 4 – Results and Discussion

Introduction

In order to develop a comprehensive understanding of the effective hydrogen permeability of a thin film Pd-Y / PSS composite membrane, both the material properties and hydrogen transport mechanism must be quantified through each individual component. Due to the different transport mechanisms active in the metallic layer and porous substrate, the relative resistance of each layer will vary with operating conditions such as temperature and pressure. The data reported in this chapter has been gathered and analysed specifically to assess the dynamic contribution of each layer to the overall hydrogen transport resistance, and is presented in three separate sections. The first section details the dense Pd-Y alloy layer, the second details the porous support and in particular the modified support surface, whilst the third section presents both structure and hydrogen transport analysis through the complete composite membrane including the Pd-Y / PSS interface layer. Understanding the contribution of each component to the overall hydrogen transport resistance, should make it possible to identify the limiting factors for composite membrane design and selection.

Section 9 – Dense Pd-Y Membrane

In contrast to the substrate, the fragility of the dense thin film section of a composite membrane precludes isolation for direct analysis, thus preventing important properties such as

hydrogen permeability and activation energy from being determined independently. Therefore in order to fully quantify the properties and performance of thin film Pd-Y, direct comparisons to bulk Pd-Y must be made. Throughout this section, comparisons are drawn between Pd-Y and both pure Pd and Pd-Ag alloys as they are by far the most widely studied in terms of composite membrane systems and are generally accepted as the benchmark for high hydrogen permeability. In particular, rolled Pd-Ag alloys are currently the standard material system for commercial hydrogen purification and offer a useful comparison for both Pd-Y bulk properties and the effective permeability of any composite membrane.

9.1. – Rolled Foils

9.1.1 – Alloy Assessment and Composition

The production of the homogenous, single-phase alloys studied within this work has been described previously in Section 8.2.1. Six individual Pd-Y alloys were produced with nominal compositions of 2, 4, 6, 8, 9 and 10 at.% Y, whilst a single Pd-Ag alloy was produced with a nominal composition of 24 at.% Ag, thus replicating the alloy composition used in commercial purifiers. After homogenisation, the alloys were all single phase with a grain size of approximately 2 mm visible on the surface. Such as large grain size is expected due to the prolonged exposure above the recrystallisation temperature during homogenisation, thus leading to extensive grain growth. Prior to homogenisation, the alloys with a high Y content (Pd-Y_9 and Pd-Y_{10}) both contained small secondary phases which EDX analysis found to have a Y concentration of ~ 25 at.%. The secondary phases were therefore identified as the intermetallic compound Pd_3Y. The presence of Pd_3Y has previously been observed in partially homogenised Pd-Y alloys by Doyle [46].

Although the single-phase nature of the homogenised alloys was confirmed, accurate compositions were not determined at this stage due to the possibility of Y segregation during the subsequent heat treatment. Fort et al [15] have shown that Y_2O_3 forms on the surface of oxidised Pd-Y alloys leaving the bulk alloy Y depleted. Similarly, Doyle [46] found that after exposure to air at 800°C for 6 hrs, a Pd-Y_{10} alloy had a thick surface oxide with an underlying composition of just Pd-Y_6. Although any further heat treatment was performed under a vacuum of at least 10^{-5} mbar, surface oxidation of the samples cannot be ruled out completely.

Once the alloys had been cold-rolled to the target membrane thickness of 100 µm, they were subject to a final recrystallisation anneal (10^{-5} mbar, 4 hrs, 650ºC) prior to any analysis. Incidentally, in agreement with previous studies [15, 46, 55], all the Pd-Y alloys studied within this work experienced greater strain hardening during rolling than the Pd-Ag alloy and required more frequent recovery anneals, particularly the Pd-Y_8, Pd-Y_9 and Pd-Y_{10} alloys. The microstructure of Pd-Y_8 and Pd-Ag_{24} rolled membranes after a final recrystallisation anneal are shown in Figures 9.1 and 9.2 respectively.

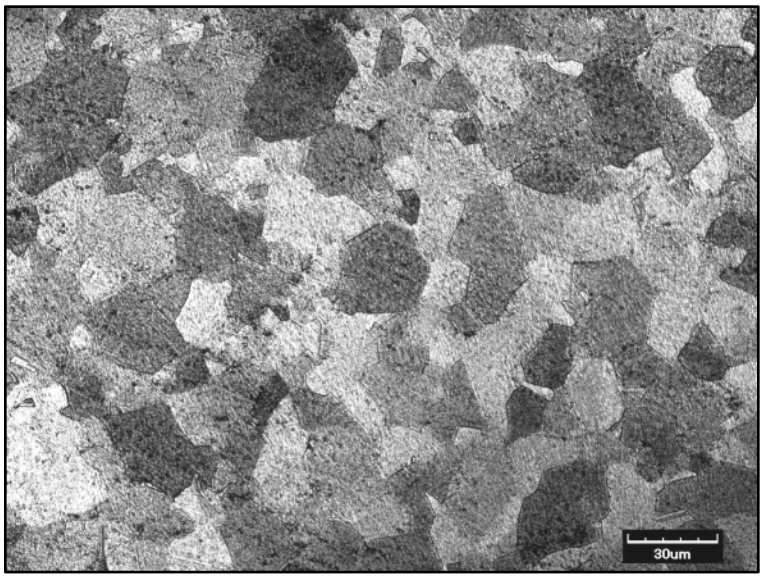

Figure 9.1 – Confocal laser microscope image of a cold-rolled and vacuum annealed Pd-Y_8 alloy.

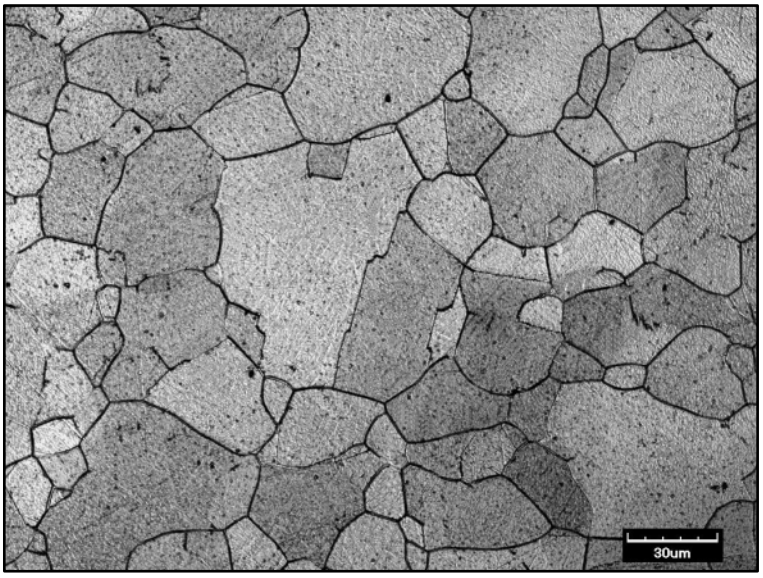

Figure 9.2 – Confocal laser microscope image of a cold-rolled and vacuum annealed Pd-Ag_{24} alloy

The microstructure of the Pd-Y_8 alloy is representative of the range of Pd-Y alloys studied within this work with a grain size of approximately 20 – 30 µm, whilst the grain size of the Pd-Ag_{24} alloy is somewhat larger being between 30 – 60 µm. This would be expected due to the lower recrystallisation temperature of Pd-Ag.

The rolled Pd-Ag and Pd-Y foils all exhibited single-phase FCC X-ray diffraction patterns (Figures. 9.3 and 9.4). The Pd-$Y_{6,\ 8,\ 9\ \&\ 10}$ alloys all demonstrated some degree of preferential texture along the [220] plane, presumably due to the cold-rolling (Figure 9.3). Accurate compositions were determined through comparison of the lattice parameter (*a*) to established literature data [42, 86]. The lattice parameters were calculated using the *d* – spacings from the [111], [200], [220] and [311] peaks.

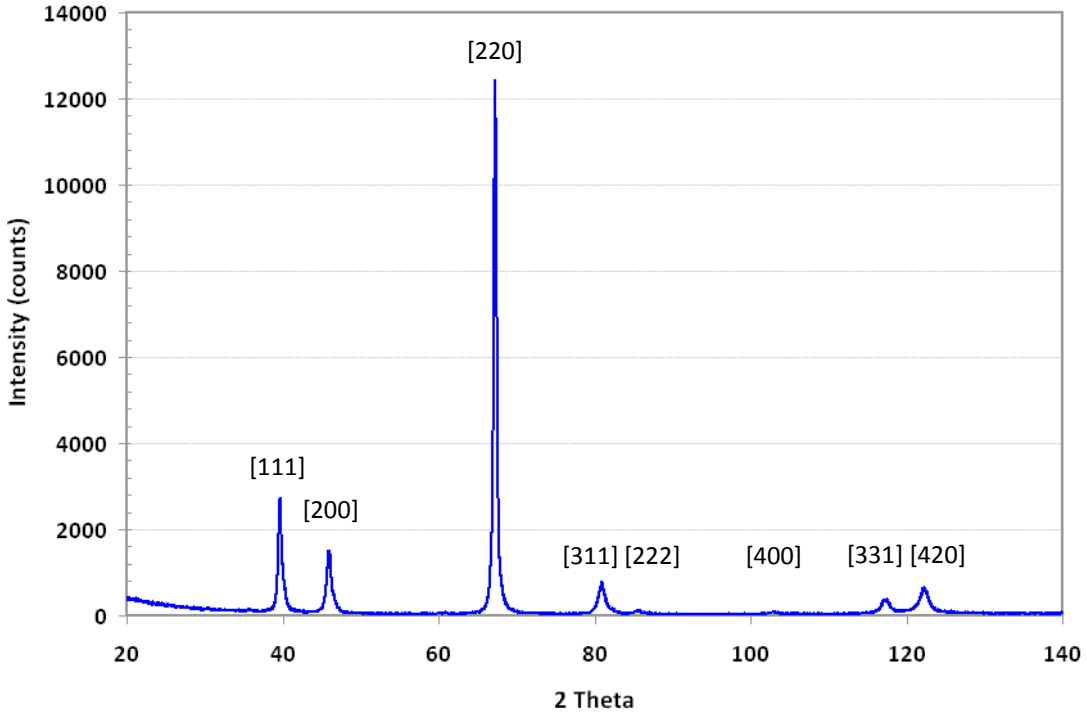

Figure 9.3 – X-ray diffraction pattern of Pd-Y_6 exhibiting a single-phase FCC structure

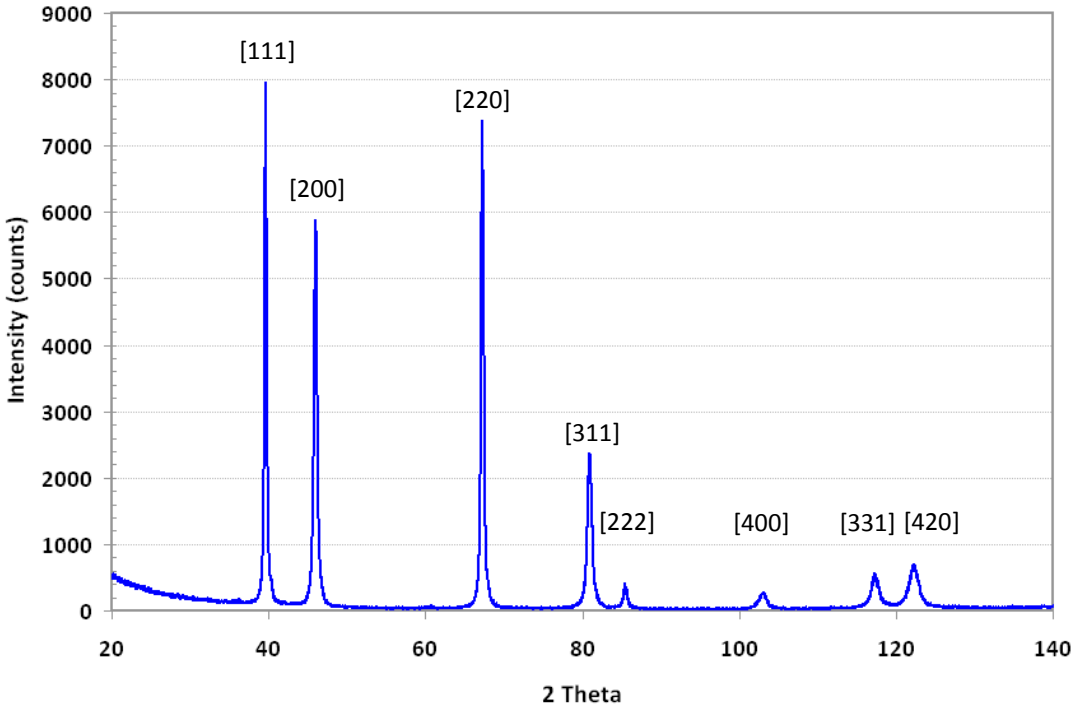

Figure 9.4 – X-ray diffraction pattern of Pd-Ag_{24} exhibiting a single-phase FCC structure

The calculated lattice parameters (*a*) of the Pd-Y alloys increased linearly with Y content (Figure 9.5), and are in excellent agreement with the previous work of Harris & Norman [42]. In order to calculate the alloy compositions, the lattice parameters were fit to the values reported by Harris & Norman using the linear equation,

$$y = (7.357 * 10^{-3})x + 3.8896 \qquad \textit{Eqn 9.1}$$

where y is the measured lattice parameter (Å) and x is the atomic concentration of Y. The same technique was used in order to calculate the composition of the Pd-Ag alloy using the data reported by Zeng [86],

$$y = (1.93 * 10^{-3})x + 3.887 \qquad \textit{Eqn 9.2}$$

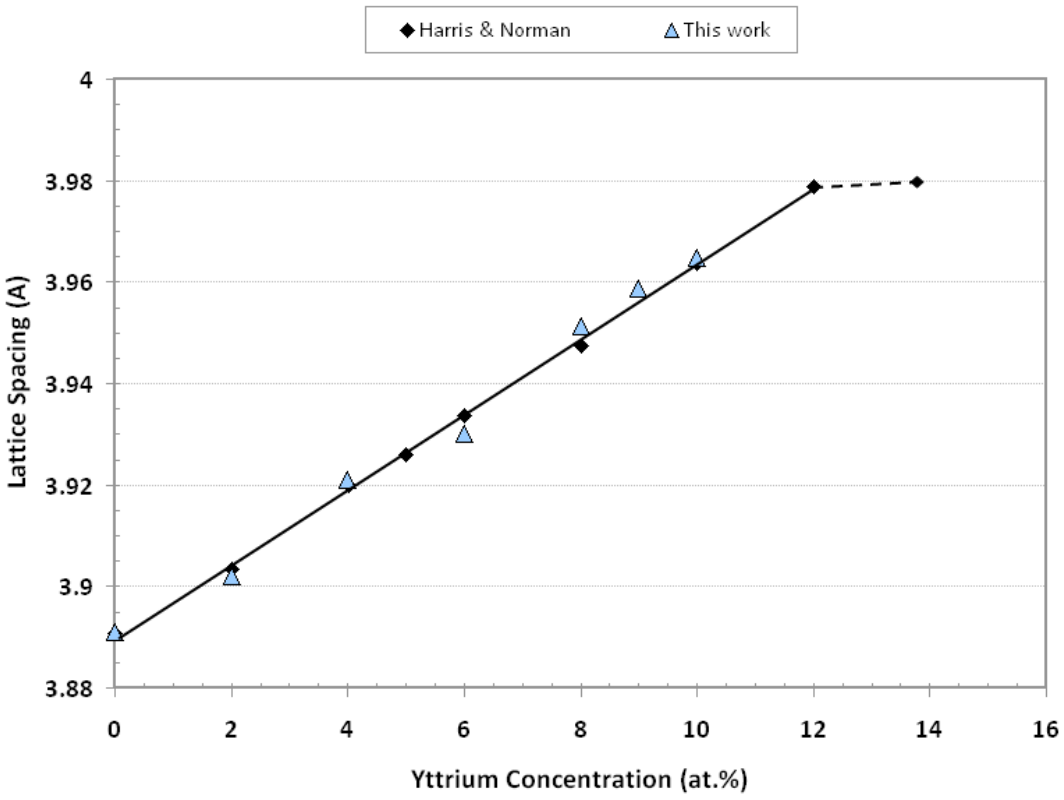

Figure 9.5 – Variation in lattice parameter (a) with Y content of Pd-Y alloys.

The lattice parameters of the Pd-Ag and Pd-Y samples are listed in Table 9.1, along with the calculated alloy compositions. With the exception of Pd-Y_6, the calculated compositions fall within ± 0.4 at.% of the nominal value. Interestingly, the Pd-Y_6 alloy was the only sample to experience significant oxidation during production. The segregation of Y to the surface forming Y_2O_3 and leaving the bulk alloy Pd rich, as observed previously by Doyle [46] and Fort [15], may explain the observed Y depletion. For simplicity, throughout the remaining sections the bulk alloys will be referred to by the nominal composition unless otherwise stated.

Table 9.1 – Lattice parameter and compositions of the bulk alloys.

Nominal Composition (at. %)	Lattice Parameter (a) (Å) ±0.0005	Calculated Composition (at. %) ±0.07	EDX (at. %)
Pd	3.8901	Pd	-
Pd-Y_2	3.9021	Pd-$Y_{1.68}$	-
Pd-Y_4	3.9211	Pd-$Y_{4.28}$	-
Pd-Y_6	3.930	Pd-$Y_{5.48}$	-
Pd-Y_8	3.9514	Pd-$Y_{8.38}$	Pd-$Y_{8.17}$
Pd-Y_9	3.9588	Pd-$Y_{9.40}$	Pd-$Y_{9.31}$
Pd-Y_{10}	3.9647	Pd-$Y_{10.20}$	Pd-$Y_{10.20}$
Pd-Ag_{24}	3.9338	Pd-$Ag_{24.22}$	Pd-$Ag_{23.74}$

9.1.2 – Hydrogen Permeability

Pure Palladium

Initial permeability measurements were performed on pure palladium membranes to act as both a baseline result and to validate the experimental procedure and assembly. There is a considerable volume of published work regarding the permeability of hydrogen in bulk Pd membranes, providing an excellent basis for comparison [65, 79, 180-183]. The independently determined permeability values also provide a useful comparative measure for the Pd alloy membranes, in both bulk and composite form, investigated within this work.

The variation of permeability with temperature of a pure Pd membrane is shown in Figure 9.6. Throughout the measurement the pressure conditions were kept constant, with an applied pressure (P_i) of 445 kPa and a permeate pressure (P_{ii}) of 100 kPa, thus producing a constant pressure gradient of 345 kPa (50 psi). Throughout the remaining sections the hydrogen flux analysis is described simply in terms of a pressure gradient, where a permeate pressure (P_{ii}) of 100 kPa is assumed unless otherwise stated.

In the absence of surface contamination, the hydrogen permeability of a Pd membrane exhibits Arrhenius-type behaviour with temperature, which may be expressed as,

$$\phi = \phi_o exp\left(-E_A/_{RT}\right) \qquad \textit{Eqn 9.3}$$

where ϕ is the permeability, ϕ_o a pre-exponential constant, E_A the activation energy for permeation, R the gas constant and T the absolute temperature. A plot of $ln\phi$ Vs $1/T$ should therefore result in a straight line, where the gradient gives the activation energy, E_A, and the intercept gives the pre-exponential factor, ϕ_o, (Figure 9.7).

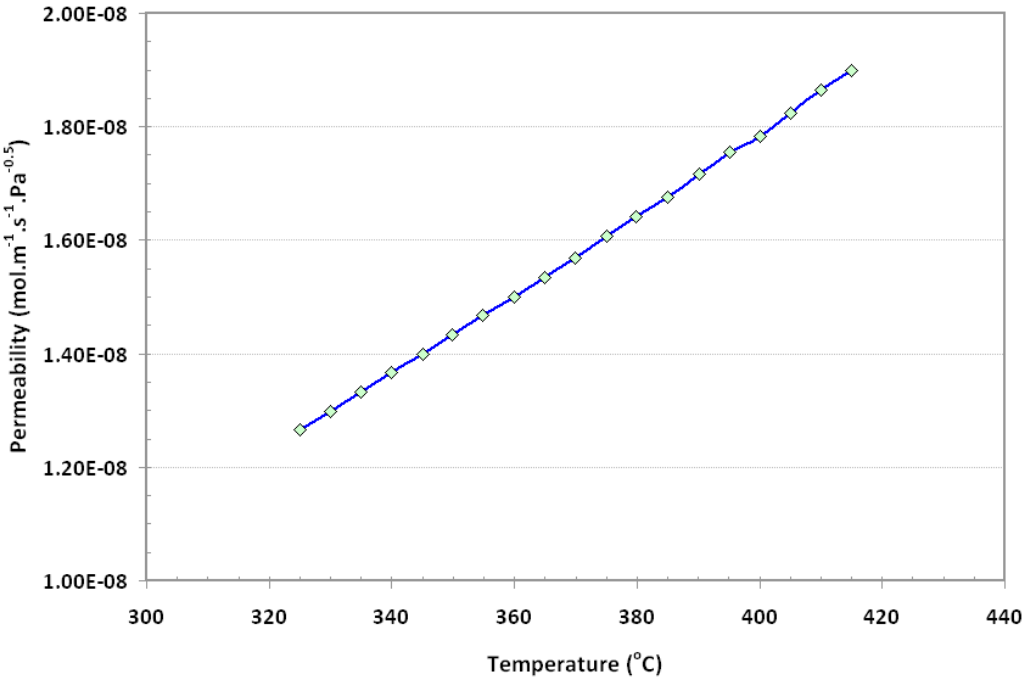

Figure 9.6 – Effect of temperature on the hydrogen permeability of a pure Pd membrane (t = 70µm)

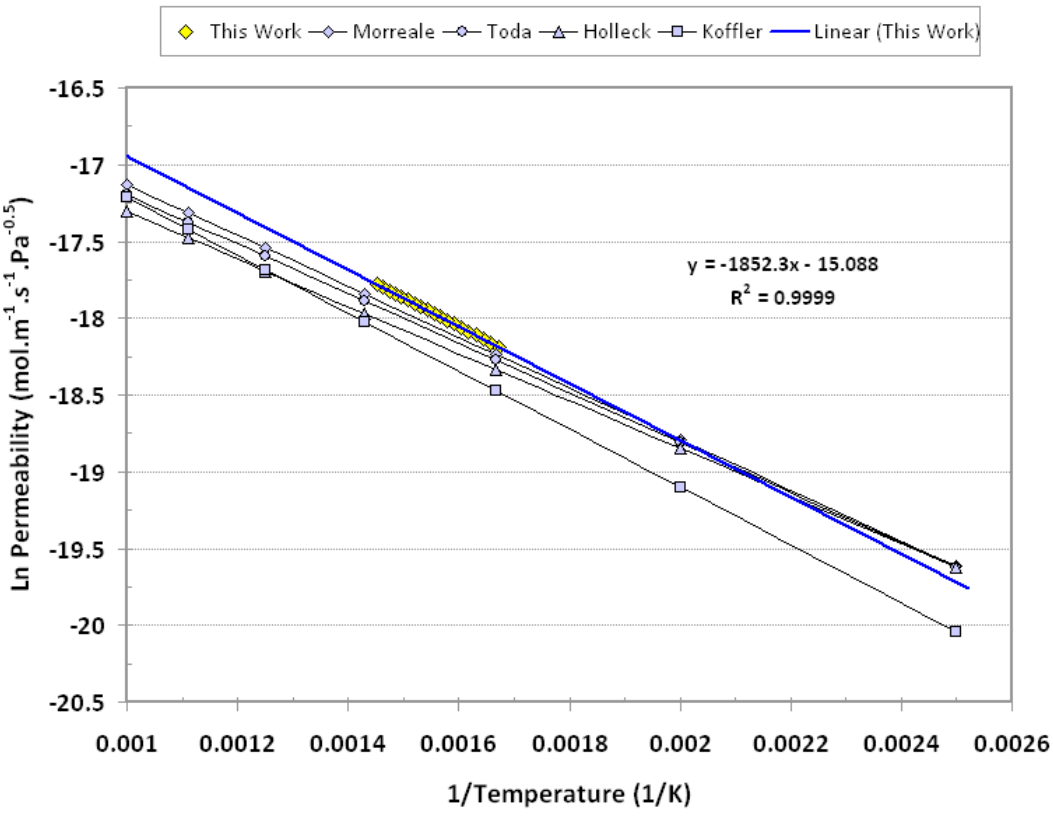

Figure 9.7 – Arrhenius plot of Pd permeability compared to literature values. (References given in Table 9.2)

As shown in Figure 9.7, the permeability exhibits an excellent linear fit to Arrhenius-type behaviour with temperature, with a regression coefficient of 0.9999. Additionally, the measured hydrogen permeability values are in good agreement with those reported in the literature. From the resultant linear equation (Figure 9.7), an activation energy of 15.4 $kJ.mol^{-1}$ and pre-exponential constant of 2.80 $x10^{-7}$ $mol.m^{-1}.s^{-1}.Pa^{-0.5}$ can be calculated. These values are compared to a range of previously published results in Table 9.2.

Table 9.2 – Published data for permeability of hydrogen in bulk palladium

	Thickness (μm)	Geometry	*n* value	Activation Energy ($kJ.mol^{-1}$)	Permeability Constant ($mol.m^{-1}.s^{-1}.Pa^{-0.5}$)
Morreale [79]	1000	Disc	0.5	13.81	$1.92 x10^{-7}$
Holleck [65]	800-2025	Disc	0.5	12.81	$1.42 x10^{-7}$
Davis [180]	130-729	Disc	0.5	18.56	$3.85 x10^{-7}$
Toda [181]	11500	Wire	0.5	13.46	$1.72 x10^{-7}$
Balavnev [182]	100-1000	Disc	0.5	15.46	$1.89 x10^{-7}$
Koffler [183]	486-762	Disc	0.5	15.67	$2.20 x10^{-7}$
Present Work	70	Disc	0.5	15.40	$2.80 x10^{-7}$

The E_A and the ϕ_o values calculated during the present work are well within the range reported in the literature. Therefore, the experimental procedure and apparatus are assumed to be valid, and further permeability values can be analysed and compared to those in the literature with a high degree of confidence.

Interestingly, the permeability measurements resulted in significant membrane deformation. The membrane 'bowed' uniformly across the surface due, presumably, to a combination of the pressure gradient and also the Pd lattice expansion gradient (arising from the solubility gradient). The maximum vertical displacement observed was 2.1 mm. As a result, both the initial membrane surface area and thickness, which were used to calculate permeability, were invalid. Therefore, the effective surface area of the deformed disc was re-calculated using simple geometry, whilst the effective thickness was estimated assuming a constant membrane volume. A full description of this procedure is given in Appendix I. The relative increase in surface area and reduction of thickness significantly affected the apparent permeability. A vertical displacement of 2.1 mm gave rise to a 10.1 % increase in apparent permeability. Therefore, throughout this work the permeability values have been calculated using the 'deformed' surface area and membrane thickness.

Palladium – Yttrium Alloys

Hydrogen permeability isobars were performed for each of the Pd-Y membranes at a constant pressure gradient of 345 kPa, and are compared to that of pure Pd in Figure 9.8 All the permeability measurements were performed on membranes in the as-annealed condition (10^{-5} mbar, 650°C, 4 hrs). Given that β-hydride formation was expected for the 2, 4 and 6 at.% Y alloys above room temperature, these membranes were pre-heated under argon to above the critical temperature for β-hydride formation. The critical temperature for each alloy was estimated using the hydrogen solubility data of the Pd-Y system reported by Doyle [46].

Figure 9.8 clearly demonstrates the considerable effect alloying additions of Y has on the hydrogen permeability of Pd. The addition of just 1.68 at.%Y (Pd-Y_2) increases the

permeability at 300°C by about 80 % compared to pure Pd, whilst adding ~ 8 at.%Y increases the permeability by over a factor of 5. Although each alloy composition displays a unique permeability isobar, a number of approximate comparisons can be drawn. Firstly, there is a general trend of increasing permeability with increasing Y concentration, particularly above 400°C. Secondly, the Pd-Y_8 membrane exhibits the maximum observed permeability within the measured temperature range of 25 to 460°C. At 350°C the permeability of hydrogen in Pd-Y_8 is found to be 5.92 x10^{-8} mol.m^{-1}.s^{-1}.$Pa^{-0.5}$, which is in excellent agreement with the value of 5.78 x10^{-8} mol.m^{-1}.s^{-1}.$Pa^{-0.5}$ reported by Wileman [55]. Finally, with the exception of Pd-Y_2, each composition exhibits a clear permeability maximum within the temperature range studied. Although no distinct maximum was observed for the Pd-Y_2 sample, the shape of the curve suggests that a maximum may occur at lower temperatures. Additionally, the temperature at which the permeability maxima are observed, increases with Y concentration.

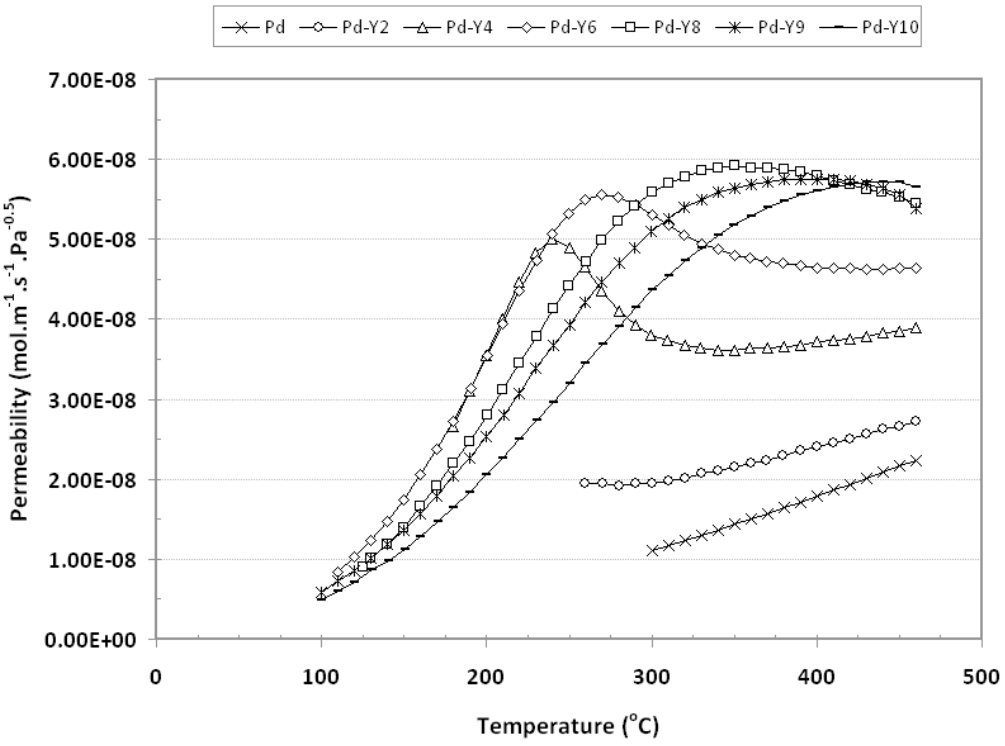

Figure 9.8 – Variation of hydrogen permeability with temperature of Pd-Y bulk membranes

The shape of the permeability isobars is largely determined by the hydrogen concentration gradient acting across the membrane. Indeed, as discussed in Section 3.5, the enhanced permeability of Pd-Y compared to Pd-Ag has been attributed to the concentration (solubility) gradient [53]. The effect of the solubility gradient on the permeability is discussed later within this section, however, fundamental analysis on the effect of Y concentration on hydrogen solubility and diffusivity does not fall within the scope of this work, and indeed, has largely been covered previously [46, 47, 54-57]. The primary focus of the current work was to establish a trend between composition and permeability, which can then be applied to the thin film Pd-Y membranes. The expected composition control of the co-sputtered thin film membranes was approximately ± 1 at.% Y, therefore, it was necessary to quantify the permeability across the solid solution range. Thus permitting the interpolation of permeability in a thin film membrane with an intermediate composition. The effect of Y concentration on the hydrogen permeability at typical membrane operating temperatures is shown in Figure 9.9.

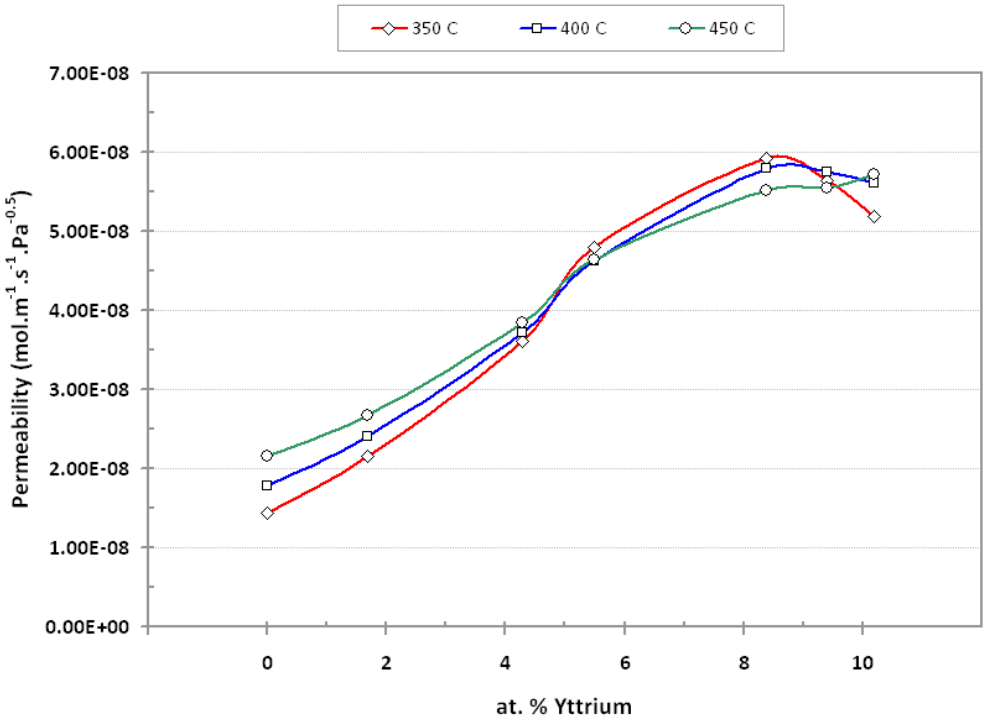

Figure 9.9 – Effect of yttrium concentration on the hydrogen permeability of Pd-Y at 350, 400 and 450°C

Above 350°C the hydrogen permeability increases almost linearly with Y concentration until ~ 8 at.% (Figure 9.9). At temperatures below 420°C the permeability then decreases with additional Y content, whilst above this temperature the permeability continues to increase, albeit at a reduced rate. The data presented in Figure 9.9 can be used to estimate, at corresponding temperatures, the permeability of any Pd-Y alloy composition with a reasonable degree of certainty.

Interestingly, at temperatures below 290°C, the Pd-Y_6 alloy demonstrates the highest permeability of the Pd-Y system (Figure 9.8). However, the critical temperature for β-hydride phase formation in Pd-Y_6 remains above room temperature. Based on hydrogen solubility measurements, the miscibility gap in Pd-Y_6 closes between 25 and 100°C [46]. Therefore, in order to avoid membrane failure, a thin film Pd-Y_6 membrane would require inert pre-heating before exposure to hydrogen. Of the compositions for which the miscibility gap is suppressed beneath room temperature, Pd-Y_8 exhibits the greatest permeability below 400°C. As a result, Pd-Y_8 was chosen as the target composition for the thin film membranes.

The hydrogen permeability of Pd-Y_8 is compared to that measured in Pd-Ag_{24} and pure Pd in Figure 9.10 Not only is Pd-Ag_{24} the industry standard alloy for self-supporting hydrogen separation membranes it is, along with pure Pd, by far the most widely studied in terms of thin film composite membranes. Therefore, both Pd and Pd-Ag serve as a useful basis for comparison to the results reported within this work.

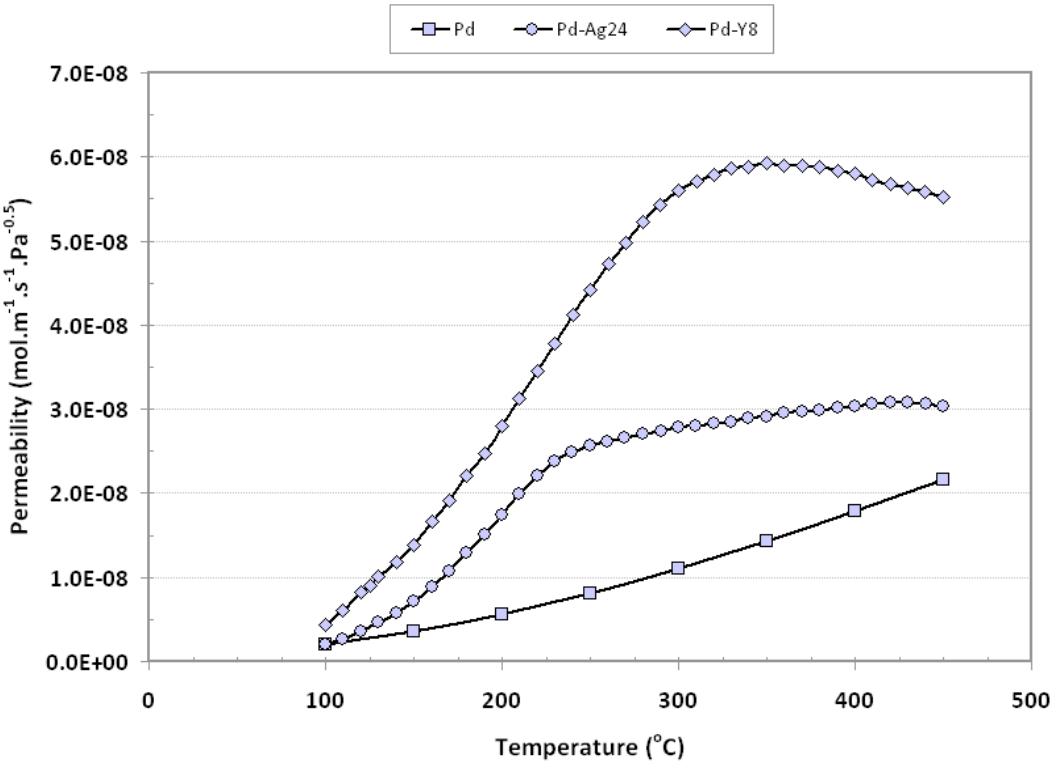

Figure 9.10 – Comparison of the hydrogen permeability of Pd-Y_8, Pd-Ag_{24} and Pd

Figure 9.10 clearly shows the enhanced permeability of Pd-Y_8 when compared to Pd-Ag_{24}, particularly above 200°C. At lower temperatures (< 200°C) both alloys exhibit a similar variation of permeability with temperature, although the permeability of Pd-Y_8 remains approximately 70 % greater than in Pd-Ag_{24}. At roughly 225°C there is a distinct change in the temperature dependence of the permeability in Pd-Ag_{24}. Above this temperature, there is only a modest increase in permeability. In contrast, the permeability of Pd-Y_8 continues to increase rapidly until a maximum is reached at ~ 350°C. Between 350°C and 450°C there is a gradual reduction in permeability as the temperature increases.

Figure 9.10 clearly highlights the potential advantage of Pd-Y_8 compared to Pd-Ag_{24} for use in thin film composite membranes. Firstly, the maximum permeability is double that in Pd-Ag_{24}, secondly, and perhaps most significantly, equivalent flux rates can be achieved at much lower temperatures. The permeability of Pd-Ag_{24} at 400°C is exceeded by the Pd-Y_8 alloy at

just 220°C. The potential to reduce operating temperatures whilst retaining reasonable hydrogen flux is a major virtue of Pd-Y_8. Many of the problems associated with composite membranes, such as delamination and film / substrate intermetallic diffusion, are propagated by high operating temperatures.

Similar to pure Pd, the hydrogen permeability of both Pd-Y_8 and Pd-Ag_{24} demonstrate an Arrhenius-type relationship with temperature (Figure 9.11). Interestingly, both the low (< 250°C) and high (> 250°C) temperature regions of the Pd-Ag_{24} permeability curve exhibit Arrhenius-type behaviour, whilst in Pd-Y_8, only the low temperature region (< 300°C) fits such behaviour. The calculated E_A and ϕ_o values for both alloys are compared to those reported in the literature and those measured for Pd, Pd-Y_9 and Pd-Y_{10} in Table 9.3.

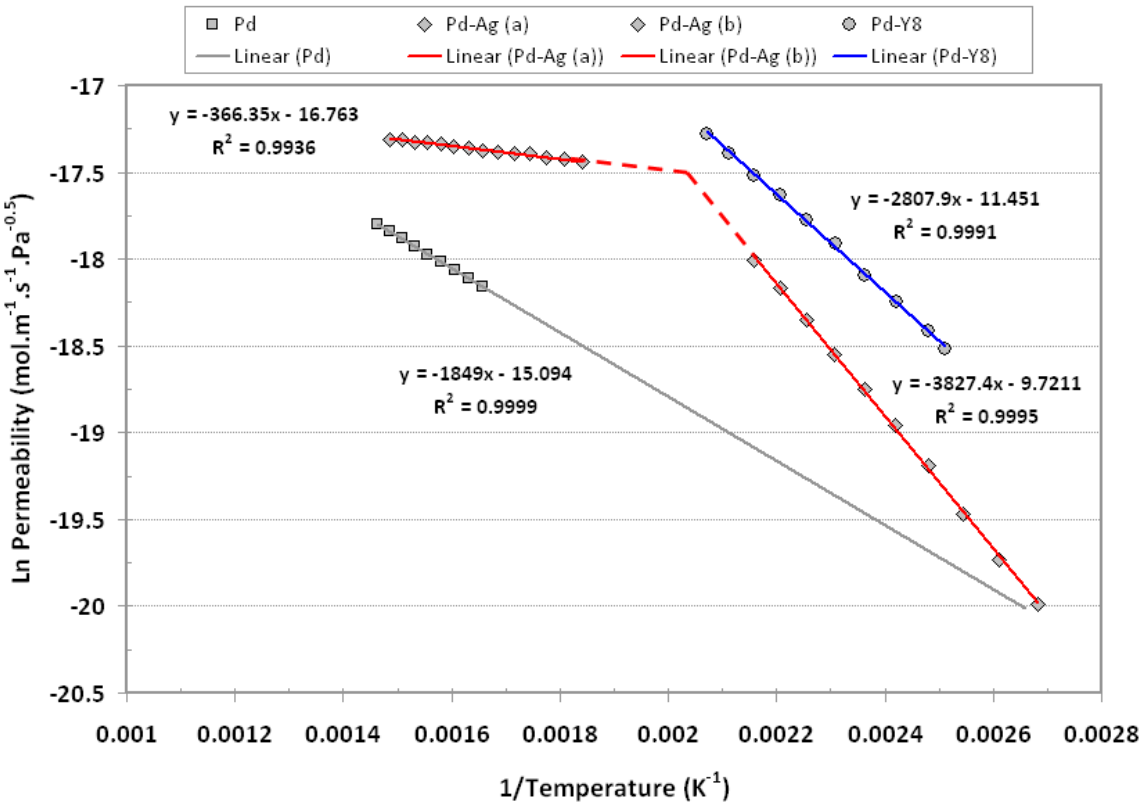

Figure 9.11 –Arrhenius-type plot of the measured hydrogen permeability in Pd-Y_8, Pd-Ag_{24} and Pd

Table 9.3 – Calculated E_A and ϕ_o values of Pd, Pd-Ag_{24} and Pd-$Y_{8, 9, 10}$ compared to various literature values

Alloy / Composition	Activation Energy (E_A) kJ.mol^{-1}	Permeability Constant (Φ_o) (mol^{-1}.m^{-1}.s^{-1}.Pa$^{-0.5}$)	Reference
Pd	15.4	2.80 x10^{-7}	This work
Pd	13.8	3.31 x10^{-7}	Morreale [79]
Pd-Ag_{24} (A)	3.1	5.25 x10^{-8}	This work
Pd-$Ag_{25wt.\%}$	6.3	5.58 x10^{-8}	Serra et al [37]
Pd-$Ag_{25wt.\%}$	5.7	3.85 x10^{-8}	Yoshida [184]
Pd-Ag_{24} (B)	31.8	6.00 x10^{-5}	This work
Pd-Ag_{24}	39.4	1.52 x10^{-4}	Wileman [55]
Pd-Y_8	23.3	1.06 x10^{-5}	This Work
Pd-$Y_{8\ Ordered}$	25.3	2.06 x10^{-5}	Wileman [55]
Pd-$Y_{8\ Disordered}$	34.2	4.48 x10^{-5}	Wileman [55]
Pd-Y_9	21.9	6.80 x10^{-6}	This work
Pd-Y_{10}	19.5	2.89 x10^{-6}	This work

Unlike the pre-exponential constant, ϕ_o, whose value can be influenced by experimental uncertainties such as membrane thickness or effective area, the activation energy E_A of a membrane represents the temperature dependence of the permeability and is indicative of the active permeation mechanism. The value of E_A is dependent on many fundamental properties of a membrane and is sensitive to crystal structure, degree of ordering, trapping mechanisms, and alloy composition. As noted previously, several investigators including Wileman [55, 56], Hughes [57], Doyle [46, 47] and Poyser [58] have all reported evidence of ordering in bulk Pd-Y alloys with high Y contents. When cooled under vacuum from above a certain critical temperature, estimated as 495°C in Pd-Y_{12} and 455°C in Pd-Y_{10} by Doyle [46], the alloy forms the ordered cubic Pd_7Y-type structure. However, when cooled in a hydrogen atmosphere the

alloy remains disordered. Wileman [55] determined the hydrogen permeability of Pd-Y_8 in both the ordered and disordered condition. The E_A and Φ_o values reported for each condition are listed in Table 9.3. Clearly, the activation energy of the ordered alloy is considerably lower than that in the disordered alloy. As described in Chapter 2, although there was a small difference in solubility, the ordered alloy exhibited a much greater diffusivity, hence the enhanced permeability and lower activation energy [55]. The E_A value of the Pd-Y_8 membrane observed in the present work is in good agreement with the 'ordered' value reported by Wileman [55]. When considering that the bulk Pd-Y alloys in the present work were investigated in the as-annealed condition (10^{-5} mbar, 650°C, 4hrs) hence, cooled under vacuum, it seems reasonable to conclude that the Pd-Y alloys exhibit the 'ordered' condition described by Wileman [55]. Although the ordered superlattice peaks were not observed using X-ray diffraction, the associated reflections are particularly weak. Using the greater resolution offered by neutron diffraction, Poyser [58] was able to detect superlattice reflections in Pd-Y_{10}.

Hydrogen permeation in composite membranes is frequently reported to exhibit non-diffusion limited behaviour. Given the sensitivity of the activation energy to hydrogen diffusion, the calculated E_A values for the bulk membranes serve as a useful comparative tool for the analysis of the thin film composite membrane. Any deviation in E_A between the thin films and the bulk alloy would signify different active transport mechanisms *i.e.* possible substrate resistance.

The superior hydrogen permeability of Pd-Y_8 compared to Pd-Ag_{24} has previously been attributed to an enhanced concentration gradient across the membrane [53, 54, 56]. Assuming the

near surface regions of the membrane are in equilibrium with the external gas-phase pressure, the effective concentration gradient may be calculated from the hydrogen solubility at either side of the membrane. As noted previously, the hydrogen permeability measurements were performed using an applied pressure of 445 kPa and a permeate pressure of 100 kPa. Therefore, equilibrium hydrogen solubility isobars were taken for both alloys at corresponding pressures (Figures 9.12 and 9.13).

Figures 9.12 and 9.13 clearly show the exothermic nature of hydrogen absorption in Pd alloys, as the maximum solubility decreases with increasing temperature. It is also apparent that at both pressures, Pd-Y_8 exhibits greater hydrogen solubility over the entire temperature range. Although the absolute values are somewhat lower than those reported previously, the general shape of the curves are in good agreement [53, 55]. The solubility gradient acting across the membrane is then determined simply by subtracting the low pressure solubility from the high pressure solubility (Figure 9.14).

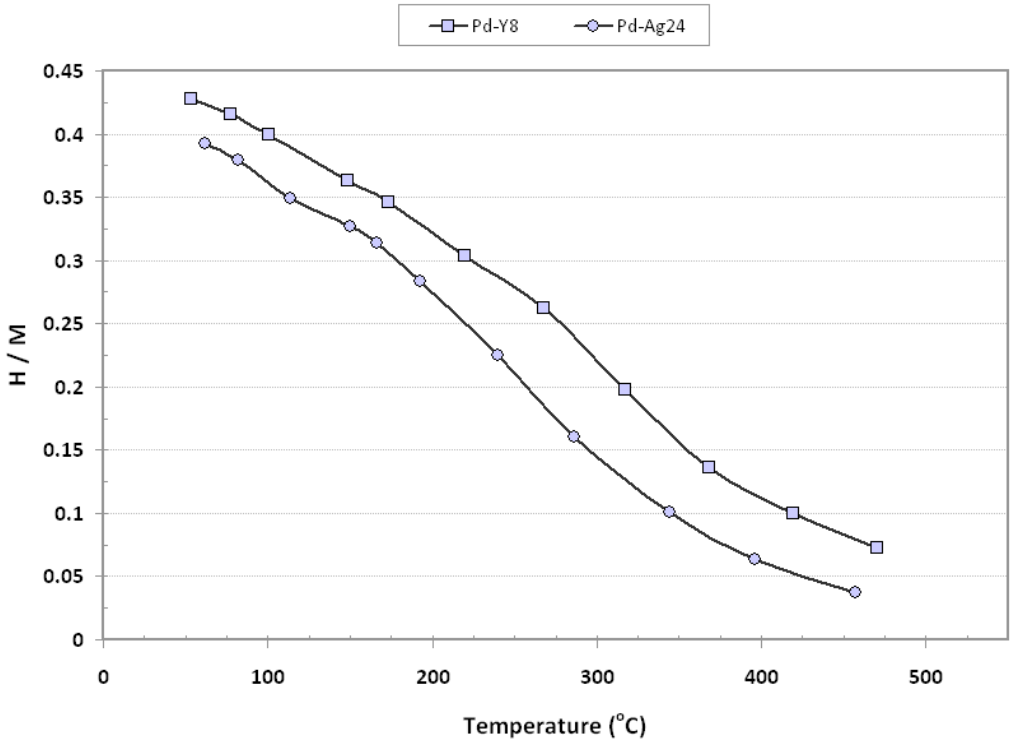

Figure 9.12 – Equilibrium hydrogen solubility of Pd-Y_8 and Pd-Ag_{24} at a hydrogen pressure of 445 kPa

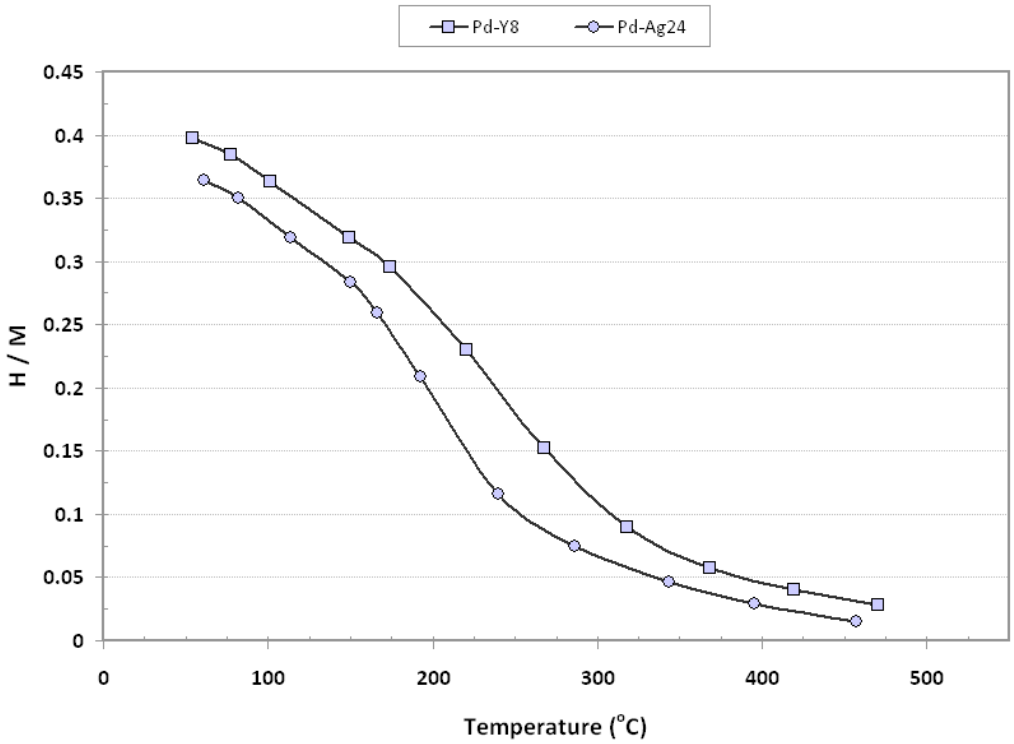

Figure 9.13 – Equilibrium hydrogen solubility of Pd-Y_8 and Pd-Ag_{24} at a hydrogen pressure of 100 kPa

The calculated solubility gradients are compared to those reported by Wileman [55] and, discounting the low temperature Pd-Y_8 values, are in good agreement (Figure 9.14). The Pd-Y_8 alloy displays a significantly greater solubility gradient above ~ 250°C and appears to support the conclusion that the superior permeability of Pd-Y_8 when compared to Pd-Ag_{24} is due to the enhanced solubility gradient [53, 56].

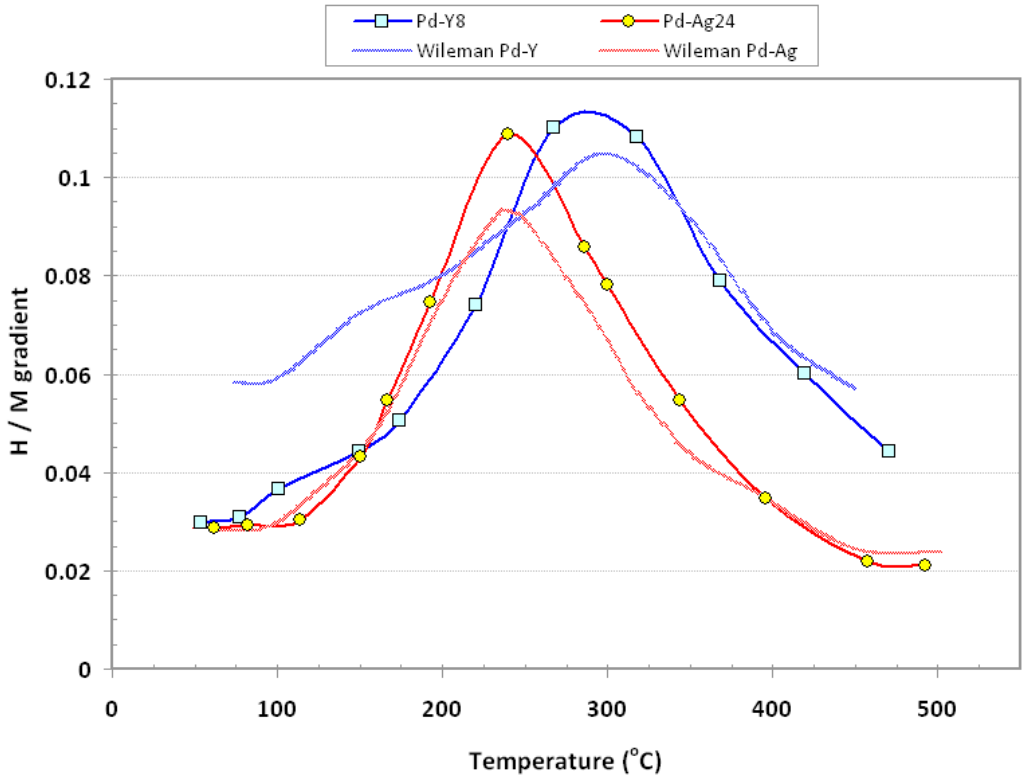

Figure 9.14 – Solubility gradient across Pd-Y_8 and Pd-Ag_{24} at a hydrogen pressure gradient of 345 kPa

The low temperature difference observed between the Pd-Y_8 alloys, is most probably due to the degree of order. The Pd-Y_8 alloy reported by Wileman [55] was measured in the 'ordered' condition. Although the alloy investigated in the present work was prepared in the vacuum annealed condition, and therefore the ordered condition, the alloy was activated in hydrogen prior to the solubility measurements. The activation step was performed in an attempt to remove any surface oxidation, thus increasing the reaction kinetics. During activation, the

alloy was heated to 400°C under a hydrogen pressure of 2000 kPa. The alloy would then be expected to be in the disordered condition. Although the sample was degassed at 10^{-6} mbar prior to cooling, the alloy may not have fully re-ordered. The excellent agreement observed at high temperatures, where both samples would be expected to be in the disordered condition, supports this suggestion.

From Figure 9.14 it is evident that, although the maximum solubility gradients observed in the current work are slightly greater than those reported by Wileman [55], they occur at almost identical temperatures; ~ 230°C and ~ 290°C for Pd-Ag_{24} and Pd-Y_8 respectively. These temperatures correspond to the 'switch over' point in the temperature dependence of the permeability. When overlaid, the influence of the solubility gradient on the permeability of Pd-Y_8 and Pd-Ag_{24} is clearly seen (Figures 9.15 and 9.16).

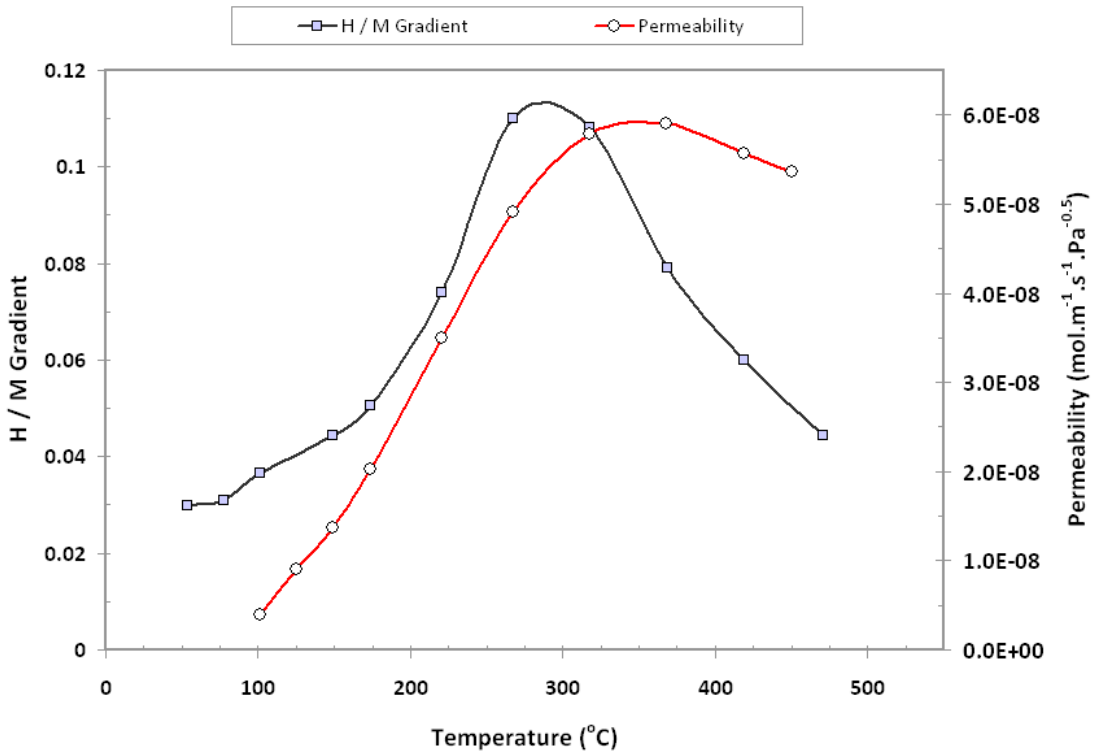

Figure 9.15 – Hydrogen permeability and solubility gradient across Pd-Y_8 at a pressure gradient of 345 kPa

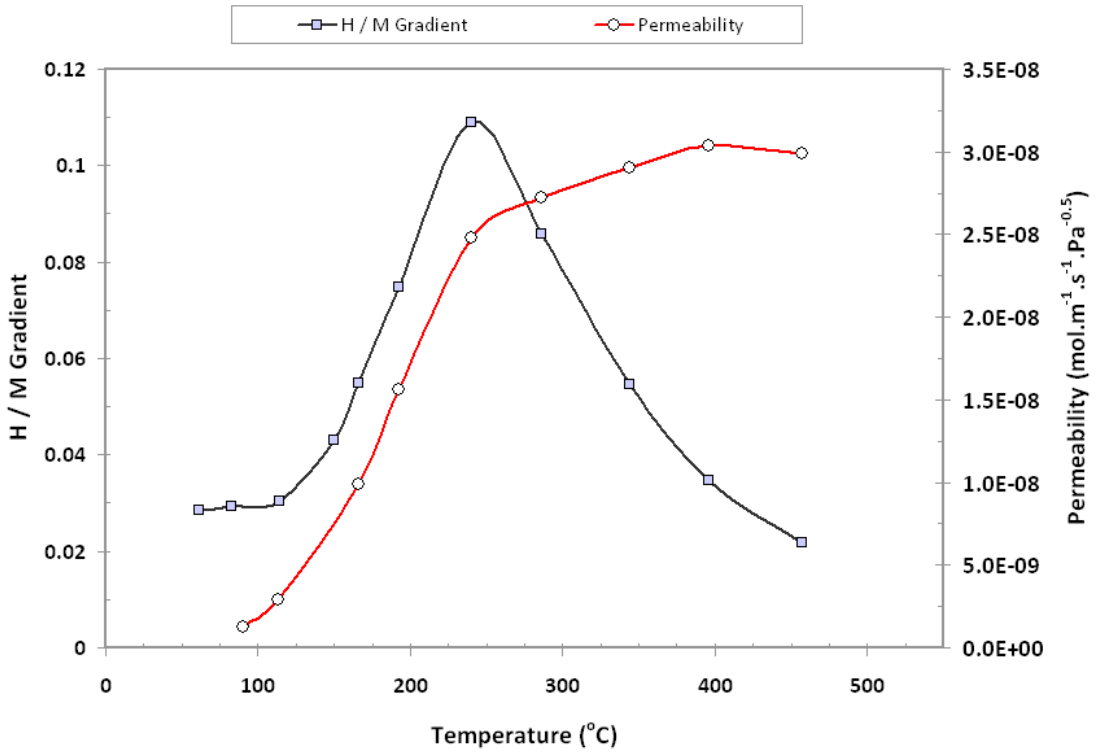

Figure 9.16 – Hydrogen permeability and solubility gradient across Pd-Ag_{24} at a pressure gradient of 345 kPa

Given that in both Pd-Y_8 and Pd-Ag_{24} the solubility gradient maxima corresponds to the point at which the relationship between permeability and temperature changes, it is a reasonable assumption that the similar permeability curves observed for Pd-$Y_{4,\ 6,\ 9,\ 10}$ are also due to the solubility gradient. Therefore, it can be deduced that increasing Y concentration increases the temperature at which the maximum solubility gradient is attained.

Establishing the temperature at which the maximum solubility gradient occurs is particularly important for an alloy used in a composite membrane. The lattice expansion due to hydrogen absorption introduces stresses which can contribute to membrane failure. Although the equilibrium solubility is greater at lower temperatures (Figures 9.12 and 9.13), the solubility gradient induces an effective expansion gradient across the membrane. Such non-uniform expansion may contribute to film delamination or rupture, resulting in membrane failure.

Pressure Dependency of Hydrogen Flux in Bulk Pd-Y

The value of *n*, assigned to the exponential pressure dependence of hydrogen flux in composite membranes (see Eqn 9.4) is frequently reported to deviate significantly from 0.5, the value for atomic diffusion limited permeation.

$$J_{H_2} = \Phi \frac{\left(Pi_{H_2}^n - Pii_{H_2}^n\right)}{l(x)} \qquad Eqn\ 9.4$$

Values of *n* as high as 1 have been reported for composite Pd membranes with thicknesses < 3 μm [88, 93, 153], however, most values range between 0.6 and 0.75 [121, 156-159]. The reason for the observed deviations is subject to a great deal of speculation. A common explanation is that the film is sufficiently thin so that atomic diffusion no longer limits the permeation, and that surface dissociation and absorption limit the reaction for which an *n*-value of 1 would be appropriate. However, recent studies on free-standing thin films suggest the permeation is diffusion limited at thicknesses of just 1.3 μm [84, 85]. These effects, and the possible reasons for such, are discussed further in Section 11.3. However, in order to facilitate analysis of the flux through the Pd-Y composite membranes, the *n*-value of the bulk alloys must be established. Therefore, permeability isotherms were taken at various temperatures for both the Pd-Y_8 and Pd-Y_9 membranes (Figures 9.17, 9.18, 9.19 and 9.20). The respective *n*-values were calculated by least squares regression of the experimental data

.

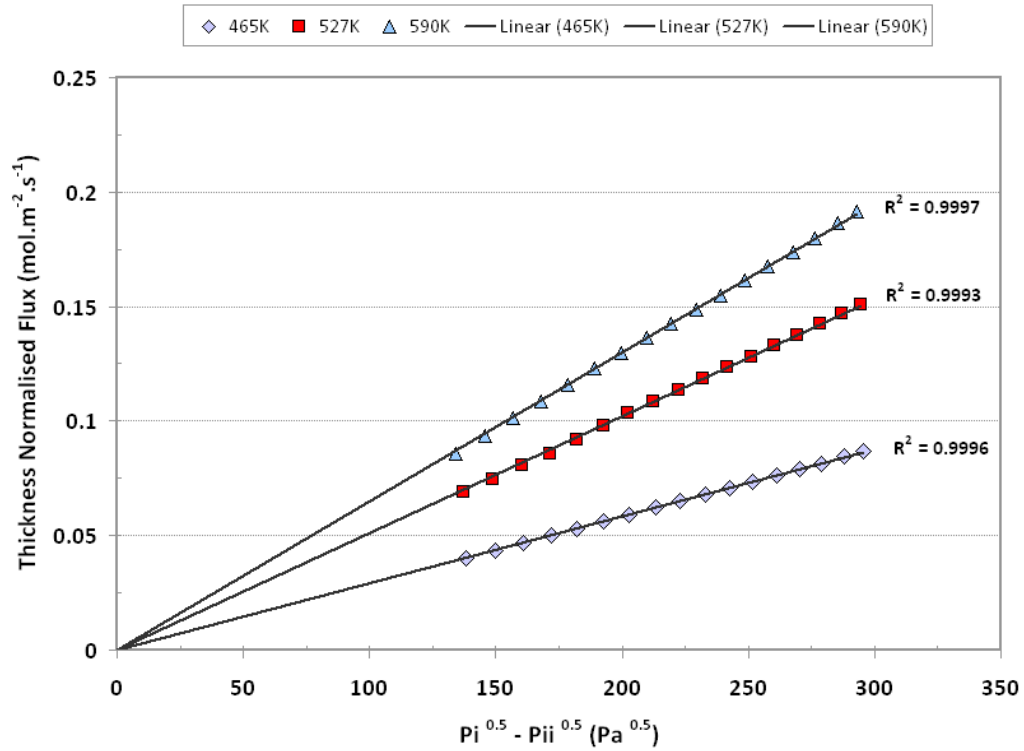

Figure 9.17 – Hydrogen permeability of Pd-Y_8 when pressure exponent 'n' is constrained to 0.5

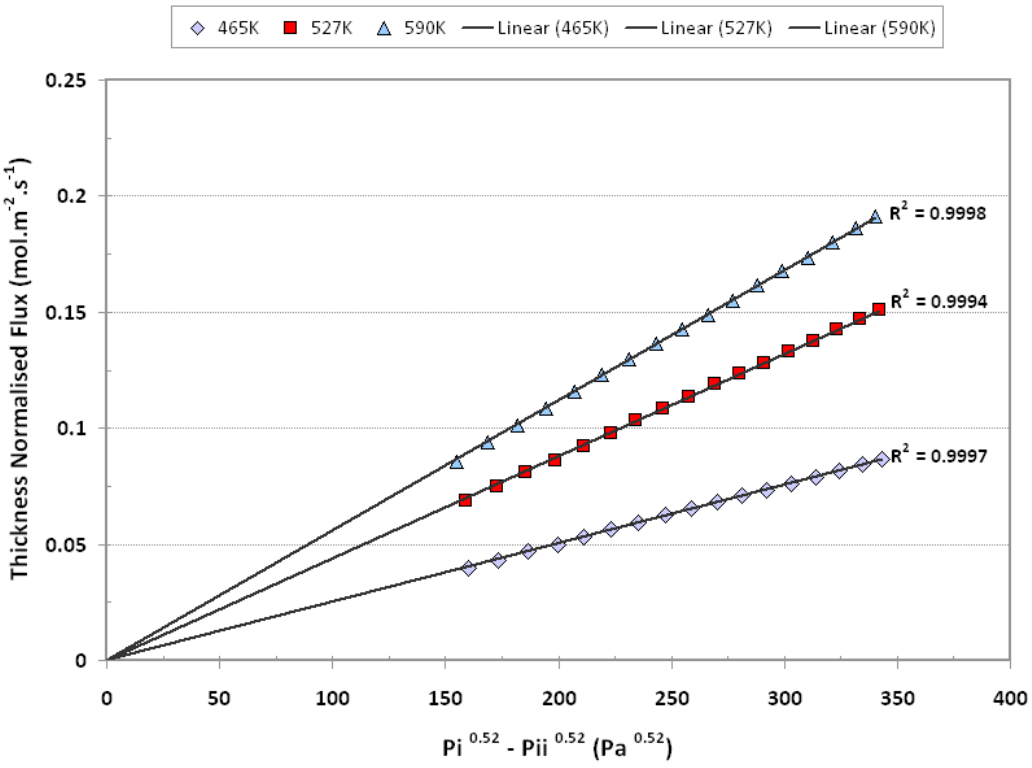

Figure 9.18 – Hydrogen permeability of Pd-Y_8 when pressure exponent 'n' fixed to the best fit value of 0.52

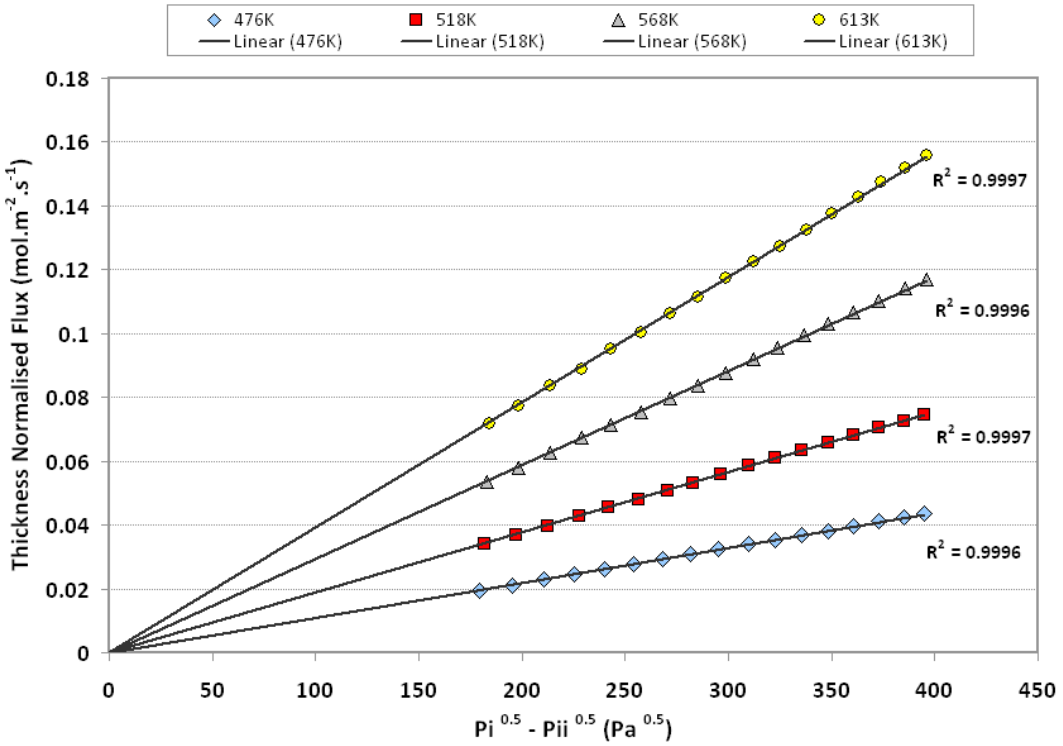

Figure 9.19 – Hydrogen permeability of Pd-Y_9 when pressure exponent 'n' is constrained to 0.5

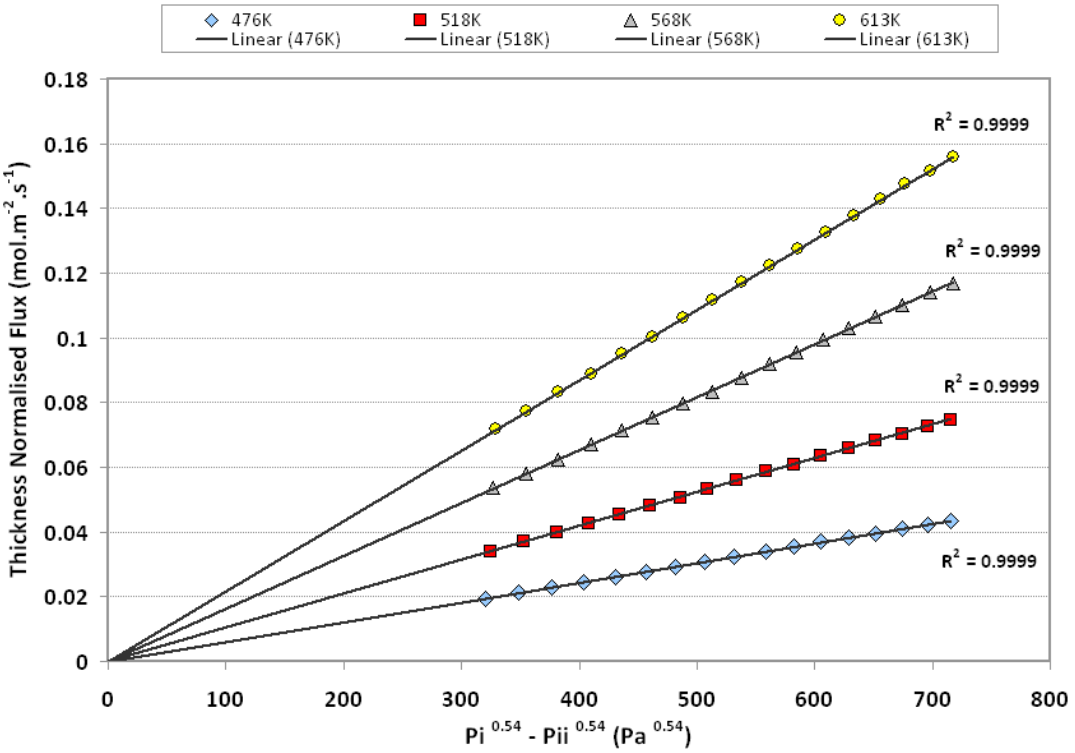

Figure 9.20 – Hydrogen permeability of Pd-Y_9 when pressure exponent 'n' is fixed to the best fit value 0.54

As shown in Figures 9.17 and 9.19 the measured flux across both membranes exhibits a good linear fit when $n = 0.5$, with high R^2 values. However, the best fit values were determined as 0.52 and 0.54 for Pd-Y_8 and Pd-Y_9 respectively (Figure 9.18 and 9.20). Although many authors do not report *n*-values of bulk membranes, the calculated values are in excellent agreement with those reported for 1 mm thick Pd by Morreale et al [79]: at pressures < 1000 kPa they reported an *n*-value of 0.54, although greater *n*-values were observed at high pressures (2500 kPa). Morreale [79] suggested the significant high pressure deviations were the result of non-ideal behaviour of either Sievert's constant or the diffusion coefficient at such high hydrogen concentrations. Small deviations from 0.5, as seen in the present work, may fall within the experimental error or arise due to a slight drop in the hydrogen partial pressure due to contaminants. Nevertheless, the calculated *n*-values of 0.52 and 0.54 signify that hydrogen permeation in bulk Pd-Y is predominantly diffusion limited.

9.2. – Thin Films

The co-sputtered Pd-Y films used within this work were produced by Teer Coatings Ltd. The production process has been described previously in Section 8.2.2. A wide range of solid solution Pd-Y alloys were produced with compositions ranging between 2 and 14 at.%Y, thus exceeding the reported maximum equilibrium solubility of Y in bulk Pd of 12.5 at.%Y [42]. The formation of super-saturated FCC solid solution alloys by co-sputtering has been observed previously [118]. Although the Y concentration of the thin films was found to be approximately linear with Y target voltage, the actual sputter rate of each element, and therefore the resultant composition is dependent on many factors including target thickness, target surface condition and vacuum level. Therefore, in order to facilitate reliable comparisons between samples, the thin film Pd-Y membranes were batch produced in two single processes, each with a target composition of 8 at.% Y, designated Batch A and Batch B.

9.2.1 – Alloy Assessment and Composition

The room temperature X-ray diffraction patterns of Batch A and Batch B thin films are shown in Figures 9.21 and 9.22 respectively. Diffraction patterns were taken using three samples from both batches, each clearly demonstrating a single phase FCC structure with a high degree of preferential texture along the [111] plane. Although the [200], [220] and [311] FCC diffraction peaks were present, the relative intensity of these peaks were extremely low compared to the [111] peak. Hence, the lattice spacings (a) of the thin film membranes were established using the low angle [111] peak (Figure 9.23).

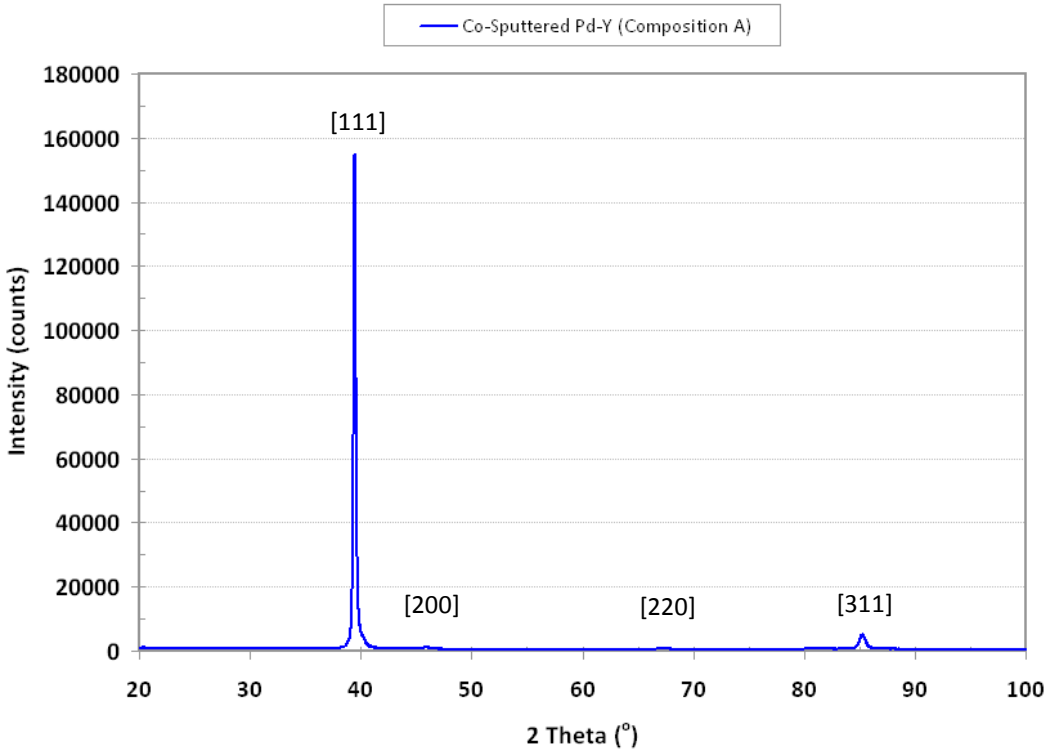

Figure 9.21 – XRD pattern of co-sputtered solid solution Pd-Y (Batch / Composition A)

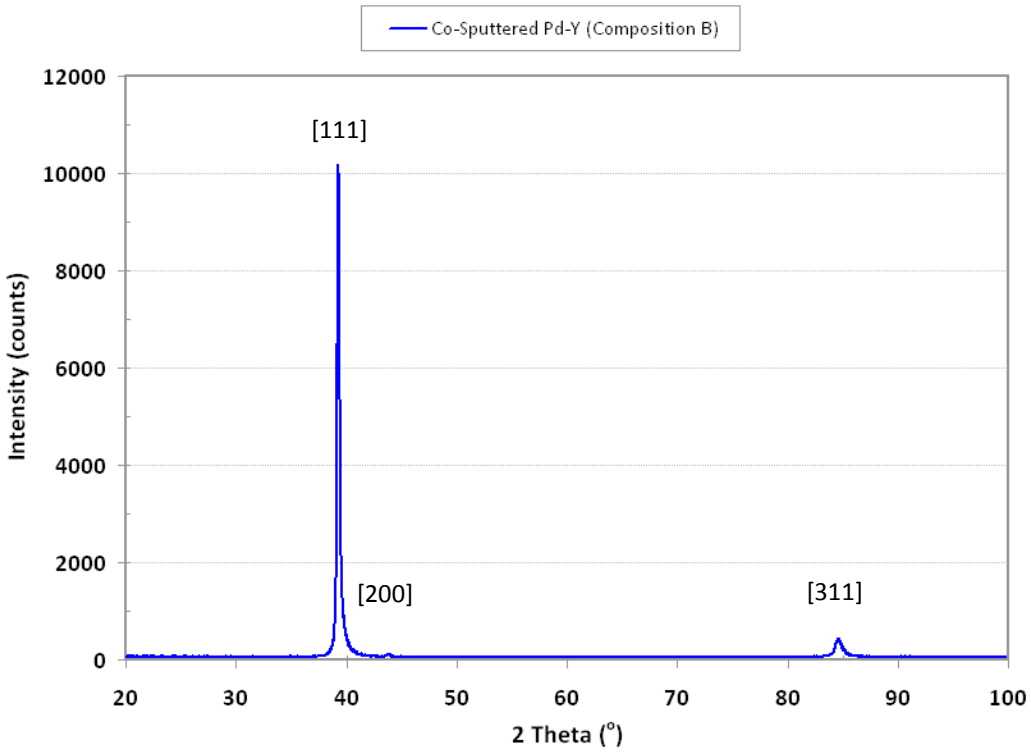

Figure 9.22 – XRD pattern of co-sputtered solid solution Pd-Y (Batch / Composition B)

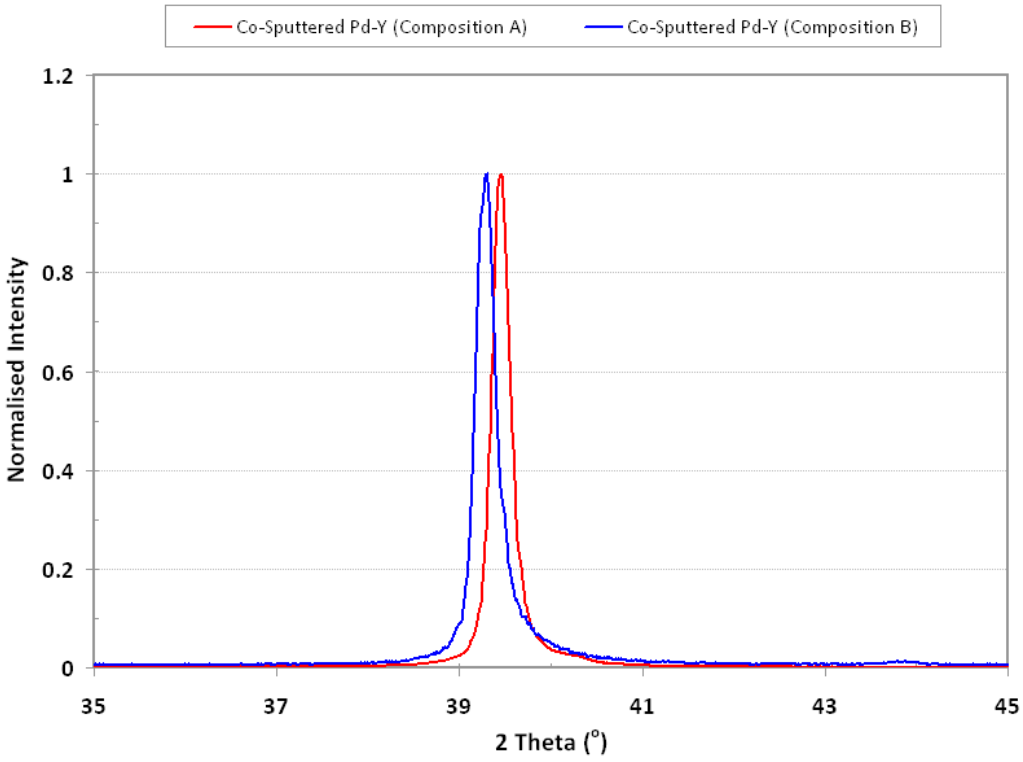

Figure 9.23 – Variation in FCC [111] diffraction peak between Batch A and Batch B thin films

Closer inspection of the [111] peaks reveals a small difference in [111] reflection angle between the two batches. In a similar manner to the bulk alloys, accurate compositions were determined via comparison with the data of Harris & Norman [42] using the linear equation,

$$y = (7.357 * 10^{-3})x + 3.8896 \qquad \textit{Eqn 9.5}$$

where *y* is the measured lattice parameter (Å) and *x* is the atomic concentration of Y. Both the XRD data and calculated alloy compositions are listed in Table 9.5 and are compared to those of the bulk Pd-Y alloys in Figure 9.24.

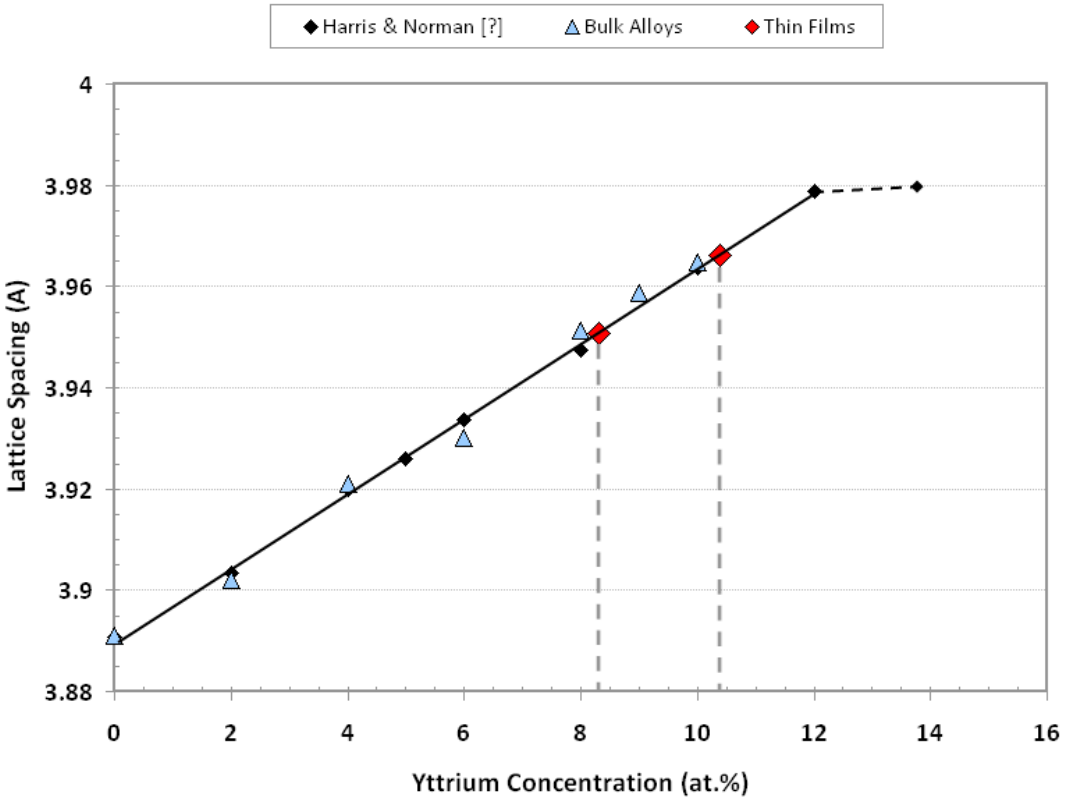

Figure 9.24 – The lattice spacings of the co-sputtered Pd-Y thin films compared to bulk alloy values

Table 9.5 – Composition of the sputtered Pd-Y thin films calculated using [111] diffraction data

Sample	*d* - spacing (Å) ±0.0005	Lattice Parameter (a) (Å) ±0.0005	Calculated Composition (at. %) ± 0.07
Batch A	2.2810	3.95081	$Pd\text{-}Y_{8.31}$
Batch B	2.2898	3.96605	$Pd\text{-}Y_{10.38}$

9.2.2 – Film Adhesion, Integrity and Thickness

In order to assess both the film quality, in terms of adhesion and defect level, and the thickness of the films, non-porous 316L stainless steel tokens were coated during the deposition of both Batch A and Batch B membranes.

The coverage and defect level of the as-deposited films were assessed by SEM and confocal laser microscopy. Macroscopic defects were not detected for either Batch A or Batch B samples, thus it was concluded that any defects within the composite Pd-Y membranes would, predominantly, be due to the topography of the substrate surface rather than the deposition process. The surface topography of a typical defect-free Pd-Y film deposited on non-porous stainless steel is shown in Figure 9.25.

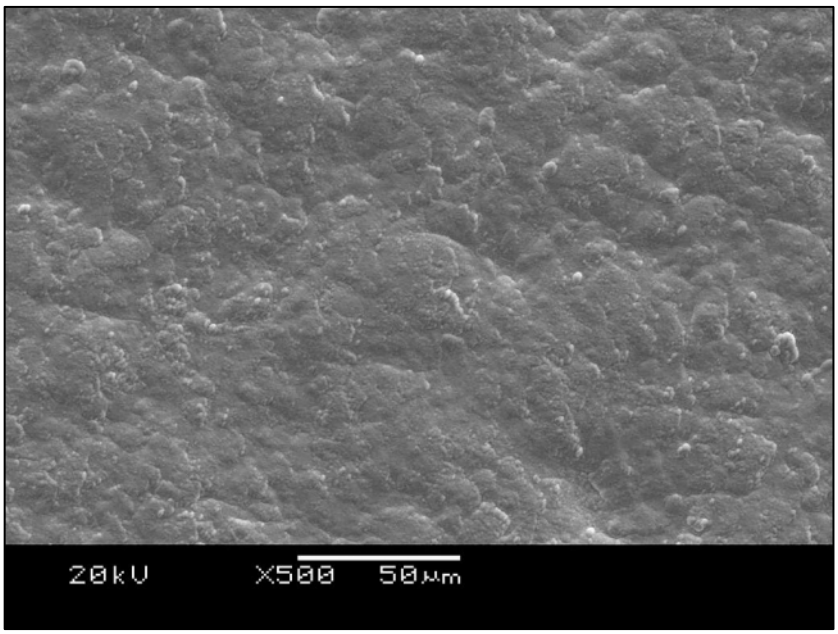

Figure 9.25 – SEM image of the surface topography of a typical defect-free solid solution Pd-Y sputtered film

The adhesion of the Pd-Y films was assessed using a simple peel test. The as-deposited films demonstrated excellent adhesion to the non-porous stainless steel tokens, thus indicating that the pre-deposition cleaning procedures were effective. Interestingly however, upon exposure

to hydrogen at room temperature, the as-deposited films delaminated from the stainless steel tokens and failed in strips, replicating the underlying surface topography, particularly around the edges of the sample (Figure 9.26).

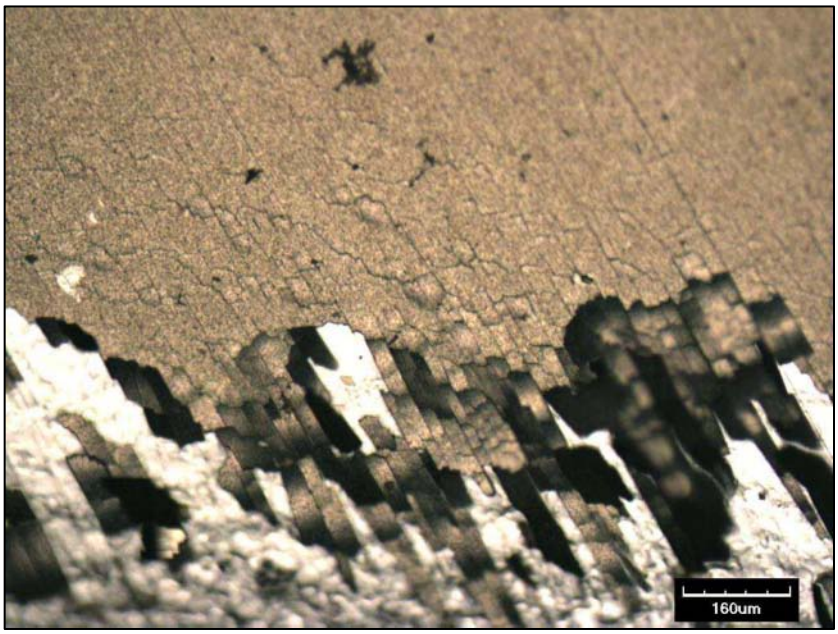

Figure 9.26 – Effect of hydrogen absorption at room temperature on as-deposited thin film Pd-Y_8.

The miscibility gap in both Batch A and Batch B Pd-Y compositions is expected to be closed at room temperature, thus preventing β-hydride phase formation. The failure and delamination of the as-deposited Pd-Y films therefore, is presumably due to the high hydrogen solubility and associated lattice expansion. The hydrogen solubility measurements performed on bulk Pd-Y_8, described previously in Section 9.1.2, reveal considerable solubility at ~ 50°C with a H / M ratio of > 0.4 observed at an applied pressure of just 100 kPa.

In order to prevent film delamination it was found to be necessary to anneal the as-deposited Pd-Y films under vacuum (10^{-5} mbar) at 400°C for 6 hrs prior to hydrogen exposure. The annealed Pd-Y films remained defect-free and continued to demonstrate good adhesion with repeated hydrogen exposure and thermal cycling. Accordingly, both the Batch A and Batch B

composite membranes, which are discussed further in Section 11, were annealed under the above conditions prior to any gas permeation measurements.

An unanticipated beneficial aspect of the hydrogen induced delamination was that it facilitated accurate thickness measurements. Typically, the films delaminated in uniform strips replicating the underlying surface scratches and topography, thus resulting in well defined film edges which are easy to analyse using a confocal laser microscope (Figure 9.27).

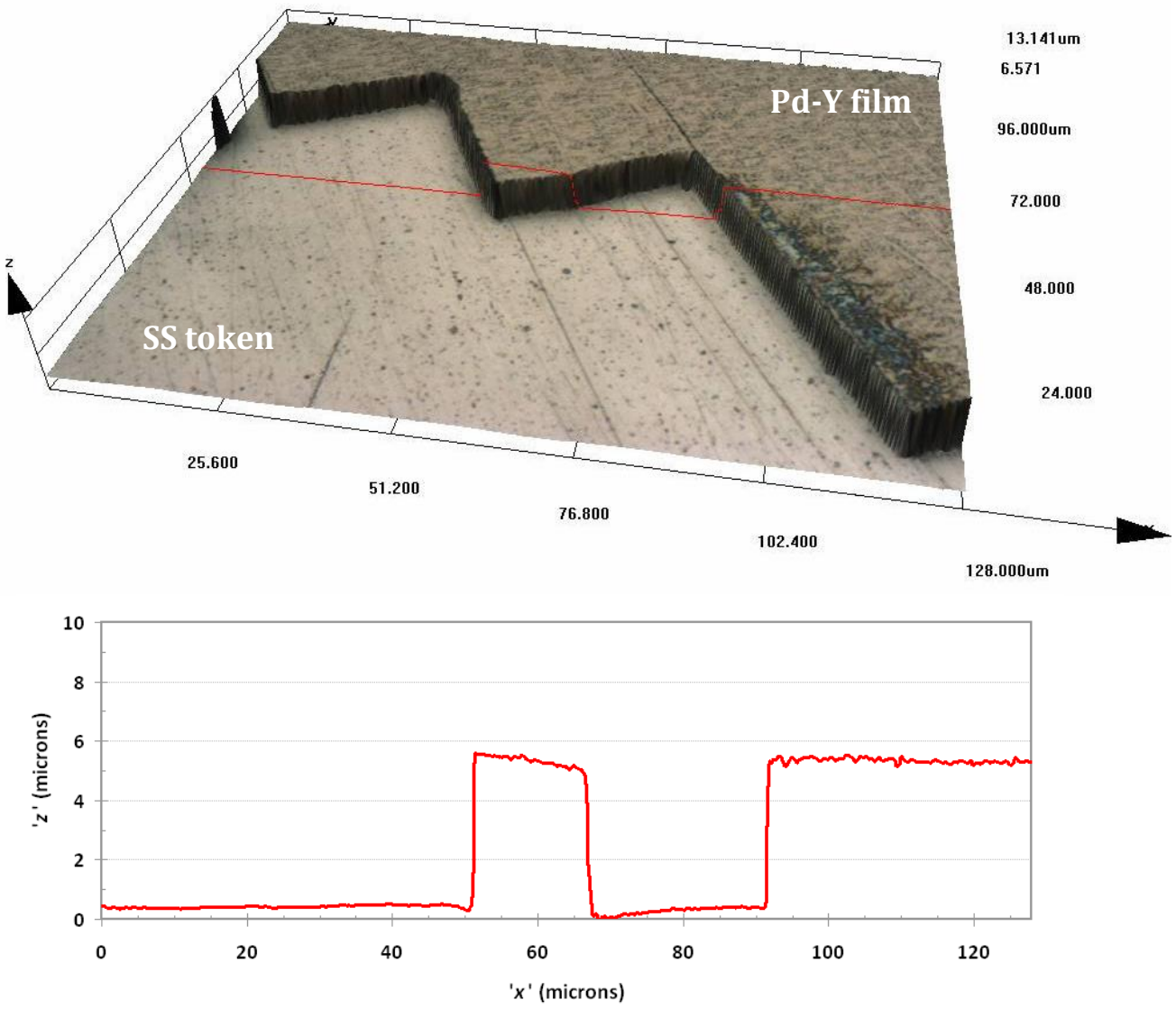

Figure 9.27 – Confocal laser image with line profile of a partly delaminated Batch A Pd-Y film on a SS token

The thickness analysis carried out using the confocal microscope is particularly accurate, with a *z* resolution of ± 10 nm. The average thickness, over 10 different regions, were found to be 5.06 ± 0.11 µm and 4.90 ± 0.08 µm for the Batch A and Batch B films, respectively.

9.2.3 – Projected Hydrogen Flux

The hydrogen permeability of free-standing Pd, Pd-Ag and Pd-Cu thin films has been shown to correspond to that in bulk alloys [84, 85]. Therefore, assuming similar behaviour in Pd-Y alloys, the hydrogen flux across both film compositions may be estimated. Considering that the calculated compositions of the Batch A and Batch B thin films are within 0.2 at.% of the Pd-Y_8 and Pd-Y_{10} bulk alloys respectively, it is reasonable to apply the permeability determined in the bulk alloys to the thin films directly. Therefore, under the temperature and pressure conditions of 400°C and 138 kPa as specified by the US DoE [8], both films, at least in theory, have the potential to exceed the 2015 flux targets (Figure 9.28).

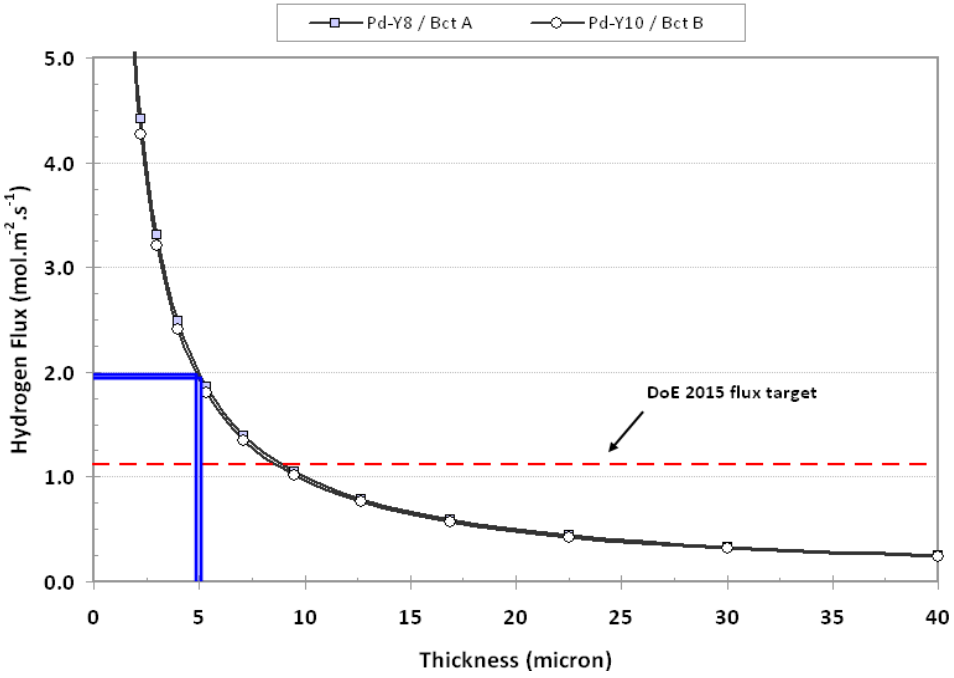

Figure 9.28 – Maximum membrane thickness for Pd-$Y_{8\ \&\ 10}$ membranes to meet the DoE 2015 flux targets

Section 10 – Porous Substrate

10.1 – Introduction

The porous substrates used throughout this work were sintered austenitic 316L stainless steel (PSS), purchased from Mott Corp, replicating those used by numerous authors for Pd and Pd-Ag composite membranes. Thus, direct comparisons can be drawn between the experimental results gathered and those reported in the literature. The substrates were supplied in disc form (21 mm diameter, 1 mm thickness) fabricated by stamping from sheet material and were cleaned with acetone in an ultra-sonic bath prior to any analysis.

10.2 – Structure and Topography

10.2.1 – As-Received PSS

The PSS substrates had a designated media filtration grade of 0.1 µm, which is defined by the manufacturer, as the minimum size of a hard spherical particle retained by the interconnected porosity [135]. The surface topography of an as-received PSS substrate is shown in Figure 10.1.

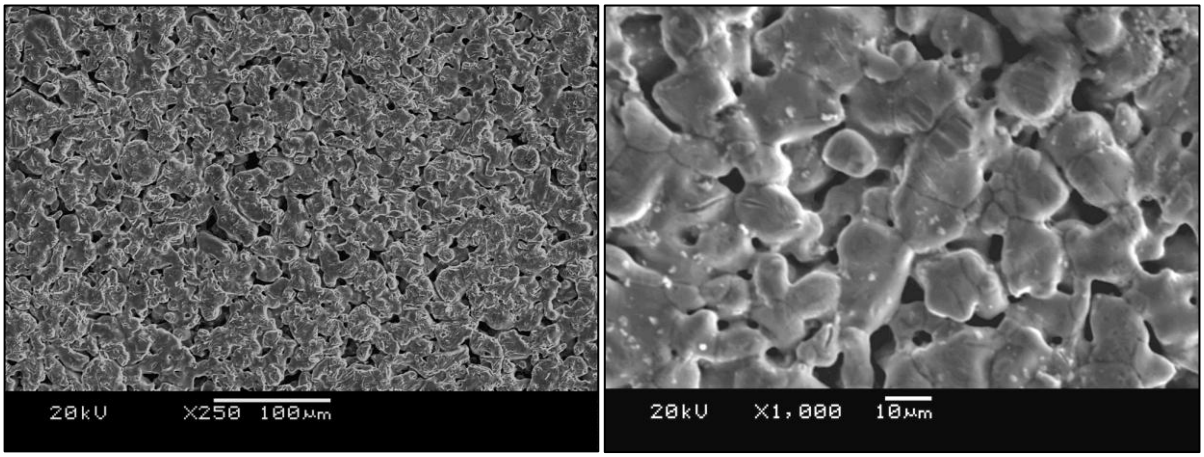

Figure 10.1 – SEM image of the surface topography of as-received 0.1 µm PSS substrates

Both the surface pore diameter and pore depth ranged between 10 and 25 µm (Figure 10.2), with an average of ~ 15 µm which is in good agreement with those reported in the literature [136]. The average density was determined as 6.34 g.cm^{-3} which, compared to the value for dense 316L stainless steel of 7.99 g.cm^{-3} [185], suggests an overall volume porosity of ~ 20 %.

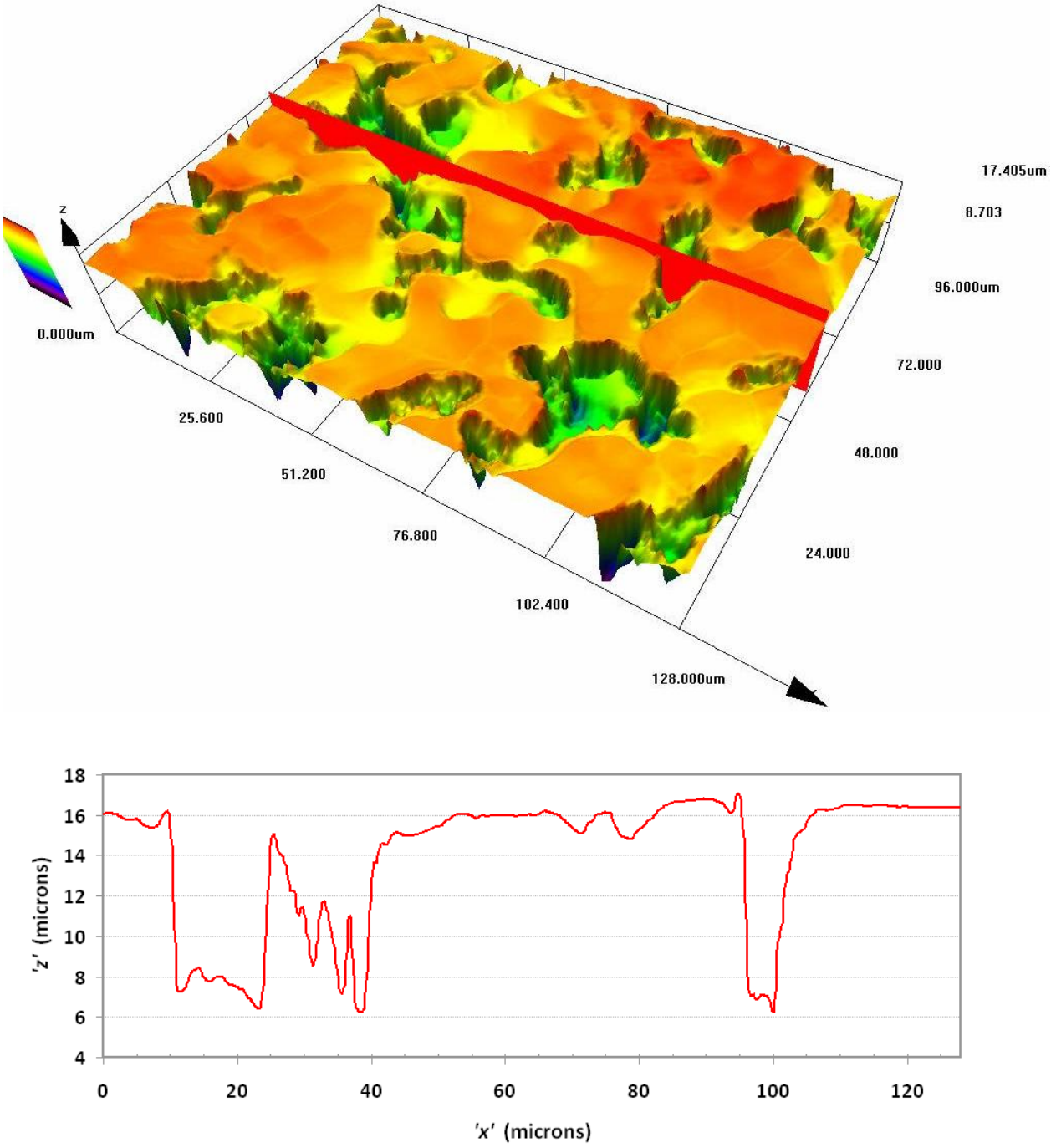

Figure 10.2 – Confocal laser image of as-received PSS surface with line profile clearly showing pores of ~20µm

10.2.2 – Stainless Steel Coated PSS

The unsuitability of as-received 0.1 µm PSS, the finest commercially available grade, as a substrate for thin Pd based films was demonstrated by depositing stainless steel layers with successively greater thicknesses and observing the resultant surface topography. Stainless steel layers of up to 20 µm were deposited. As would be expected, there is a progressive reduction in surface pore size with increasing deposition thickness (Figure 10.3).

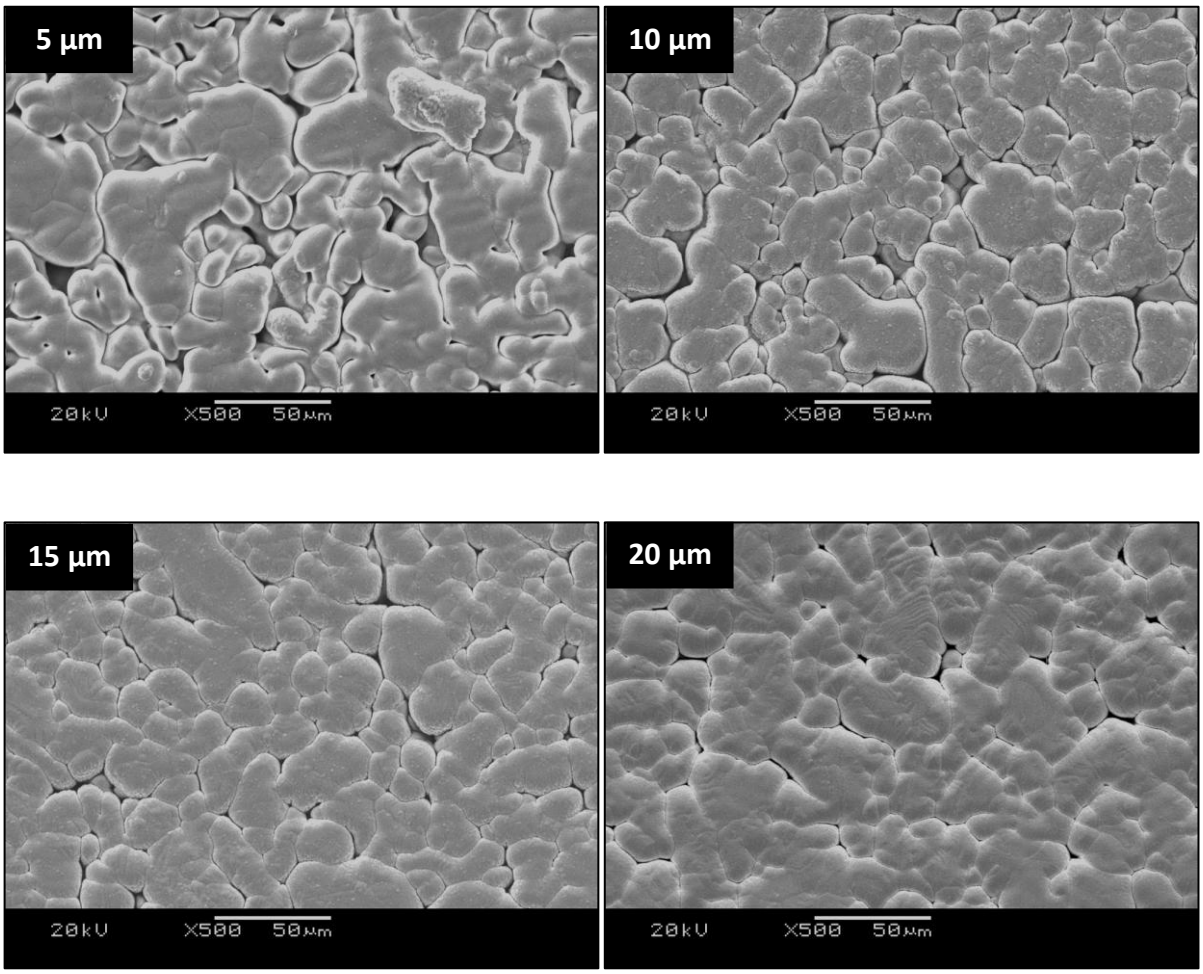

Figure 10.3 – SEM images showing the effect of SS coating thickness on the surface pore size of as-received PSS

When compared to the as-received surface described in the previous section (Figure 10.1), it is clear that a 5 µm deposited film has little effect on the surface pore size, whilst even after 20 µm numerous pores persist. The progressive reduction in surface pore size with increasing

deposition thickness suggests that a fully continuous, pore-free film may be achieved with a layer approximately 40 µm in thickness. Considering that the average surface pore size of the as-received substrates is ~ 15 µm, this is in excellent agreement with the approximate 3 times film / pore size rule proposed by Ma [126] in order to achieve a defect-free layer.

10.2.3 – Laser Melted PSS

Both as-received and stainless steel coated substrates were surface melted with an excimer laser. As described previously in Section 8.2.4, although the use of lasers is relatively common for sintering metal powders [186, 187], as far as we are aware, there is no preceding literature that describes the use of lasers to melt the near-surface region of porous metals. Accordingly, initial experiments focussed on establishing a set of general operating parameters, from which small adjustments could be made to optimise the final surface. As described in Section 8.2.4, the parameters that were kept constant throughout, were the laser frequency (50 Hz), beam dimension / pulse time (12 ns), percentage overlap (50 %) and path direction. The only variables were: the laser energy, or fluence which was varied between 400 and 3000 $mJ.cm^{-2}$; the number of pulses (100 – 400); and the initial surface condition, *i.e.* either as-received or coated with 5, 10 or 15 microns of stainless steel.

The surface topography of various laser melted substrates, initially in the as-received condition, are shown in Figure 10.4. In general, both the average surface pore size and surface roughness of the PSS substrates were found to decrease with increasing laser fluence.

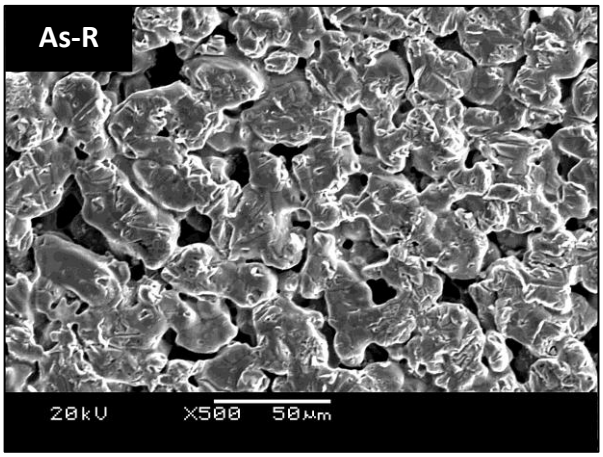
As-R
20kV X500 50µm

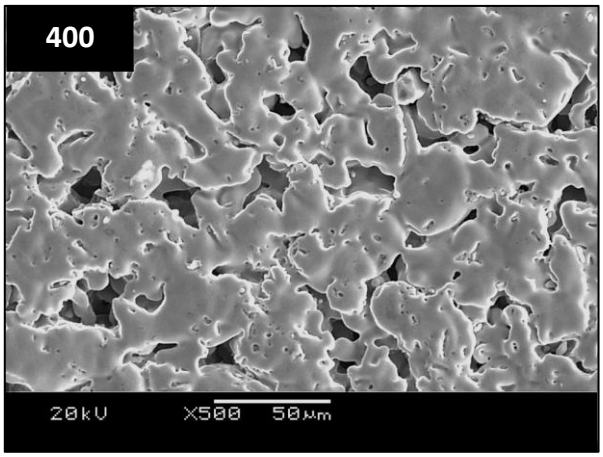
400
20kV X500 50µm

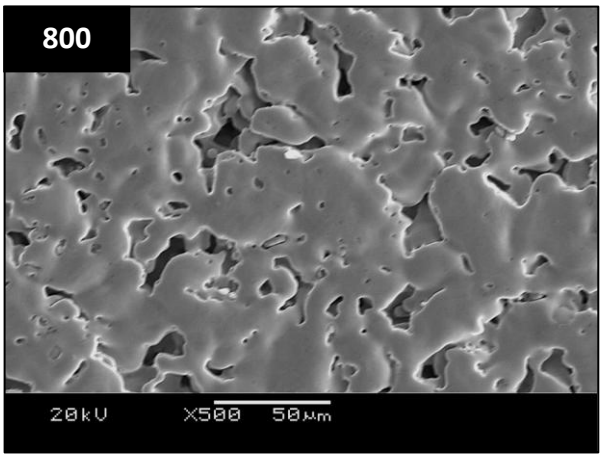
800
20kV X500 50µm

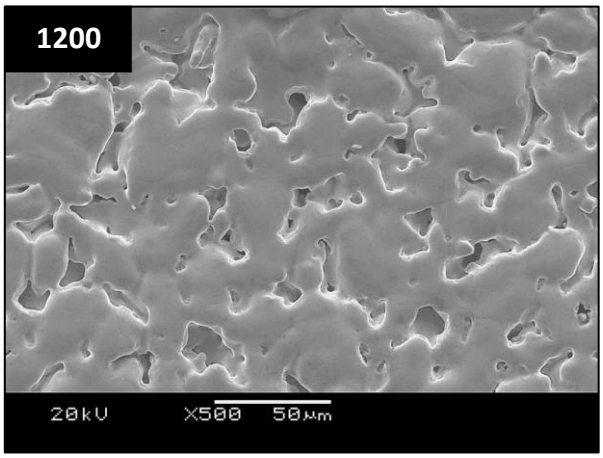
1200
20kV X500 50µm

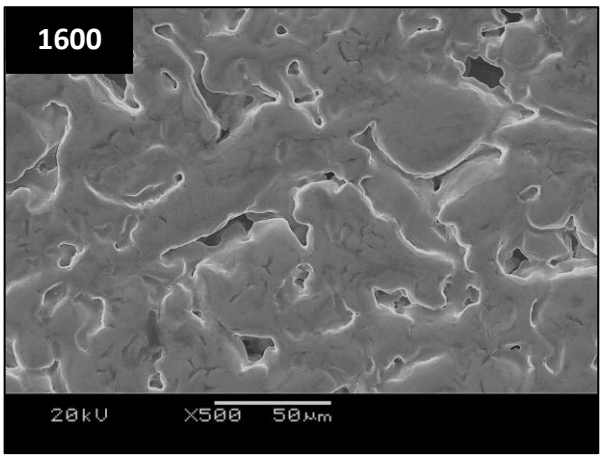
1600
20kV X500 50µm

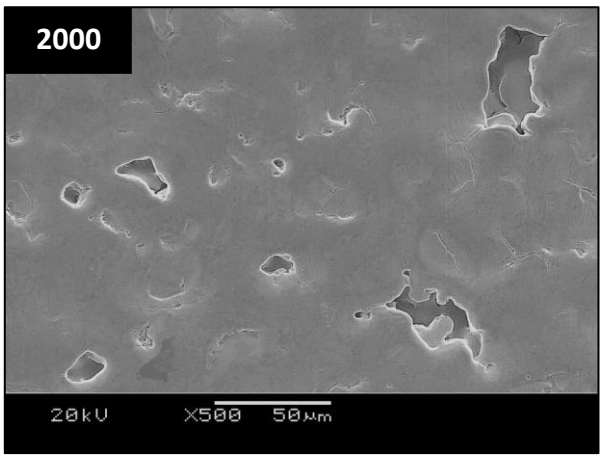
2000
20kV X500 50µm

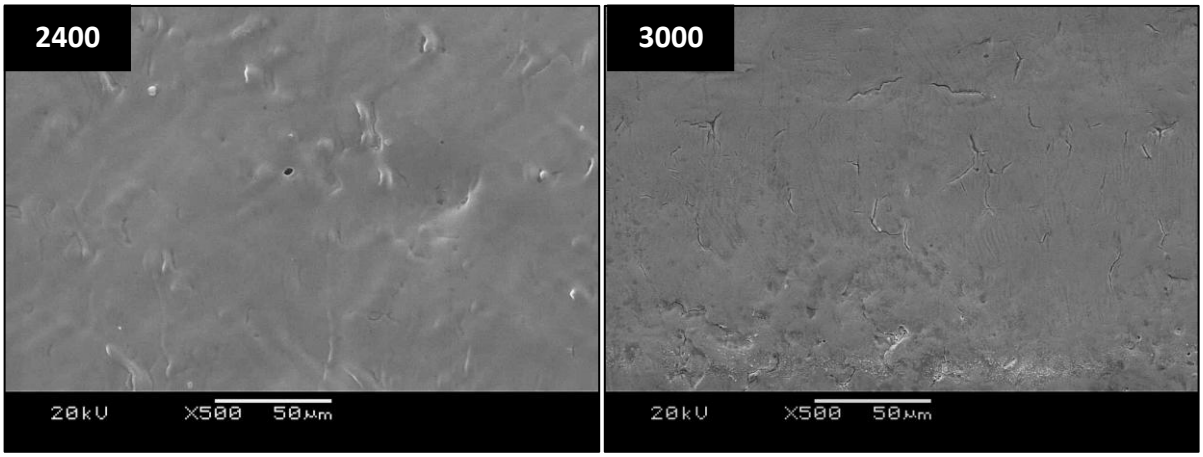

Figure 10.4 – A series of SEM images showing the effect of laser fluence (mJ.cm^{-2}) on the surface topography of PSS. All discs were melted with 100 pulses in the as-received starting condition.

At low fluences (< 1200 mJ.cm^{-2}), the effect of the laser is largely confined to the upper most regions of the stainless steel particles, presumably due to a low melt depth. The spreading effect of the laser melting leads to an effective increase in particle surface area, although the net result is mostly a reduction in the number of pores, rather than in the average pore size. As the fluence is increased, and hence the melt depth, there is progressively less distinction between individual SS particles. At a fluence of 2000 mJ.cm^{-2} the surface is largely continuous with a number of large pores 10 to 50 µm in diameter. As the fluence is increased further both the number and size of the remaining pores is reduced until, at 3000 mJ.cm^{-2}, the surface is virtually continuous and appears fully dense. Although the surface roughness is reduced sufficiently for the deposition of a defect-free Pd-Y film, the dense SS layer would act as a barrier to hydrogen transport; NB the hydrogen permeability of austenitic 316 SS is over 3 orders of magnitude lower than that of Pd-Y [188]. Although reducing the fluence does produce a porous surface, the melting mechanism preferentially closes the small pores. The remaining pores are too large to be adequately covered by a 5 µm deposited film.

In contrast to the fluence, increasing the number of pulses was found to have little effect on the average pore size. Rather, the predominant effect appeared simply to be an increase in the degree of surface oxidation, suggesting a higher melt temperature (Figure 10.5). Considering the laser melting procedure was performed under air, some degree of surface oxidation would be expected. The surface oxide was identified as a mixture of $FeCrO_4$, Fe_3O_4 and Cr_2O_3 using Raman Spectroscopy. Excimer laser processing of dense 316 stainless steel has previously been shown to induce substantial mobility of Cr in the melted layer, leading to a Cr rich surface oxide [189]. In addition, Cr_2O_3 has been proposed as a desirable oxide phase for use as an interface layer in Pd-PSS composite membranes due to its high chemical stability under hydrogen [108, 147].

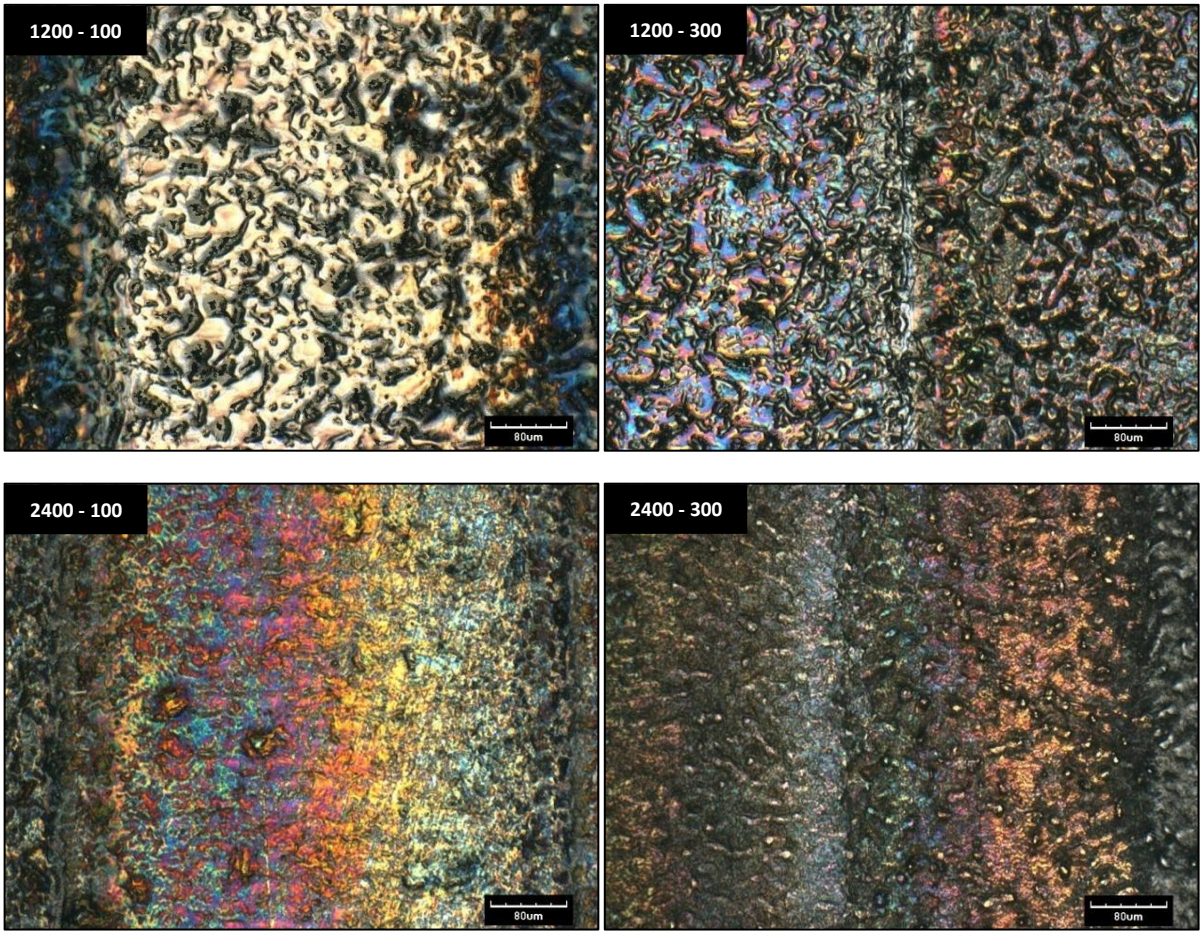

Figure 10.5 – Confocal laser microscope image showing the effect of laser pulse number on the surface oxidation of as-received PSS. The legend gives the fluence ($mJ.cm^{-2}$) and the number of pulses.

On inspection at high magnifications however, increasing the number of pulses from 100 to ≥ 300 was found to induce a network of sub-micron cracks within the melted layer (Figures 10.6 to 10.8). Crack formation was observed in all cases using either 300 or 400 pulses where the fluence was greater than 1200 mJ.cm^{-2}, although cracking was more prevalent at higher fluences. Importantly however, the crack width (< 1 µm) remained relatively independent of the fluence, whilst both the crack length and number increased with the fluence. The formation of micro-cracks in austenitic stainless steel is relatively common during pulsed laser welding and is a result of the rapid cooling [190]. Austenitic stainless steel is known to lack tensile strength between the solidus temperature and 980°C [190], hence, stresses arising from thermal contraction tend to cause crack formation within the cooling melt layer.

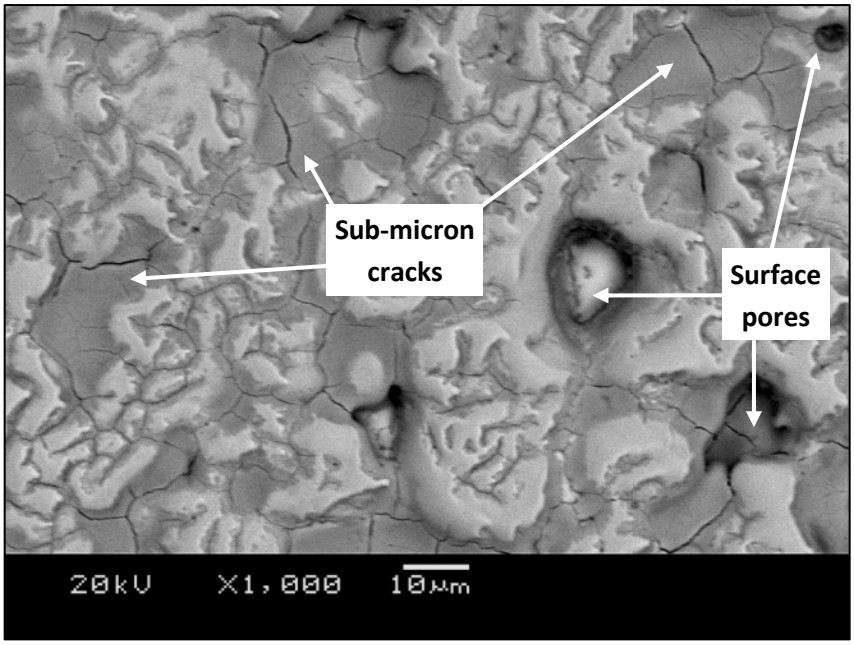

Figure 10.6 – SEM image showing micro-cracks and open pores within the melted layer formed on as-received PSS using a laser fluence of 1200 mJ.cm^{-2} and 300 pulses.

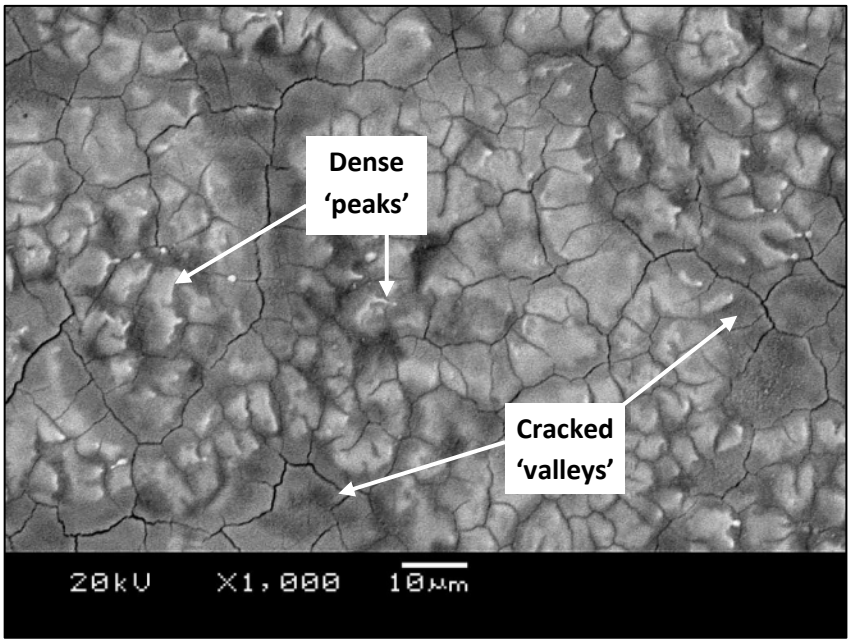

Figure 10.7 – SEM image showing micro-cracks and open pores within the melted layer formed on as-received PSS using a laser fluence of 2400 mJ.cm^{-2} and 300 pulses.

Figures 10.6 and 10.7 clearly demonstrate the effect of laser fluence on both the degree of cracking and the surface pores. An interesting parallel between the low and high fluence samples is the crack location. On both surfaces, the cracking is predominantly located within the flat 'valleys'. At higher magnifications, the full extent of the cracking in these areas is revealed (Figure 10.8). The largest cracks extend up to 100 µm in length, whilst not exceeding 1 µm in width. Between these large cracks are a network of smaller cracks < 500 nm in width.

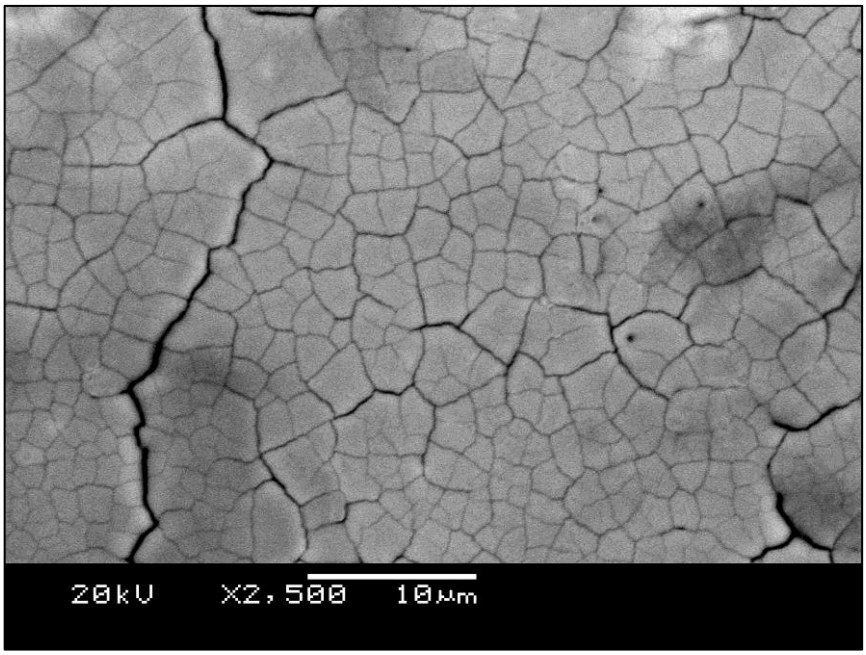

Figure 10.8 – SEM image showing the network of micro-cracks formed on as-received PSS melted with a laser fluence of 3000 mJ.cm^{-2} and 300 pulses.

In terms of crack density and surface roughness, no discernible difference was observed between fluence levels of 2400 to 3000 mJ.cm^{-2}. The minimum thickness rule proposed by Ma et al [126] recommends a film thickness 3 times greater than the surface pore size. This suggests therefore, that the sub-micron cracks exhibited by the high fluence-high pulse surfaces (Figures 10.7 and 10.8) are likely to be completely covered by the deposition of 5 µm Pd-Y films, thus producing a defect-free membrane. However, the peak and valley type topography of the substrates are a potential source of defects, particularly if they possess high angle sides. This adverse surface topography was largely reduced by pre-coating the substrates with ≥ 10 µm stainless steel by magnetron sputtering (as described in Section 8.2.2). It is interesting to note that the deposition of < 10µm SS was found to have minimal effect on the surface topography. The sputtered SS coating reduced the surface roughness and increased the uniformity of the melted surfaces, without adversely affecting the micro-crack formation (Figure 10.9).

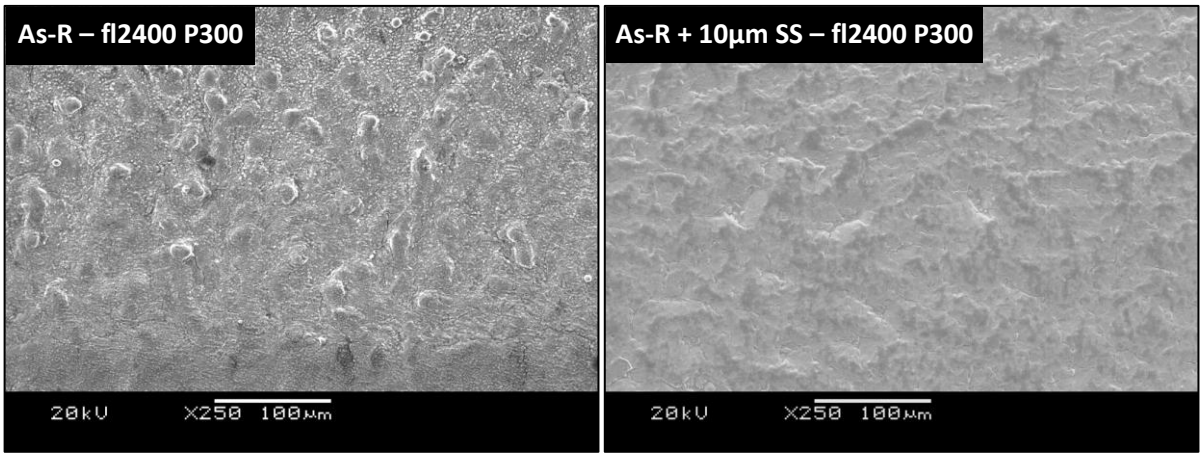

Figure 10.9 – SEM image showing the effect of SS coating prior to laser melting on final surface topography.

In summary, a desirable surface for Pd-Y thin film deposition has been produced via near surface melting of PSS with an excimer laser. The optimum surface for deposition was achieved using a PSS substrate pre-coated with ≥ 10 µm SS, which was then melted using a fluence of 2400 – 3000 mJ.cm^{-2} and 300 – 400 pulses. The surface topography produced using these parameters is compared to that of as-received PSS in Figure 10.10, which clearly emphasises the extent to which the laser melting process successfully eliminates the large, un-coatable, surface pores.

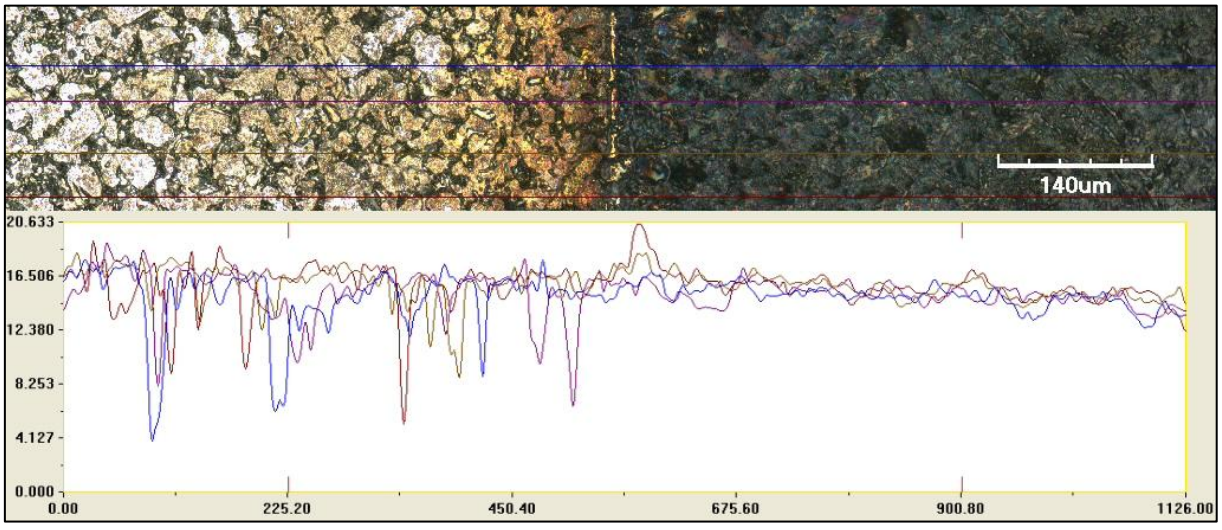

Figure 10.10 – Confocal laser microscope image and associated surface profile showing the topography of as-received PSS (left) and laser-melted PSS (right).

10.3 – Gas Permeability

Hydrogen transport across a porous substrate with an average pore radius of greater than 1.5 nm will be a combination of viscous, or Poiseuille flow and Knudsen diffusion [173]. As described in the previous section, the typical surface pores size of as-received PSS is 10 - 15 µm, whilst the surface cracking observed on the laser melted substrates ranges between 0.5 - 1 µm. Therefore the total hydrogen flux, *J*, across both substrates types may be expressed as the sum of Poiseuille flow and Knudsen diffusion,

$$J_{Total} = \left[\frac{2}{3}\frac{\varepsilon\, r}{\tau}\frac{1}{l}\left(\frac{8}{\pi\, R\, T\, M}\right)^{0.5}\right] + \left[\left(\frac{1}{8}\frac{\varepsilon}{\tau\,\eta}\frac{r^2}{R\, T\, l}\right) P_{av}\right] \Delta P \qquad \textit{Eqn 10.1}$$

where ε is the porosity, r the average pore radius, τ the tortuosity, M and η the molecular mass and viscosity of the gas respectively, and R T and l denote the gas constant, absolute temperature and substrate thickness. A full derivation of Eqn 10.1 is given in Section 5.3. This relationship is usually simplified to give the linear expression,

$$J_{Total} = [\, \alpha_K + (\beta_V\, P_{av}) \,]\, \Delta P \qquad \textit{Eqn 10.2}$$

where α_K and β_V denote the Knudsen and Poiseuille permeation coefficients respectively. Assuming a linear pressure drop across the substrate, the values of α_K and β_V can be calculated using the experimentally determined values of *J*, P*i* and P*ii*. The α_K and β_V coefficients not only allow the calculation of the geometrical factors ε, r and τ of the substrate, they also

permit the gas flux to be predicted under any conditions of both temperature and pressure. Therefore, in order to fully characterise the hydrogen transport across a composite membrane, it is essential to establish values of the substrate α_K and β_V coefficients.

10.3.1 – As-Received PSS

Room temperature hydrogen permeability measurements were performed on a large number of as-received PSS discs. Although each disc was taken from the same batch number and demonstrated almost identical surface pore sizes, the hydrogen permeance was found to vary widely between discs. It should be noted that, within the field of porous separation membranes, it is the convention to quantify gas transport in terms of a permeance *i.e.* $mol.m^{-2}.s^{-1}.Pa^{-1}$, rather than as a thickness-independent permeability as used for dense membranes. Therefore, throughout this work, molecular gas transport through porous structures is given as a permeance. The room temperature hydrogen permeance of 4 as-received PSS discs are shown in Figure 10.11. Discs 1 and 2 exhibited the lower and upper observed limits respectively, whilst Discs 3 and 4 were more typical of the range.

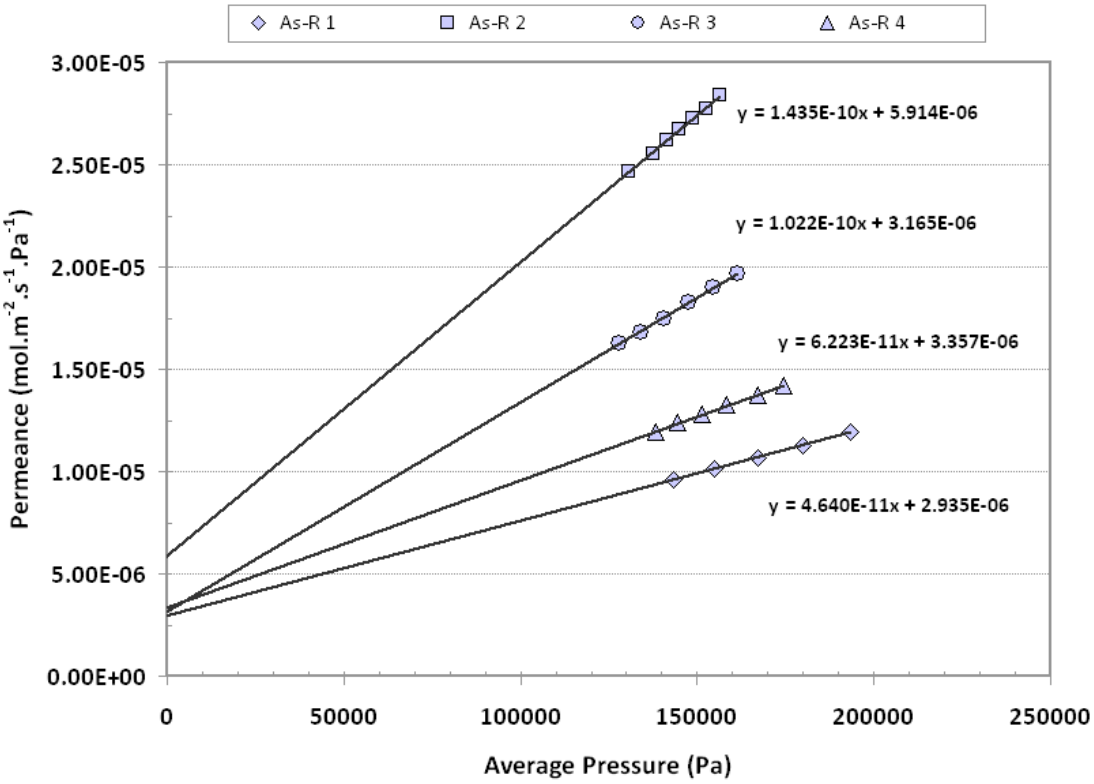

Figure 10.11 – Variation in room temperature hydrogen permeance through as-received 0.1 µm PSS substrates

The α_K and β_V coefficients of each disc are displayed within Figure 10.11. When comparing Disc 1 and Disc 2, the low and high extremes, there is an approximate factor of two difference between α_K values whilst the β_V value of Disc 2 is more than three times greater than in Disc 1. The net result is that Disc 2 achieves a hydrogen flux 2.77 times greater than Disc 1. In order to qualify the observed differences it is necessary to calculate the geometrical factors of each substrate.

For simplicity, the numerical parameters in Eqn 10.1 may be combined to give the following expressions for α_K and β_V,

$$\alpha_K = 1.06\,\frac{\left(\frac{1}{l}\right)\left(\frac{\varepsilon}{\tau}\right)r}{\sqrt{RTM}} \qquad \textit{Eqn 10.3}$$

$$\beta_V = 0.125\ \frac{\left(\frac{1}{l}\right)\left(\frac{\varepsilon}{\tau}\right)r^2}{\eta RT} \qquad \textit{Eqn 10.4}$$

Of the terms in Equations 10.3 and 10.4, *R*, *T* and *M* are constants whilst α_K and β_V are determined experimentally. Therefore, an expression for the average pore size, *r*, can be derived [88, 174],

$$r = \left[8.48\,\eta\,\left(\frac{RT}{M}\right)^{0.5}\right]\left(\frac{\beta_V}{\alpha_K}\right) \qquad \textit{Eqn 10.5}$$

The calculated geometrical factors ε, τ and *r* of Discs 1 – 4 are listed in Table 10.1. Comparison of the geometrical factors clearly demonstrates that the average pore size across the entire disc (0.83 – 1.7 μm) is significantly lower than the average pore size at the surface (10 – 15 μm). This is in good agreement with Mardilovich et al [82] who used a mercury intrusion method to determine the average pore size of various PSS grades. The average pore size of Mott Corp 0.1 μm PSS, as used in the present work, was approximately 2 μm.

Assuming a mean free path (λ) of hydrogen at atmospheric pressure and 0°C of 110.6 nm [23], the Knudsen number K_n, which is the ratio of λ to mean pore diameter, can be determined. The Knudsen numbers of all discs are listed in Table 10.1 and fall within the transition region between Poiseuille flow and Knudsen diffusion (0.01-10), thus confirming both transport mechanisms will contribute significantly to the overall hydrogen flux [163].

Table 10.1 – Comparison of the hydrogen permeance coefficients and geometrical factors in as-received 0.1μm PSS substrates

Sample	α_K (mol.m^{-2}.s^{-1}.Pa^{-1})	β_V (mol.m^{-2}.s^{-1}.Pa^{-2})	r (μm)	ε/τ	*Kn*	Flux @ RT & 1 bar ΔP (mol.m^{-2}.s^{-1})
Disc 1	2.935 x10^{-6}	4.640 x10^{-11}	0.415	0.471	~ 0.133	0.980
Disc 2	5.914 x10^{-6}	1.435 x10^{-10}	0.637	0.618	~ 0.087	2.717
Disc 3	3.165 x10^{-6}	1.022 x10^{-10}	0.851	0.248	~ 0.065	1.840
Disc 4	3.357 x10^{-6}	6.223 x10^{-11}	0.486	0.459	~ 0.114	1.257

Interestingly, the disc with the largest average pore size, Disc 3, does not demonstrate the highest flux or permeance. An explanation for this, perhaps counter-intuitive, finding may be deduced from the ratio of porosity (ε) to the tortuosity (τ). The porosity is generally defined as the fraction of the media in any particular plane that is open space, whilst the tortuosity is a factor accounting for the increase in distance travelled when compared to the total substrate thickness, due to the tortuous nature of the structure. Neither of these parameters are directly measureable, thus average values across the whole substrate must be calculated from the experimental α_K and β_V values.

The calculated ε / τ ratios of Discs 1 – 4 are listed in Table 10.1. The values for Discs 1, 2 and 4 are all similar to the average pore size *r*, whilst the value for Disc 3 is considerably lower. It is a reasonable assumption that average pore size *r* is closely correlated to average porosity ε, which suggests that Discs 1, 2 and 4 possess similar values of tortuosity. This would imply that Disc 3, although possessing the largest average pore size, has a considerably more tortuous structure, thus inhibiting the observed hydrogen permeation. The variation in permeance between nominally similar porous substrates gives further support for the need to

independently assess the hydrogen transport characteristics of each component of a composite membrane.

10.3.1.1– The Effect of Temperature

In order to quantify the relative contribution of the substrate towards the total resistance of a composite membrane, an understanding of the effect of temperature is required. From Equation 10.1, it is clear that hydrogen flux through the porous substrate has a complex relationship with temperature. The α_K coefficient is approximately proportional to $T^{-0.5}$, whilst the β_V coefficient is dependent on both the temperature and the gas viscosity, which in turn is temperature dependent. Within the range of temperature and pressure conditions experienced by a composite membrane during operation, the gas viscosity is independent of pressure and is proportional to $T^{0.5}$ [172]. The overall temperature dependence of β_V would therefore be expected to be approximately proportional to $T^{-3/2}$.

Considering that the Knudsen number K_n of each disc falls within the Poiseuille / Knudsen transition region, the total flux is likely to be due to a combination of α_K and β_V. Therefore, the precise temperature dependence of permeation in a particular porous substrate will depend on the relative contributions of α_K and β_V, which in turn are dynamically dependent on r, ε, τ, η, applied pressure and temperature.

Assuming that the geometrical factors are constant with respect to temperature, Equations 10.3 and 10.4 can be applied to calculate the values of α_K and β_V at any given temperature. The calculated values of α_K and β_V are then inserted into Eqn 10.2, thus enabling the hydrogen flux to be calculated under any given conditions of temperature and pressure. Using the geometrical factors established at room temperature and the hydrogen viscosity data reported

by Assael et al [191], the projected variation in hydrogen flux with temperature through Disc 3 has been calculated. The projected flux is compared to experimentally determined values in Figure 10.12.

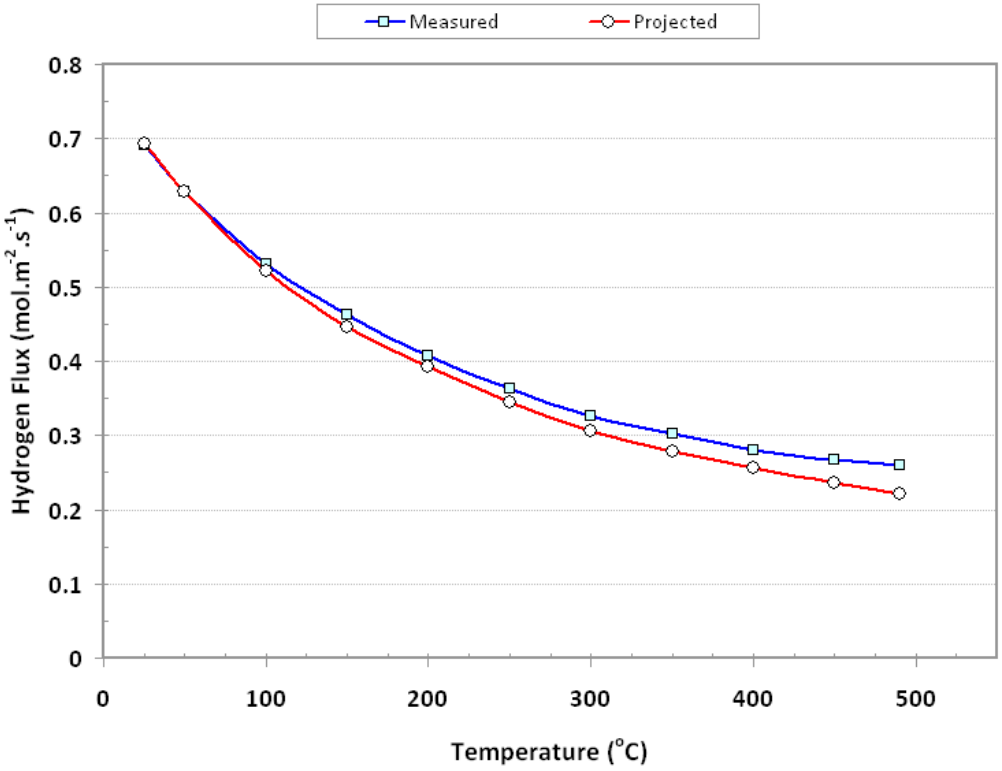

Figure 10.12 – Comparison of projected hydrogen flux (calculated using the experimentally determined geometrical factors listed in Table 10.1) through as-received PSS Disc 3 with experimentally measured values

Figure 10.12 clearly shows significant divergence between the calculated and measured traces. Therefore, any projected high temperature flux based purely on room temperature α_K and β_V coefficients would be invalid. In order to establish the source of the disparity between measured and calculated values, the α_K and β_V coefficients were measured at 490°C and are compared to those calculated using Equations 10.3 and 10.4, in Table 10.2.

Table 10.2 – Comparison of the measured and calculated α_K and β_V coefficients of as-received PSS Disc 3.

	Measured @ RT	Measured @ 490°C	Calculated @ 490°C
α_K	3.165 x10^{-6}	2.852 x10^{-6}	1.975 x10^{-6}
$\alpha_K \frac{\varepsilon}{\tau} r$	0.211	0.304	0.211
β_V	1.022 x10^{-10}	2.002 x10^{-11}	2.074 x10^{-11}
$\beta_V \frac{\varepsilon}{\tau} r^2$	0.179	0.173	0.179

As expected, both the α_K and β_V coefficients were found to decrease with increasing temperature. The projected β_V coefficient is in good agreement with the measured value, whilst the α_K coefficient is significantly lower than the measured value, hence the projected flux is lower than the measured flux.

Comparison of the geometric factors (Table 10.2) reveals the source of the deviation. The projected α_K and β_V coefficients were calculated assuming the geometrical factors remained constant with temperature. Although this appears to be valid for the β_V geometric factor $\frac{\varepsilon r^2}{\tau}$, hence the projected β_V coefficient is in good agreement with the measured value, the α_K geometric factor $\frac{\varepsilon r}{\tau}$ increased significantly. The reason for this is unclear, however there are several possibilities.

Firstly; the assumption that the geometrical factors remain constant with temperature is invalid. Over the measured temperature range, the thermal expansion coefficient of 316 SS correlates to a linear expansion of 0.81 %. The net result on ε, τ and r is difficult to propose, however it is unlikely to account for the 44 % increase in $\frac{\varepsilon r}{\tau}$. In addition, the β_V geometrical

factors do not demonstrate the same deviation. Indeed, the 3.4 % reduction observed in β_V geometrical factors is more likely a result of the 2.4 % volume expansion of the SS particles. Therefore, although there will undoubtedly be some reduction in pore size with increasing temperature, it is unlikely to account for the large increase observed in the α_K coefficient.

Secondly; Equations 10.3 and 10.4 are largely based on the kinetic gas model which assumes ideal gas behaviour.

Thirdly; the derivation of α_K does not account for the diffuse scattering of a gas molecule after a collision with a pore wall. To account for this collision characteristic, some authors use an additional geometric term, the reflection factor θ, which only applies to the α_K coefficient [22]. In light of this, the projected α_K coefficient was re-calculated using a modified geometrical factor, in order to account for the reflection factor. It was assumed that the effect of the reflection factor was linear with temperature. Using the original calculated β_V coefficient and the θ-modified α_K coefficient ($\alpha_{K\theta}$) the projected flux was recalculated (Figure 10.13).

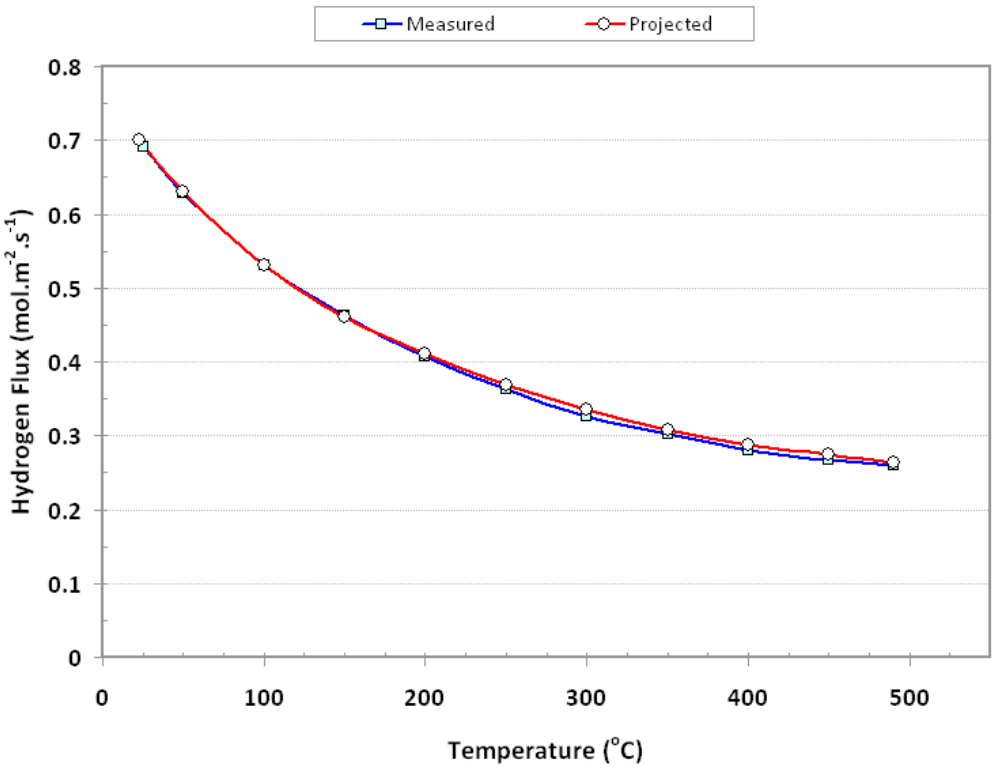

Figure 10.13 – Comparison of projected hydrogen flux calculated using the θ-modified geometric factor to the measured values for as-received PSS Disc 3.

Figure 10.13 clearly shows the projected flux is in excellent agreement with the measured values across the entire temperature range. The $\alpha_{K\theta}$ and β_V coefficients can now be used to predict the flux under any given temperature and pressure conditions, investigated within this work, to within ± 3 %.

It is possible, perhaps even likely, that as opposed to being a genuine physical characteristic, the reflection factor simply acts as a fitting parameter for non-ideal gas behaviour. Nevertheless, the linear modification of $\alpha_K \frac{\varepsilon r}{\tau}$ with temperature was found to be applicable to each of the examined substrates and is therefore used throughout this work to project the flux through porous substrates.

10.3.2 – Laser Melted PSS

The effect of laser melting on the topography and surface porosity of porous stainless steel was described in Section 10.2.3. The general trends observed were: i) a progressive reduction in both surface pore number and size as the laser fluence increased and, ii) increasing the number of pulses was found to induce a network of sub-micron cracks within the melted layer (Figure 10.14). In a similar manner to the as-received PSS discs, room temperature permeation measurements were performed for a wide range of laser melted discs in order to determine the α_K and β_V permeation coefficients. Although the low-pulse discs were deemed unsuitable for Pd-Y deposition due to the size of the remaining pores, they serve as a useful permeation comparison for the high-pulse discs. The room temperature hydrogen permeation of a typical low-pulse and a typical high-pulse disc are compared to as-received Disc 1 in Figure 10.15. Whilst the permeance of the low-pulse disc has been reduced by approximately an order of magnitude, the permeance of the high-pulse disc remains within 60 - 70 % of the as-received disc.

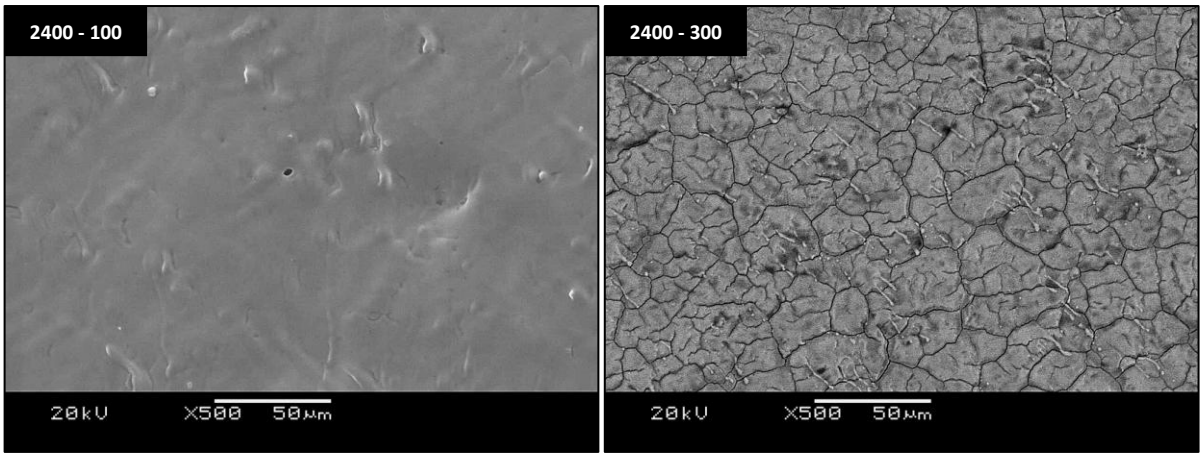

Figure 10.14 – SEM images showing the surface topography of the laser melted discs. The legends give the laser fluence (mJ.cm^{-2}) and the number of pulses.

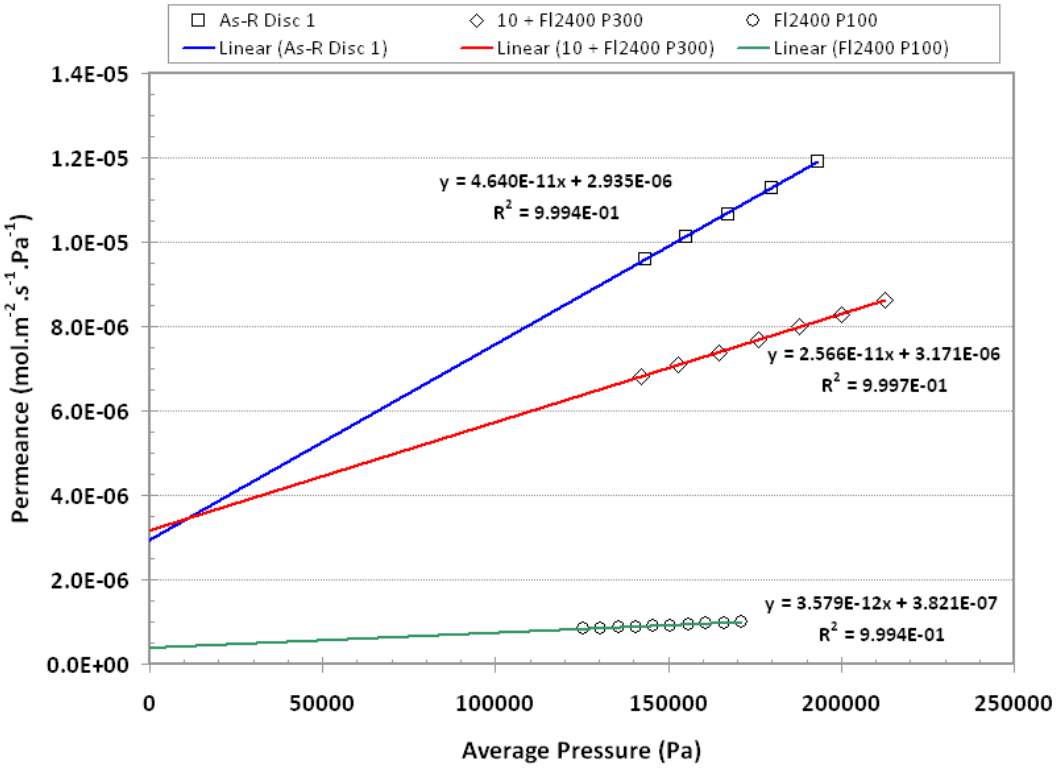

Figure 10.15 – The room temperature hydrogen permeance of PSS substrates laser melted with a high number of pulses and a low number of pulses compared to as-received Disc 1. Both discs were melted with a laser fluence of 2400 mJ.cm^{-2}

Interestingly, although the permeance of the low-pulse disc is considerably lower than the high-pulse disc, the average pore size *r* of the low-pulse disc is greater than that of the high-pulse disc; 0.246 µm compared to 0.212 µm. This is in good agreement with the topographical analysis presented in Section 10.2.3. The surface of the low-pulse disc appears almost fully dense, with a small number of relatively large pores or defects, whilst the high-pulse disc appears defect-free with a network of sub-micron cracks covering the surface (Figure 10.14). Figure 10.15 clearly demonstrates the efficacy of the sub-micron cracks in retaining the permeance of as-received PSS, whilst reducing the surface pore size.

Whereas the as-received PSS discs exhibited a wide range of hydrogen permeation values, the permeance of the high-pulse laser melted discs fell within a much narrower range. Figure 10.16 shows the room temperature permeance in a range of discs, all of which were melted using the same laser parameters: a fluence of 2400 mJ.cm^{-2} and 300 pulses. The initial surface condition of the discs was either as-received, or coated with 5, 10 or 15 µm SS prior to laser melting.

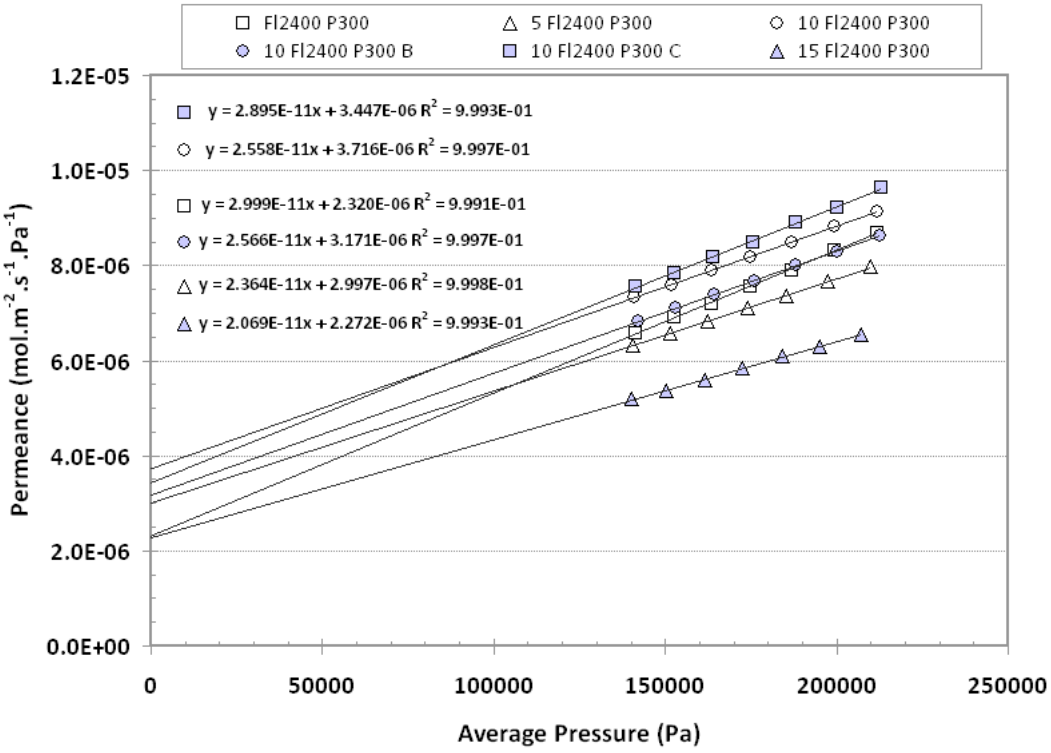

Figure 10.16 – Comparison of the room temperature hydrogen permeance in a range of substrates melted with a fluence of 2400 mJ.cm^{-2} and 300 pulses. The surface condition prior to melting is shown in the legend.

The α_K and β_V coefficients for each disc are displayed within Figure 10.16. It should be noted that the laser melted substrates are effectively multilayered structures, thus the permeation coefficients are average values for the whole structure. As discussed previously in Section 5.4, subtraction methods may be used to establish the permeation coefficients of each layer [174]. However, as we are primarily concerned with the hydrogen flux across each layer

in series, the multilayered structure may be viewed as a single entity adequately described by a single set of average α_K and β_V coefficients. In a similar manner to the as-received substrates, the average permeation coefficients have been used to calculate the geometrical factors of the laser melted discs (Table 10.3).

Table 10.3 – Comparison of the permeance coefficients and geometrical factors of laser melted PSS substrates

Sample	α_K (mol.m^{-2}.s^{-1}.Pa^{-1})	β_V (mol.m^{-2}.s^{-1}.Pa^{-2})	r (µm)	ε/τ	*Kn*	Flux @ RT & 1 bar ΔP (mol.m^{-2}.s^{-1})
As-R 2400 300	2.320 x10^{-6}	2.999 x10^{-11}	0.340	0.454	0.163	0.677
+ 5 SS 2400 300	2.997 x10^{-6}	2.364 x10^{-11}	0.208	0.961	0.266	0.651
+ 10 SS A 2400 300	3.716 x10^{-6}	2.558 x10^{-11}	0.178	1.379	0.311	0.741
+ 10 SS B 2400 300	3.171 x10^{-6}	2.566 x10^{-11}	0.212	0.994	0.261	0.695
+ 10 SS C 2400 300	3.447 x10^{-6}	2.895 x10^{-11}	0.221	1.04	0.250	0.774
+ 15 SS 2400 300	2.272 x10^{-6}	2.069 x10^{-11}	0.237	0.636	0.233	0.529

With the exception of the disc that was melted in the as-received condition (As-R 2400 300), there is good agreement between the calculated average pore sizes. This is consistent with the topographical analysis, in which no discernible difference was found between initial SS coating thickness and extent of surface cracking. Although the average pore size is considerably lower than in as-received PSS, the Knudsen numbers (K_n) of each disc still falls within the transition region between Poiseuille flow and Knudsen diffusion, confirming both transport mechanisms will contribute significantly to the overall hydrogen flux.

10.3.2.1 – The Effect of Temperature

In the same manner described in Section 10.3.1.1, the room temperature α_K and β_V coefficients of the laser melted substrates may be used to predict the flux at any given temperature or pressure. Experiments on the as-received discs showed that the β_V geometric factor remained relatively constant with temperature whilst the α_K geometric factor required modifying to account for the reflection factor θ. With this in mind, the geometrical factors established at room temperature were used to project the variation in hydrogen flux with temperature through a laser melted disc. The variation of hydrogen viscosity with temperature was taken from data reported by Assael et al [191]. The projected flux is compared to experimentally determined values in Figure 10.17.

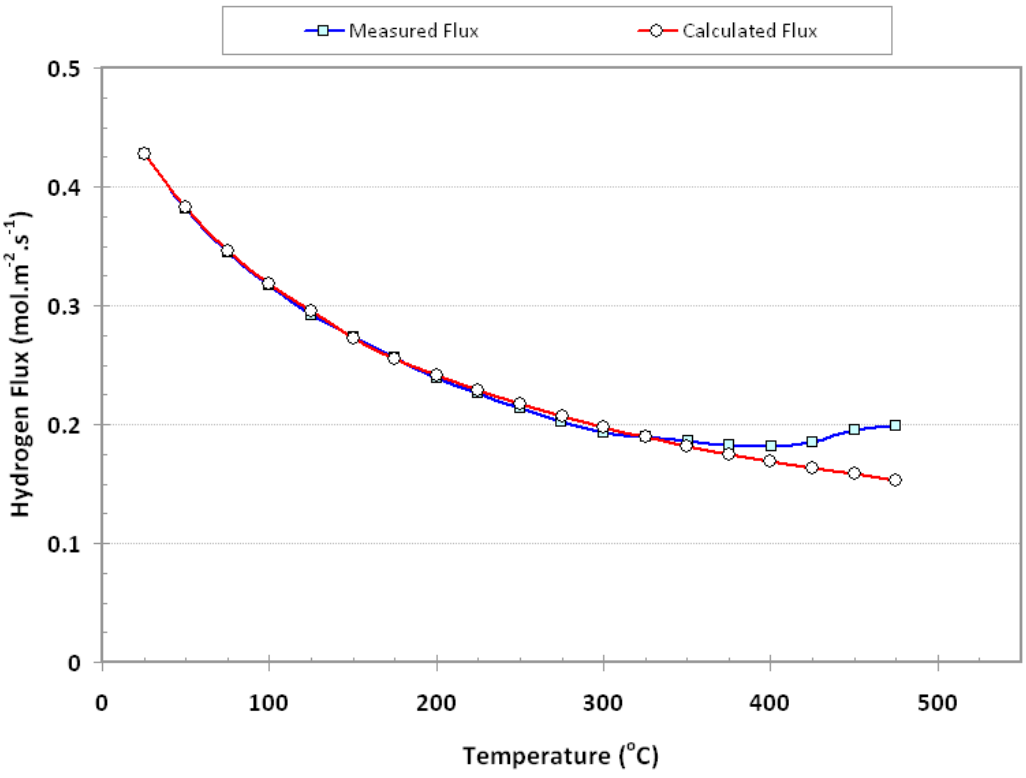

Figure 10.17 – The variation in measured hydrogen flux with temperature compared to the projected hydrogen flux. The as-received substrate was melted with a laser fluence of 2400 mJ.cm^{-2} and 300 pulses.

Figure 10.17 clearly shows the projected values are in excellent agreement with the measured values until, at a temperature of around 350°C, the measured flux begins to deviate from the projected flux. At approximately 420°C, there is a significant increase in the measured flux, which ultimately leads to a 33 % greater flux at 470°C. Upon cooling, the high temperature deviations were not reversible and the measured flux follows a higher curve (Figure 10.18).

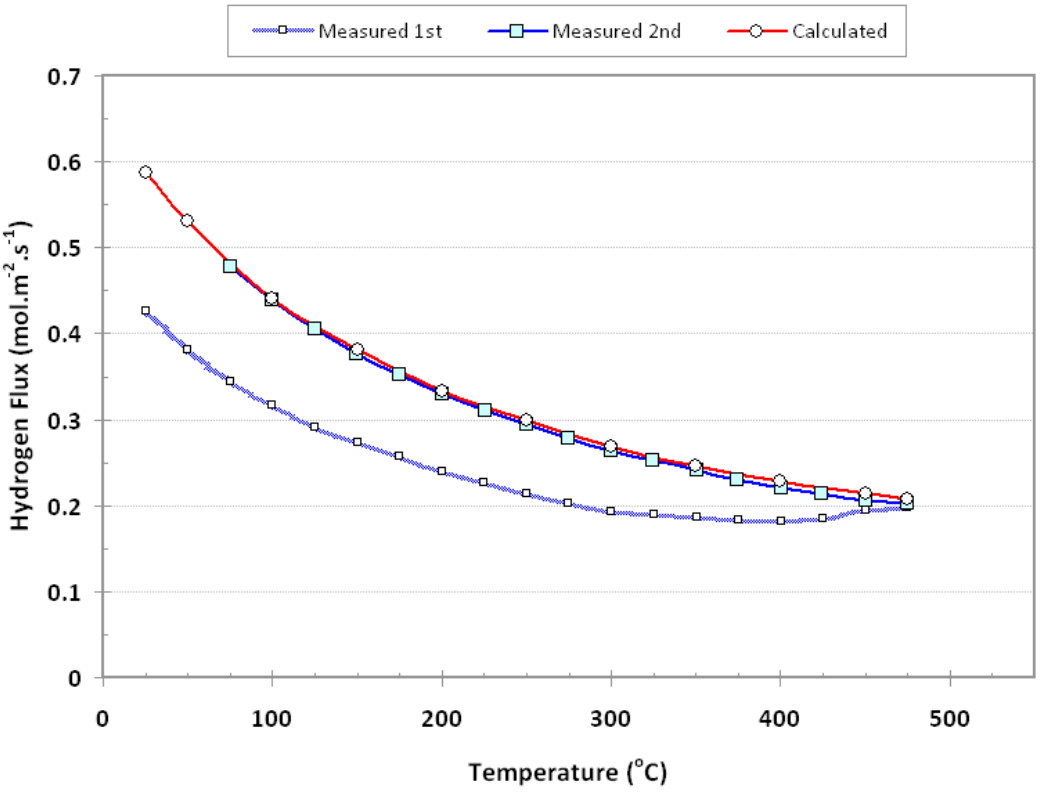

Figure 10.18 – Comparison of the measured hydrogen flux during the 1st thermal cycle to the 2nd thermal cycle and the calculated flux using the permeation coefficients obtained after the 1st heating run.

After the thermal cycle, the original α_K and β_V coefficients are no longer valid, thus the room temperature permeation measurements were repeated in order to establish a new set of α_K and β_V coefficients (Table 10.4). Upon comparison with the original values, the source of the high temperature deviation is apparent.

Table 10.4 – Comparison of the permeation coefficients & geometrical factors before and after heating to 470°C

Condition	α_K (mol.m^{-2}.s^{-1}.Pa^{-1})	β_V (mol.m^{-2}.s^{-1}.Pa^{-2})	r (µm)	ε/τ
Original	2.070 x10^{-6}	2.477 x10^{-11}	0.314	0.438
Temp Cycled	2.736 x10^{-6}	3.484 x10^{-11}	0.334	0.544

As expected, both the α_K and β_V coefficients have increased significantly. The reason for this appears to be an increase in the surface porosity. The average pore size, *r*, has increased by 6.4 %, whilst the ε/τ ratio has increased by 24.2 %.

Considering that no such effects were observed in the as-received discs, it can be assumed that the changes are either within the melted layer, or the interface between the two. As noted previously, the surface oxide was identified as a mixture of $FeCrO_4$, Fe_3O_4 and Cr_2O_3 using Raman Spectroscopy. Although Fe_3O_4 is reduced by hydrogen above 400°C [192], thus approximately coinciding with the temperature at which the permeance increases, identical effects were observed when the substrates were heated in argon, nitrogen and under vacuum. Additionally, the surface of the disc was examined visually with no obvious defects, pore formation or evidence of oxide reduction.

It would appear therefore, that above a certain critical temperature the surface cracks are slightly augmented, presumably due to thermal expansion of the melted layer and the underlying SS particles. Such small changes in surface crack size would be difficult to detect visually, especially when the measurements are performed ex-situ. The increase in average pore size was observed in the majority of laser melted discs tested, however the extent of the

increase varied considerably. The consequences of this for composite membrane operation are discussed further in Section 11.3.

Importantly however, with subsequent temperature cycles the measured flux was found to follow the same repeatable curve. The α_K and β_V coefficients calculated after the original temperature cycle accurately project the flux across the measured temperature range (Figure 10.18).

10.3.2.2 – The Effect of Gas Species

In addition to hydrogen, room temperature permeation measurements were performed using nitrogen and argon. Just as with hydrogen, the experimental data is applied to Equation 10.2 to calculate the appropriate α_K and β_V coefficients. The room temperature permeance of N_2 and Ar through a laser melted substrate are compared to that observed for H_2 in Figure 10.19.

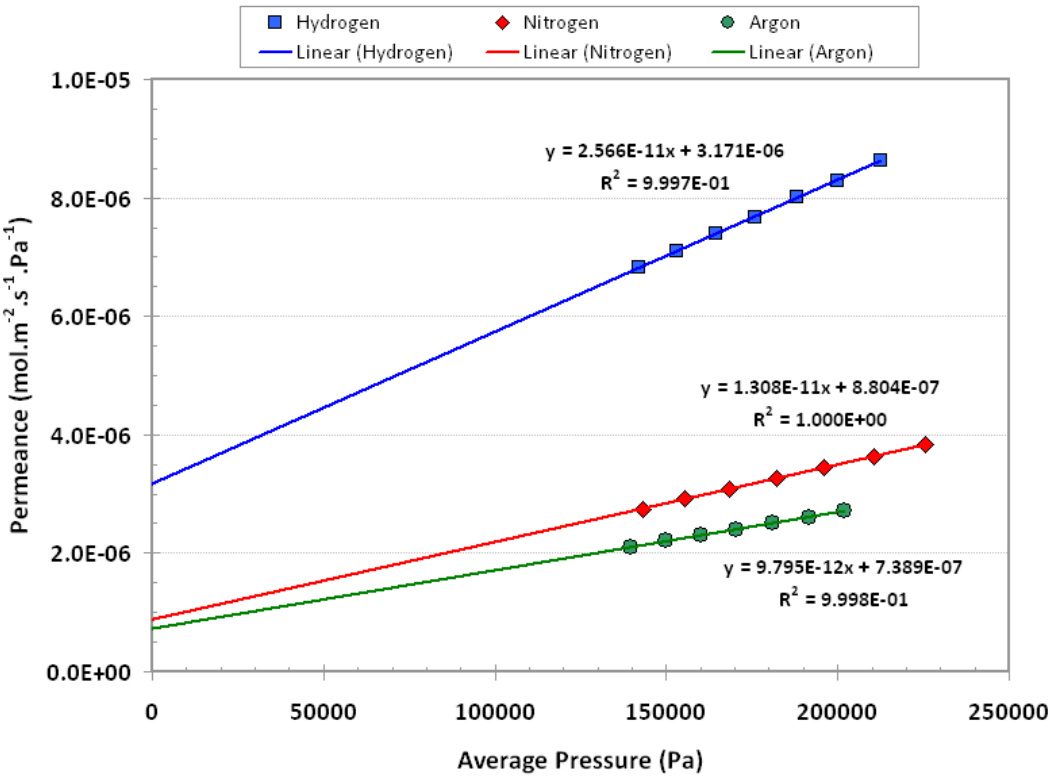

Figure 10.19 – Comparison of the room temperature permeance of hydrogen, nitrogen and argon through a laser melted substrate. The substrate was coated with 10µm SS prior to melting with fluence of 2400mJ.cm^{-2}& 300 pulses

The α_K and β_V coefficients for each gas are shown within Figure 10.19. The measured permeation of each gas may be quantified proportionally using the following expressions for α_K and β_V (Equations 10.6 and 10.7), as discussed previously in Section 10.3.

$$\alpha_K = 1.06 \frac{\left(\frac{1}{l}\right)\left(\frac{\varepsilon}{\tau}\right) r}{\sqrt{RTM}} \qquad \textit{Eqn 10.6}$$

$$\beta_V = 0.125 \frac{\left(\frac{1}{l}\right)\left(\frac{\varepsilon}{\tau}\right) r^2}{\eta RT} \qquad \textit{Eqn 10.7}$$

From Equations 10.6 and 10.7 it is clear that the ratio of the α_K coefficient between any two gases should be equal to the ratio of the square roots of the molecular mass, $\sqrt{M_1}/\sqrt{M_2}$, whereas the ratio of the β_V coefficients is equal to the viscosity ratio, η_1/η_2. This ratio of gas species permeation is basis of separation in porous membranes. The theoretical maximum ratio, or ideal selectivity, of the Knudsen coefficient, α_K, between hydrogen and nitrogen is 3.73, whilst using the nitrogen viscosity data reported by Liley [193], the theoretical ratio of the β_V coefficients at 25ºC should be 2.01.

The α_K and β_V coefficients and H_2 / N_2 ratios for a wide range of laser melted discs are listed in Table 10.5. The average α_K H_2 / N_2 ratio was calculated as 3.70 whilst the average β_V H_2 / N_2 ratio was 1.97. Both the experimentally determined values are in good agreement with the theoretically calculated values.

Of particular importance to the present work, this relationship allows projections of gas permeation through a given substrate to be made using the α_K and β_V coefficients established with a different gas species. Most thin film composite membranes contain a certain level of pinholes, as evidenced by the selectivity values, which will contribute to the overall measured hydrogen flux. In order to fully quantify the permeation of hydrogen across the dense thin film, it is imperative that the flux through pinholes is accounted for. The room temperature α_K and β_V permeation coefficients of a composite membrane established with nitrogen, and thus entirely through pinholes, may be scaled to project the equivalent hydrogen permeation coefficients due to pinholes.

Table 10.5 – Comparison of the α_K and β_V coefficient ratios of H_2 and N_2 for a range of laser melted substrates.

Sample	α_{av} H_2 (x10^{-6})	α_{av} N_2 (x10^{-6})	H_2/N_2	β_{av} H_2 (x10^{-11})	β_{av} N_2 (x10^{-11})	H_2/N_2
As-R Disc 1	2.935	0.8754	*3.35*	4.64	2.301	*2.017*
As-R Disc 2	5.914	1.545	*3.83*	14.35	7.053	*2.035*
Fl2400 P300	3.441	0.8303	*4.14*	5.416	2.803	*1.932*
Fl2400 P300 B	2.169	0.5603	*3.87*	2.283	1.218	*1.874*
Fl2400 P400	2.503	0.7475	*3.35*	4.039	2.006	*2.013*
5+Fl2400 P300	2.997	0.9129	*3.28*	2.364	1.145	*2.065*
10+Fl2400 P300	3.716	1.06	*3.51*	2.558	1.27	*2.014*
10+Fl2400 P300 B	3.171	0.8804	*3.6*	2.566	1.308	*1.962*
10+Fl2400 P300 C	3.447	0.8279	*4.16*	2.895	1.561	*1.855*
15+Fl2400 P300	2.272	0.5797	*3.92*	2.069	1.081	*1.914*
Avg	-	-	***3.70***	-	-	***1.97***

Section 11 – Composite Pd-Y / PSS membrane

11.1 – Introduction

The results and analysis presented within this section are largely a combination of the observations and analysis techniques presented in the previous two sections. The established hydrogen permeation characteristics of each layer are applied to the measured permeation data of the composite membranes which, combined with the structural analysis, allows the deduction of the overall hydrogen transport mechanism.

During the course of this work a large number of composite membranes were produced. However, in the interest of brevity, the experimental details of just two composite membranes are presented; CM–A and CM–B. The designation represents the particular Pd-Y deposition process of each membrane, as described in Section 9.2. Both CM–A and CM–B were selected as they exhibited most of the desirable characteristics in terms of substrate topography and micro-cracking. Overall, in terms of structure and hydrogen permeation characteristics, they were found to be typical of all the composite membranes analysed. The structural properties of both membranes are listed in Table 11.1.

Table 11.1 – Properties of the composite Pd-Y membrane analysed within this section

	Pd-Y film		Porous Substrate		
Sample	Thickness	Composition	Laser Parameters	PSS surface	PSS grade
CM – A	5.06 µm ± 0.11	$Pd\text{-}Y_{8.31 \pm 0.07}$	Fl 2400 – P 300	10 µm SS	0.1 µm
CM – B	4.90 µm ± 0.08	$Pd\text{-}Y_{10.38 \pm 0.07}$	Fl 2400 – P 300	15 µm SS	0.1 µm

11.2 – Composite Membrane Structure

In terms of structure, particularly the porous substrate, CM–A and CM–B possessed similar characteristics. The surface of both substrates were melted using identical laser parameters, the only difference being the thickness of the SS coating prior to laser melting. However, as discussed in Section 10.2.3, no discernible difference in the resultant surface was observed for the deposition of either 10 or 15 µm SS prior to laser melting. Therefore, the surface topography and characteristics of both discs were concurrent at each stage of production. The evolution of the surface topography of CM–A as it progressed along the membrane production sequence is shown in Figures 11.1 to 11.4.

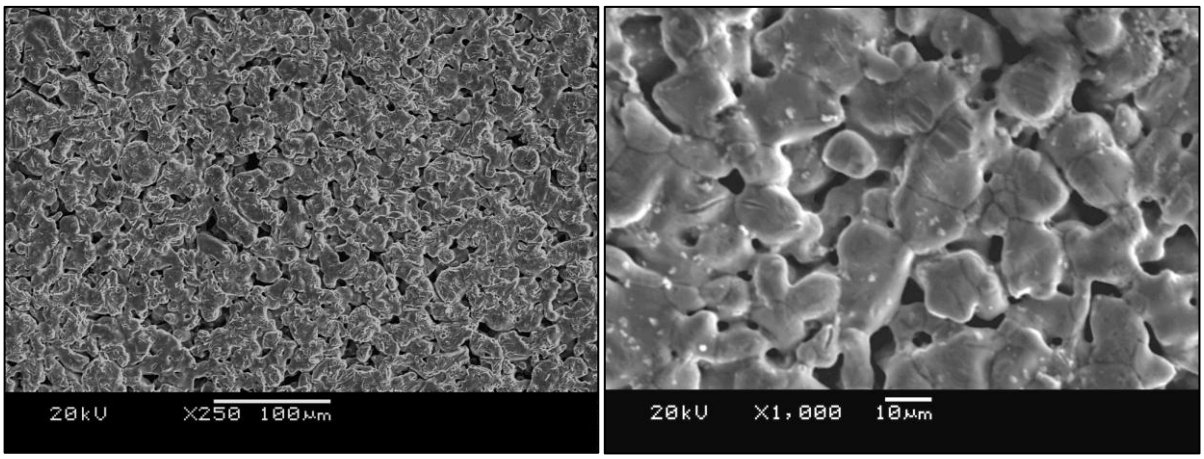

Figure 11.1 – SEM image showing the surface topography of as-received 0.1 µm PSS

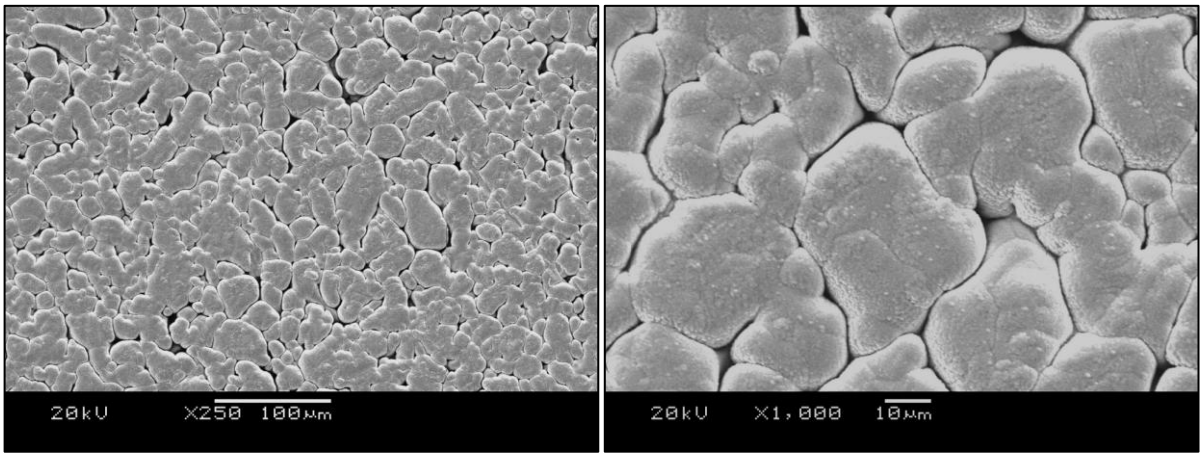

Figure 11.2 – SEM image showing the surface topography of as-received 0.1µm PSS coated with 10µm SS

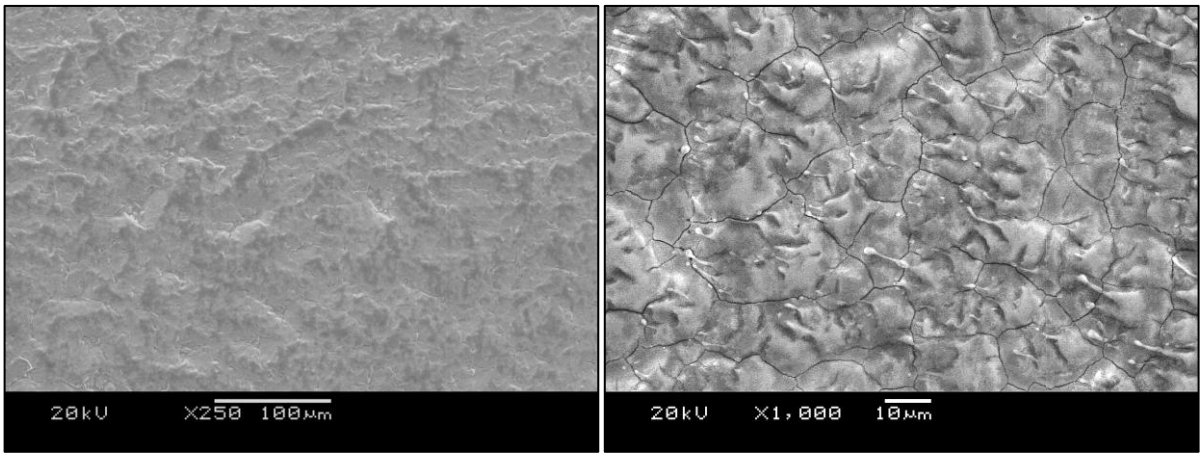

Figure 11.3 – SEM image showing the surface topography of CM–A after laser melting with a fluence of 2400 mJ.cm^{-2} and 300 pulses.

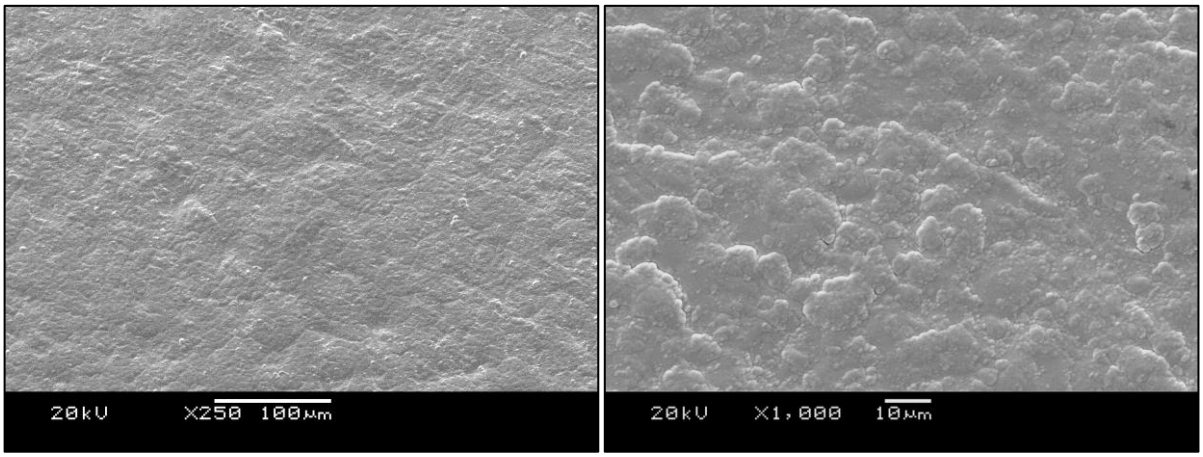

Figure 11.4 – SEM image showing the surface topography of CM–A after deposition of 5 µm Pd-$Y_{8.31}$

Figure 11.3 clearly demonstrates the uniform, defect-free surface produced by the laser melting technique. In particular, the high magnification image (x1000) reveals the network of sub-micron cracks which, as discussed in Section 10.2.3, are most likely formed due to the rapid cooling experienced during laser melting. The deposition of approximately 5 µm Pd-Y appeared to sufficiently cover the submicron cracks, thus forming a defect-free membrane layer (Figure 11.4). However, as described in Section 8.2.5, prior to the Pd-Y deposition the laser melted substrates required laser spot welding to the inner section of an ultra-high vacuum copper gasket, in order to provide the necessary gas seal for testing. Prior to the laser

spot welding, the disc diameter was reduced using a lathe. Either or both of these stages contributed toward significant additional cracking around the outer edge of the disc surface (Figures 11.5 and 11.6).

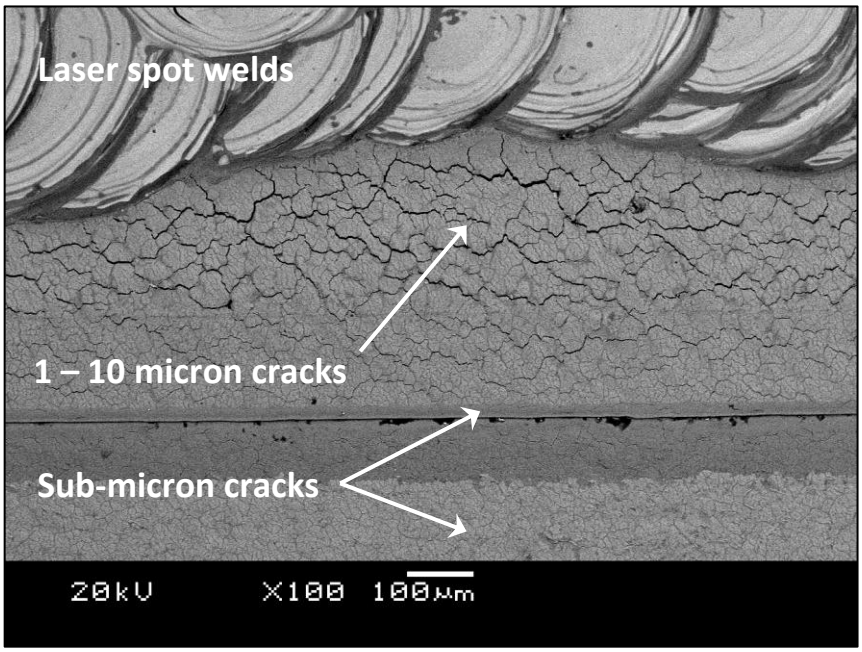

Figure 11.5 – SEM image showing increased cracking in CM–A around the laser spot weld

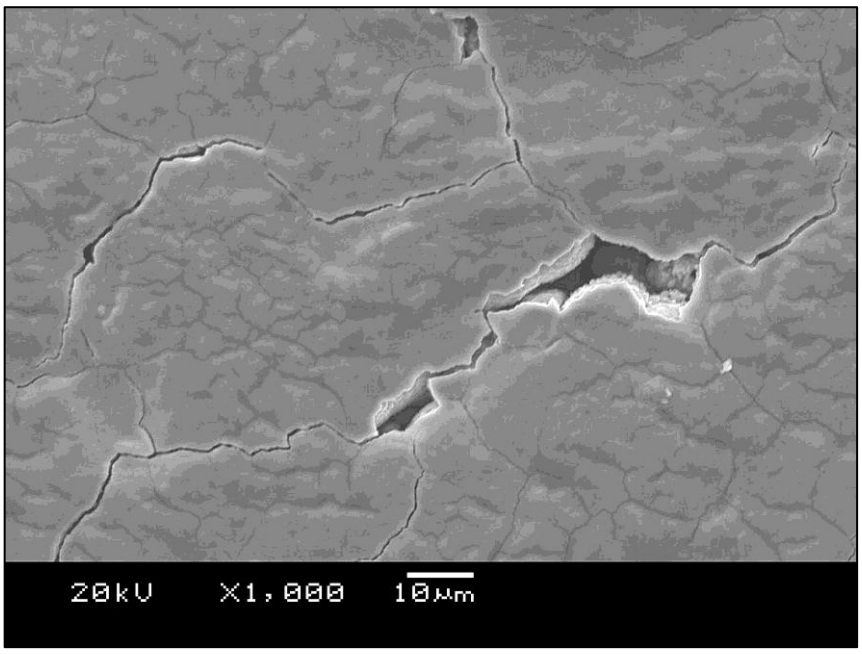

Figure 11.6 – SEM image showing the additional cracking around the weld ranged between 1 – 10 µm in size.

The increased cracking around the laser weld largely appeared to follow the existing crack network *i.e.* it appeared to augment the existing crack width. However, in certain regions whole fragments have been removed leaving relatively large defects of up to 10 µm in diameter (Figure 11.6). It should be noted that despite the formation of some large defects, the vast majority of the cracks remained < 2 µm in diameter. Comparable peripheral cracking was observed in all the samples produced using the laser welding technique, with no apparent trend between the individual conditions and the extent of the additional cracking.

As a consequence of the increased cracking, the deposited Pd-Y films exhibited pinholes around the periphery of the laser weld (Figure 11.7).

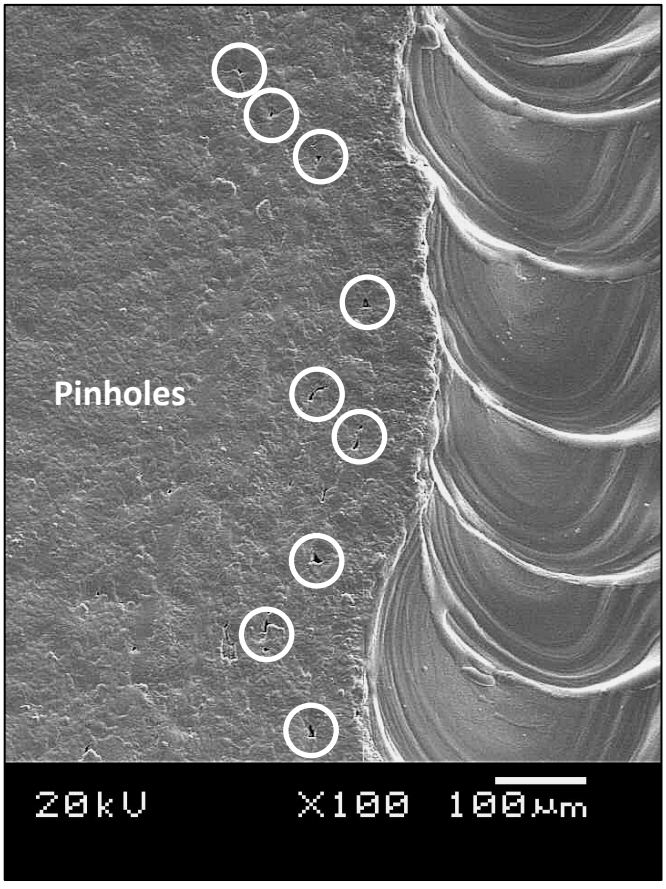

Figure 11.7 – SEM image showing pinhole formation in CM–A along the periphery of the laser spot weld

The size and shape of the pinholes suggest they are formed over the regions where small fragments of the surface have been removed, as highlighted in Figure 11.6. Additionally, although increased crack sizes were observed relatively uniformly around the entire circumference, many areas were found to be pinhole-free after Pd-Y deposition (Figure 11.8).

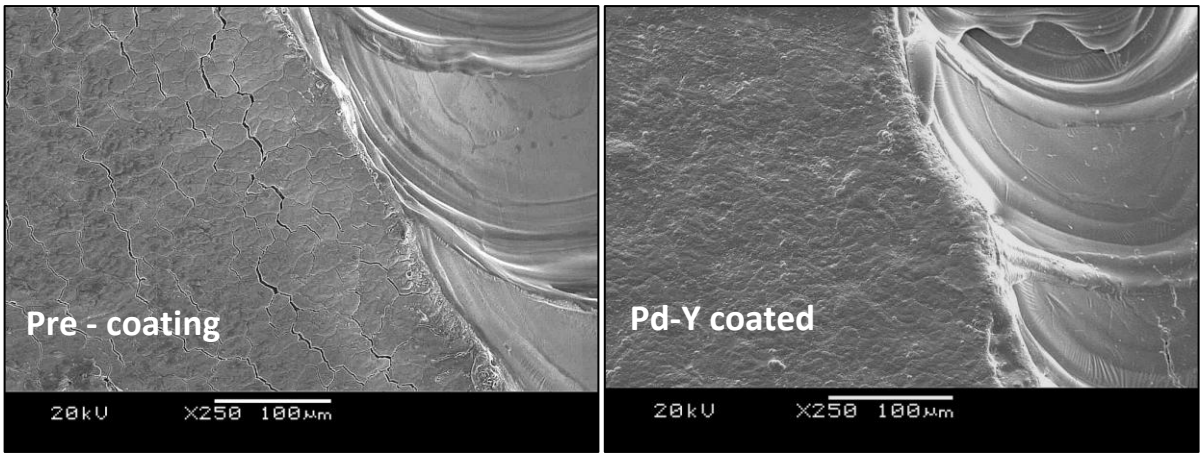

Figure 11.8 – SEM image showing the areas of increased crack width were largely covered by the deposition of 5 µm Pd-Y

Presumably, these pinhole-free areas correspond to those regions where the effect was to simply augment the existing cracks, rather than form fragments which subsequently break off. Pinhole assessments were made at numerous locations around the circumference of both CM–A and CM–B, and it was estimated that the average distance between pinholes was 105 µm. Given that the disc diameter was 16 mm and that the inner section of both membranes were effectively pinhole-free, the average pinhole density was calculated to be approximately 2.4 pinholes.mm^{-2}.

The effective structure of both composite membranes can be represented schematically by Figure 11.9. The porous stainless steel surface has been successfully planarised using an excimer laser. The laser induces a network of sub-micron cracks across the surface due to the rapid cooling rates and the inherent low strength of austenitic stainless steel during cooling.

The network of sub-micron cracks enables the deposition of defect-free Pd-Y layers approximately 5 µm thick, whilst remaining porous and thus permitting molecular transport. However, the process of sealing the discs augments the existing crack network along the disc circumference. Whilst the majority of these larger cracks are < 2 µm in diameter, and are covered by the Pd-Y film, a minority are too large (5 – 10 µm) and form pinholes within the Pd-Y layer. The presence of pinholes will reduce the potential gas selectivity of the membrane and contribute to the measured permeation of hydrogen across the membrane (Figure 11.9).

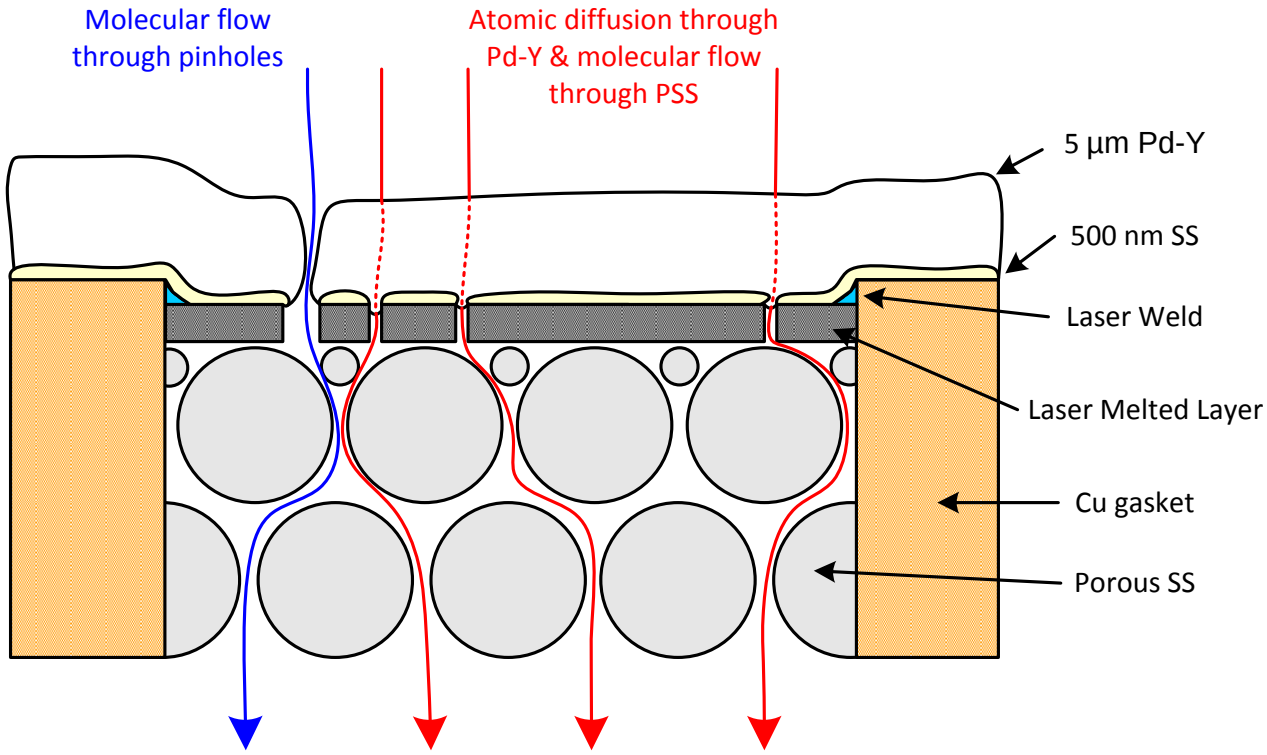

Figure 11.9 – Schematic drawing of the structure of composite membranes CM–A and CM–B

Although the pinhole density is estimated to be approximately 2.4 mm^{-2} and, assuming an average pinhole diameter of 5 µm, a percent surface area of just 0.0061 %, the pinholes are expected to contribute significantly to the gas transport. In order to analyse the permeation across the Pd-Y film, the contribution of the pinholes must be accounted for.

11.3 – Composite Membrane Permeability

The permeation measurements and observations presented within this section are divided into four parts: the first section presents details on the molecular flow through the substrate and pinholes; the second section details the measured hydrogen flux across the membranes; whilst the third and fourth sections present analysis of the hydrogen flux. In the third section, the hydrogen flux is analysed using the traditional general permeability equation and is compared to a range of values reported in the literature. Whereas in the fourth section, the hydrogen flux is analysed in terms of the individual components, thus making allowance for the active transport mechanism within each layer.

11.3.1 – Molecular Transport

As discussed previously, in order to accurately analyse the permeation of hydrogen across a composite membrane, prior knowledge of the specific transport characteristics of the porous substrate is essential. Therefore, hydrogen, nitrogen and argon permeation measurements were performed at each stage of the membrane production process (described in detail in Section 8.2.5). For the purpose of analysing the permeation characteristics of the substrate, four distinct production stages may be defined, each describing the surface condition of the discs; at Stage I the discs are in the as-melted condition, Stage II is after the deposition of a 500 nm SS adhesion layer, Stage III is after high temperature annealing (10^{-5} mbar, 750°C, 30 mins) and Stage IV is after the deposition of the Pd-Y membrane. The room temperature nitrogen permeance of both composite membranes at production Stages I – IV, are shown in Figures 11.10 and 11.11.

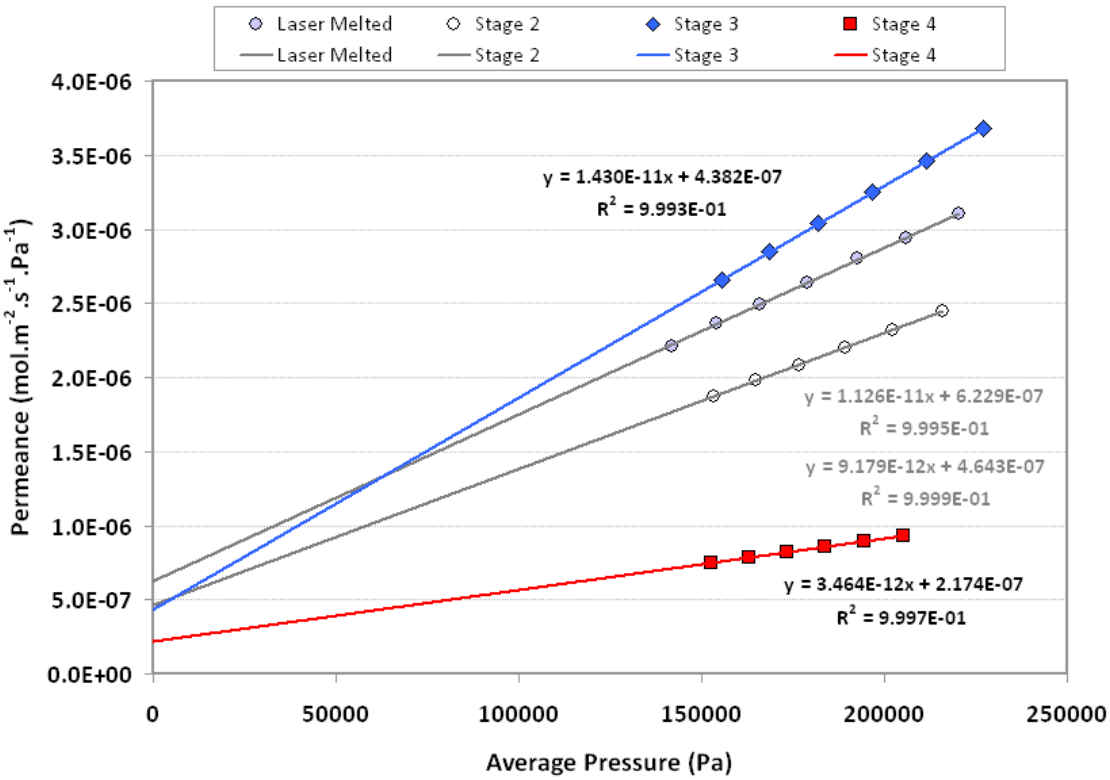

Figure 11.10 – Room temperature nitrogen permeance of CM – A at Stages I-IV of production

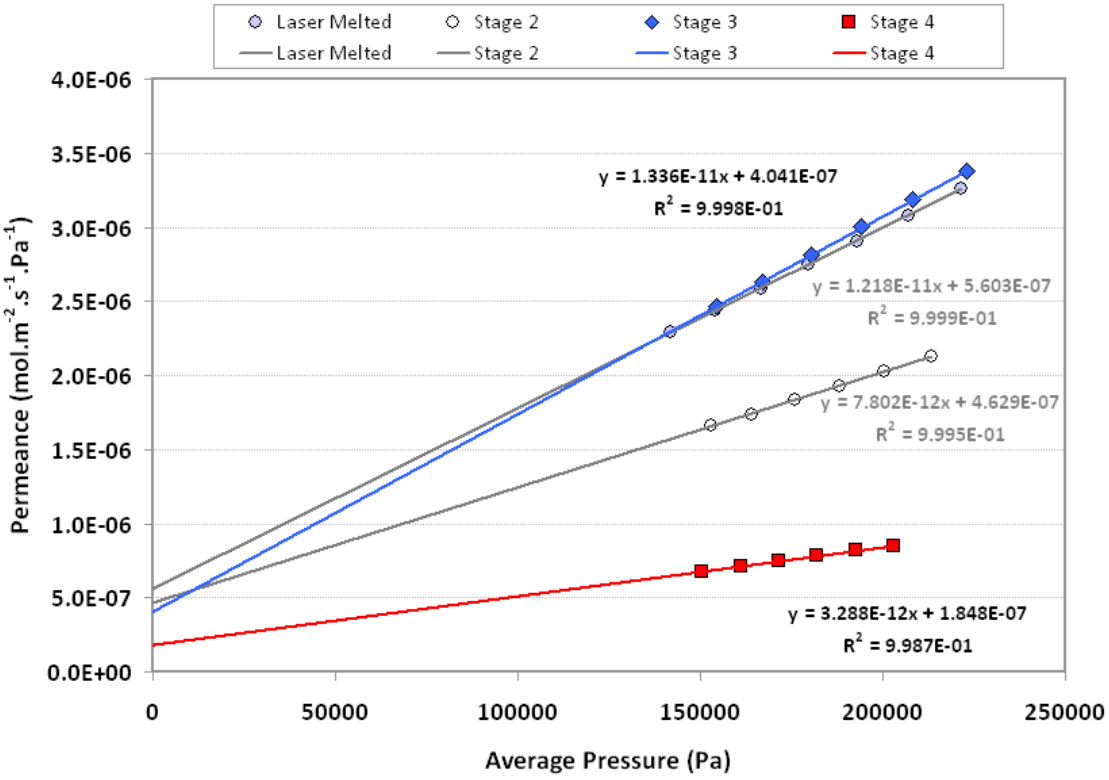

Figure 11.11 – Room temperature nitrogen permeance of CM – B at Stages I-IV of production

The permeation coefficients α_K and β_V determined at each production stage are shown within Figures 11.10 and 11.11. It should be noted that hydrogen permeation measurements were also performed throughout Stages I – III, and will be discussed later. However, at Stage IV, only nitrogen measurements were performed at room temperature, therefore to facilitate direct comparison at each stage, only the nitrogen permeation data is shown.

Both composite membranes exhibit similar permeation behaviour at each production stage. The effect of depositing the 500 nm stainless steel adhesion layer (Stage II) is a reduction of both the α_K and β_V coefficients, hence an increase in resistance and a subsequent reduction in the observed permeation. A 500 nm layer would not be expected to cover any pore greater than about 150 to 200 nm in diameter, which suggests a significant number of the surface cracks induced during laser melting fall beneath these dimensions.

As discussed in Section 10.3.1.1, heating the laser melted discs beyond about 350°C was found to induce a non-reversible increase in the average surface crack size. The reason for which is presumed to be thermal expansion of the stainless steel within the melted layer. As a consequence, the α_K and β_V coefficients of the substrate established prior to membrane deposition would no longer be valid, thus preventing accurate analysis of the observed flux. In light of this, both composite membranes were vacuum annealed (10^{-6} mbar, 750°C, 30 mins) prior to Pd-Y deposition (Stages III and IV respectively). Figures 11.10 and 11.11 clearly show both discs demonstrate significantly greater permeance after annealing, suggesting that the thermal expansion has augmented the surface cracks. As discussed in Section 10.3.1.1, these changes are non-reversible and are relatively stable, thus the permeation exhibits repeatable behaviour with further temperature cycles. Therefore, throughout the remaining sections, the α_K and β_V permeation coefficients determined at this point (Stage III) are

assumed to be valid and are used to calculate / project the gas flux through the substrate of composite membranes CM – A and CM – B.

After Pd-Y deposition, both membranes exhibited pinholes around the circumference of the substrate. Whilst the pinhole density is relatively low, 2.4 per mm^2, the molecular flux through these peripheral pinholes is expected to contribute significantly to the overall observed hydrogen flux. Therefore, room temperature nitrogen permeation measurements were performed after Pd-Y deposition (Stage IV). The α_K and β_V pinhole permeation coefficients calculated using nitrogen are shown within Figures 11.10 and 11.11.

As discussed previously in Section 10.3.2.2, the ratio of H_2 / N_2 α_K and β_V coefficients were determined for 10 uncoated substrates. The calculated average values of 3.70 and 1.97 are in good agreement with the theoretical values of 3.73 and 2.01 for α_K and β_V respectively. Using the experimentally determined average ratios, the nitrogen α_K and β_V pinhole permeation coefficients were scaled for hydrogen. These values, along with the room temperature hydrogen permeation coefficients determined at Stage III, are listed in Table 11.2. Throughout the remaining sections, these values are used for the analysis of the measured composite membrane flux.

Table 11.2 – Room temperature molecular permeation coefficients of CM – A and CM – B.

Transport Mechanism	Coefficient	CM – A	CM – B
Pinhole Contribution (Stage IV)	Measured N_2 α_K	2.174 x10^{-7}	1.848 x10^{-7}
	Measured N_2 β_V	3.464 x10^{-12}	3.288 x10^{-12}
	Calculated H_2 α_K	8.044 x10^{-7}	6.838 x10^{-7}
	Calculated H_2 β_V	6.824 x10^{-12}	2.174 x10^{-12}
Substrate Resistance (Stage III)	Measured H_2 α_K	1.687 x10^{-6}	1.439 x10^{-6}
	Measured H_2 β_V	2.903 x10^{-11}	2.645 x10^{-11}

11.3.2 – Measured Hydrogen Flux

The measured hydrogen flux of CM–A and CM–B between 180 and 450°C is shown in Figure 11.12. Although CM–A exhibits significantly greater flux across the whole temperature range, both discs demonstrate remarkably similar behaviour with temperature.

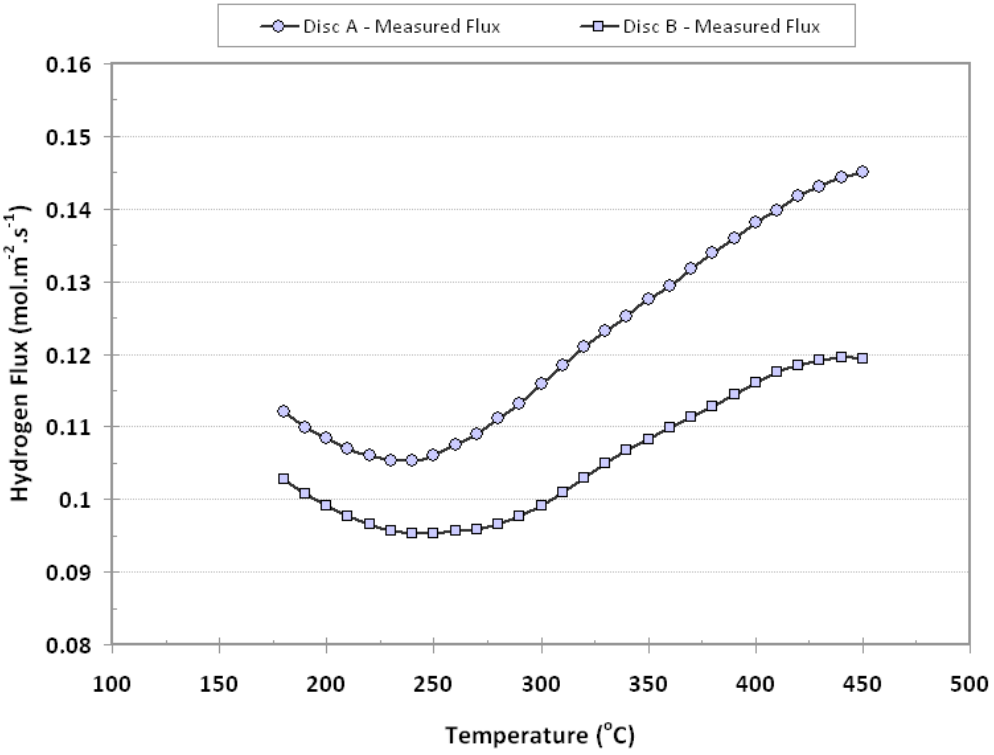

Figure 11.12 – Measured hydrogen flux through Pd-Y / PSS composite membranes A and B (ΔP = 100 kPa)

As expected, the flux at low temperatures (< 250°C) appears to be dominated by molecular flow through pinholes, as evidenced by decreasing flux with increasing temperature. In order to perform any form of meaningful hydrogen permeability analysis, it is necessary to fully account for such molecular flow. Using the methodology described in Section 10.3, the α_K and β_V pinhole coefficients, as listed in Table 11.2, are employed to accurately project the total pinhole contribution across the entire temperature range (Figures 11.13 and 11.14).

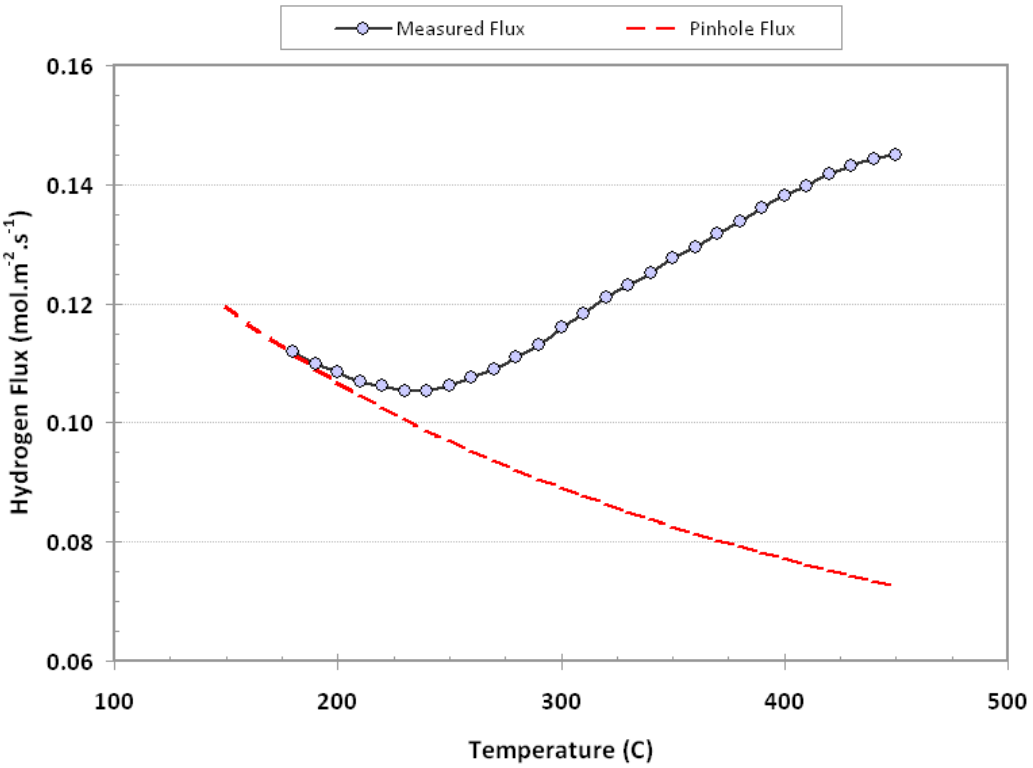

Figure 11.13 – Measured hydrogen flux and project pinhole flux through CM – A (ΔP =100kPa)

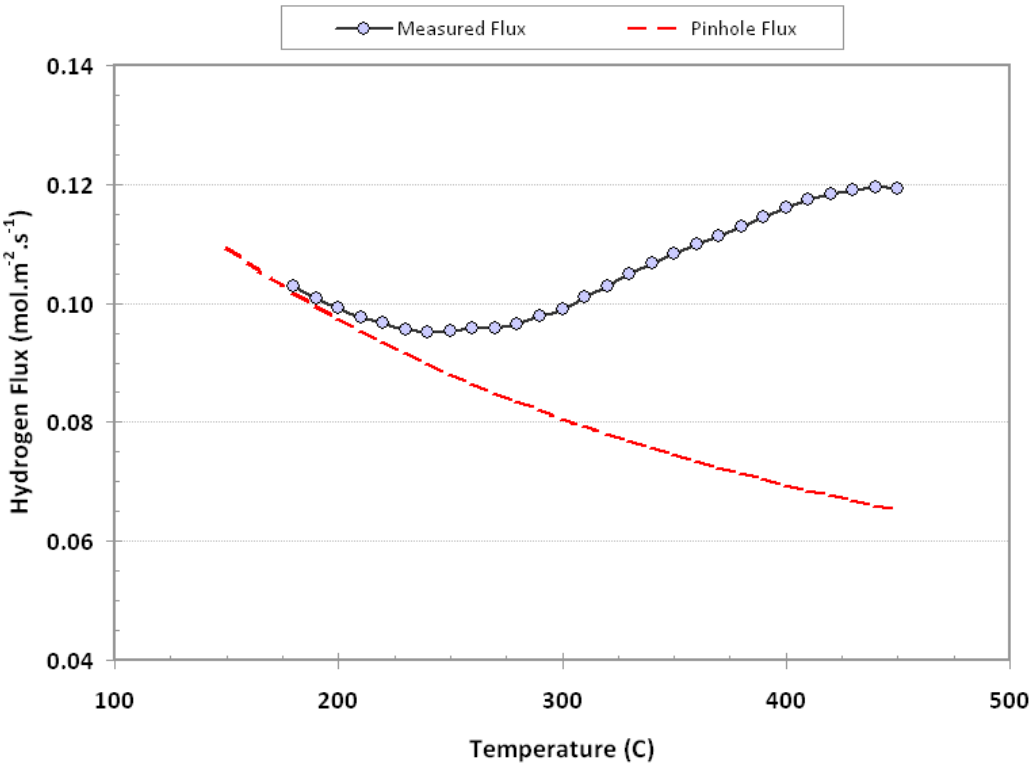

Figure 11.14 – Measured hydrogen flux and project pinhole flux through CM – B (ΔP =100kPa)

As shown in Figures 11.13 and 11.14, the projected pinhole contributions suggest that the measured flux at 180°C is almost entirely due to molecular flow through pinholes. As the temperature increases, the relative contribution of pinhole flux decreases whilst the proportion of atomic diffusion across the Pd-Y increases. At 450ºC, the H_2 / N_2 selectivity factor of CM – A and CM – B were calculated as 5.86 and 5.40 respectively. Although these values are relatively low, they fall within the range reported in the literature and are similar to the value of 5.7 reported by Jayaraman [88].

In order to isolate the pinhole flux and establish the hydrogen flux due purely to diffusion across the Pd-Y film, J_{Film}, a simple subtraction model was used,

$$J_{Film} = J_{Measured} - J_{Pinhole} \qquad \textit{Eqn 11.1}$$

The calculated values of J_{Film} in both composite membranes are shown in Figure 11.15.

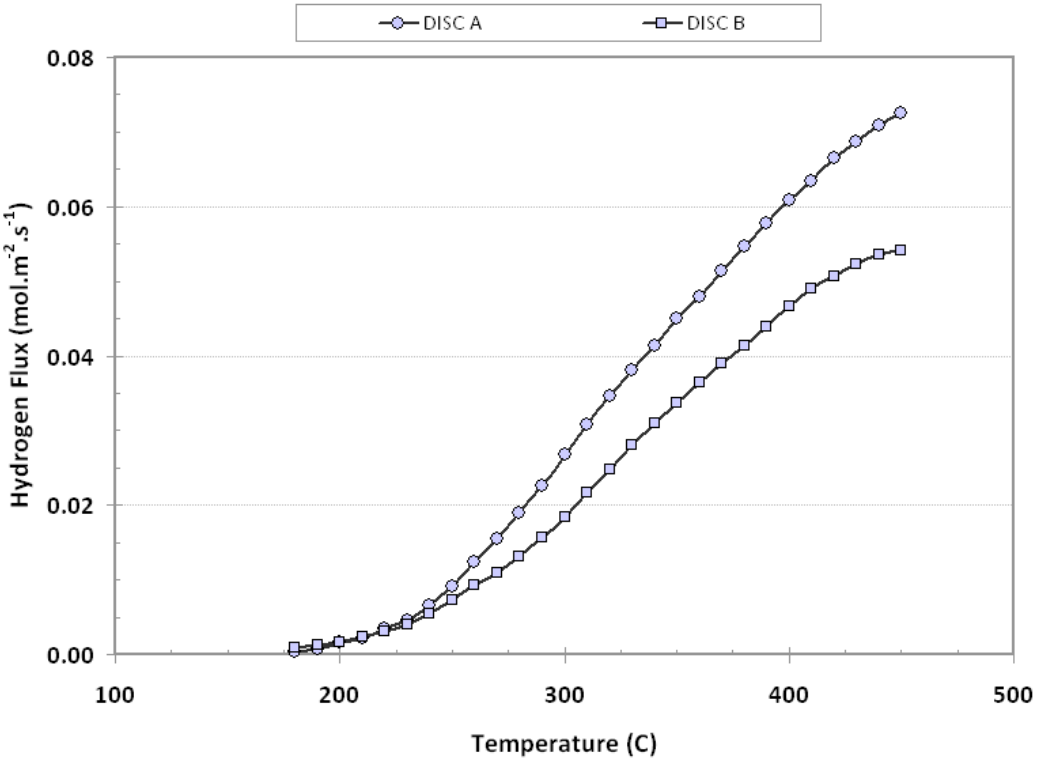

Figure 11.15 – Pinhole-stripped hydrogen flux, J_{Film}, though CM – A and CM – B (ΔP = 100 kPa)

From Figure 11.15, it is clear that the differences in measured flux observed between the composite membranes at low temperature are due solely to pinholes. However, at temperatures > 250ºC, despite being measured under identical conditions, CM–B exhibits significantly lower flux than CM–A. The reason for these differences will be discussed further in Section 11.3.4.

All further analysis of the hydrogen flux through both composite membranes is performed using measured values, from which, any pinhole contributions have been subtracted.

11.3.3 – Composite Membrane Permeability - General Permeability Equation

As noted previously in Section 4.5, the majority of investigators express the observed hydrogen flux through a composite membrane (J_{H2}) in terms of the general permeability equation, Equation 11.2,

$$J_{H_2} = \Phi \frac{\left(Pi_{H_2}^{n} - Pii_{H_2}^{n}\right)}{l(x)} \qquad \textit{Eqn 11.2}$$

where *Pi* and *Pii* denote the measured external hydrogen pressure at the high pressure and low pressure sides respectively, *l(x)* is the membrane thickness and Φ is the apparent permeability. The permeability of Pd composite membranes reported by numerous authors have been compared to that of bulk Pd in Section 4.5. The composite membrane permeability values varied considerably and, almost without exception, fell between 1 – 4 orders of magnitude

beneath that found in bulk Pd. Similar trends were also observed for both Pd-Ag and Pd-Cu composite membranes.

Equation 11.2 has been experimentally validated for self-supporting membranes with thicknesses as low as 1.3 µm [84]. Indeed, the equation was applicable to the bulk Pd, Pd-Ag and Pd-Y membranes investigated during this work. However, the work of Liang & Hughes [160], Goto et al [161] and Ryi et al [162], demonstrated that when the measured flux is analysed using Eqn 11.2, the apparent permeability of a composite membrane is dependent on permeation direction. This would suggest that the substrate offers significant resistance to hydrogen flux, the presence of which is likely to contribute to the observed deviations in composite membrane permeability when compared to bulk membranes.

Therefore, in order to quantify the extent to which the substrate affects the apparent permeability, it is necessary to analyse the measured hydrogen flux both in terms of the general permeability equation and as a series resistance model. The analysis presented within the current section is based on the general permeability equation, and assumes that the substrate offers zero resistance to flow, thus corresponding to the majority of published composite membrane data.

The average Pd-Y thickness of CM–A and CM–B were calculated as 5.06 µm and 4.90 µm respectively. Using the measured values at the high pressure (P_i = 200 kPa) and low pressure (P_{ii} = 100 kPa) sides of the composite membrane and the measured hydrogen flux, as shown in Figure 11.15, the apparent permeability can be calculated. The calculated permeability values are compared to the range of Pd composite membranes reviewed previously in Section 4.5 (Figure 11.16).

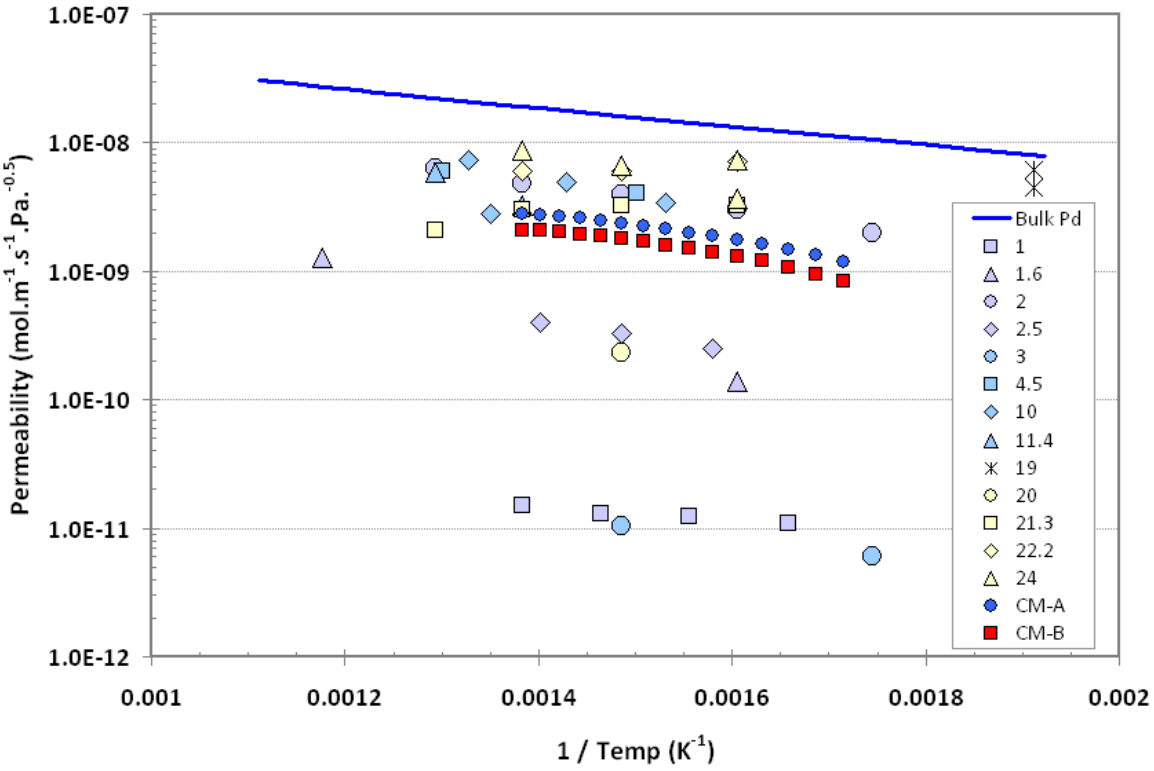

Figure 11.16 – Comparison of the permeability of CM–A and CM–B composite membranes, with various literature values for Pd composite membranes and self-supporting Pd. (Legend = membrane thickness in µm)

From Figure 11.16, two main observations can be drawn. Firstly, the permeability of both CM–A and CM–B fall well within the reported range for Pd composite membranes. Secondly, the permeability values are approximately an order of magnitude lower than in bulk palladium across the whole temperature range studied. Considering that the permeability of the equivalent bulk Pd-Y membranes is several times greater than Pd, it is clear that both composite membranes experience a permeability impeding mechanism.

The permeability at 400°C of CM–A and CM–B are compared to those measured in the equivalent bulk alloys in Table 11.3. The extent of the reduction in permeability is clear, with CM–A demonstrating 4.1 % and CM–B just 3.2 % of bulk Pd-Y_8 and Pd-Y_{10} respectively.

Table 11.3 – Comparison of the composite membrane permeability at 400ºC with the equivalent bulk membranes

	CM–A	Bulk Pd-Y_8	CM–B	Bulk Pd-Y_{10}
Permeability @ 400 ºC ($mol.m^{-1}.s^{-1}.Pa^{-0.5}$)	2.37×10^{-9}	5.80×10^{-8}	1.80×10^{-9}	5.61×10^{-8}
Composite % of bulk	4.1 %		3.2 %	

In addition to low permeability values, the pressure exponent, *n*, (see Eqn 11.2) of composite membranes is frequently reported to deviate significantly from 0.5. Values of *n* as high as 1 have been reported for composite Pd membranes with thicknesses < 3 µm [88, 93, 153], whilst most values range between 0.6 and 0.75 [121, 156-159]. Interestingly, both Liang & Hughes [160] and Ryi et al [162] reported that in addition to affecting the observed permeability, the direction of permeation also affects the *n*-value of a composite membrane. Liang & Hughes [160] reported an *n*-value of 0.66 when measured in the conventional film → substrate (FS) direction, whilst in the substrate → film (SF) direction the observed *n*-value was 0.5. A similar trend was reported by Ryi et al [162] who observed an *n*-value of 0.75 when measured in the FS direction, whilst in the SF direction the value dropped to 0.6.

In order to calculate the pressure exponent *n* of both CM–A and CM–B, the variation in hydrogen flux with feed pressure P*i* (200 – 300 kPa) was determined at constant membrane temperature. The *n*-value is then calculated by least squares regression of the experimental data. The variation in hydrogen flux with feed pressure at 450°C of CM–A and CM–B are shown in Figures 11.17 and 11.18 respectively. Although the flux is presented with *n* constrained to 0.5, 0.6, 0.7, 0.8, 0.9 and 1 it should be noted that this does not represent the best fit value. These values merely represent the range of exponents reported in the literature.

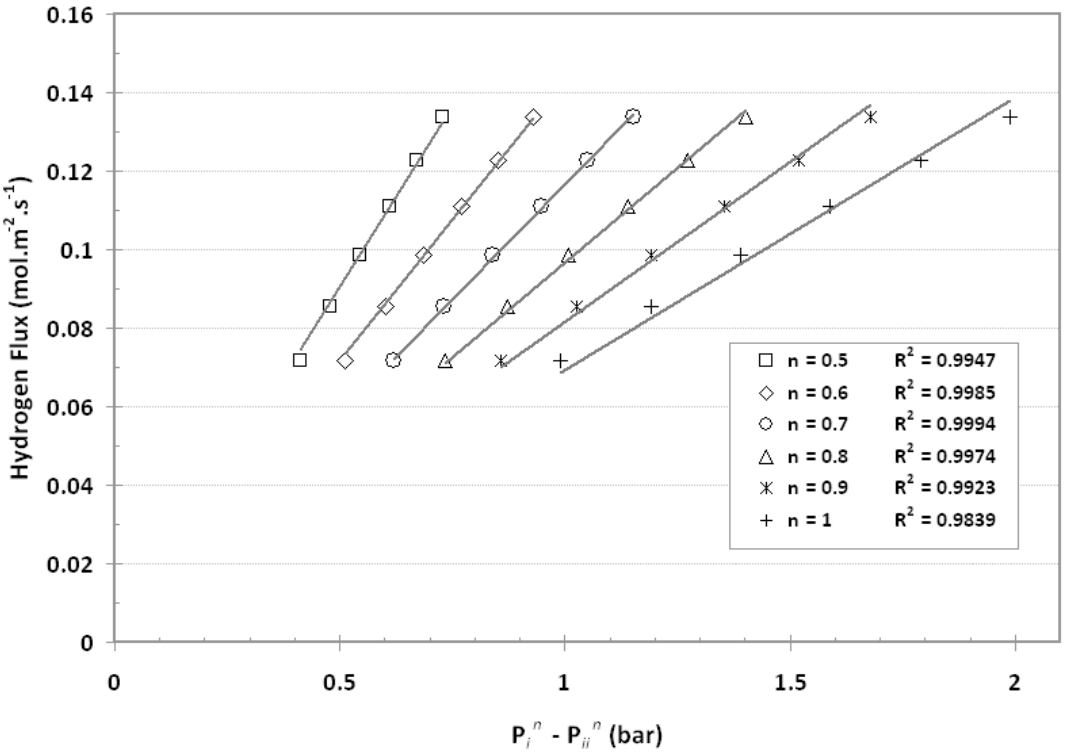

Figure 11.17 – Hydrogen flux through composite membrane CM–A at 450°C using the measured Pi and Pii

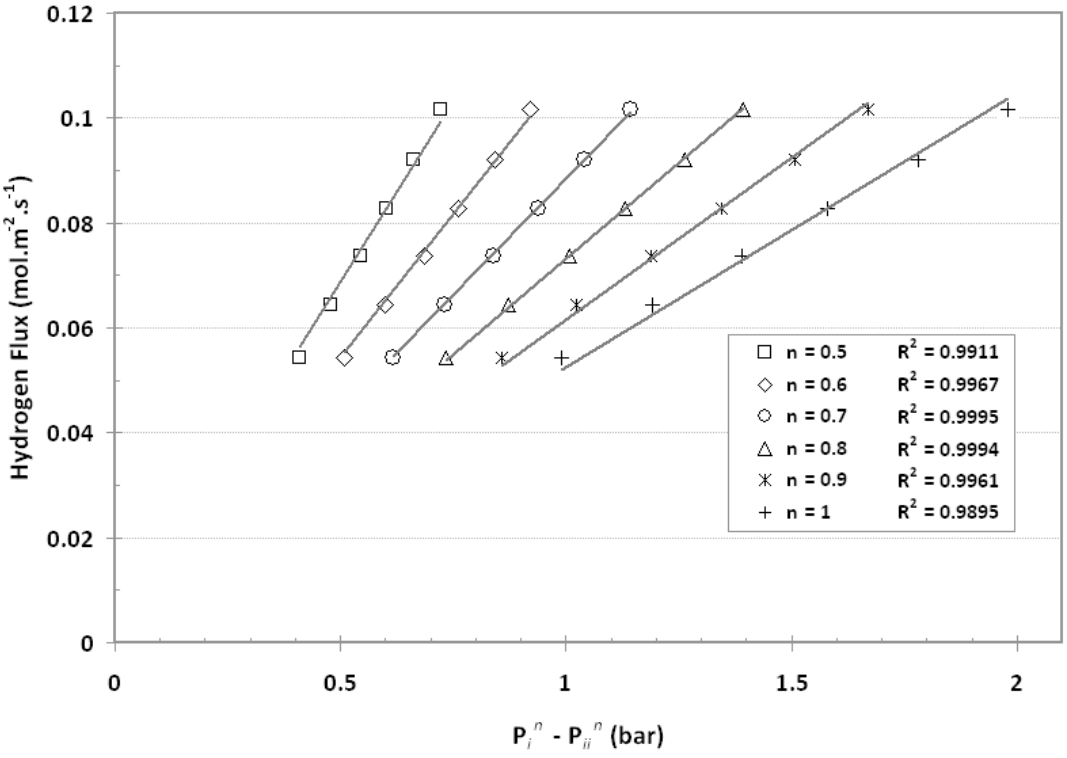

Figure 11.18 –Hydrogen flux through composite membrane CM–B at 450°C using the measured Pi and Pii

From Figures 11.17 and 11.18, it is clear that both membranes exhibit significant deviations from Sievert's type behaviour (n = 0.5). The best fit n-values were calculated as 0.70 and 0.74 for CM–A and CM–B respectively. When compared to the values determined for the bulk alloys, 0.52 and 0.54, the extent of the deviation is clear. However, the n-values of both membranes are in excellent agreement with a wide range of values reported for similar composite membranes including Ryi et al (n = 0.75) [162], Uemiya (n = 0.76) [159] and Rothenburger (n = 0.72) [149].

The deviation in n-value away from 0.5 is indicative of non-diffusion limited permeation. As discussed previously in Section 4.5, many authors assign such deviations simply to surface absorption / dissociation effects controlling the rate of permeation due to the relative thinness of the Pd layer. However, recent studies on free-standing Pd, Pd-Ag and Pd-Cu thin films have shown diffusion limited permeation in films of just 1.3 µm thickness [84, 85, 165]. It would appear therefore that, in addition to low permeability values, the substrate may contribute to the n-value deviations experienced by composite membranes. Further evidence for this may be drawn from the results of Rothenburger et al [149], Guazzone et al [158] and Roa et al [194] who all reported increasing n-values with increasing temperature. As described in Section 10.3.1.1, molecular flow across a porous substrate decreases with increasing temperature. Hence, as the resistance of the substrate increases, it has an ever greater effect on the n-value.

Temperature dependent n-values suggest that the dominant transport mechanism, or relative contribution of the active mechanisms, is also dependent on temperature. The activation energy for permeation (E_A) of a membrane is particularly sensitive to the active hydrogen transport mechanism. The activation energy of bulk palladium generally falls within 13 to 16 kJ.mol^{-1} [65, 79, 181-183]. The value established in the present work of 15.4 kJ.mol^{-1} is thus in good agreement with previous studies. However, in a similar manner to n-values, the E_A

values reported for composite membranes frequently deviate significantly from the equivalent bulk metal / alloy, thus providing further evidence of mechanisms other than classical diffusion controlling the permeation. Although many authors do not report activation energies and some report significantly greater E_A values [100], there appears to be a general trend of lower activation energy in composite membranes than the equivalent bulk metal / alloy. Values between 8 and 10 kJ.mol^{-1} have been reported for Pd composite membranes by Y. Huang et al [145], T.C Huang et al [163] and Uemiya et al [130].

Low activation energies represent less variation in permeability with temperature. Given that the substrate will offer greater resistance to flow at higher temperatures, the measured flux across a composite membrane is likely to exhibit non-Arrhenius type behaviour with temperature. Therefore, the effect of the substrate will be to mask the true temperature dependence of the permeability, *i.e.* as the effective resistance increases with temperature, the measured flow increases at a proportionally slower rate.

Interestingly, Tong et al [87] found that the activation energy of a Pd composite membrane was highly dependent on the pore size of the substrate. Palladium films of similar thickness were deposited onto both porous stainless steel and porous alumina. The activation energy of the Pd / alumina membranes were approximately 40 % lower than those for the Pd / PSS membranes. As described previously in Section 5.3, the permeance of a porous substrate is highly dependent on the average pore size. Therefore, the alumina substrate used by Tong et al [87] will offer greater resistance to flow and is likely to effect the apparent permeability to a greater extent than the porous stainless steel substrate.

In order to quantify the effect of the substrate on the activation energy of a composite membrane, the apparent permeability of CM–A and CM–B (as shown in Figure 11.16) have been compared to that determined in bulk Pd-Y in an Arrhenius-type plot (Figure 11.19).

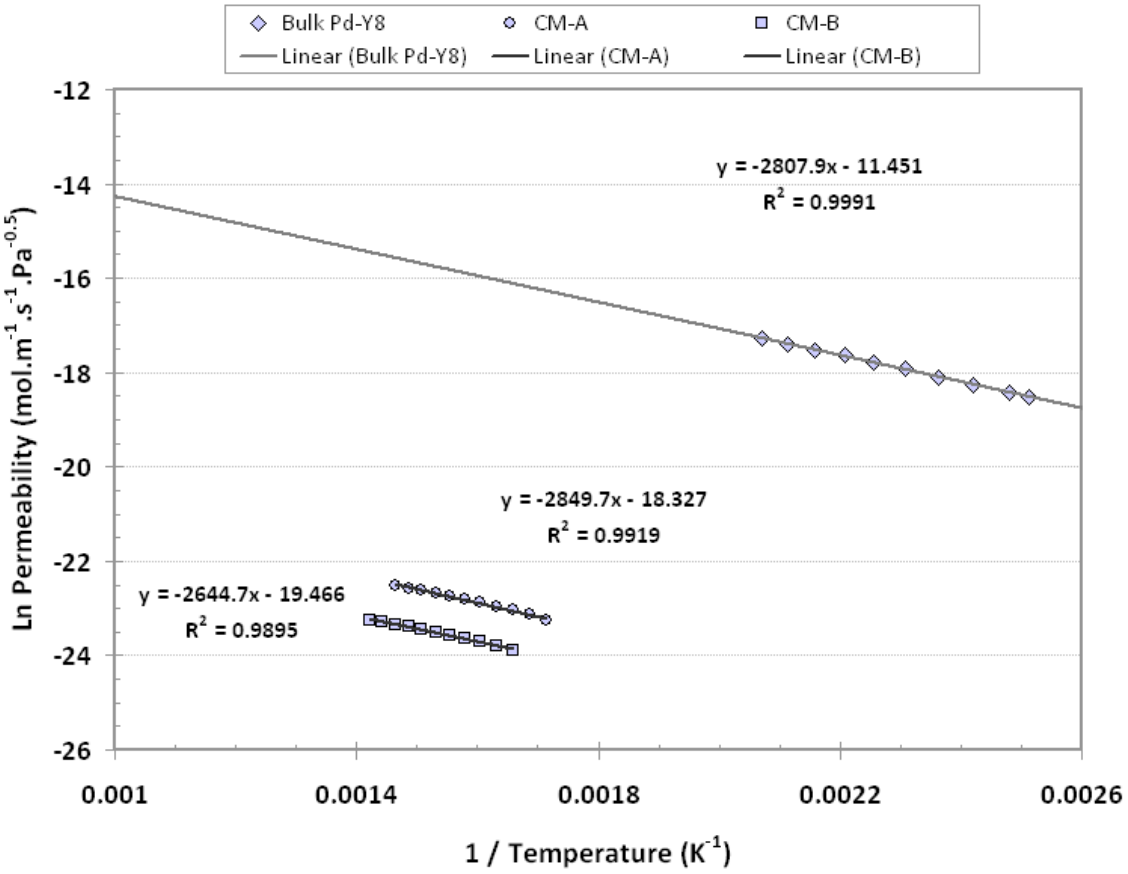

Figure 11.19 – Arrhenius-type plot of hydrogen permeability of CM–A and CM–B compared to bulk Pd-Y_8

Figure 11.19 clearly shows that both CM–A and CM–B exhibit inferior linear fits of permeability versus 1 / temperature when compared to the bulk alloy. The inferior fit of both composite membranes to the linearity expected for Arrhenius-type behaviour is further evidence that the relative contribution of the active permeation mechanisms to the observed flux is temperature dependent.

The quality of the Arrhenius-type linearity and, therefore, the validity of the associated E_A and Φ_o values, are difficult to compare to those reported in the literature because most authors do not report the regression coefficient of the data. Nevertheless, the Arrhenius plot has been used to calculate the E_A and Φ_o values of CM–A and CM–B, which are listed in Table 11.4.

Table 11.4 – Activation energy of CM–A and CM–B compared to the equivalent bulk Pd-Y alloys

	CM–A	Bulk Pd-Y_8	CM–B	Bulk Pd-Y_{10}
Activation Energy E_A ($kJ.mol^{-1}$)	23.7	23.3	22.0	19.5
Permeability Factor Φ_o ($mol.m^{-1}.s^{-1}.Pa^{-0.5}$)	1.66×10^{-7}	1.06×10^{-5}	9.02×10^{-8}	2.89×10^{-6}

As described previously, the permeability values at 400°C of CM–A and CM–B were just 4.1 % and 3.2 % that of the equivalent bulk alloys. As expected, these differences correspond to significantly lower Φ_o values. However, the apparent activation energy of both composite membranes are in good agreement with the bulk alloys. Indeed, the activation energy of CM–A is within 2 % of the bulk Pd-Y_8 value. The validity of this apparent conformity is uncertain. The regression coefficients of both composite membranes fall well beneath those of the bulk alloys, presumably due to the temperature dependent nature of the relative contribution of the active transport mechanisms. In addition, comparison with E_A values reported in the literature has to be done with qualification due to the absence of associated regression coefficient data.

In summary, when analysed using the general permeability equation, the permeability characteristics of both the composite membranes deviated significantly from that observed in the bulk alloys. The permeability was over an order a magnitude lower across the whole

temperature range studied and the pressure exponent *n* was found to increase from 0.52 and 0.54 in the bulk alloys to 0.70 and 0.74 in CM–A and CM–B membranes respectively. In addition, unlike the bulk membranes, the permeability of the composite membranes did not exhibit purely Arrhenius-type behaviour with temperature. However, it should be noted that the permeation behaviour observed for both the Pd-Y composite membranes is extremely similar to that reported in the literature for a wide range of Pd, Pd-Ag and Pd-Cu composite membranes. Considering these agreements and the close similarities of the composite-type structures, it is a reasonable assumption that the source of the deviations is common. These deviations are analysed further in the following section.

11.3.4 – Composite Membrane Permeability - Series Resistance Model

The analysis presented within this section assumes that both the Pd-Y film and the underlying substrate offer significant resistance to hydrogen transport. Therefore, each component requires a driving force for hydrogen permeation and, in order to quantify the observed permeation, knowledge of the driving force across each component is essential. In order to determine the driving force across each component, both the measured hydrogen flux and the α_K and β_V permeation coefficients of the substrate are applied to a series resistance type model, similar to that proposed by Huang et al [163].

The series resistance model assumes that the permeation resistance of each component are additive. Therefore the total pressure gradient measured across the membrane, ΔP, is equal to the sum of the pressure gradient across the Pd-Y film and the pressure gradient across the substrate. The model is represented schematically in Figure 11.20, from which, it is clear that

establishing the pressure at the interface between the Pd-Y film and the substrate, P_{int}, is the essential step. Once P_{int} is established, it is straight forward to characterise the flux across each layer.

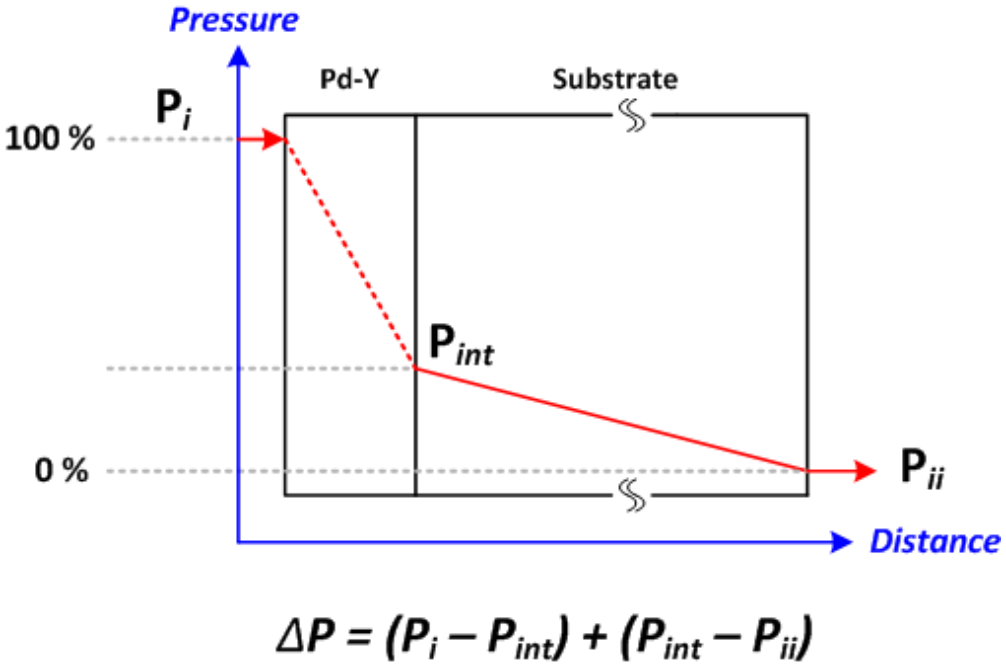

Figure 11.20 – Schematic drawing of the series resistance model with the effective pressure gradient across each layer shown as a percentage of the total measured pressure gradient

However, there are no direct measurement techniques for P_{int}, therefore it must be calculated from the experimental data. This is further complicated by the fact that the permeation mechanisms active in each component respond differently to temperature and pressure. In terms of permeation resistance, a composite membrane is a dynamic system. Therefore, the value of P_{int} is dependent on the instantaneous conditions of temperature and pressure.

In order to determine the value of P_{int} a steady-state model is adopted (Figure 11.21).

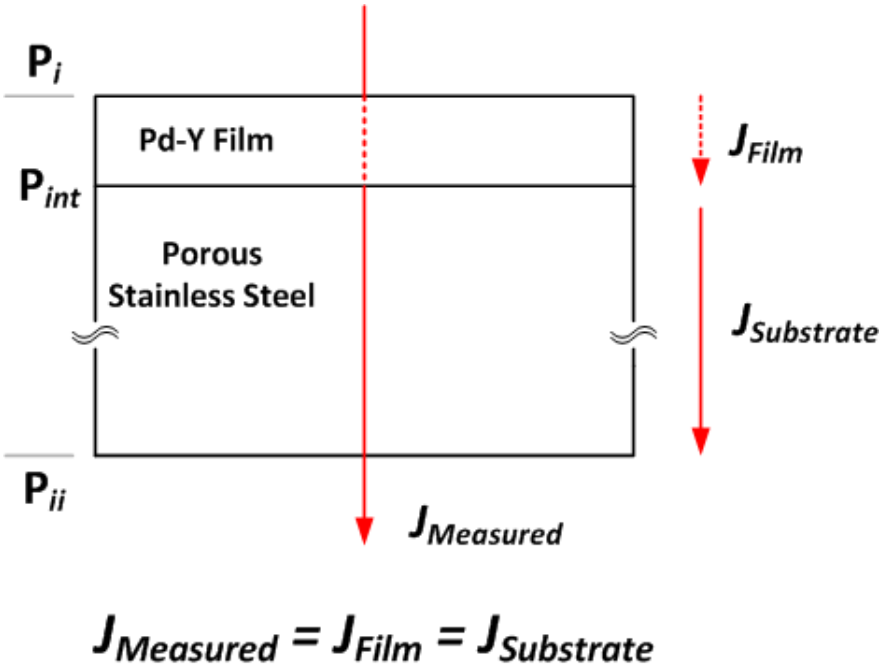

Figure 11.21 – Schematic drawing of flux through a composite membrane under steady state conditions

Of the terms used in Figure 11.21, the high pressure *Pi*, the low pressure *Pii* and the total hydrogen flux across the membrane, $J_{Measured}$, are determined experimentally. Under steady-state conditions, the measured flux, $J_{Measured}$, must be equal to both the flux across the Pd-Y film, J_{Film}, and the flux across the substrate $J_{Substrate}$.

As shown previously in Section 10.3, the permeation of hydrogen across a porous substrate, J_{H2}, may be expressed as,

$$J_{H_2} = [\, \alpha_K + (\beta_V \, P_{av}) \,] \, \Delta P \qquad \textit{Eqn 11.3}$$

where P_{av}, ΔP, α_K and β_V denote the average pressure, pressure gradient and the Knudsen and Poiseuille permeation coefficients respectively. Equation 11.3 may be modified to express the hydrogen flux across the composite membrane substrate in terms of P*int* and P*ii*,

$$J_{Substrate} = \left[\alpha_K + \left(\beta_V \left(\frac{P_{int} + P_{ii}}{2} \right) \right) \right] (P_{int} - P_{ii}) \qquad Eqn\ 11.4$$

As described in Section 11.3.1, the room temperature α_K and β_V permeation coefficients were determined for the substrate sections of both CM–A and CM–B prior to Pd-Y deposition. The values are listed with the calculated geometrical factors ε/τ and r in Table 11.5.

Table 11.5 – Permeation coefficients and geometrical factors of the CM–A and CM–B substrates

Membrane	α_K (mol.m^{-2}.s^{-1}.Pa^{-1})	β_V (mol.m^{-2}.s^{-1}.Pa^{-2})	ε/τ	r (µm)
CM – A	1.687 x10^{-6}	2.903 x10^{-11}	0.248	0.453
CM – B	1.439 x10^{-6}	2.645 x10^{-11}	0.198	0.484

Given that $J_{Substrate}$ and P*ii* are measured experimentally, Eqn. 11.4 may thus be re-arranged to give a quadratic expression for P_{int}. Full details of this process are given in Appendix II.

Therefore, assuming thermal equilibrium across the composite membrane, the value of P_{int} may be calculated at any given point during the permeation measurements. As shown in Figure 11.20, the value of P_{int} may be expressed in terms of a percentage of the overall pressure gradient across the membrane (P*i* – P*ii*). Analysing the interface pressure this way gives a clear indication of the relative resistance offered by each component. Using the calculated P_{int} values and the hydrogen viscosity data of Assael [191], the measured hydrogen flux across both composite membranes are compared to the percentage pressure gradient acting across the Pd-Y film in Figures 11.22 and 11.23.

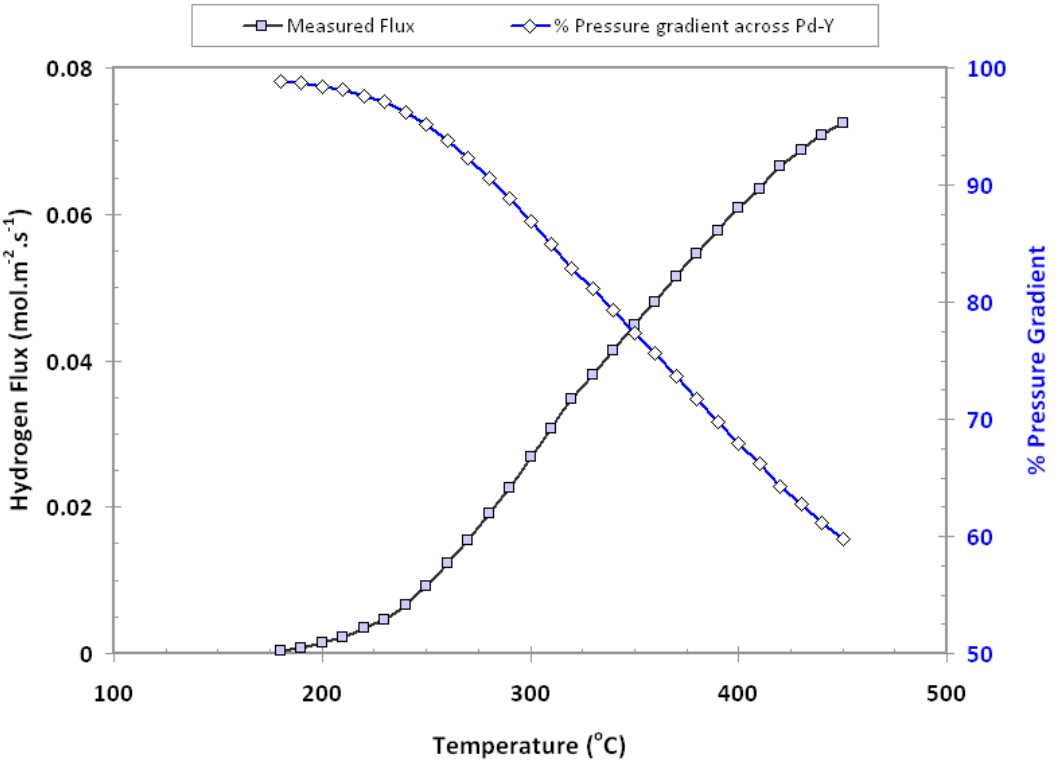

Figure 11.22 – Comparison of the measured flux and effective pressure gradient across the Pd-Y film – CM–A

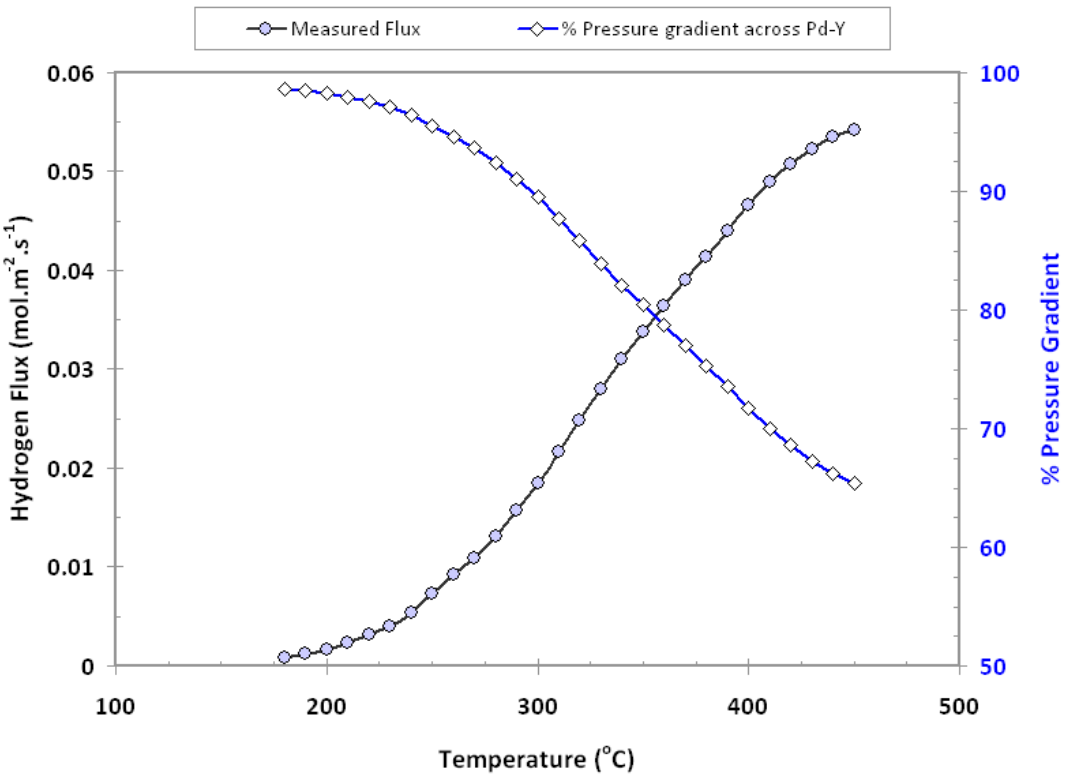

Figure 11.23 – Comparison of the measured flux and effective pressure gradient across the Pd-Y film – CM–B

Figures 11.22 and 11.23 clearly show that the effective pressure gradient acting across the Pd-Y film ($Pi - P_{int}$) decreases significantly with increasing temperature. At 180ºC, the Pd-Y film accounts for 98.6 % and 98.8 % of the total resistance of CM–A and CM–B respectively. As the temperature increases, so does the resistance of the substrate. Accordingly, the resistance of the Pd-Y film decreases proportionally until, at 450ºC, the Pd-Y film only accounts for 59.8 % and 65.4 % of the total resistance in CM–A and CM–B respectively.

Clearly, the assumption that the substrate offers minimal permeation resistance is invalid. Therefore, the values of composite membrane permeability based on the general permeability equation, discussed in the previous section, are not representative of the Pd-Y film. In order to establish accurate permeability values, the measured flux across the Pd-Y film must be characterised using a modified version of the general permeability equation,

$$J_{H_2} = \Phi \frac{\left(Pi_{H_2}^n - Pint_{H_2}^n\right)}{l(x)} \qquad Eqn\ 11.5$$

where the low pressure term P*ii* is replaced by the calculated value of P*int*, the internal film-substrate interface pressure. When the measured hydrogen flux (J_{H2}), Pd-Y film thickness (l) and feed pressure (P*i*) along with the calculated interface pressure (P*int*) for both CM–A and CM–B are inserted into Equation 11.5, thus accounting for the substrate resistance, the resultant permeability value is that of the Pd-Y film alone. Throughout the remaining sections the Pd-Y film component of the composite membranes are referred to as Pd-$Y_{Film\text{-}A}$ and Pd-$Y_{Film\text{-}B}$. The permeability of Pd-$Y_{Film\text{-}A}$ and Pd-$Y_{Film\text{-}B}$, calculated using Equation 11.5, are compared to those originally calculated for CM–A and CM–B using the general permeability equation in Figures 11.24 and 11.25.

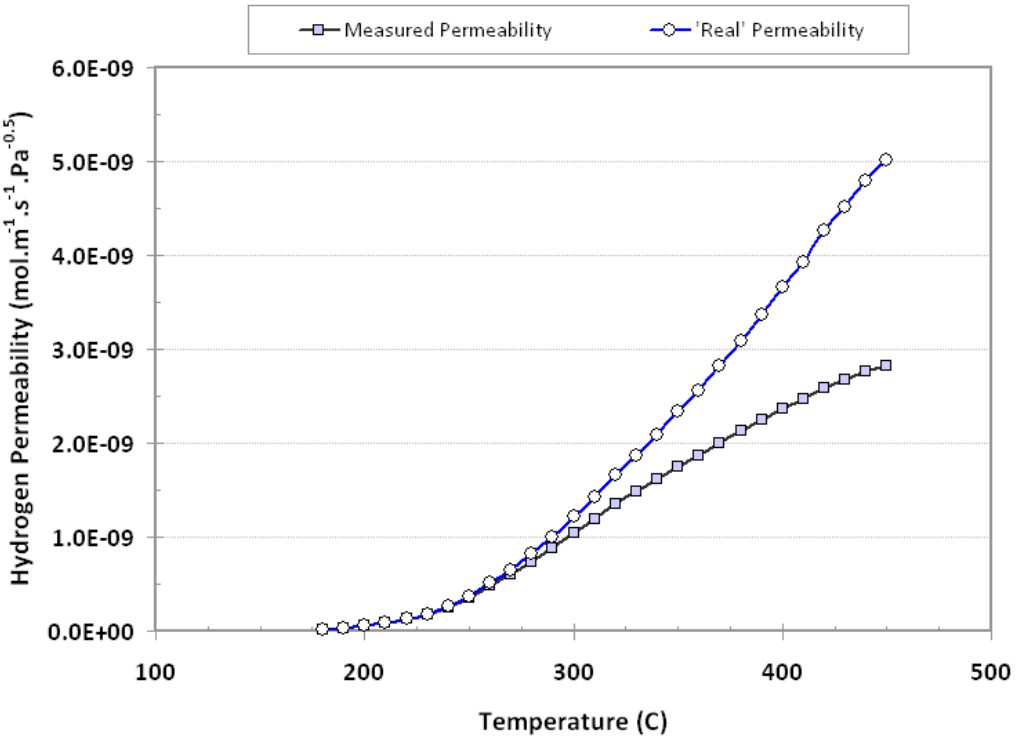

Figure 11.24 – Measured permeability of CM–A compared to the calculated 'real' permeability of Pd-Y_{Film-A}

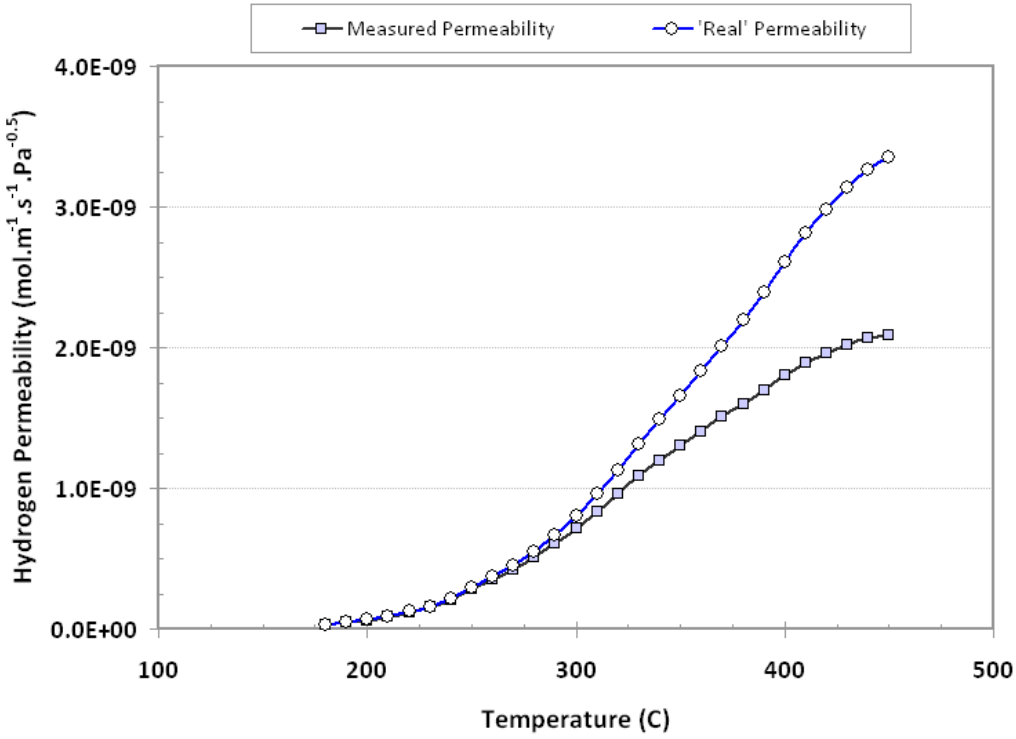

Figure 11.25 – Measured permeability of CM–B compared to the calculated 'real' permeability of Pd-Y_{Film-B}

Figures 11.24 and 11.25 clearly show the extent to which the substrate affects the apparent permeability. At low temperatures (< 250°C) the substrate offers less than 5 % of the total resistance, hence there is little difference between the apparent permeability and the real permeability. As the temperature increases, the rate of atomic diffusion through the Pd-Y film increases whilst the molecular flow through the substrate decreases. The relative resistance of the substrate increases proportionally with temperature. At 450°C, the substrate contributes approximately 40 % of the total resistance, thus resulting in a considerable reduction in the 'apparent' permeability of CM–A and CM–B.

The extent to which the substrate influences the temperature dependence of the permeability is further emphasised when the Arrhenius-type relationship is used to analyse the data. The permeability of Pd-$Y_{Films\text{-}A\ \&\ B}$ are compared to that measured in bulk Pd-Y_8 in Figure 11.26.

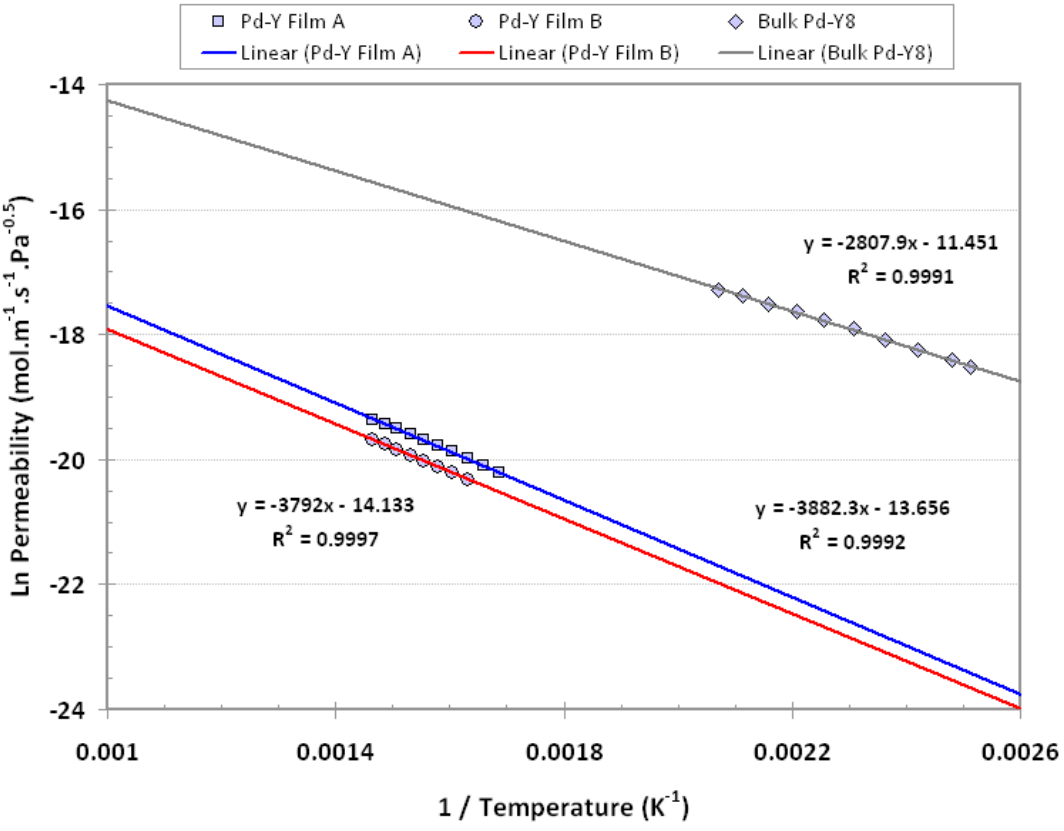

Figure 11.26 – Arrhenius-type plot of hydrogen permeability of Pd-Y films A and B compared to bulk Pd-Y_8

As shown in Figure 11.26, both Pd-Y films exhibit a good linear fit to Arrhenius-type behaviour with high regression coefficients. This is in contrast to the behaviour observed in CM–A and CM–B where the substrate was assumed to offer zero resistance. The activation energy, E_A, and permeability factor, Φ_o, of both Pd-Y films have been calculated and are compared to the values established for the equivalent bulk alloys in Table 11.6.

Table 11.6 – Activation energy of Pd-Y Films A and B compared to the equivalent bulk Pd-Y alloys

	Pd-$Y_{Film\ A}$	CM – A	Bulk Pd-Y_8	**Pd-$Y_{Film\ B}$**	CM – B	Bulk Pd-Y_{10}
Activation Energy E_A ($kJ.mol^{-1}$)	**32.3**	23.7	23.3	**31.5**	22.0	19.5
Permeability Factor Φ_o ($mol.m^{-1}.s^{-1}.Pa^{-0.5}$)	**1.17×10^{-6}**	1.66×10^{-7}	1.06×10^{-5}	**7.28×10^{-7}**	9.02×10^{-8}	2.89×10^{-6}

Interestingly, the calculated activation energies of both Pd-Y films are considerably greater than those determined for the equivalent bulk alloys. As discussed in the previous section, although many authors do not report the activation energy of composite membranes, the general observed trend appears to be lower E_A values in composite membranes than the equivalent bulk metal / alloy [130, 145, 163]. The only reported attempt to isolate the E_A value of the thin film, thus eliminating any contribution by the substrate, is that by Huang et al [163]. Huang et al measured the E_A values of a 7 µm Pd / α-alumina composite membrane between 327 and 396°C. The reported composite membrane E_A value was 8.73 $kJ.mol^{-1}$, significantly below the widely reported values for bulk Pd of 13 – 16 $kJ.mol^{-1}$ [65, 79, 181-183]. After accounting for the substrate resistance, using a similar series resistance model as used in the current work, an E_A value of 15.6 $kJ.mol^{-1}$ was calculated for the 7 µm Pd film, which is in excellent agreement with the bulk values. In the present work however, although the

observation that the E_A of the composite membranes are significantly lower than in the thin films is similar to Huang et al [163], the values calculated for the Pd-Y films are considerably greater than the equivalent bulk alloys. It should be noted that there is a lack of available data for comparison. Indeed, the recent studies by Gade et al [85] and Mejdell et al [84] on free-standing Pd, Pd-Cu and Pd-Ag thin films do not report activation energy values.

A possible explanation for the high E_A values is the presence of an additional alloy layer formed by interdiffusion at the Pd-Y / SS interface. As mentioned previously, due to the high degree of surface oxidation after laser melting, it was necessary to deposit a 500 nm stainless steel adhesion layer on the substrate surface prior to Pd-Y deposition. The deposited Pd-Y films were then annealed (10^{-6} mbar, 400°C, 6 hrs) in order to promote the adhesion. Therefore, although significant Pd / SS interdiffusion would not be expected until around 600°C [112], there will undoubtedly be some degree of diffusion across the interface. Based on the work of Prosperi [112], the dominant migration will be that of Fe from the SS layer into the overlying Pd-Y film. However, the interdiffusion is likely to be restricted to the near surface region of the Pd-Y / SS interface layer, rather than across the whole Pd-Y film. Using the diffusion coefficient of Fe at 400°C derived by Prosperi [112] it is estimated that penetration will be less than 100 nm after 6 hrs. Further evidence for limited interdiffusion comes from x-ray diffraction studies on parallel composite membranes which did not reveal any evidence of Fe out-diffusion within the Pd-Y layer after vacuum annealing.

Initially, the out-diffusion of Fe into Pd-Y forms a dilute solid solution however, larger and more significant Pd / Fe interdiffusion can result in the formation of Pd_3Fe [112]. Both effects would almost certainly have a significant effect on the hydrogen permeation across the Pd-Y film. Given the relatively low level of interdiffusion expected at 400°C, the effect is likely to be the formation of a very thin layer of solid solution Pd-Y-Fe. Although there is no published

information regarding the effect of Fe content on the permeability of Pd-Y, Bryden & Ying [81] reported that the permeability of Pd-$Fe_{2.5at.\%}$ is over 50 % lower than pure Pd. However, the effect on activation energy was not reported.

The possibility of Pd-Y / SS interdiffusion affecting the activation energy of the Pd-Y films would coincide with Huang et al [163] who found that, once corrected for substrate resistance, the activation energy of a 7 μm Pd film supported on α-alumina was in good agreement with the values for bulk Pd. Over the temperature range studied by Huang et al (327 – 396°C) it is reasonable to assume minimal Pd / α-alumina interaction.

However, the contribution of the region of the Pd-Y film directly in contact with the SS layer, and thus the likely initiation sites of the Pd-Y / Fe interdiffusion, to the overall permeation is debateable. This is discussed further later within the current section.

A further possibility however, is that the E_A values exhibited by the bulk alloys and the thin films are dependent on the degree of order / disorder within the Pd-Y lattice. As previously discussed, several investigators including Wileman [55, 56], Hughes [57], Doyle [46, 47] and Poyser [58] have all reported evidence of the ordered cubic Pd_7Y type structure in bulk Pd-Y alloys with high Y content. When cooled under vacuum from above a certain critical temperature, estimated as 455 ± 5°C in Pd-Y_{10} by Doyle [46], the alloy forms the ordered Pd_7Y structure. However, when cooled in a hydrogen atmosphere the alloy remains disordered. Wileman [55] determined the hydrogen permeability of Pd-Y_8 in both the ordered and disordered condition. The activation energy of the ordered alloy (25.3 $kJ.mol^{-1}$) was found to be considerably lower than that in the disordered alloy (34.2 $kJ.mol^{-1}$). As described in Section 9.1.2, the activation energy of the bulk Pd-Y_8 alloy determined in the present work was 23.3 $kJ.mol^{-1}$. Considering all the bulk Pd-Y alloys were measured in the vacuum-annealed condition it was concluded

that the bulk Pd-Y_8 membrane exhibited the 'ordered' structure as described by Wileman [55]. Interestingly, the activation energy of Pd-$Y_{Film\text{-}A,}$ (32.3 kJ.mol^{-1}), which has a composition Pd-$Y_{8.31at\%}$, closely matches the disordered value reported by Wileman (34.2 kJ.mol^{-1}) [55].

It would appear therefore, that the co-sputtered Pd-Y thin films are deposited with a disordered FCC structure. Although no direct evidence for any order / disorder effect, in either the bulk alloys or thin films, was observed using XRD, it would seem reasonable especially as similar effects have been observed in the Fe-Pt system. Bulk Fe-Pt alloys form the tetragonal AuCu-type structure at temperatures below 1300°C. However, sputtered Fe-Pt films exhibit a disordered FCC structure [195, 196]. Takahashi et al reported that the deposited Fe-Pt films only ordered after annealing at 600°C [196].

Given the similarity between the Pd-Y film E_A values and the disordered bulk values reported by Wileman [55], it is a reasonable assumption that the Pd-Y films are in the disordered condition. Therefore, after the substrate resistance is accounted for, the high E_A values exhibited by Pd-Y films A and B compared to those measured in the bulk alloys may be due to the state of order. Hence, the effect of the substrate resistance was to reduce the apparent activation energy compared to the bulk alloys. Therefore, the similarity between the E_A observed for the uncorrected composite membranes and the bulk alloys appears to be a coincidence.

After the substrate resistance was accounted for, the permeability of both Pd-$Y_{Film\text{-}A}$ and Pd-$Y_{Film\text{-}B}$ demonstrate Arrhenius-type variation with temperature. Such behaviour is indicative of thermally activated, diffusion controlled permeation Therefore, it would be expected that the pressure exponent n of the Pd-Y films will also correspond to diffusion controlled permeation. As described in the previous section, the value of n is determined by

least squares regression of the variation in hydrogen flux with applied pressure. In order to calculate the *n*-value of the Pd-Y films, the measured flux must be analysed in terms of the feed pressure P*i* and the interface pressure P*int*. In an identical manner to that described above, the value of P*int* has been determined using the steady-state model. The variation in hydrogen flux with applied pressure ($Pi^n - Pint^n$) across Pd-Y_{Film-A} and Pd-Y_{Film-B} at 450°C are shown in Figures 11.27 and 11.28, respectively. It should be noted that although *n*-values of 0.5, 0.6, 0.7, 0.8, 0.9 and 1 are plotted, these values does not represent the best fit value of *n*. These values represent the range of exponents reported in the literature for composite membranes.

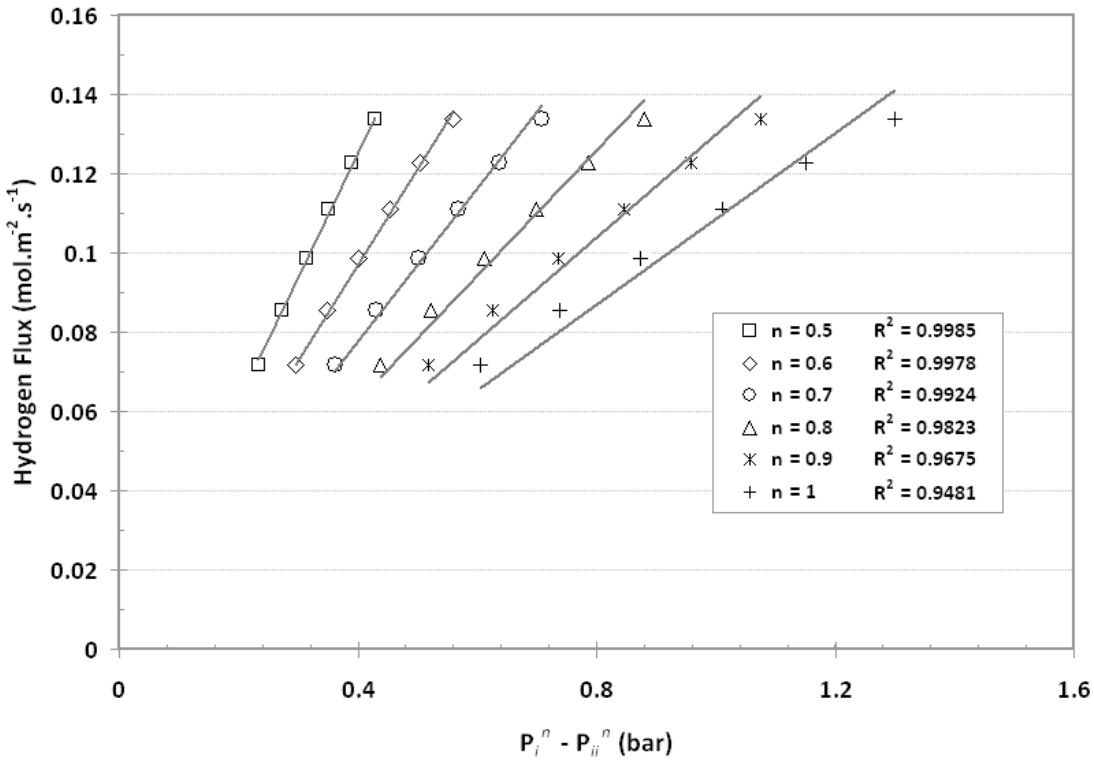

Figure 11.27 – Pressure dependency n of hydrogen flux across Pd-Y_{Film-A} using Pi and Pint

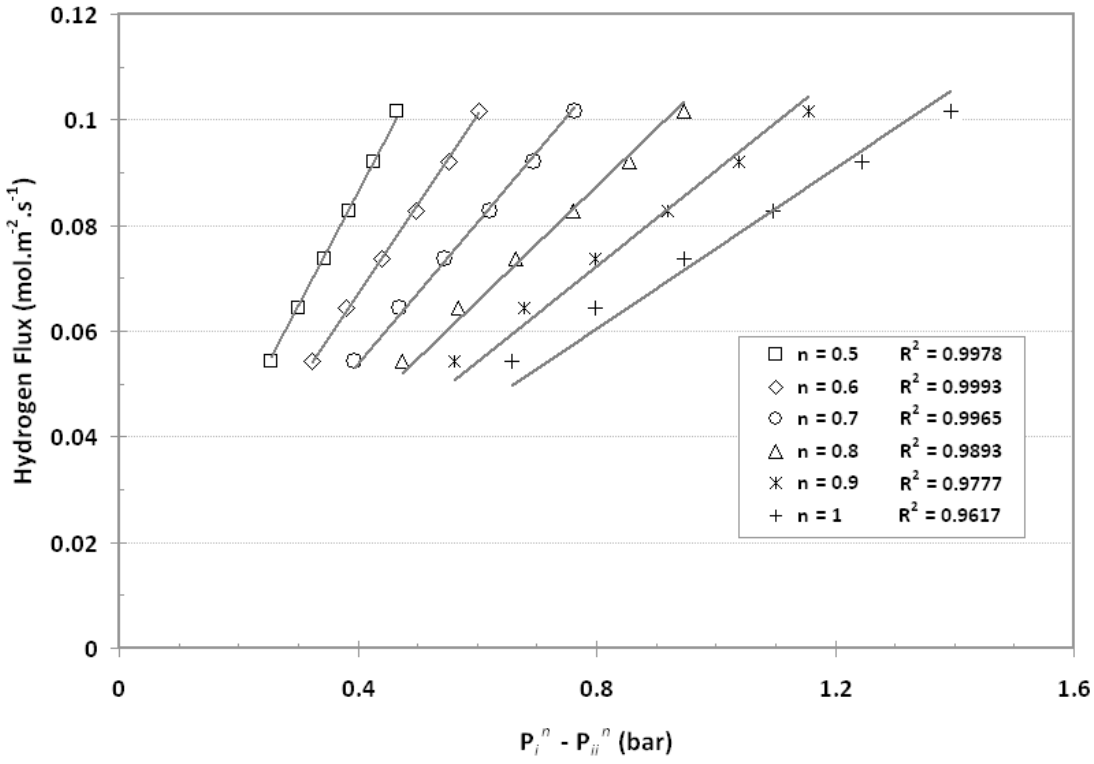

Figure 11.28 – Pressure dependency n of hydrogen flux across Pd-Y_{Film-B} using Pi and Pint

When compared to Figures 11.17 and 11.18 in the previous section, the effect of the substrate on *n*-value is clear. The *n*-values of Pd-Y_{Film-A} and Pd-Y_{Film-B} were calculated as 0.53 and 0.58 respectively and are compared to those calculated in the CM–A, CM–B and the bulk membranes in Table 11.7.

Table 11.7 – Pressure exponent n of Pd-Y films A and B compared to composite membranes and bulk Pd-Y alloys

	Pd-$Y_{Film\ A}$	CM–A	Bulk Pd-Y_8	**Pd-$Y_{Film\ B}$**	CM–B	Bulk Pd-Y_{10}
n-value	**0.53**	0.70	0.52	**0.58**	0.74	0.54

As described previously, the *n*-values of composite membranes are frequently reported to deviate from Sievert's law ($n = 0.5$), thus implying non-diffusion limited permeation. The values of 0.70 and 0.74, observed in CM–A and CM–B respectively, are in good agreement with a wide range of previously reported values for similar composite membranes [149, 159, 162]. Many authors ascribe these deviations to the increasingly role of surface adsorption / dissociation effects controlling the rate of permeation due to the relative thinness of the Pd layer. However, such deviations were not observed in recent studies on free-standing Pd, Pd-Ag and Pd-Cu thin film membranes [84, 85, 165]. As shown in Table 11.7, when the resistance of the substrate is accounted for, the observed *n*-value of both Pd-Y films return toward 0.5 and are in good agreement with the values determined for the bulk alloys.

The contrasting hydrogen transport mechanisms active in each layer of the composite membrane are further demonstrated by the variation of the interface pressure P*int* with applied pressure P*i*. At 450°C, and an applied pressure of 200 kPa (P*ii* = 100 kPa), CM–A and CM–B exhibit an interface pressure P*int* of 139 kPa and 134 kPa respectively. Therefore, the substrate contributes 39 % of the total transport resistance of CM–A and 34 % of CM–B. When the applied pressure is raised to 300 kPa (P*ii* = 100 kPa), the values of P*int* are calculated as 170 kPa and 161 kPa, which represent 35 % and 30.5 % of the total resistance in CM–A and CM–B respectively. Hence, the relative contribution of the substrate to the overall resistance decreases with increasing applied pressure. The underlying reason for this is the different pressure dependencies of atomic diffusion and molecular flow. Although both mechanisms are proportional to the pressure gradient, $Pi^n - Pii^n$, the exponent *n* differs between the two mechanisms. As described above, the *n*-value of Pd-$Y_{Film\text{-}A}$ was 0.53 whilst for the molecular flow across the substrate the *n*-value would be 1. Additionally, the viscous

component of the molecular flow is proportional to the average pressure P_{av}. Hence, as the applied pressure increases the effective resistance of the substrate decreases.

The variation of P*int* with applied pressure coupled with the large variations due to temperature, as described previously, highlights the complex nature of hydrogen permeation in composite membranes. The dominant permeation mechanism of each component displays an opposite resistance behaviour with increasing temperature, and exhibits different responses to variations in applied pressure. The value of P*int* depends strongly on the instantaneous conditions of temperature and applied pressure. This variation of P*int*, and indeed the very existence of P*int*, significantly affects the permeation characteristics of a composite membrane and contributes to deviations in permeability Φ, pressure exponent n and activation energy E_A when compared to the equivalent bulk metal / alloy.

Based on the results presented within this section, it would appear that the permeation resistance of the substrate is likely to be the predominant cause of non-diffusion limited permeation in the Pd-Y / PSS composite membranes. After the substrate resistance was accounted for, thereby isolating the Pd-Y permeation, both Pd-Y films exhibited Arrhenius-type behaviour with temperature and pressure exponents n of close to 0.5. Such hydrogen permeation behaviour is in good agreement with that observed in bulk Pd-Y and is strongly indicative of diffusion limited permeation.

The composite membranes studied within this work share many similarities with the range of Pd-based composite membranes reported in the literature, both in terms of structure and observed permeation characteristics. It is a reasonable assumption, therefore, that substrate resistance is the likely source of the widely reported non-diffusion limited permeation in Pd and Pd alloy composite membranes.

However, the permeation resistance of the substrate does not account for all the observed permeability deviations. In addition to non-diffusion limited permeation, the permeability of the composite membranes fell over an order of magnitude beneath that determined for the equivalent bulk alloys over the entire temperature range studied (180 – 450ºC). This observation is in good agreement with other investigators who, almost without exception, report composite membrane permeability values 1 – 3 orders of magnitude below that for the equivalent bulk metal / alloy (see Section 4.5). Although application of the steady-state model reveals that the substrate contributes significantly to the overall resistance, and therefore the low permeability values (Figures 11.24 and 11.25), the resultant reduction in effective pressure gradient across the Pd-Y film does not fully account for the observed differences in permeability. Comparison of the permeability in each system at 400ºC illustrates the extent of the deviations and the effect of the substrate (Table 11.8).

Table 11.8 – Comparison of the composite membrane permeability at 400ºC to the equivalent bulk membranes

	Hydrogen Permeability Φ @ 400ºC (mol.m^{-1}.s^{-1}.Pa$^{-0.5}$)				
	Composite Φ	Substrate Resistance %	Thin Film Φ	Bulk Alloy Φ	Thin Film % of Bulk
Membrane A	2.37 x10^{-9}	55 % →	3.67 x10^{-9}	5.80 x10^{-8}	6.3 %
Membrane B	1.80 x10^{-9}	45 % →	2.61 x10^{-9}	5.61 x10^{-8}	4.7 %

As shown in Table 11.8, when the substrate resistance is accounted for, the apparent permeability of Pd-Y films A and B increases by 55 % and 45 % respectively. However, these corrected permeability values still only represent 6.3 % and 4.7 % of the permeability observed in the equivalent bulk membranes. Such large differences in permeability cannot be

accounted for by experimental uncertainties such as small variations in membrane thickness or interface pressure calculations. It would appear that some aspect of the composite membrane, or production procedure, has a detrimental effect on the apparent permeability of the thin film. The possibility of contamination or surface inactivity may be discounted due to the observation that, after the substrate resistance was accounted for, both Pd-Y films exhibit diffusion-limited permeation.

A possible source of the low apparent permeability is the presence of Fe within the Pd-Y film. As mentioned earlier in this section, due to the level of surface oxidation during the laser melting process, it was necessary to deposit a 500 nm stainless steel adhesion layer prior to Pd-Y deposition. The interdiffusion of Fe and Pd is a common problem regarding Pd / PSS composite membranes and even small amounts of Fe is known to significantly reduce the hydrogen permeability of Pd [81] . Bryden & Ying reported that the hydrogen permeability of Pd-$Fe_{2.5at.\%}$ is over 50 % lower than pure Pd [81]. Although there will undoubtedly be some level of Pd-Y / Fe interdiffusion during operation of the membranes, the extent of the Pd-Y-Fe solid solution layer is likely to be limited. As noted previously, based on the work of Prosperi [112] the penetration of Fe into the Pd-Y film is estimated to be < 100 nm. Indeed, x-ray diffraction of parallel composite membranes did not exhibit any evidence of Fe after vacuum annealing at 400ºC for 6 hrs. However, the presence of small amounts of Fe within the interface region of the Pd-Y film would be unlikely to account for the order of magnitude difference in apparent permeability.

Another possible source of the permeability differences is the uncertainty over the active membrane area. Although the permeability equation is usually expressed using the measured hydrogen flux, J_{H2}, the flux is given by the gas flow per unit area. Therefore, the permeability equation may be expressed in terms of the flow rate F_{H2} as,

$$F_{H_2} = \Phi . A . \frac{\left(Pi_{H_2}^{n} - Pint_{H_2}^{n}\right)}{l(x)} \qquad Eqn\ 11.6$$

Where F_{H2} is the flow rate (mol.s^{-1}) and A is the active area (m^2). The observed hydrogen flow rate is directly proportional to the active area. Therefore any experimental variations in the active area are directly proportional to the apparent permeability.

Medjell et al [84] reported that the apparent permeability of sputtered, free-standing Pd-Ag membranes doubled after heating the films in air to 300ºC. Similar effects were observed for Pd and Pd-Cu composite membranes heated to 350ºC by Roa et al [98]. In both cases, Atomic Force Microscopy (AFM) studies of the membrane surface revealed that exposure to oxygen above 300ºC significantly increased the surface roughness, thereby increasing the surface area. Roa et al [98] estimated that the total surface area was increased by 30 % compared to the as-deposited surface. Although the effect of air annealing prior to hydrogen exposure was not investigated during this work, it is conceivable that it may have an effect similar to that observed by Medjell et al [84] and Roa et al [98]. Indeed, Fort et al [15] have previously reported that the apparent permeability of bulk Pd-Y alloys may be improved by exposing the membrane to air at > 327ºC. Fort et al [15] ascribed the improvements in apparent permeability to the formation of Y_2O_3 flakes on the membrane surface, which subsequently expose a clean, highly active Pd-Y layer. However, similar to the possibility of Pd-Y / Fe interdiffusion, the potential effect on permeability is relatively small in comparison to the observed differences.

An inherent similarity between all composites membranes is that only a certain proportion of the substrate surface is open space *i.e.* the surface porosity. The remaining surface area consists of the dense particles which form the porous structure. However, the area used to

calculate the permeability (Equation 11.6) of a composite membrane is typically calculated using the dimensions of the external surface exposed to the feed gas. Presumably, this is due to the difficulty in establishing an effective interface surface area. Any attempt to estimate the interface surface area involves many uncertainties. Firstly, most porous substrates possess extremely non-uniform particle shapes and sizes. Secondly, the precise mechanism of pore coverage is unknown and is likely to vary between deposition techniques and thirdly, the degree of film / substrate adhesion at contact points is unknown.

Recently, Okazaki et al [197] produced 4 μm Pd / alumina composite membranes and successfully removed the deposited Pd film from the alumina substrate. Interestingly, this achievement demonstrates the relative lack of film / substrate adhesion typical of ceramic substrates. However, the interface surface of the Pd film exhibited a very different topography to the external surface (Figure 11.29).

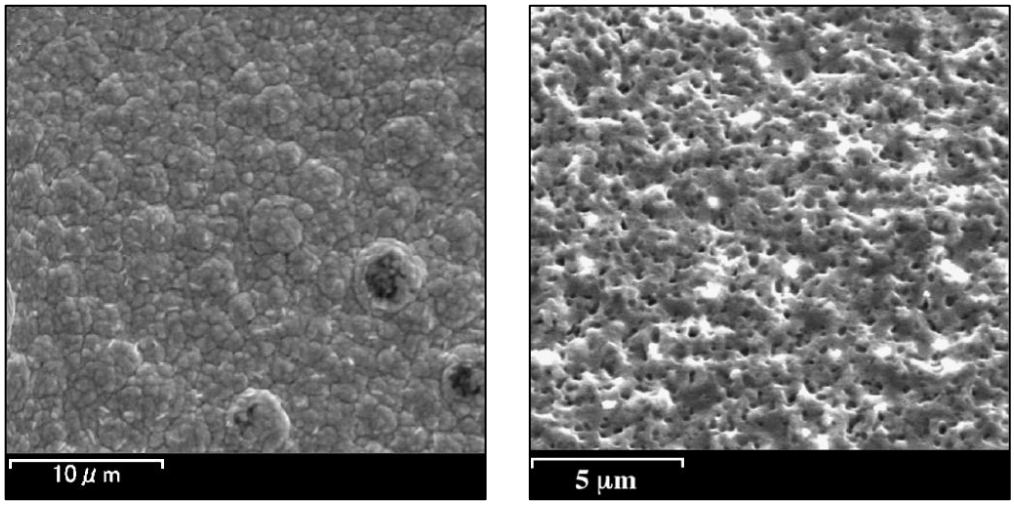

Figure 11.29 – SEM images showing the external and internal surface topography of a 4 μm Pd film deposited on alumina. Taken from Okazaki et al [197]

As shown in Figure 11.29, the external surface appears relatively uniform and defect-free, and is remarkably similar to that observed in the present work. The internal surface however, is particularly non-uniform and exhibits a large number of small pores. Although Okazaki et al [197] do not present any details of the alumina substrate surface topography, the average pore size of the substrate is reported as 150 nm, approximately matching the diameter of the pores observed within the Pd interface surface. Although the precise mechanism controlling pore coverage is unknown, *i.e.* whether the deposited film fills the surface pores or whether they are bridged by increasing film thickness on the surrounding particles, it is possible that the pores within the interface surface correspond to the open fraction of the alumina substrate surface.

When compared to a porous ceramic or unmodified PSS substrate, the laser melted substrates used within the present work exhibit particularly uniform surfaces with clearly defined pores (cracks). Thus, the internal active surface area of the Pd-Y films may be estimated with a relative degree of certainty. The laser melted surfaces of both composite membranes were analysed using Digimizer image analysis software (Figures 11.30 and 11.31).

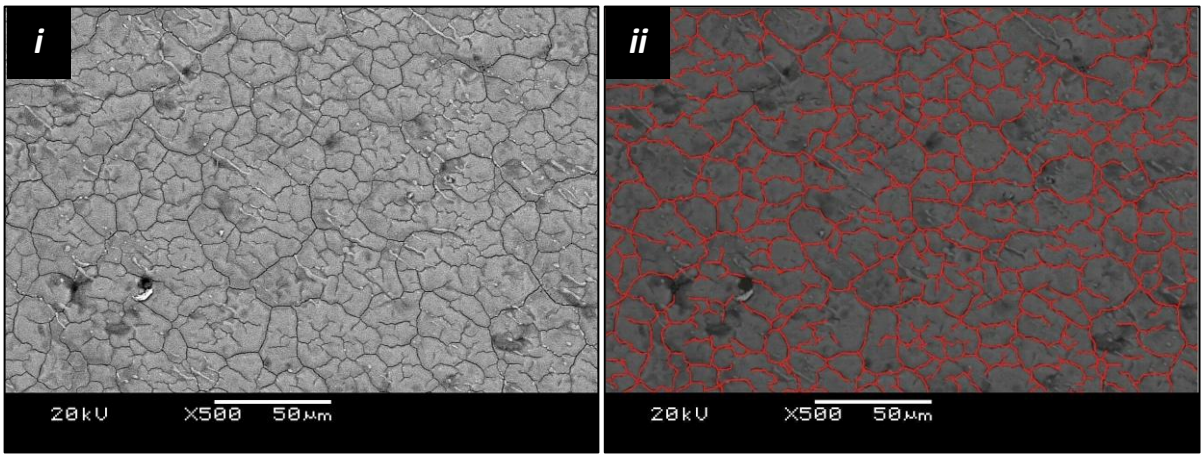

Figure 11.30 – SEM images showing the laser melted surface (i) of CM A substrate with highlighted surface cracking (ii)

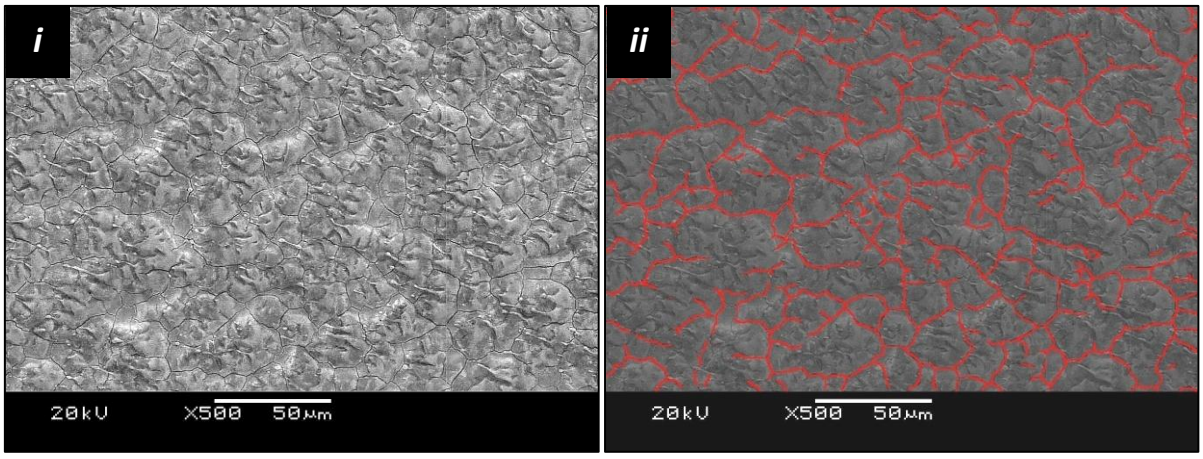

Figure 11.32 – SEM image of laser melted surface (i) of CM B substrate with highlighted surface cracking(ii)

Figures 11.31 and 11.32 show the as-melted surface of both composite membranes (image *i*). The surface cracking was identified and is highlighted in red (image *ii*). Assuming the regions between the cracks are fully dense, and thus impermeable to hydrogen, the total crack area may be regarded as the porosity of the substrate surface. Therefore, assuming good film / substrate adhesion, the active Pd-Y interface area may be estimated. Digimizer image analysis software was used to calculate the percentage surface area of the crack network. The total crack area was calculated as 9.8 % and 5.2 % in membranes A and B respectively. This observation is in good agreement with the previous analysis of both discs including the room temperature hydrogen permeation measurements. Substrate A demonstrates the highest permeance and exhibits an ε / τ ratio of 0.248 compared to 0.198 in substrate B. Considering the similarity in substrate structure and crack shape, the tortuosity τ would be expected to be relatively similar for both discs. Therefore, the greater ε / τ ratio observed in substrate A was attributed to a higher porosity ε, which corresponds to the greater number of surface cracks. Additionally, after the substrate resistance is accounted for, the apparent permeability of Pd-$Y_{Film\text{-}B}$ is significantly lower than that in Pd-$Y_{Film\text{-}A}$. An explanation of lower active membrane area would be compatible with this observation.

Assuming hydrogen only desorbs from the regions of the Pd-Y film directly above the open cracks (the effective interface area), the permeability of each Pd-Y film may be re-calculated using Equation 11.6. The area-corrected permeability values are compared to the uncorrected values and those observed in the bulk alloys in Table 11.9.

Table 11.9 – Comparison of the calculated Pd-Y thin film permeability values with those in bulk Pd-Y

	Hydrogen Permeability Φ @ 400ºC (mol.m^{-1}.s^{-1}.Pa$^{-0.5}$)				
	Thin Film Φ Total Area	Effective Area %	Thin Film Φ Active Area	Bulk Alloy Φ	Thin Film % of Bulk
Membrane A	3.67 x10^{-9}	9.8	3.74 x10^{-8}	5.80 x10^{-8}	64.5 %
Membrane B	2.61 x10^{-9}	5.2	5.02 x10^{-8}	5.61 x10^{-8}	89.5 %

The area-corrected permeability values of both Pd-Y thin films are in much better agreement with the measured bulk values. Pd-Y_{Film-A} exhibits 64.5 % of the permeability of bulk Pd-Y_8 whilst the permeability of Pd-Y_{Film-B} is almost 90 % that of bulk Pd-Y_{10}. Although the crack area calculations are somewhat speculative, several substantiating observations for this approach may be drawn. Firstly, the dense regions of the substrate surface are virtually impermeable to hydrogen and act as barrier to hydrogen flux. Secondly, the surface porosity, or open area for hydrogen transport, is considerably lower than the total geometric area of the substrate surface. Thirdly, it is a reasonable assumption that the regions of the Pd-Y film directly in contact with the dense regions of the substrate surface do not permeate hydrogen. In such a situation, although the hydrogen concentration within the Pd-Y film will be in equilibrium with the applied gas pressure, there is no pressure (concentration) gradient acting across the film, hence there is no driving force for permeation. Fourthly, although the precise pore coverage mechanism in unknown, it is a reasonable assumption that only the regions of

the Pd-Y directly above, or within the close vicinity, of the surface pores have an exposed interface area available for hydrogen desorption.

A useful comparison may be drawn with the data reported by Zhang et al [133], who were able to make an accurate assessment of the active interface area. Zhang [133] deposited 2.5 μm Pd films onto a Si wafer via sputtering. In order to support the Pd film, a grid of Ni strips, each 50 μm wide, was created using photolithography. After removal of the Si wafer, the Pd film had a clearly defined interface area. When corrected for the reduced active surface area, the permeability values were within 50 – 60 % of those measured for self-supporting Pd (700 μm thickness) measured under identical conditions of pressure and temperature. Zhang et al [133] detected residual photo-resist on the Pd surface, which could account for the remaining permeability differences. Thereby demonstrating, in combination with the data on free-standing films reported by Medjell [84] and Gade [85], that with a known active surface area the permeability of thin film Pd and Pd-alloys is in good agreement with the equivalent bulk alloys. Thus supporting the estimation of active surface area made within the current work.

Interestingly, the 10.5 % and 35.5 % differences between the area-corrected Pd-Y film permeability and the bulk alloys are also on a similar scale to what might be expected as a result of Pd-Y / Fe interdiffusion. As previously mentioned, Bryden & Ying [81] reported that the hydrogen permeability of Pd-$Fe_{2.5at.\%}$ is over 50 % lower than pure Pd. Given that the amount of Fe within the Pd-Y film is likely to be much lower than 2.5 at%, and as noted previously is likely to be restricted to the near surface region of the Pd-Y / PSS interface layer, a reduction of permeability by 10 – 35 % would appear reasonable.

Section 12 – General Discussion

Analysis of the structural and permeation characteristics of the individual components that comprise a composite membrane, reveals that the porous substrate contributes significantly to the observed permeation. The porous substrate effects the membrane permeability in two ways: by adding gas-phase transport resistance; and via a reduction in the active membrane area.

The gas phase transport resistance of the porous substrate forms a significant proportion of the total resistance, thus reducing the effective pressure gradient acting across the Pd-Y film. The resistive effect of the porous substrate is likely to be the major source of the observed non-diffusion limited permeation, particularly at high temperatures. In terms of the active area, only a small proportion of the substrate surface is open space, *i.e.* the surface porosity. The remaining area consists of the dense particles which form the substrate structure. The regions of the Pd-Y film in direct contact with the dense sections are unlikely to contribute to the observed hydrogen flux. Although the whole Pd-Y film is exposed to hydrogen, only the regions within the immediate vicinity of a substrate pore, and thus a low-pressure gas phase region, have a hydrogen concentration gradient acting across them.

The multilayer, series resistance approach employed presenting this work, permits the calculation of the hydrogen permeability of the Pd-Y thin film. With the appropriate corrections for resistance and area applied, the thin films exhibit diffusion-controlled permeation and the values of permeability are within 35 % of that in the equivalent bulk Pd-Y alloy. This is in good agreement with the work of Huang et al [163] and Zhang et al [132] who accounted for the resistance and surface area effects of the substrate respectively. In combination with the studies on free-standing Pd, Pd-Ag and Pd-Cu films by Mejdell et al [84]

and Gade et al [85], it is reasonable to assume that the commonly reported 1 to 3 order of magnitude reduction in composite membrane permeability, compared to the equivalent bulk metal / alloy, is predominantly due to the porous substrate. Although several other mechanisms are likely to influence the permeability of the thin film, the effects are likely to be relatively small in comparison to those noted above.

For instance, the inherent structure of deposited thin films differ from that of the equivalent bulk alloy. Grain boundary densities and defect levels generally are likely to be higher in deposited films. In addition, when a porous metallic substrate is employed, as opposed to a ceramic material, there will almost certainly be some degree of intermetallic diffusion at the interface layer. All of these factors could influence the hydrogen permeability of Pd and Pd alloy thin films. However, they are unlikely to account for the reduction in permeability of 1 to 3 orders of magnitude that has typically been reported.

A key factor determining the success of a composite membrane appears to be the interface layer between the dense film and the porous substrate. A major difficulty in refining the interface layer is the lack of direct measurements techniques. Although the surface pore size of the substrate is relatively easy to characterise, the precise pore coverage mechanism is unknown and is likely to vary between deposition techniques, substrate types and pore geometry. Thus, the active area of a composite membrane is specific to the individual structure and must be estimated, often with a great deal of uncertainty. The presence of an interface pressure during operation, due to substrate resistance, results in non-diffusion limited permeation. Therefore, the active permeation mechanism is strongly dependent on the temperature and pressure conditions. In addition, the relative contribution of the active permeation mechanisms is sensitive to the specific structure of each component. Although both composite membranes investigated in the present work were produced almost identically

and exhibited nominally similar structures, there was a 26 % difference in apparent permeability at 400°C, due mainly to a difference in surface porosity.

The effect of the interface porosity on the observed permeability highlights the apparent paradoxical requirements of the substrate surface. To increase the potential hydrogen flux, it is desirable to minimise the membrane thickness. Accordingly, in order to deposit thinner defect-free films, the surface pore size of the substrate must be reduced. However, as shown in the present work, the permeance of the substrate is highly dependent on pore size. Thus a reduction in surface pore size adds considerable resistance to the permeation. Lin and Burggraaf [174] estimated that a reduction in average pore size by a factor of 3 results in a 150 times reduction in permeance. Additionally, a lower surface porosity inevitably leads to a reduction in the active membrane area. Therefore, although by reducing the membrane thickness the potential hydrogen flux increases, the necessary modifications to the substrate surface reduce the permeance of the substrate. As a consequence, the potential benefits of thinner films are likely to be offset by the modified substrate.

The maximum flux of a composite membrane is proportional to the membrane interface area which is available for hydrogen desorption. Therefore, it is desirable to maximise the surface porosity of the substrate, whilst restricting the maximum pore size in order to allow the deposition of a defect-free thin film. The very nature of this duel requirement portends a maximum surface porosity, which must be < 50 %. Given that the maximum pore size is determined by the target membrane thickness, the approach must be to increase the number of pores. With this in mind, the laser melting technique used within the present work may offer a viable substrate surface. The diameter of the surface cracks did not exceed 1.5 μm and, although the porosity fell below 10 %, there is considerable scope for optimising the procedure in an attempt to increase the number of surface cracks / porosity.

The findings of the present work point to interesting consequences for the use of Pd and Pd alloy composite membranes as possible replacements for self-supporting membranes. In combination with the results of Mejdell et al [84], Gade et al [85] and Zhang et al [132], it may be concluded that the inherent permeability of thin film Pd, Pd-Ag, Pd-Cu and Pd-Y is equivalent to that observed in bulk material. However, reducing the thickness of a self-supporting membrane of 25 μm to a composite membrane of 5 μm, will not yield an equivalent increase in observed hydrogen flux, due to the substrate and interface effects. Therefore, larger membrane areas would be required to give equivalent hydrogen throughput. As a consequence, the potential reduction in cost offered by a thinner layer of Pd or Pd alloy might be offset by the greater area of required support and the greater processing costs associated with constructing a composite membrane.

The porous substrate contributes significantly to the overall resistance of a composite membrane, particularly at high temperatures. As a result, the membrane exhibits non-diffusion limited permeation and is inadequately described by the general permeability equation. The observed permeation is highly dependent on the structural characteristics of the composite membrane, even small variations of which have a large effect on hydrogen flux. Thus, unlike for self-supporting membranes, predicting the performance of a composite membrane is a complex process and specific to each individual membrane.

Additionally, considering the inherent structure of deposited films and the nature of reducing film thickness whilst retaining a certain surface pore size, it is doubtful that a deposited composite membrane will be completely defect-free. Although defect-free composite membranes have been reported, the selectivity is reduced considerably during operation as defects form, thus precluding ultra-pure applications. It is likely therefore, that composite

membranes might have a role where a low density of pinholes could be tolerated and lower grade gas purity was acceptable.

Chapter 5 - Conclusions

Section 13 – General Conclusions

The hydrogen permeability of thin film Pd-Y composite membranes has been determined for the first time. In order to make a valid comparison with the permeability of bulk alloys, a series of self-supporting Pd-Y membranes were also investigated. The Pd-Y thin film membranes were co-deposited, with compositions of Pd-$Y_{8.31}$ and Pd-$Y_{10.38}$, onto porous stainless steel substrates by magnetron sputtering. Prior to membrane deposition, a novel laser melting technique was employed to melt the near-surface region of the porous stainless steel substrates.

Laser-melting was found to reduce the roughness and pore size of the porous stainless steel surface. The extent of the pore size reduction was found to be proportional to the laser fluence. A fluence of ≥ 2400 mJ.cm^{-2} produced a smooth, almost fully-dense, surface layer. While a degree of surface porosity was retained by controlling the laser pulse number. High pulse numbers (≥ 300) were found to induce a network of sub-micron cracks within the melted layer. Crack formation was observed in all cases with a pulse number greater than 300, when the laser fluence was at least 1200 mJ.cm^{-2}, although cracking was more prevalent at higher fluences.

Coating the porous stainless discs with either 10 or 15 μm of stainless steel prior to laser melting was found to further reduce the roughness of the melted surface and increase uniformity. It is proposed that the formation of micro-cracks in the melted layer is a result of

the rapid cooling experienced during laser-melting. The optimum surface conditions for Pd-Y membrane deposition, *i.e.* low roughness and a high number of sub-micron pores, were achieved using a laser fluence of ≥ 2400 mJ.cm^{-2}, ≥ 300 pulses and a pre-coated (10-15 μm SS) substrate.

The laser melting procedure was carried out in air, thus the surfaces exhibited a degree of surface oxidation which was identified as a mixture of $FeCrO_4$, Fe_3O_4 and Cr_2O_3 by Raman Spectroscopy. The presence of the surface oxide limited the Pd-Y membrane adhesion, particularly during hydrogen absorption. It was necessary to deposit a thin (500 nm) stainless steel adhesion layer followed by high temperature annealing (10^{-5} mbar, 750°C, 30 mins) prior to Pd-Y deposition, to prevent delamination during membrane operation.

The near-surface laser melting reduced the hydrogen permeability of the substrates by approximately 50 %, although the actual reduction was dependent on the laser parameters. Heating the laser melted substrate above 350°C induced a non-reversible increase in surface porosity, as evidenced by an increase in permeability. It was proposed that thermal expansion of the melted layer and underlying particles creates stresses within the melted layer, thus augmenting the existing surface cracks.

The permeation of hydrogen, nitrogen and argon through the porous substrates was found to be a combination of Knudsen diffusion and Poiseuille flow. The Knudsen and Poiseuille permeation coefficients were determined experimentally for each substrate. The calculated H_2 / N_2 Knudsen coefficient ratio of 3.70 is in good agreement with the theoretical value of 3.73, as indeed were the Poiseuille H_2 / N_2 ratio of 1.97 compared to 2.01. Using the measured Knudsen and Poiseuille coefficients, the geometrical factors of the substrate: the pore size; porosity; and tortuosity may be calculated. The geometric factors can then be used

to project the observed gas flux under any conditions of pressure and temperature to within ± 3 %.

In order to create a gas-tight seal across the Pd-Y / PSS composite membranes, the laser melted substrates were pressed into the inner section of UHV copper gaskets and circumferentially laser welded prior to Pd-Y deposition. This process resulted in significant additional cracking along the laser weld. After Pd-Y deposition, the composite membranes exhibited pinholes in and around these regions.

The presence of pinholes within the Pd-Y layer affects the selectivity of the composite membrane. At 450ºC, the H_2 / N_2 selectivity factors were calculated as 5.86 and 5.40. Therefore, a significant proportion of the observed hydrogen flux across the composite membranes was due to molecular transport through the pinholes. In order to account for the molecular transport, permeation measurements were performed using nitrogen. The nitrogen / hydrogen Knudsen diffusion and Poiseuille flow ratios were established using non-coated substrates and were found to be in good agreement with the theoretically calculated values. Therefore, the measured nitrogen Knudsen and Poiseuille coefficients were factored to calculated the appropriate hydrogen coefficients.

When corrected for pinholes, the effective permeability was calculated. Both composite membranes exhibited non-diffusion limited permeation. The exponential pressure dependence *n* of the membranes was calculated to be 0.70 and 0.74. This is in contrast to the values obtained for the equivalent bulk alloys of 0.52 and 0.54. In addition, the permeability of the thin film composite membranes at 400°C was just 4.1 and 3.2 % of the bulk alloys. This observation is in good agreement with those typically reported for Pd, Pd-Ag and Pd-Cu composite membranes.

A series resistance model was used to calculate the contribution of the substrate to the total transport resistance. The hydrogen permeation coefficients, measured for each substrate prior to Pd-Y deposition, were used to calculate the pressure gradient across the substrate. At 180°C the substrate accounted for approximately 1 % of the total resistance in each composite membrane. As the temperature increased, the resistance of the Pd-Y film decreased whilst the resistance of the substrate increased. At 450°C, the substrate accounted for 40.2 % and 34.6 % of the total resistance in composite membranes A and B, respectively.

When corrected for the resistance of the substrate, both composite membranes, and therefore the Pd-Y thin films, exhibited diffusion limited permeation. The calculated pressure exponents *n* of 0.53 and 0.58 are in good agreement with those calculated for the bulk alloys. It may be concluded therefore, that the non-diffusion limited permeation observed for the composite membranes was a result of the substrate resistance.

However, the resistance of the substrate does not fully explain the low permeability values. After correcting for the resistance, the permeability of the Pd-Y thin films were only 6.3 % and 4.7 % of that in the equivalent bulk alloys. It was proposed that the low permeability values were due to a reduction in active membrane area. The dense regions of the substrate surface are impermeable to hydrogen, thus the areas of Pd-Y film in contact with these regions are unlikely to contribute to the observed flux. Therefore, in order to estimate the active area of the Pd-Y thin films, the surface porosity of the substrates was calculated. The average surface porosity of the substrates was calculated to be 9.8 % and 5.2 %.

When the appropriate corrections have been made for the reduced active area, and the substrate resistance, the permeability of the Pd-Y thin films at 400°C are 65.5 % and 90.5 % of the equivalent bulk alloys. Although no direct evidence was found, some degree of

Pd-Y / Fe interdiffusion at the interface is likely to have occurred, forming a dilute Pd-Y-Fe solid solution, the presence of which may account for the remaining differences in permeability. Although, based on the work of Prosperi [112], the penetration of Fe into the Pd-Y film was estimated to be less than 100 nm, Fe additions of just 2.5 at.% to Pd are known to reduce the permeability by over 50 % [81].

The activation energies for hydrogen permeation through the Pd-Y thin films (32.3 and 31.5 $kJ.mol^{-1}$) were significantly higher than those for the bulk alloys (23.3 and 19.5 $kJ.mol^{-1}$). The occurrence of Pd-Y / Fe interdiffusion may account for this variation. Another possibility is that the thin film alloys and the bulk alloys display different states of order. The activation energy of the bulk Pd-Y_8 alloy (23.3 $kJ.mol^{-1}$) is in good agreement with the previously reported value for 'ordered' Pd-Y_8 (25.3 $kJ.mol^{-1}$) [55], whilst the thin film Pd-Y_8 value (32.3 $kJ.mol^{-1}$) is a close match to the 'disordered' value (34.2 $kJ.mol^{-1}$) [55].

When considering that the presence of the substrate was found to be the predominant source of the differences in permeability between the composite membranes and the bulk alloys, there is considerable scope for refining the structure of the substrate. Graded, asymmetric structures offer less permeation resistance, whilst the surface porosity may be increased whilst retaining the necessary pore dimensions required for the deposition of a defect-free film. It would appear therefore, that further investigations into composite membranes should be focussed on developing more suitable porous structures.

Section 14 – Further Work

The permeability of thin film Pd-Y alloys have been shown to be similar to that in bulk Pd-Y. This observation, in combination with studies on free-standing Pd, Pd-Ag and Pd-Cu thin films, demonstrates that the poor performance of composite membranes compared to bulk membranes is due to the porous substrate. Thus, there is considerable justification for refining the structure of the substrate.

- In order to retain the potential permeability of the thin film, any refinements to the substrate should be made with 3 objectives: to reduce the transport resistance; to increase the surface porosity; and to limit the maximum surface pore size.
- Near-surface melting with an excimer laser produced consistent surface crack sizes of less than 1 µm. Therefore, further development of this technique should focus on increasing the number of surface cracks, *i.e.* the surface porosity.
- The observation of increased surface cracking with the number of laser pulses, suggests that the crack formation is dependent of the laser / surface interaction time. Therefore, adjustment of the laser parameters to maximise the interaction time should be made. During this work the laser frequency (50 Hz) and pulse time (12 ns) remained constant. Increasing these parameters would significantly increase the laser / surface interaction time.
- Further modification to the laser melting process would include the use of an inert gas shroud. Some of the problems experienced during this work arose from the high degree of surface oxidation during laser melting. The use of an argon shroud may limit the oxide formation whilst retaining the surface crack development.

- The transport resistance of the substrate may be reduced through the use of higher media grade substrates. Although only 0.1 µm media grade PSS was investigated during this work, the versatility of the laser melting process suggest that surfaces with greater pores sizes could be treated effectively.
- Further development of the substrate structure would include the use of graded, multilayered porous media. Although this approach is relatively common for ceramic porous separation membranes, there is little information regarding graded porous metals.

Another way of interpreting the corresponding permeability of thin films to the equivalent bulk alloys, is that for any given substrate, the maximum achievable flux will be higher for Pd-Y thin films than for Pd, Pd-Ag or Pd-Cu thin films. Accordingly, there are several possible areas for further investigation.

- Further investigation of the possible order / disorder of thin film Pd-Y. Based on activation energy calculations, it was proposed that the Pd-Y thin films investigated during this work exhibited the disordered structure. The ordered structure has been reported to possess much higher permeability than the disordered structure, particularly at lower temperatures (< 300°C). In addition, to higher permeability, an ordered Pd-Y thin film could be operated at lower temperatures, thus reducing the resistance of the substrate and any film / substrate interdiffusion effects. Therefore, an ordered Pd-Y thin film would offer substantially greater flux than a disordered film.
- Further investigation of the Pd-Y film / substrate interface. A profiling technique such as SIMS, may allow the extent of any possible Pd-Y / Fe interdiffusion to be detected.
- Investigate the deposition of Pd-Y- ternary alloys, in an attempt to add tolerance to certain impurities including sulphur species.

Appendix I

Method for Determining Membrane Geometry

The combination of lattice expansion due to hydrogen absorption and a pressure gradient acting across the membrane caused the self-supporting rolled foil membranes to deform uniformly across the diameter (Figure i).

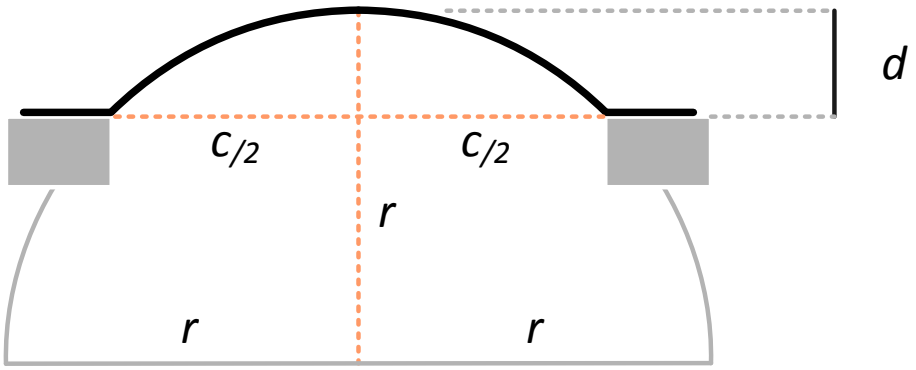

Figure i – Schematic drawing of the uniform deformation of rolled foil membranes after permeability testing

The vertical displacement, *d*, was established using a con-focal microscope, described in Section 8.3.2. Assuming uniform deformation over the active surface, the actual surface area was calculated using simple geometry. The surface area of a hemisphere is given by,

$$A = 2\pi r^2 \qquad \textit{Eqn. i}$$

therefore, the surface area of the deformed membrane is given by,

$$A_m = 2\pi r d \qquad \textit{Eqn. ii}$$

where d is the vertical displacement and r is the radius of the sphere which, in the current circumstances, can be calculated by,

$$r = \frac{c^2 + 4d^2}{8d} \qquad \textit{Eqn. iii}$$

where c is the original membrane diameter. Combining equations *ii* and *iii* gives,

$$A_m = 2\pi d \left[\frac{c^2 + 4d^2}{8d}\right] \qquad \textit{Eqn. iv}$$

which can be reduced to,

$$A_m = \pi \left[\frac{c^2}{4} + d^2\right] \qquad \textit{Eqn. v}$$

In all cases the original membrane diameter, c, was equal to 18 mm, whilst the vertical displacement was determined for each membrane and ranged between 1 and 2.1 mm.

Assuming constant membrane volume, the membrane thickness must decrease proportionally as the membrane area increases. The actual membrane thickness, t_m, was calculated as,

$$t_m = \frac{A_o\, t_o}{A_m} \qquad \textit{Eqn. vi}$$

where, A_o and t_o are the original membrane area and thickness respectively. If the permeability is calculated using the original membrane area and thickness, a vertical displacement of 1 mm was found to increase the apparent permeability by 5.3 %, whilst a displacement of 2.1 mm produced a 10.05 % shift.

Appendix II

Calculating the Composite Membrane Interface Pressure

The transport of pure gases through porous media with a pore radius > 1.5 nm is due to a combination of Knudsen diffusion and Poiseuille flow [173]. Therefore, the hydrogen flux, $J_{H2,}$ across a porous stainless steel substrate may be described by the linear expression,

$$J_{H_2} = \left[\alpha_K + \beta_V \left(\frac{P_i + P_{ii}}{2}\right)\right](P_i - P_{ii}) \qquad \textit{Eqn. i}$$

where α_K and β_V represent the Knudsen and Poiseuille permeation coefficients respectively, *Pi* denotes the feed gas pressure and *Pii* the permeate gas pressure. The values J_{H2}, *Pi* and *Pii* are usually determined experimentally whilst α_K and β_V are calculated through regression of the experimental data. When a composite membrane is operated in the film → substrate direction, the high pressure term *Pi* is replaced by the pressure at the film / substrate interface, P_{int}.

However, the value of P_{int} may not be determined experimentally. Therefore, equation *i* is re-arranged to give a quadratic expression for P_{int}. After substitution of P_{int} for *Pi*, equation *i* may be expanded to give,

$$2J_{H_2} = 2\alpha_K P_{int} - 2\alpha_K P_{ii} + \beta_V P_{int}^2 - \beta_V P_{ii}^2 \qquad \textit{Eqn. ii}$$

Equation *ii* is then re-arranged to give the general form,

$$\beta_V P_{int}^2 + 2\alpha_K P_{int} - \left(2\alpha_K P_{ii} + \beta_V P_{ii}^2 + 2J_{H_2}\right) = 0 \qquad \textit{Eqn. iii}$$

$$ax^2 + bx + c = 0$$

where the variable *x* and the numerical coefficients *a*, *b* and *c* are assigned as,

$x = P_{int}$

$a = \beta_V$

$b = 2\alpha_K$

$c = -\left(2\alpha_K Pii + \beta_V Pii^2 + 2J_{H2}\right)$

The numerical coefficients *a*, *b* and *c* are inserted into the quadratic formula,

$$x = \frac{-b \pm \sqrt{b^2 - 4ac}}{2a}$$

To give the value of P_{int} as,

$$P_{int} = \frac{-2\alpha_K \pm \sqrt{2\alpha_K^2 - 4\beta_V\left(-\left(2\alpha_K P_{ii} + \beta_V P_{ii}^2 + 2J_{H_2}\right)\right)}}{2\beta_V} \qquad \textit{Eqn. iv}$$

Reference List

1. Meyers, R.A., *Handbook of petroleum refining processes. Third edition.* 2004, New York: McGraw-Hill.
2. Nenoff, T.M., Spontak, R.J., and Aberg, C.M., *Membranes for hydrogen purification: An important step toward a hydrogen based economy.* MRS Bulletin, 2006. **31**: p. 735.
3. Lu, G.Q., Costa, J.C., Duke, M., Giessler, S., Socolow, R., Williams, R.H., and Kreutz, T., *Inorganic membranes for hydrogen production and purification: A critical review and perspective.* Journal of Colloid and Interface Science, 2007. **314**: p. 589.
4. Dolan, M.D., Dave, N.C., Ilyushecechkin, A.Y., Morpeth, L.D., and McLennan, K.G., *Composition and operation of hydrogen selective amorphous alloy membranes.* Journal of Membrane Science, 2006. **285**: p. 30.
5. Cheng, X., Shi, Z., Glass, N., Zhang, L., Zhang, J., Song, D., Liu, Z.S., Wang, H., and Shen, J., *A review of PEM hydrogen fuel cell contamination: Impacts, mechanisms and mitigation.* Journal of Power Sources, 2007. **165**: p. 739.
6. *The hydrogen economy: Opportunities, Costs, Barriers and R&D needs.* Commitee on alternatives and strategies for future hydrogen production and use. National research council, National academy of engineering. (National academy press, Washington, DC), 2005.
7. Hagg, M.B. and Quinn, R., *Polymeric facilitated transport membranes for hydrogen purification.* MRS Bulletin, 2006. **31**: p. 750.
8. DoE, U.S., *Technical plan - Hydrogen production.* 2003. **3.1**: p. 17.
9. Tosti, S., *Sputtered, electroless and rolled Pd ceramic membranes.* Journal of Membrane Science, 2002. **196**: p. 241.
10. Starkov, V., *Highly efficient to hydrogen permeability Pd membranes supported in porous Si.* Phys. Stat. Sol, 2005. **9**: p. 3457.
11. Lee, D.W., Lee, Y.G., Nam, S.E., Ihm, S.K., and Lee, K.H., *Study on the variation of morphology and separation behaviour of the stainless steel supported membranes at high temperature.* Journal of Membrane Science, 2003. **220**: p. 137.
12. Ryi, S.K., Park, J.S., Kim, S.H., Cho, S.H., Park, J.S., and Kim, D.W., *Development of a new porous metal support of metallic dense membrane for hydrogen separation.* Journal of Membrane Science, 2006. **279**: p. 439.
13. Uemiya, S., Kude, Y., Sugino, K., Sato, N., Matsuda, T., and Kikuchi, E., *A Pd / porous glass composite membrane for hydrogen separation.* Chem. Lett, 1988: p. 1687.
14. Mardilovich, P.P., She, Y., Ma, Y.H., and Rei, M.H., *Defect free Pd membranes on porous stainless steel support.* AICHEJ, 1998. **44**(2): p. 310.
15. Fort, D., Farr, J.P.G., and Harris, I.R., *A comparison of Pd-Ag and Pd-Y alloys as hydrogen separation membranes.* Journal of Less Common Metals, 1975. **39**: p. 293.
16. Miller, G.Q. and Stocker, J., *Selection of a hydrogen separation process.* National Petrochemical and Refiners Association: San Francisco, CA, 1989.
17. NETL, *Capital and operating cost of hydrogen production from coal gasification.* National Energy Technology Laboratory, US DoE, 2005.
18. Hinchcliffe, A.B. and Porter, K.E., *A comparison of membrane separation and distillation.* Trans. Inst. Chem. Eng, 2000. **78**: p. 255.
19. Burggraaf, A.J., *Single gas permeation of thin zeolite (MFI) membranes: theory and analysis of experimental observations.* Journal of Membrane Science, 1999. **155**: p. 45.
20. Hsieh, H.P., *Membranes for separation and reaction*. Membrane Science and Technology Series 3. 1996, Amsterdam: Elsevier.

21. Ryi, S.K., Park, J.S., Choi, S.H., Cho, S.H., and Kim, S.H., *Fabrication and characterisation of metal porous membrane made of Ni powder for hydrogen separation.* 2006.
22. Burggraaf, A.J., *Transport and separation properties of membranes with gases and vapours*. Fundamental of inorganic membrane science and technology, ed. A.J. Burggraaf and L. Cot. 1996: Elsevier Science.
23. Hirschfelder, Curtiss, and Bird, *Molecular theory of gases and liquids*. 1954, New York: Wiley.
24. Beuscher, U. and Gooding, C.H., *Characterization of the porous support layer of composite permeation membranes.* Journal of Membrane Science, 1997. **132**: p. 213.
25. Hollein, V., Thornton, M., Quicker, P., and Dittmeyer, R., *Preparation and characterisation of Pd composite membranes for hydrogen removal in hydorcarbon dehydrogenation membrane reactors.* Catal. Today, 2001. **67**: p. 33.
26. IUPAC, *Terminology for membranes and membrane processes.* Journal of Membrane Science, 1996. **120**: p. 149.
27. Paglieri, S.N. and Way, J.D., *Innovations in Palladium Membrane Research.* Separation and Purification Methods, 2002. **31**(1): p. 1.
28. Quicker, P., Hollein, V., and Dittmeyer, R., *Catalytic dehydrogenation of hydrocarbons in Pd composite membrane reactors.* Catal. Today, 2000. **56**(1-3): p. 21.
29. *Johnson Matthey - Pd membrane hydrogen purifiers: "Outside-in or Inside-out" flow - Which design is best for compound semiconductors*, in *Tech Bulletin O303*.
30. Sandrock, G., *A panoramic overview of hydrogen storage alloys from a gas reaction point of view.* Journal of Alloys and Compounds, 1999. **293-295**: p. 877.
31. Buxbaum, R.E. and Marker, T.L., *Hydrogen transport through non-porous membranes of Pd coated Nb, Ta & V.* Journal of Membrane Science, 1993. **85**: p. 29.
32. Graham, T., *Absorption and separation of gases by colloid septa.* Phil. Trans. Roy. Soc, 1866. **156**(399): p. 426.
33. Sakamoto, F., Kinari, Y., Chen, F.L., and Sakamoto, Y., *Hydrogen permeation through Pd alloy membranes in mixture gases of 10% nitrogen and ammonia in the hydrogen.* International Journal of Hydrogen Energy, 1997. **22**(4): p. 369.
34. Jewell, L.L. and Davies, B.H., *Review of absorption and adsorption in the Pd-H system.* Applied Catalysis A: General, 2006. **310**: p. 1.
35. Wise, M.L.H., Farr, J.P.G., and Harris, I.R., *X-Ray studies of the a/b miscibility gaps of some Pd solid solution hydrogen systems*. Journal of Less Common Metals, 1975. **41**: p. 115.
36. Ackerman, F.J. and Koskinas, G.J., *Permeation of hydrogen and deuterium through Pd-Ag alloys.* Journal of Chemical and Engineering Data, 1972. **17**(1): p. 51.
37. Serra, E., Kemali, M., Perujo, A., and Ross, D.K., *Hydrogen and deuterium in Pd-25 Pct Ag alloy: Permeation, Diffusion, Solubilization and Surface reaction.* Met. Mat. Trans. A, 1998. **29**(A): p. 1023.
38. Howard, B.H., Killmeyer, R.P., Rothenberger, K.S., Cugini, A.V., Morreale, B.D., Enick, R.M., and Bustamante, F., *Hydrogen permeance of Pd-Cu alloy membrane over a wide range of tmepratures and pressures.* Journal of Membrane Science, 2004. **241**: p. 207.
39. Morreale, B.D., Ciocco, M.V., Howard, B.H., Killmeyer, R.P., Cugini, A.V., and Enick, R.M., *Effect of H2S on the hydrogen permeance of Pd-Cu alloys at elevated temperatures.* Journal of Membrane Science, 2004. **241**: p. 219.
40. Iyoha, O., Enick, R.M., Killmeyer, R.P., and Morreale, B.D., *The influence of H2S to H2 partial pressure on the sulfiization of Pd and 70mol% Pd-Cu membranes.* Journal of Membrane Science, 2007. **305**: p. 77.
41. Piper, J., *Diffusion of hydrogen in Copper-Palladium alloys.* Journal of Applied Physics, 1966. **37**(2): p. 715.
42. Harris, I.R. and Norman, M., *The electronic state of cerium in some Pd alloys.* Journal of Less Common Metals, 1968. **15**: p. 285.
43. Hume-Rothery, W., *Electrons, Atoms, Metals and Alloys. III Edition*. 1963, New York: Dover Publications.

44. Loebich, O. and Raub, E., *Die Liegierungen des Palladiums mit Yttrium, Samariam, Gadolinium, Dysprosium, Hafnium & Erbium.* Journal of Less Common Metals, 1973. **30**: p. 47.
45. Eastman, D.E., Cashion, J.K., and Switendick, A.C., Phys. Rev. Lett., 1971. **27**: p. 35.
46. Doyle, M., *Order-Disorder solid state transformations and hydrogen solubility in a range of Pd-Y solid solution alloys*. 1989, Ph.D Thesis. University of Birmingham.
47. Doyle, M. and Harris, I.R., *Pd rare earth alloys: Their order-disorder transformations and behaviour with hydrogen.* Platinum Metals Rev., 1988. **32**(3): p. 130.
48. Baranowski, B., Majchrzak, S., and Flanagan, T.B., *The volume increase of FCC metals and alloys due to interstitial hydrogen over a wide range of hydrogen contents.* J. Phys. F: Metal Phys, 1971. **1**: p. 258.
49. Knapton, A.G., *Palladium alloys for hydrogen diffusion membranes.* Platinum Metals Rev., 1977. **21**(2): p. 44.
50. Ward, T.L. and Dao, T., *Model of hydrogen permeation behaviour in palladium membranes.* Journal of Membrane Science, 1999. **153**: p. 211.
51. Yoshihara, M. and McLellan, B., *The thermodynamics of hydrogen in Pd-Y solid solutions.* Acta Metall., 1988. **36**(2): p. 385.
52. Yoshinari, O., Matsuda, H., Fukuhara, K., and Tanaka, K., *Hydrogen diffusivity and solubility in Pd-Y alloys.* Materials Transactions, 1997. **38**(6): p. 508.
53. Hughes, D.T. and Harris, I.R., *A comparative study of hydrogen permeabilities and solubilities in some palladium solid solution alloys.* Journal of Less Common Metals, 1978. **61**: p. 9.
54. Doyle, M., Wileman, R.C., and Harris, I.R., *Electrical resistance and hydrogen solubility anomalies in a PdY8at% solid solution alloy.* Journal of Less Common Metals, 1987. **130**: p. 79.
55. Wileman, R.C., *A study of the uses of some Pd alloy membranes for use in hydrogen isotope separation*. 1987, Ph.D Thesis. The University of Birmingham.
56. Wileman, R.C. and Harris, I.R., *The permeability behaviour of protium and deuterium through a Pd-7.5at% Y membrane.* Journal of Less Common Metals, 1985. **109**: p. 367.
57. Hughes, D.T., Evans, J., and Harris, I.R., *The influence of order on hydrogen diffusion in the solid solution alloys Pd-Ce5.75 and Pd-Y8.* Journal of Less Common Metals, 1980. **74**: p. 255.
58. Poyser, P.A., Kemali, M., and Ross, D.K., *Deuterium absorption in Pd-Y10 alloy*. Journal of Alloys and Compounds, 1997. **253-254**: p. 175.
59. Fukai, Y. and Sugimoto, H., *Diffusion of hydrogen in metals.* Advances in Physics, 1985. **34**(2): p. 263.
60. Wert, C.A. and Zener, C., *Interstitial atomic diffusion coefficients.* Phys. Rev. Lett., 1949. **76**(8): p. 1169.
61. Vargas, P., Miranda, L., and Rodriguez, L., *Quantum diffusion in transition metals.* Journal of Less Common Metals, 1991. **172-174**: p. 557.
62. Kehr, K.W., *Hydrogen in metals I*. Hydrogen in metals, ed. G. Alefeld and J. Volkl. 1978, Berlin: Springer Verlag.
63. Volkl, J. and Alefeld, G., *Hydrogen in Metals I*, ed. J. Volkl and G. Alefeld. 1978, Berlin: Springer-Verlag. 321.
64. Barlag, H., Opara, L., and Zuchner, H., *Hydrogen Diffusion in Pd based FCC alloys.* Journal of Alloys and Compounds, 2002. **330-332**: p. 434.
65. Holleck, G.L., *Diffusion and solubility of hydrogen in Pd and Pd-Ag alloys.* J. Phys. Chem., 1970. **73**(3): p. 503.
66. Sakamoto, Y., Kaneko, T., Tsukahara, T., and Hirata, S., Scripta Metall., 1987. **21**: p. 415.
67. Ishikawa, T. and McLellan, B., *The diffusivity of hydrogen in Pd-Y-H ternary solid solutions.* Acta Metall., 1987. **35**(3): p. 781.
68. Buchold, H., Sicking, G., and Wicke, E., Journal of Less Common Metals, 1976. **49**: p. 85.

69. Unemoto, A., Kaimai, A., Otake, T., Yashiro, K., Kawada, T., Mizusaki, J., Tsuneki, T., and Yasuda, I., *Hydrogen permeability of Pd alloy membrane at high temperatures in the impurity gases co-existing atmospheres.* WHEC 16, 2006. **13-16 June**: p. 1.
70. Li, A. and Hughes, R., *The effect of carbon monoxide and steam on the hydrogen permeability of a Pd / SS membrane.* Journal of Membrane Science, 2000. **165**: p. 135.
71. Nam, S.E. and Lee, K.H., *A study on the Pd-Ni composite membrane by vacuum electrodeposition.* Journal of Membrane Science, 2000. **170**(1): p. 91.
72. Gielens, F.C., Knibbeler, R.J.J., Duysinx, P.F.J., Tong, H.D., Vorstman, M.A.G., and Keurentjes, J.T.F., *Influence of steam and CO2 on the hydrogen flux through thin Pd/Ag and Pd membranes.* Journal of Membrane Science, 2006. **279**: p. 176.
73. Iyoha, O., Enick, R.M., Killmeyer, R.P., and Morreale, B.D., *The influence of H2S to hydrogen partial pressure ratio on the sulfidization of Pd and 70mol% Pd-Cu membranes.* Journal of Membrane Science, 2007. **305**: p. 77.
74. Kamakoti, P. and Sholl, D.S., *Towards first principles based identification of ternary alloys for hydrogen purification membranes.* Journal of Membrane Science, 2006. **279**: p. 94.
75. Hashi, K., Ishikawa, K., Matsuda, T., and Aoki, K., *Hydrogen permeation characterisitcs of (V, Ta)-Ti-Ni alloys.* Journal of Alloys and Compounds, 2005. **404-406**: p. 273.
76. Hashi, K., Ishikawa, K., Matsuda, T., and Aoki, K., *Hydrogen permeation characterisitcs of multi-phase Ni-Ti-Nb alloys.* Journal of Alloys and Compounds, 2004. **368**: p. 215.
77. Hashi, K., Ishikawa, K., Matsuda, T., and Aoki, K., *Microstructure and hydrogen permeability in Nb-Ti-Co multiphase alloys.* Journal of Alloys and Compounds, 2006. **425**: p. 284.
78. Sakamoto, Y., Chen, F.L., Furukawa, M., and Noguchi, M., *Permeability and diffusivity of hydrogen in Pd rich Pd-Y(Gd)-Ag ternary alloys.* Journal of Alloys and Compounds, 1992. **185**: p. 191.
79. Morreale, B.D., Ciocco, M.V., Enick, R.M., Morsi, B.I., Howard, B.H., Cugini, A.V., and Rothenberger, K.S., *The permeability of hydrogen in bulk Pd at elevated temperatures and pressures.* Journal of Membrane Science, 2003. **212**: p. 87.
80. McKinley, D.L. 1967: US Patent 3,350,845.
81. Bryden, K.J. and Ying, J.Y., *Nanostructured Pd-Fe membranes for hydrogen separation and membrane hydrogenation reactions.* Journal of Membrane Science, 2002. **203**: p. 29.
82. Mardilovich, I.P., Engwall, E.E., and Ma, Y.H., *Dependence of hydrogen flux on the pore size and plating surface topology of asymmetric Pd-PSS membranes.* Desalination, 2002. **144**: p. 85.
83. Balachandran, U., Lee, T.H., Chen, L., Song, S.J., Picciolo, J.J., and Dorris, S.E., *Hydrogen separation by dense cermet membranes.* Fuel, 2006. **85**: p. 150.
84. Mejdell, A.L., Klette, H., Ramachandran, A., Borg, A., and Bredesen, R., *Hydrogen permeation of thin, free standing Pd-Ag23 membranes before and after heat treatment in air.* Journal of Membrane Science, 2008. **307**: p. 96.
85. Gade, S.K., Thoen, P.M., and Way, D., *Unsupported Pd alloy foil membranes fabricated by electroless plating.* Journal of Membrane Science, 2008. **316**: p. 112.
86. Zeng, G., Goldbach, A., and Xu, H.Y., *Impact of support mass flow resistance on low temperature H2 permeation characterisitcs of a Pd-Ag / Al2O3 composite membrane.* Journal of Membrane Science, 2009. **326**: p. 681.
87. Tong, J., Matsumura, Y., Suda, H., and Haraya, K., *Thin and dense Pd/CeO_2/MPSS composite membrane for hydrogen separation and steam reforming of methane.* Separation and Purification Technology, 2005. **46**: p. 1.
88. Jayaraman, V. and Lin, Y.S., *Synthesis and hydrogen permeation properties of ultrathin Pd-Ag alloy membranes.* Journal of Membrane Science, 1995. **104**: p. 251.
89. Keuler, J.N. and Lorenzen, L., *Developing a heating procedure to optimise hydrogen permeance through Pd-Ag membranes of thickness less than 2.2micron.* Journal of Membrane Science, 2002. **195**: p. 203.

90. Thoen, P.M., Roa, F., and Way, D., *High flux palladium copper composite membranes for hydrogen separations.* Desalination, 2006. **193**: p. 224.
91. Meng, G.Y., *Preparation and characterisation of Pd and Pd-Ni alloy membranes on porous substrates by MOCVD with mixed metal B-diketone precursors.* Mat. Res. Bull. , 1997. **32**(4): p. 385.
92. Gryaznov, V.M., *Preparation and catalysis over Pd composite membranes.* Applied Catalysis, 1993. **96**: p. 15.
93. Keuler, J.N., Lorenzen, L., and Miachon, S., *Preparing and testing Pd films of thickness 1-2 micron with high selectivity and high hydrogen permeance.* Separation Science and Technology, 2002. **37**: p. 379.
94. Sun, G.B., Hidajat, K., and Kawi, S., *Ultra thin Pd membrane on a-Al2O3 hollow fibre by electroless plating: High permeance and selectivity.* Journal of Membrane Science, 2006. **284**: p. 110.
95. Keuler, J.N., Lorenzen, L., Sanderson, R.N., and Linkov, V., *Optimising Pd conversion in electroless Pd plating of alumina membranes.* Plat. Surf. Finish, 1997. **84**(8): p. 34.
96. Shi, Z., Wu, S., Szpunar, J.A., and Roshd, M., *An observation of palladium membrane formation on a porous stainless steel substrate by electroless deposition.* Journal of Membrane Science, 2006. **280**: p. 705.
97. Huang, T.C., Wei, M.C., and Chen, H.I., *Preparation of hydrogen permselective palladium silver alloy composite membrane by electroless co-deposition.* Separation and Purification Technology, 2003. **32**: p. 239.
98. Roa, F. and Way, J.D., *The effect of air exposure on Pd-Cu composite membranes.* Applied Surface Science, 2005. **240**: p. 85.
99. Honma, H. and Kanemitsu, K., *Electroless nickel plating on alumina ceramics.* Plat. Surf. Finish, 1987. **74**(9): p. 62.
100. Tong, J., Shirai, R., Kashima, Y., and Matsumura, Y., *Preparation of a pinhole-free Pd-Ag membrane on a porous metal support for pure hydrogen separation.* Journal of Membrane Science, 2005. **260**: p. 84.
101. Shu, J., Grandjean, B.P.A., Ghali, E., and Kaliaguire, S., *Simultaneous deposition of Pd and Ag on porous stainless steel by electroless plating*. Journal of Membrane Science, 1993. **77**: p. 181.
102. Okazaki, J., *Hydrogen permeability study ofthe thin Pd-Ag alloy membranes in the temperature range across the a-b phase transition.* Journal of Membrane Science, 2006.
103. Bosko, M.L., *Characterisation of Pd-Ag membranes after exposure to hydrogen flux at high temperatures.* Journal of Membrane Science, 2007. **306**: p. 56.
104. Hou, K. and Hughes, R., *The effect of external mass transfer, competitive adsorption and coking on hydrogen permeation through thin Pd-Ag membranes.* Journal of Membrane Science, 2002. **206**: p. 119.
105. Hou, K. and Hughes, R., *Preparation of thin and highly stable Pd-Ag composite membranes and simulative analysis of transfer resistance for hydrogen separation.* Journal of Membrane Science, 2003. **214**: p. 43.
106. Yepes, D., Cornaglia, L.M., Irusta, S., and Lombardo, E.A., *Different oxides used as diffusion barriers in composite hydrogen permeable membranes.* Journal of Membrane Science, 2006. **274**: p. 92.
107. Uemiya, S., Matsuda, T., and Kikuchi, E., *Hydrogen permeable Pd-Ag alloy membranes supported on porous ceramics.* Journal of Membrane Science, 1991. **56**: p. 315.
108. Ma, Y.H., Akis, B.C., Ayturk, M.E., Guazzone, F., Engwall, E.E., and Mardilovich, I.P., *Characterisation of intermetallic diffusion barrier and alloy formation for Pd-Cu and Pd-Ag porous stainless steel composite membranes.* Ind. Eng. Chem. Res., 2004. **43**: p. 2936.
109. Roa, F., Way, D., McCormick, R.L., and Paglieri, S.N., *Preparation and characterisation of Pd-Cu composite membranes for hydrogen separation.* Chemical Engineering Journal, 2003. **93**: p. 11.

110. Gao, H., Lin, J., Li, Y., and Zhang, B., *Electroless plating synthesis, characterisation and permeation properties of Pd-Cu membranes supported on ZrO_2 modified porous stainless steel.* Journal of Membrane Science, 2005. **265**: p. 142.
111. Flanagan, T.B. and Park, C.N., *Hydrogen induced rearrangements in Pd-rich alloys.* Journal of Alloys and Compounds, 1999. **161**: p. 293.
112. Prosperi, D., *Investigation of Pd / SS membranes for use in hydrogen separation applications*. 2006, MRes Thesis, University of Birmingham.
113. Nam, S.E. and Lee, K.H., *Hydrogen separation by Pd alloy composite membranes: introduction of diffusion barrier.* Journal of Membrane Science, 2001. **192**: p. 177.
114. Lu, S.Y. and Lin, Y.Z., *Pd-Ag alloy films prepared by metallorganic chemical vapour deposition process.* Thin Solid Films, 2000. **376**: p. 67.
115. McCool, B., Xomeritakis, G., and Lin, Y.S., *Composition control and hydrogen permeation characteristics of sputter deposited palladium silver membranes.* Journal of Membrane Science, 1999. **161**: p. 67.
116. Yang, J.Y., Nishimura, C., and Komaki, M., *Preparation and characterisation of Pd-Cu/V-15Ni composite membrane for hydrogen permeation.* Journal of Alloys and Compounds, 2007. **431**: p. 180.
117. Xomeritakis, G. and Lin, Y.S., *Fabrication of thin metallic membranes by MOCVD and sputtering.* Journal of Membrane Science, 1997. **133**: p. 217.
118. Zhang, Y., Ozaki, T., Komaki, M., and Nishimura, C., *Hydrogen permeation of Pd-Ag alloy coated V-15Ni composite membrane: effects of overlayer composition.* Journal of Membrane Science, 2003. **224**: p. 81.
119. Zhang, Y., Komaki, M., and Nishimura, C., *Morphological study of supported thin Pd and Pd-Ag25 membranes upon hydrogen permeation.* Journal of Membrane Science, 2005. **246**: p. 173.
120. Zhang, Y., Maeda, R., Komaki, M., and Nishimura, C., *Hydrogen permeation and diffusion of metallic composite membranes.* Journal of Membrane Science, 2006. **269**: p. 60.
121. Ryi, S.K., Park, J.S., Kim, S.H., Cho, S.H., Kim, D.W., and Um, K.Y., *Characterisation of Pd-Cu-Ni ternary alloy membrane prepared by magnetron sputtering and Cu reflow on porous nickel support for hydrogen separation.* Separation and Purification Technology, 2006. **50**: p. 82.
122. Checchetto, R., Bazzanella, N., Patton, B., and Miotello, A., *Pd membranes prepared by r.f. magnetron sputtering for hydrogen purification.* Surface and Coatings Technology, 2004. **177-178**: p. 73.
123. Jayaraman, V., Lin, Y.S., Pakala, M., and Lin, R.Y., *Fabrication of ultra thin metallic membranes on ceramic supports by sputter deposition.* Journal of Membrane Science, 1995. **99**: p. 89.
124. Zhao, H.B., Xiong, G.X., and Baron, G.V., *Preparation and characterisation of Pd based composite membranes by electroless plating and magnetron sputtering.* Catal. Today, 2000. **56**(1-3): p. 89.
125. Ye, J., Dan, G., and Yuan, Q., *The permeation of ultrathin Pd membranes.* Key Eng. Mater., 1991. **61-62**: p. 437.
126. Ma, Y.H., Mardilovich, I.P., and Mardilovich, P.P., *Effects of porosity and pore size distribution of the porous stainless steel on the thickness and hydrogen flux of palladium membranes.* J. Amer. Chem. Soc, 2001. **46**(2).
127. Li, A., Liang, W., and Hughes, R., *Repair of a Pd/a-Al_2O_3 composite membrane containing defects.* Separation and Purification Technology, 1999. **15**: p. 113.
128. Wu, L.Q., Xu, N., and Shi, J., *Preparation of a Pd composite membrane by an improved electroless plating technique.* Ind. Eng. Chem. Res., 2000. **39**: p. 342.
129. Li, X., Fan, Y., Jin, W., Huang, Y., and Xu, N., *Improved photocatalytic deposition of Pd membranes.* Journal of Membrane Science, 2006. **282**: p. 1.

130. Uemiya, S., Sato, N., Ando, H., Kude, Y., Matsuda, T., and Kikuchi, E., *Separation of hydrogen through Pd thin film supported on a porous glass tube.* Journal of Membrane Science, 1991. **56**: p. 303.
131. Jarosch, K. and de Lasa, H.I., *Novel risor simulator for methane reforming using high temperature membranes.* Chem. Eng. Sci., 1999. **54**: p. 1455.
132. Zhang, Y., Gwak, J., Murakoshi, Y., Ikehara, T., Maeda, R., and Nishimura, C., *Hydrogen permeation characteristics of thin Pd membrane prepared by microfabrication technology.* Journal of Membrane Science, 2006. **277**: p. 203.
133. Zhang, Y., Jian, L., Ikehara, T., Maeda, R., and Nishimura, C., *Characterisation and Permeation of Microfabricated Palladium Membrane.* Materials Transactions, 2006. **47**(2): p. 255.
134. Verweij, H., Lin, Y.S., and Dong, J., *Microporous silica and zeolite membranes for hydrogen purification.* MRS Bulletin, 2006. **31**: p. 756.
135. Mottcorp, *Porous Metal Design Guidebook.* www.mottcorp.com.
136. Li, A., Grace, J.R., and Lim, C.J., *Preparation of thin Pd-based composite membrane on planar metallic substrate. Part I: Pre-treatment of porous stainless steel substrate.* Journal of Membrane Science, 2007. **298**: p. 175.
137. Li, A., Grace, J.R., and Lim, C.J., *Preparation of thin Pd-based composite membrane on planar metallic substrate. Part II Preparation of membranes by electroless plating and characterisation.* Journal of Membrane Science, 2007. **306**: p. 159.
138. Huang, Y. and Dittmeyer, R., *Preparation and characterisation of composite Pd membranes on sinter metal supports with a ceramic barrier against intermetallic diffusion.* Journal of Membrane Science, 2006. **282**: p. 296.
139. Nam, S.E., Lee, S.H., and Lee, K.H., *Preparation of a Pd alloy composite membrane supported in a porous stainless steel by vacuum electrodeposition.* Journal of Membrane Science, 1999. **153**: p. 163.
140. Uemiya, S., *State of the art supported metal membrane for gas separation.* Separation and Purification Methods, 1999. **28**: p. 51.
141. Chen, S.C., Tu, G.C., and Huang, C.A., *The electrochemical polishing behaviour of porous austenitic stainless steel (AISI 316L) in phosphoric-sulfuric mixed acids.* Surface and Coatings Technology, 2005. **200**: p. 2065.
142. Shu, J., Adnot, A., Grandjean, B.P.A., and Kaliaguire, S., *Structurally stable composite Pd-Ag alloy membranes: introduction of a diffusion barrier.* Thin Solid Films, 1996. **286**: p. 72.
143. Nam, S.E. and Lee, K.H., *Preparation and characterisation of Pd alloy composite membranes with a diffusion barrier for hydrogen separation.* Ind. Eng. Chem. Res., 2005. **44**: p. 100.
144. Wang, D., Tong, H.H., Xu, H.Y., and Matsumura, Y., *Preparation of Pd membrane over PSS tube modified with zirconium oxide.* Catal. Today, 2004. **93-05**: p. 689.
145. Huang, Y. and Dittmeyer, R., *Preparation of thin Pd membranes on a porous support with rough surface.* Journal of Membrane Science, 2007. **302**: p. 160.
146. Ayturk, M.E., Mardilovich, I.P., Engwall, E.E., and Ma, Y.H., *Synthesis of composite Pd-PSS membranes with a Pd/Ag intermetallic diffusion barrier.* Journal of Membrane Science, 2006. **285**: p. 385.
147. Ma, Y.H., Mardilovich, P.P., and She, Y. 2000: US Patent 6152987.
148. Beuscher, U. and Gooding, C.H., *The influence of the porous support layer of composite membranes on the separation of binary gas mixtures.* Journal of Membrane Science, 1999. **152**: p. 99.
149. Rothenberger, K.S., Cugini, A.V., Howard, B.H., Killmeyer, R.P., Ciocco, M.V., Morreale, B.D., Enick, R.M., Bustamante, F., Mardilovich, I.P., and Ma, Y.H., *High pressure hydrogen permeance of porous stainless steel coated with a thin Pd film via electroless plating.* Journal of Membrane Science, 2004. **244**: p. 55.
150. Yeung, K., Christiansen, S., and Varma, A., *Pd composite membranes by electroless plating technique, relationship between plating kinetics, film microstructure and membrane performance*. Journal of Membrane Science, 1999. **159**: p. 107.

151. Shu, J., Grandjean, B.P.A., Van Neste, A., Kaliaguire, S., Giroir-Fendler, A., and Dalmon, J., *Hysteresis in hydrogen permeation through Pd membranes.* J. Chem. Soc. Faraday Trans., 1996: p. 2475.
152. Zhang, K., Wei, X., Rui, Z., Li, Y., and Lin, Y.S., *Effect of metal support interface on hydrogen permeation through Pd membranes.* American Institute of Chemical Engineers Journal, 2009. **55**(3): p. 630.
153. Kusakabe, K., Takahashi, M., Maeda, H., and Morooka, S., *Preparation of thin Pd membranes by a novel method based of photolithography and electrolysis.* J. Chem. Eng. Jpn, 2001. **34**: p. 703.
154. Kikuchi, E., *Pd / Ceramic membranes for selective hydrogen permeation and their application to membrane reactor.* Catal. Today, 1995. **25**: p. 333.
155. Li, A., Liang, W., and Hughes, R., *Characterisation and permeation of Pd /PSS composite membranes.* Journal of Membrane Science, 1998. **149**: p. 259.
156. Li, A., Liang, W., and Hughes, R., *Fabrication of dense Pd composite membranes for hydrogen separation.* Catal. Today, 2000. **56**: p. 45.
157. Collins, J.P. and Way, J.D., *Preparation and characteridisation of a composite Pd-ceramic membrane.* Ind. Eng. Chem. Res., 1993. **32**: p. 3006.
158. Guazzone, F., Engwall, E.E., and Ma, Y.H., *Effects of surface activity, defects and mass transfer on hydrogen permeance and n-value in composite Pd-PSS membranes.* Catal. Today, 2006. **118**: p. 24.
159. Uemiya, S., Sato, N., Ando, H., and Kikuchi, E., *The water gas shift reaction assisted by a Pd membrane reactor.* Ind. Eng. Chem. Res., 1991. **67**: p. 585.
160. Liang, W. and Hughes, R., *The effect of diffusion direction on the permeation rate of hydrogen in Pd composite membranes.* Chemical Engineering Journal, 2005. **112**: p. 81.
161. Goto, S., Assabumrungrat, S., Tagawa, T., and Praserthdam, P., *The effect of direction of hydrogen permeation on the rate through a composite Pd membrane.* Journal of Membrane Science, 2000. **175**: p. 19.
162. Ryi, S.K., Park, J.S., Kim, S.H., Cho, S.H., and Kim, D.W., *The effect of support resistance on the hydrogen permeation behaviour in Pd-Cu-Ni ternary alloy membranes deposited on a porous Ni support.* Journal of Membrane Science, 2006. **280**: p. 883.
163. Huang, T.C., Wei, M.C., and Chen, H.I., *Permeation of hydrogen through Pd / Alumina composite membranes.* Separation Science and Technology, 2001. **36**(2): p. 199.
164. Henis, J.M.S. and Tripodi, M.K., *Composite hollow fiber membranes for gas separation: The resistance model approach.* Journal of Membrane Science, 1981. **8**: p. 233.
165. McLeod, L.S., Degertekin, F.L., and Fedorov, A.G., *Determination of the rate limiting mechanism for permeance of hydrogen through microfabricated Pd-Ag alloy membranes.* Journal of Membrane Science, 2009. **341**: p. 225.
166. Beuscher, U. and Gooding, C.H., *The permeation of binary gas mixtures through support structures of composite membranes.* Journal of Membrane Science, 1998. **150**: p. 57.
167. Mason, E.A., Malinauskas, A.P., and Evans, R.B., *Flow and diffusion of gases in porous media.* J. Chem. Phys., 1967. **46**: p. 3199.
168. Mason, E.A. and Malinauskas, A.P., *Gas transport in porous media: The dusty gas model*. Chemical Engineering Monographs 17. 1983, Amsterdam: Elsevier.
169. Veldsink, J.W., Van Damme, R.M.J., Versteeg, G.F., and Van Swaaij, W.P.M., *The use of the dusty gas model for the description of mass transport with chemical reaction in porous media.* Chemical Engineering Journal, 1995. **57**: p. 115.
170. Gabitto, J. and Tsouris, C., *Hydrogen transport in composite inorganic membranes.* Journal of Membrane Science, 2008. **312**(312): p. 132.
171. Shapiro, A.A. and Wesselingh, J.A., *Gas transport in tight porous media. Gas kinetic approach.* Chemical Engineering Journal, 2008. **142**: p. 14.
172. Atkins, P.W., *Physical Chemistry: Sixth Edition*. 1999: Oxford University Press.
173. Uhlhorn, R.J.R., Keizer, K., and Burggraaf, A.J., *Gas and surface diffusion in modified gamme alumina systems.* Journal of Membrane Science, 1989. **46**: p. 225.

174. Lin, Y.S. and Burggraaf, A.J., *Experimental studies onpore size change of porous ceramic membranes after modification.* Journal of Membrane Science, 1993. **79**: p. 65.
175. Caravella, A., Barbieri, G., and Drioli, E., *Modelling and simulation of hydrogen permeation through supported Pd-alloy membranes with a multi-component approach.* Chem. Eng. Sci., 2008. **63**: p. 2149.
176. Evans, J., Harris, I.R., and Ross, D.K., *A proposed method of hydrogen isotope separation using Pd alloy membranes.* Journal of Less Common Metals, 1983. **89**: p. 407.
177. Hirst, J.R., Wise, M.L.H., Fort, D., Farr, J.P.G., and Harris, I.R., *Hydrogen softening in some palladium-rare earth solid solution alloys.* Journal of Less Common Metals, 1976. **49**: p. 193.
178. *UK Patent Number 2,258,343. Teer Coatings Ltd.*
179. Guidebook, P.M.D., *Mottcorp 2*.
180. Davis, W.D., *Diffusion of gases through metals. 1. Diffusion of gases through Pd.* US Atomic Energy Commission Report No. KAPL 1227, 1954.
181. Toda, G., *Rate of permeation and diffusion coefficent of hydrogen through Pd.* J. Res. Inst. Catal, 1958. **6**: p. 13.
182. Balovnev, Y.A., *Diffusion of hydrogen in Pd.* Russ. J. Phys. Chem, 1974. **48**(3): p. 409.
183. Koffler, S.A., Hudson, J.B., and Ansell, G.S., *Hydrogen permeation through alpha-palladium.* Trans. Metall. Soc. AIME, 1969. **245**: p. 1735.
184. Yoshida, H., Konishi, S., and Naruse, Y., *Effects of impurities on hydrogen permeability through Pd alloy membranes at comparatively high pressures and temperatures.* Journal of Less Common Metals, 1983. **89**: p. 429.
185. *316 / 316L Product data sheet*. AK Steel Corporation. 2007.
186. Shen, Y.F., Gu, D.D., and Wu, P., *Development of porous 316L stainless steel with controllable microcellar features using selective laser melting.* Materials Science and Technology, 2008. **24**(12): p. 1501.
187. Gu, D.D. and Shen, Y.F., *Balling phenomena in direct laser sintering of stainless steel powder: Metallurgical mechanisms and control methods.* Materials and Design, 2009. **30**: p. 2903.
188. San Marchi, C., Somerday, B.P., and Robinson, S.L., *Permeability, solubility and diffusivity of hydrogen isotopes in stainless steels at high gas pressures.* International Journal of Hydrogen Energy, 2007. **32**: p. 100.
189. Dahotre, N.B. and Sudarshan, T.S., *Lasers in surface engineering*. 1998: ASM International. 599.
190. Migliore, L.R., *Laser materials processing*. 1996: CRC Press. 319.
191. Assael, M.J., Mixafendi, S., and Wakeham, W.A., *The viscosity and thermal conductivity of normal hydrogen in the zero limit density.* J. Phys. Chem. Ref. Data, 1986. **15**: p. 1315.
192. Jozwiak, W.K., Kaczmarek, E., Manieki, T.P., Ignaczak, W., and Maniukiewicz, W., *Reduction behaviour of iron oxides in hydrogen and carbon monoxide atmospheres.* Applied Catalysis A: General, 2007. **326**: p. 17.
193. CINDAS, *Data series on material properties*. Vol. 3-2. 1980, New York: McGraw-Hill.
194. Roa, F. and Way, J.D., *Influence of alloy compoistion and membrane fabrication on the pressure dependance of the hydrogen flux of Pd-Cu membranes.* Ind. Eng. Chem. Res., 2003. **42**: p. 5827.
195. Ristau, R.A., Barmak, K., Lewis, L.H., Coffy, K.R., and Howard, J.K., Journal of Applied Physics, 1999. **86**: p. 4527.
196. Takahashi, Y.K., Ohnuma, M., and Hono, K., *Effect of Cu on the structure and magnetic properties of FePt sputtered film.* Journal of Magnetism and Magnetic Materials, 2002. **246**: p. 259.
197. Okazaki, J., Ikeda, T., Tanaka, D.A.P., Suzuki, T.M., and Mizukami, F., *In situ high-temperature X ray diffraction studies of thin Pd / alumina composite membranes and their hydrogen permeation properties.* Journal of Membrane Science, 2009. **335**: p. 126.